The Evolution of Dark Matter Haloes in Mergers

by

Nicole Elizabeth Drakos

A thesis
presented to the University of Waterloo
in fulfillment of the
thesis requirement for the degree of
Doctor of Philosophy
in
Physics

Waterloo, Ontario, Canada, 2019

Examining Committee Membership

The following served on the Examining Committee for this thesis. The decision of the Examining Committee is by majority vote.

Supervisor:	James Taylor Associate Professor, Dept. of Physics and Astronomy, University of Waterloo
External Examiner:	Lawrence Widrow Professor, Dept. of Physics, Engineering Physics and Astronomy, Queen's University
Committee Member:	Avery Broderick Associate Professor, Dept. of Physics and Astronomy, University of Waterloo
Committee Member:	Brian McNamara Professor, Dept. of Physics and Astronomy, University of Waterloo
Internal/External Member:	Marcel Nooijin Professor, Dept. of Chemistry, University of Waterloo

This thesis consists of material all of which I co-authored: see Statement of Contributions included in the thesis. This is a true copy of the thesis, including any required final revisions, as accepted by my examiners.

I understand that my thesis may be made electronically available to the public.

Statement of Contributions

This thesis is based on the following articles:

CHAPTER 2: **Drakos, N.E.**, Taylor, J.E. and Benson A.J. The phase-space structure of tidally stripped haloes. *Monthly Notices of the Royal Astronomical Society* 468.2:2345-2358, 2017.

CHAPTER 3: **Drakos, N.E.**, Taylor, J.E. and Benson A.J. An energy-based model for the evolution of tidally stripped systems; universality and applications. In prep.

CHAPTER 4: **Drakos, N.E.**, Taylor, J.E., Berrouet, A., Robotham, A.S.G., and Power, C. Major mergers between dark matter haloes—I. Predictions for size, shape, and spin. *Monthly Notices of the Royal Astronomical Society* 487.1:993-1007, 2019.

CHAPTER 5: **Drakos, N.E.**, Taylor, J.E., Berrouet, A., Robotham, A.S.G., and Power, C. Major mergers between dark matter haloes—II. Profile and concentration changes. Accepted by *Monthly Notices of the Royal Astronomical Society* 487.1:1008-1024, 2019.

For each of these contributions, I setup, ran, and analyzed the computational simulations and did the majority of the writing and analysis. James Taylor suggested a number of the original ideas, helped with the writing (most notably in the introduction and conclusion sections of Chapter 2), and interpretation of the results. Andrew Benson provided a modified N-body code to perform simulations with a fixed background potential and provided feedback for Chapters 2 and 3. Anael Berrouet performed preliminary simulations of mergers that helped develop some of the methodology used in Chapters 4 and 5. Aaron Robotham and Chris Power contributed code and ideas to these initial studies.

Abstract

In the standard Λ-cold dark matter (ΛCDM) cosmological model, the present-day universe contains dominant components of dark energy (Λ) and cold dark matter (CDM). Fluctuations in the initial distribution of dark matter collapse to form dense, gravitationally bound dark matter haloes, which then evolve hierarchically through repeated mergers. Although the ΛCDM model is largely successful in describing our universe, the nature and identity of dark matter and dark energy remain unclear. ΛCDM may have problems describing structure on small scales, while on large scales, there are mild tensions between different estimates of the cosmological parameters. The structural properties of individual dark matter haloes, including their shape, spin, concentration, and substructure, are linked to halo growth history and thus reflect the cosmological model. The goal of this thesis is to understand how dark matter halo structural properties evolve in minor and major mergers, and to study how halo evolution can inform cosmology.

Halo mergers can be classified as either major or minor based on the mass ratio of the merging systems. In minor mergers, smaller subhaloes fall into larger host haloes and evolve through tidal stripping. Predicting the evolution of subhaloes has important applications to studies of galaxy evolution and the nature of dark matter; in particular, the dense central regions of haloes dominate the signal from dark matter annihilation, so understanding how these central regions evolve is important for predicting the strength of the annihilation signal, and thus placing constraints on dark matter particle candidates. In the first part of this thesis (Chapters 2 and 3), we develop a simple, physically motivated model of tidal stripping that can be applied to any collisionless system to predict its structural evolution.

In the second part of the thesis (Chapters 4 and 5), we perform a large suite of simulations of binary equal-mass mergers between isolated haloes with various density profiles to study the effects of major mergers on dark matter halo properties. We find that the axis ratios describing the 3D shapes of the merger remnants vary linearly with a scaled dimensionless energy parameter, κ, and an angular momentum (or spin) parameter, λ. The mass distribution is determined mainly by κ, where energetic (low-κ) encounters produce more extended remnants while mergers of strongly bound (high-κ) systems produce compact remnants. Surprisingly, major mergers seem to be relatively ineffective at changing the central densities of haloes, and thus unlikely to explain the mean trends in the concentration–mass–redshift relation.

Overall, Chapters 2–5 present models for how haloes evolve in mergers, including the evolution of tidally stripped haloes in minor mergers, as well as a description for how halo spin, shape, mass distribution, and concentration evolve in major mergers. In the final

chapter, we discuss a potential application of this work, to develop semi-analytic models of halo structural evolution and use these to predict how halo properties should vary with the cosmological model. Ultimately, the structural properties of haloes could provide powerful cosmological tests that will become feasible with the completion of next-generation surveys.

Acknowledgements

First, I would like to thank my supervisor Dr. James Taylor, for his guidance, support, patience and humor. He not only taught me about astrophysics, scientific writing, and presentations but was also always available with valuable career advice. Additionally I would like to thank the rest of the Astrophysics group, particularly the faculty, all of whom have contributed to my education as a scientist.

This work was dependent on the computing resources of the Shared Hierarchical Academic Research Computing Network (SHARCNET) and Compute Canada. Additionally, I would like to acknowledge the financial support provided through the Ontario Graduate Scholarship program, the Natural Sciences and Engineering Research Council of Canada (NSERC) and the University of Waterloo.

Finally, this would not have been possible without the support of my family. I would like to thank Mark, Ingrid, Ashley and Lindsey Drakos for their understanding and encouragement. I would also like to express my deepest gratitude to Richard Sové for his patience, insightful conversations, and unwavering support.

Table of Contents

List of Tables

List of Figures

Chapter 1

Introduction

Cosmological theory states that the universe consists of three main components; ordinary matter, dark matter, and dark energy. Ordinary, visible, matter is **baryonic**; in an astronomical context, this generally refers to matter made of protons and neutrons (including bound electrons). **Dark matter** is a hypothetical type of matter that is needed to account for observed gravitational effects in the universe. The final component of the universe, **dark energy**, is a theoretical component needed to explain the apparent acceleration of the universe. Although baryonic matter constitutes everything from planets and stars to living organisms, it accounts for a mere five per cent of the mass–energy content of the universe.

According to the current understanding of structure formation, early in the universe, fluctuations in the density of dark matter collapsed to form dark matter haloes which are connected by sheets and filaments. This created the scaffolding in which galaxies and galaxy clusters formed. Dark matter haloes are often studied using numerical **N-body simulations** of gravitationally interacting point particles. These simulations can be used to determine the distribution, abundance and structural properties of haloes; halo structural properties in turn reflect the energy content and growth history of the universe. Additionally, the centres of haloes contain the densest regions of dark matter, allowing tests of the particle nature of dark matter. Thus, understanding the formation of structure and the evolution of dark matter haloes should provide new insights into cosmology.

The outline of this chapter is as follows: the properties and evidence for dark matter will be reviewed in Section 1.1. Section 1.2 will outline the formation and evolution of dark matter haloes. Since dark matter structure is generally studied using N-body simulations, these methods will be discussed in Section 1.3. Section 1.4 will provide examples of how dark matter haloes can be used to study cosmology. Finally, an outline of the thesis will

be given in Section 1.5.

1.1 Dark Matter

There is surprisingly little known about dark matter, considering it is five times more abundant than ordinary matter; for instance, it is still not clear what comprises dark matter. However, it appears that dark matter is non-baryonic and does not interact via the electromagnetic force. For the latter reason it is almost impossible to detect, except through its gravitational effects on visible matter. This section will summarize the main observational evidence for dark matter, and its known properties.

1.1.1 Historical Evidence for Dark Matter

The first evidence for dark matter was discovered nearly 100 years ago by Fritz Zwicky (Zwicky, 1933), who found that in order to explain the velocity dispersion of the Coma galaxy cluster, there needed to be 20 times more mass present than he was able to detect visually. He called this invisible mass "dunkle Materie" or "dark matter", and thus the idea of dark matter was first introduced. The concept that the universe is filled with dark matter regained interest in the 1970s. Starting with work by Rubin & Ford (1970), it was eventually established that some unseen component, such as dark matter, was needed to explain why rotation speeds in the outskirts of galaxies were unexpectedly high.

Within a spherically symmetric mass distribution, circular velocity, v, follows the relation:

$$v(r) = \sqrt{\frac{GM(r)}{r}} \ , \tag{1.1}$$

where $M(r)$ is the mass contained inside radius r, and G is the gravitational constant. Since most of the visible mass is contained in the centre of the galaxy, this indicates that velocity should decrease as $r^{-1/2}$ at large distances; however, Rubin & Ford (1970) found no evidence of this decrease in the Andromeda galaxy. This result was strengthened a few years later, when Roberts & Whitehurst (1975) were able to measure orbital speeds of Andromeda to even greater distances. Subsequently, flat rotation curves were found for numerous other galaxies, including the Milky Way (e.g. Mróz et al., 2019, and references therein). Fig. 1.1 shows an example of a galaxy rotation curve.

In addition to the examples mentioned above, there has been plenty of other evidence that the universe contains large amounts of dark matter. For instance, dark matter has

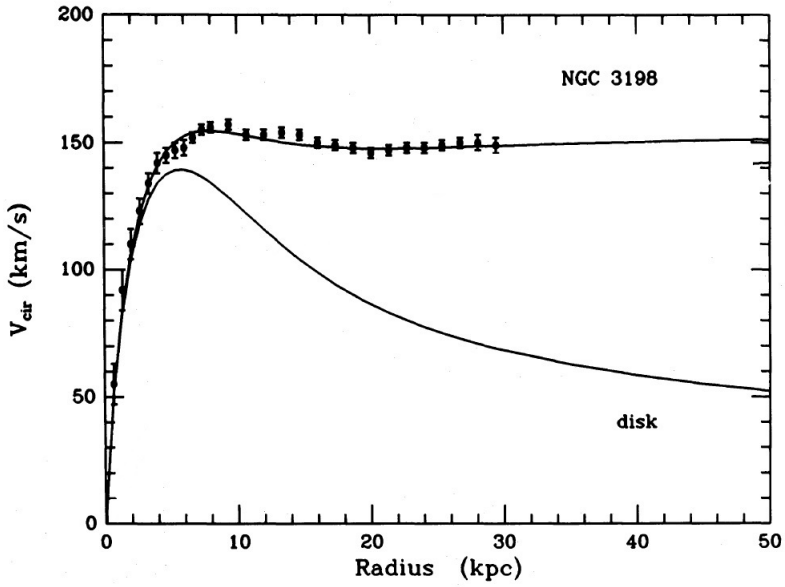

Figure 1.1: Example of a galaxy rotation curve. The observed rotation curve of the galaxy NGC 3196 (points + model fit) is compared to the curve predicted from the mass seen in the visible disk alone. An extra dark matter component is needed to fit the observations. Figure is from Van Albada et al. (1985).

been invoked to explain phenomenon such as why the Milky Way and Andromeda are approaching each other (Kahn & Woltjer, 1959), why cold flat galaxy disks are stable (Ostriker & Peebles, 1973; Ostriker et al., 1974), and why the lensing signal of the Bullet Cluster does not trace its luminous gas distribution (Clowe et al., 2004). Overall, there is an overwhelming amount of evidence supporting the notion of an invisible form of matter filling the universe. Thus, the presence of dark matter is well established, but its fundamental nature remains to be determined.

1.1.2 The Nature of Dark Matter

Dark matter is almost certainly non-baryonic, cold, and collisionless; this section will outline the main evidence for these assertions, and briefly introduce some likely particle candidates. A more thorough discussion can be found in the review by Bertone et al. (2005).

Non-Baryonic

The strongest argument for non-baryonic dark matter comes from the fact that the expected amount of baryonic matter in the universe is simply too small to account for dark matter. As mentioned above, baryonic matter makes up only five per cent of the mass–energy content of the universe. There are two main lines of reasoning that yield this number. The first is from the **Cosmic Microwave Background** (CMB), and the second is from the abundances of light elements observed in the universe.

The early universe was a hot and dense plasma filled with free protons, electrons and photons. As the universe expanded, it cooled. Eventually it reached a point called **recombination**, where protons and electrons combined to form neutral atoms. This allowed for **photon decoupling**; photons ceased to interact with electrons and were free to stream throughout the universe. This left-over radiation from the time of recombination is called the CMB. Since the universe was nearly homogeneous at the time of recombination, the CMB is fairly uniform, with a temperature of 2.725 K.

The temperature fluctuations of the CMB provide information on the conditions of the early universe, which can be seen in the CMB power spectrum. This spectrum is shown in Fig. 1.2. The x-axis shows the multipole moment, which corresponds to the angular scale on the sky. The y-axis is a measure of the temperature fluctuations. The relationship between the CMB power spectrum and energy content of the universe is quite complicated, but qualitatively, the position of the first peak reflects the total energy density of the universe,

the ratio of odd and even peaks gives the ratio of baryonic to non-baryonic matter, and the third peak gives information on the non-baryonic density. Putting this together, the most recent CMB results indicate that baryonic matter accounts for 4.93 ± 0.02 per cent of the universe (Planck Collaboration et al., 2018).

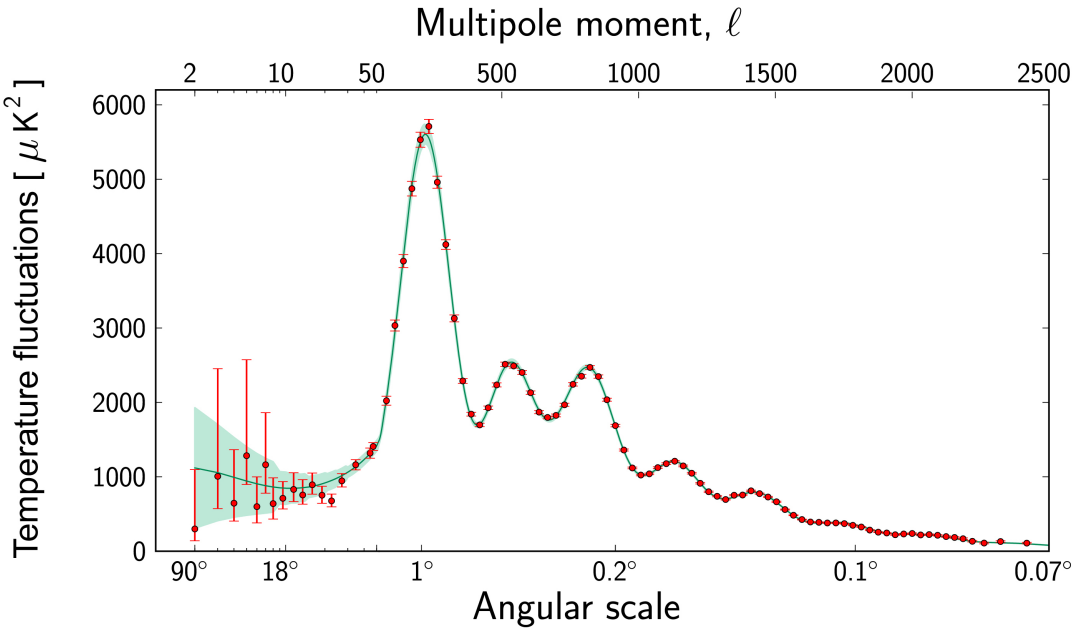

Figure 1.2: Power spectrum of temperature fluctuations in the CMB. Copyright: ESA and the Planck Collaboration.

A second, independent, measurement of the baryonic content of the universe is from the abundances of light elements. **Big Bang nucleosynthesis** is the production of atoms heavier than hydrogen (mainly helium, deuterium and lithium) that occurred shortly after photon decoupling. By determining the abundances of these primordial atoms, it can again be determined that the amount of baryonic matter in the universe today is five per cent (a recent measurement is 5.0 ± 0.2 per cent; Cyburt et al. (2016)).

It follows that since baryonic matter contributes so little to the overall matter density of the universe, dark matter consists of non-baryonic particles. Such particles would have to be at most weakly interacting, to explain why they have not been detected. The most

commonly considered particles are **weakly interacting massive particles** (WIMPs). WIMP candidates can be further divided into hot, warm and cold dark matter. **Hot dark matter** is very light, and moved at relativistic speeds at the time of decoupling, while **cold dark matter** (CDM) is more massive, and moved much more slowly. **Warm dark matter** has properties between these two extremes. Dark matter could consist of one of these types of WIMPs, or, alternatively, it could be mixed (e.g. have both a hot and cold component).

Cold

By the late 1980s, cosmologists were fairly convinced that dark matter must be almost completely cold, as described in Blumenthal et al. (1984). In the CDM paradigm, growth is **hierarchical**, or "bottom-up". In hierarchical growth, smaller structures form first, and then these merge to form larger structures. Conversely, hot dark matter forms "top-down"; first large superclusters form, and then these fragment into smaller structures.

One of the strongest arguments for CDM also comes from the temperature fluctuations in the CMB. These fluctuations correspond to small density perturbations early in the universe's history, and it is these small perturbations that give rise to the structures seen today. At the time of photon decoupling, hot dark matter would be moving too quickly to form these perturbations. Though it seems dark matter is likely cold, warm dark matter is not entirely ruled out.

Collisionless

Further, dark matter appears to be **collisionless**, in that interactions between individual particles are negligible, and thus they only move under a smooth gravitational potential (a more technical discussion of collisionless systems can be found in Section 1.3.2). The classical evidence for collisionless dark matter is from gravitational lensing results from the Bullet Cluster (Markevitch et al., 2004), which is technically composed of two colliding galaxy clusters. **Gravitational lensing** is a phenomenon where large masses act as a lens; since mass curves space, mass can cause light to follow curved trajectories. If there is a large mass in front of a bright object, the mass can be inferred through its lensing effect on the background source. Gravitational lensing results indicate that the majority of the mass present in the Bullet Cluster is invisible, as shown in Fig. 1.3. More importantly, the dark matter appears to be located on the outskirts of the cluster, indicating it bypassed the luminous gas during the collision. Although dark matter seems to be mainly collisionless,

it is still possible that dark matter is somewhat self-interacting (see, e.g. Tulin et al., 2013, for a review). If so, results from the Bullet Cluster place constraints on the cross-section for self-interaction.

Figure 1.3: The Bullet Cluster. Red represents the hot x-ray emitting gas, and blue is the dark matter distribution calculated from the gravitational lensing. The image is from NASA (from the Chandra X-ray Observatory). Credit: X-ray: NASA/CXC/CfA/ M.Markevitch et al.; Lensing Map: NASA/STScI; ESO WFI; Magellan/U.Arizona/ D.Clowe et al. Optical: NASA/STScI; Magellan/U.Arizona/D.Clowe et al.

Dark Matter Candidates

In conclusion, current evidence points towards dark matter that is non-baryonic, cold, and collisionless, although alternative models (such as warm or self-interacting dark matter) are not entirely ruled out. There are no known particles which fit the criteria for non-baryonic, CDM; however, extensions to the Standard Model of particle physics, notably supersymmetry, predict particles that are viable WIMP candidates, such as **neutralinos**.

Axions and **sterile neutrinos** are also CDM candidates. There is considerable experimental effort world-wide to detect one of these theoretical particles, and thus validate the CDM theory.

1.1.3 Dark Matter Research

The particle nature of dark matter is one of the most important questions in high-energy physics. Current research about dark matter can be broadly categorized into four main categories; direct and indirect detection of dark matter, production of dark matter particles, and theoretical studies.

First, **direct detection** methods aim to detect WIMP particles through detectors located on Earth. For example, the SNOLAB is an underground detector located in a nickel mine in Sudbury, Canada. It was originally built as the Sudbury Neutrino Observatory (SNO) to detect neutrinos, but is now actively searching for dark matter particles. Projects such as these have not detected dark matter thus far, but place increasingly stringent constraints on dark matter particle properties.

Alternatively, **indirect detection** methods attempt to detect undiscovered particles through their interactions. For example, neutralinos can annihilate with one-another in pairs, producing gamma rays. Scientists hope to detect evidence of these gamma rays in regions of high dark matter density. The Fermi Large Area Telescope, for instance, is searching for a γ-ray signal, mainly in the centre of the Milky Way, but also in nearby galaxies, such as M31 and M33. These studies have placed increasingly strong limits on dark matter annihilation, but to date have been unsuccessful at detecting a potential dark matter annihilation signal (Di Mauro et al., 2019).

Another approach is **production**; these experiments hope to prove the existence of theoretical particles that are dark matter candidates. Particle accelerators cause particle collisions at very high energies, which could potentially create new particles, such as those predicted by supersymmetry. Scientists at the world's largest particle accelerator, the Large Hadron Collider (LHC), are currently conducting experiments at unprecedented energies that could potentially create new supersymmetric particles, or other theoretical dark matter candidates (Buchmueller et al., 2017).

The final category of research, theoretical work, encompasses a wide range of studies. Theoretical particle physics has provided potential dark matter candidates, and has predicted the energies at which they will be created. Additionally, N-body simulations of galaxy formation provide information on how dark matter needs to behave in order to agree with the observed structure of the universe. It is through theoretical studies that we

obtain a deeper understanding of dark matter, and can then design experimental studies appropriately. One example of such work is the study of dark matter halo formation.

1.2 Formation of Dark Matter Haloes

At the time of the Big Bang, the universe was hot and dense. Over time, it has expanded and cooled. The expansion of the universe can be described using the Friedmann equation, which assumes **isotropy** (the universe is the same in all directions) and **homogeneity** (the universe is the same in all locations). While the Friedmann equation describes the overall growth and fate of the universe, structure in the universe forms from density perturbations in the early universe. Overdense regions collapse gravitationally, and form dark matter haloes, which later provide the gravitational wells in which gas can condense to form galaxies and galaxy clusters.

1.2.1 The Evolution of a Homogeneous Universe

The evolution of a homogeneous, isotropic universe can be described by three equations:

$$H(t)^2 = \left(\frac{\dot{a}(t)}{a(t)}\right)^2 = \frac{8\pi G\rho(t)}{3} - \frac{Kc^2}{a(t)^2} \tag{1.2a}$$

$$\dot{\mathcal{E}}(t) + 3\frac{\dot{a}(t)}{a(t)}(\mathcal{E}(t) + P) = 0 \tag{1.2b}$$

$$P = w\mathcal{E}(t) \ . \tag{1.2c}$$

The first of these equations, Equation (1.2a), is called the Friedmann equation; $H(t)$ is the **Hubble parameter** and gives the rate of expansion at time t. K is the **curvature constant** of the universe and has values of 1, 0 or -1 for a closed, flat or open universe, respectively. The parameter a is the **scale factor** which gives a measure of the size of the universe. The density, ρ, is also often expressed as a **relative density**, $\Omega = \rho/\rho_c$, where $\rho_c = 3H^2/8\pi G$ is the **critical density**, and corresponds to a flat universe ($K = 0$).

The second equation, Equation (1.2b), is called the **fluid equation**. Here, $\mathcal{E} = \rho c^2$ is the energy density and P is the pressure. Density can be expressed as a sum of radiation, matter and dark energy components, $\rho = \rho_r + \rho_m + \rho_{DE}$. Each component can be described by its **equation of state**, Equation (1.2c). This gives the relationship between pressure and energy density, and each component will evolve according to its **equation of state**

parameter, w_i; i.e, $\rho \propto a^{-3(1+w_i)}$. For radiation and matter, $w_i = 1/3$ and 0, respectively. Observations indicate that there is also a dark energy component with $w \approx -1$.

In astronomy, distance and time are often expressed in terms of **redshift**, z. Since the universe is expanding, objects further away are moving faster and are thus redder due to the Doppler effect. Additionally, since light takes a finite amount of time to reach the Earth, objects that are further away are being observed at earlier times. There is a simple relationship between the scale factor and redshift from cosmological expansion: $a \propto 1/(1+z)$. Therefore, Equations (1.2a)–(1.2c) often use z as the independent variable, rather than t.

1.2.2 Density Perturbations

While the universe evolves as outlined in the previous section, the growth of structure comes from the gravitational collapse of fluctuations in the matter density in the early universe. Thus, the growth of structure not only depends on the content of the universe, but also on the characteristics of the density perturbations. Density fluctuations in the universe are often described using $\sigma^2(R)$, which is the variance of fluctuations on a scale of size R. The size of fluctuations in the universe are usually characterized by σ_8, which is the root mean square fluctuations within $8\,\mathrm{h}^{-1}$ Mpc at the present day. An additional parameter, the scalar spectral index, n_s, describes how fluctuations vary with scale, where a value of $n_s = 1$ corresponds to scale invariant fluctuations (mathematically, it gives the relationship between the power spectrum of the initial density fluctuations, P and wavenumber, k: $P(k) \propto k^{n_s}$).

An individual density perturbation can be expressed as $\delta = (\rho - \bar{\rho})/\bar{\rho}$ where $\bar{\rho}$ is the average density; regions with $\delta > 0$ will eventually collapse into structure. In the **linear regime** ($\delta \ll 1$), density perturbations evolve as:

$$\ddot{\delta} + 2H\dot{\delta} = \frac{3}{2}\Omega_m H^2 \delta \ , \tag{1.3}$$

where $\Omega_m = \rho_m/\rho_c$ is the relative matter density. In this epoch of structure formation, the universe can be approximated as an **Einstein–de Sitter universe**. This is a simplified model which assumes the universe is flat and contains only matter (this is a valid approximation in early times, as dark energy is not yet important). Then, using $\Omega = \Omega_m = 1$ and $K = 0$ and solving Friedman's equation, this gives $a(t) \propto t^{2/3}$ and $H = 2/(3t)$. Using Equation (1.3), this means $\delta \propto a \propto t^{2/3}$ during the linear regime.

1.2.3 The Cosmic Web

While structure formation can be studied analytically in the linear regime, once it becomes non-linear, numerical simulations are needed to predict the spatial distribution of dark matter. This section will qualitatively outline the main results of dark matter structure growth; details of numerical simulations can be found in Section 1.3.

Due to gravitational attraction, overdense regions ($\delta > 0$) become denser over time, and do not expand with the overall universe; thus, the volume containing dense regions of dark matter diminishes. Conversely, underdense regions ($\delta < 0$) expand more rapidly than the overall universe, and will eventually become largely empty regions called **voids**. Where voids collide with each other, dark matter will form in **sheets** between them. When multiple voids meet, rather than two-dimensional sheets, the dark matter is arranged into one-dimensional **filaments**.

Locations where a number of filaments intersect are called **nodes**. Over time, matter will drain from filaments into the nodes. These roughly spherical regions of dark matter in nodes correspond to **dark matter haloes**. When smaller haloes merge along filaments into a central halo, they may exist as substructure, and are thus known as **subhaloes**. The resulting complex filamentary structure is known as the **cosmic web**; Fig. 1.4 shows this final structure from a dark–matter–only simulation. Galaxies and galaxy clusters form within these haloes, and thus trace the underlying dark matter structure.

1.2.4 Spherical Collapse

While the complex nature of structure formation requires numerical simulations, there are some analytical models for the formation of dark matter haloes. One of the simplest of these is the **spherical collapse model**. Consider an Einstein–de Sitter universe, with a spherical overdense region with radius r, and density $\rho = \bar{\rho}(1+\delta)$. Then, the mass within a sphere of radius r is $M = 4\pi r^3 \bar{\rho}(1+\delta)/3$.

Solving Friedmann's equation for this overdense region (with $\rho = \rho_m \propto a^{-3}$ and $K = 1$), results in the parametric equations:

$$\begin{aligned} a &= \frac{ct_{\mathrm{TA}}}{\pi}(1-\cos\theta) \\ ct &= \frac{ct_{\mathrm{TA}}}{\pi}(\theta - \sin\theta) \ . \end{aligned} \tag{1.4}$$

This solution reaches a maximum at $\theta = \pi$. We denote this time as, t_{TA}, which is commonly referred to as the **turnaround time**. The region then collapses at $\theta = 2\pi$ ($t = 2\,t_{\mathrm{TA}}$).

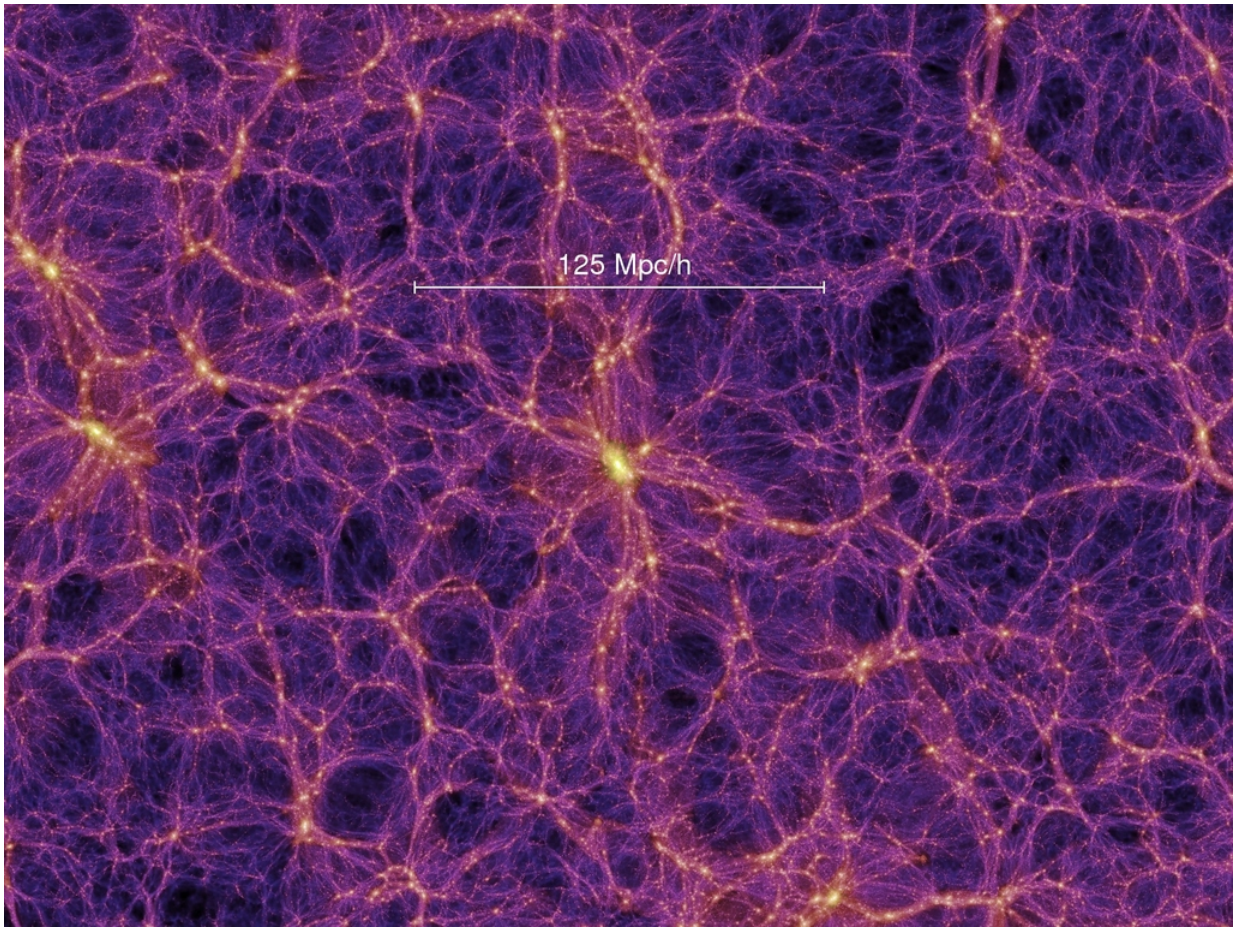

Figure 1.4: Example of dark matter structure, from the Millennium Simulation (Springel et al., 2005) Credit: https://wwwmpa.mpa-garching.mpg.de/galform/virgo/millennium.

Then, the overdensity can be expressed as:

$$1 + \delta = \frac{\rho}{\bar{\rho}} = \frac{9}{2}\frac{(\theta - \sin\theta)^2}{(1 - \cos\theta)^3} \ . \tag{1.5}$$

According to this calculation, at turnaround, $\rho/\bar{\rho} \approx 5.55$. Eventually, the system collapses to produce a spike of infinite density. However, this calculation assumes the perturbations are spherically symmetric and that shells of mass do not cross each other. In reality, the overdense region will not reach infinite density, but will undergo mixing and relaxation and collapse until the system is virialized. According to the virial theorem, a system in **virial equilibrium** obeys the relation:

$$W = -2K \ , \tag{1.6}$$

where W is potential energy and K is kinetic energy. The final size of the halo, $r_{\rm vir}$, can be found using energy conservation. At turnaround, the kinetic energy is zero: $E_{\rm TA} = W_{\rm TA}$. Then at virialization, $E_{\rm vir} = W_{\rm vir}/2$. Since mass is conserved, $W \propto 1/r$, and thus $r_{\rm TA} = 2\, r_{\rm vir}$. Therefore, the final size of the halo will be half of the turnaround radius.

In an Einstein–de Sitter universe, the background density evolves as $a^3 \propto t^2$. Therefore, $\bar{\rho}_{\rm TA} = 4\bar{\rho}_{\rm vir}$; i.e. the background density is four times less dense at the time of virialization compared to turnaround. Since the virialized halo has half the radius compared to at turnaround, the halo is eight times more dense at virialization compared to turnaround time. Putting this together with the approximation that $\rho_{\rm TA} = 5.55\bar{\rho}_{\rm TA}$, the density contrast relative to the background of a virialized halo is $\Delta_c \equiv \rho_{\rm vir}/\bar{\rho} \approx 178$. For more realistic cosmologies this value is slightly higher, and in practice, a common definition for the virial radius the radius in which the density is 200 times the critical density, ρ_c.

1.2.5 Halo Growth

Overall, halo growth can be described as an initial collapse of a density perturbation, and then mass growth through successive mergers. Mergers are often classified as minor or major based on the mass ratio of the two merging systems (there is not a clear cutoff, but a mass ratio of 1:3 or 1:4 is sometimes used). In **minor mergers**, the two haloes are very different sizes, and the smaller subhalo falls into the larger host halo. The host halo is largely unaffected, and the subhalo evolves mainly through **dynamical friction** and **tidal stripping**. Dynamical friction occurs as the subhalo travels through a distribution of background particles in the host halo; the subhalo will create a wake behind it which will cause drag, and thus cause the orbit to decay. Tidal stripping is due to the tidal forces on the subhalo; since it is not in a uniform potential, material will be stripped off the

subhalo and incorporated into the host. Eventually the subhalo may become completely disrupted. In comparison, **major mergers** are mergers between haloes of similar sizes, so both merging systems are significantly disrupted. Major mergers are thought to be one of the main determinants of halo 3D shape.

1.3 Numerical Simulations

Most knowledge about the large-scale structure of the universe and dark matter haloes comes from numerical simulations; many of these are N-body simulations, though to fully account for baryonic effects, hydrodynamical simulations are often employed. Since the universe is primarily dark matter, the simplifying assumption that, to first-order, baryonic effects can be neglected is made throughout the thesis. Thus, techniques related to dark–matter–only simulations will be described in this section.

1.3.1 N-Body Simulations

N-body simulations calculate how discrete particles interact gravitationally, and are often used to model collisionless systems, such as dark matter structures. Due to computational limitations, it is impractical to resolve individual dark matter particles. Therefore, it is common to simulate pseudo-particles that each represent thousands to millions of solar masses worth of dark matter.

In the case of N particles, each particle, i, should evolve according to:

$$\begin{aligned} \frac{\mathrm{d}\vec{r}_i}{\mathrm{d}t} &= \vec{v}_i \\ \frac{\mathrm{d}\vec{v}_i}{\mathrm{d}t} &= \frac{\vec{F}_i}{m_i} \quad , \end{aligned} \tag{1.7}$$

where F_i is the force acting on particle i. Many numerical methods exist for the time integration, but a common scheme is the **Leap Frog scheme**, which is accurate to second order and conserves energy.

In the case of N isolated, non-relativistic particles, the force can be calculated using Newton's Law:

$$\vec{F}_i = -\sum_{j \neq i} G \frac{m_i m_j (\vec{r}_i - \vec{r}_j)}{|\vec{r}_i - \vec{r}_j|^3} \quad . \tag{1.8}$$

However, since each N-body particle is not in reality a point mass, this results in numerical issues when particles get too close. **Gravitational softening** is a method to avoid this problem, by modifying the gravitational force to effectively create mass smoothing. As a simple example, the force can be calculated as:

$$F \propto \frac{1}{\sqrt{r^2 + \epsilon^2}} \ , \tag{1.9}$$

where ϵ is the **softening length**; in practice more complicated parameterizations are often used (e.g. Springel, 2005).

Algorithms which directly calculate the force on each particle according to Equation (1.8) are called **particle-particle (PP) algorithms** and the number of operations scales as N^2. These direct calculations quickly become too computationally costly to run, and therefore approximate methods are used to reduce the number of calculations needed. For example, in **tree algorithms**, particles are grouped together based on their distance from the particle, and the force from each group calculated as a multipole expansion; this method scales as $N \log N$. In **particle-mesh (PM) algorithms**, the gravitational potential is constructed over a grid from density field, and Poisson's equation is solved using fast Fourier transforms. This scales as N + $N_{\rm grid} \log N_{\rm grid}$, where $N_{\rm grid}$ is the number of grid points; a limitation to this method is that it needs a large amount of memory storage. There are also hybrid methods, such as $\mathbf{P^3M}$ wich uses PP for close particles and PM for distant particles. In this thesis, we use the publicly available code GADGET-2 (Springel, 2005), which utilizes a **PM-Tree scheme** (i.e. it uses a tree code for short range, and PM for long range forces), and is particularly well-suited for cosmological applications.

1.3.2 Timescales for Collisionless Systems

As argued in Section 1.1.2, dark matter is collisionless. Mathematically, collisionless systems are those in which two-body collisions are negligible, and therefore the gravitational force can be treated as a smooth density field rather than a collection of individual particles. A system is considered collisionless if the characteristic timescale on which the system evolves is much less than the relaxation time, and direct collisions are negligible, i.e., $t_{\rm coll} \gg t_{\rm relax} \gg t_{\rm cross}$. Therefore, to determine whether a system can be treated as collisionless, it is important to define these relevant time scales. Following the arguments in Binney & Tremaine (1987), consider a system of size R with N particles each of mass m interacting gravitationally. Each particle travels with a typical speed of $v \approx GNm/R$.

The first time scale of interest is the **crossing time**, $t_{\rm cross}$. This is the typical time for a particle to cross the system, and is given by:

$$t_{\rm cross} = \frac{R}{v} \ . \tag{1.10}$$

Secondly, the **timescale for direct collisions**, $t_{\rm coll}$ can be calculated as follows: the cross section for a direct collision is σ, and the mean free path is $\lambda = 4\pi R^3/3N\sigma$. Therefore, the number density of particles is λ/R, and thus the timescale for direct collisions is:

$$t_{\rm coll} = \frac{4\pi R^2}{3\sigma}\frac{1}{N}t_{\rm cross} \ . \tag{1.11}$$

For non self-interacting dark matter particles, σ is effectively zero, so direct collisions are negligible.

Aside from direct collisions, gravitational two-body interactions are also important, and the time scale associated with these is known as the **relaxation time**. Relaxation will cause a change in particle velocities relative to that expected if the particles were moving through a smooth distribution rather than the potential generated by individual point particles. The relaxation time can be defined as the time such that the velocity has changed by order of itself, i.e., $\mathrm{d}v/v \approx 1$.

To calculate the relaxation time, first consider the change in velocity a particle will experience from one interaction. Suppose this particle passes another with impact parameter b (assume the perturbing particle is stationary, the particle of interest moves with velocity v on a straight trajectory). Then, the force at closest approach is Gm/b^2, and the time over which it acts is approximately b/v. Therefore, the change in velocity is roughly:

$$\mathrm{d}v = \frac{Gm}{bv} \ . \tag{1.12}$$

A particle will have a number of encounters in one crossing time, and thus the next step is to approximate the number of encounters a particle will have. The density of particles is $3N/4\pi R^3$, and the particle of interest will sweep out a torus with radius b. The surface area of this torus is $4\pi^2 Rb$. Therefore, the number of encounters with an impact parameter between b and $b + \mathrm{d}b$ is:

$$\mathrm{d}n = 3\pi\frac{N}{R^2}b\mathrm{d}b \ . \tag{1.13}$$

Since the particles are traveling in random directions, the sum of the individual velocity changes, $\mathrm{d}v$, will be zero. Instead, we can consider the change in the squared velocity, by

integrating from $b = b_{\rm min} \equiv Gm/v^2$ to R. For $b < b_{\rm min}$, the assumptions of a straight line trajectory break down; encounters of this sort should be very rare, and thus will be neglected in this calculation. Therefore, the change in $\mathrm{d}v^2$ is:

$$\mathrm{d}v^2 \approx \int_{b_{\rm min}}^{R} \mathrm{d}v^2 \mathrm{d}n \approx 10 \frac{N}{v^2} \left(\frac{GM}{r}\right)^2 \ln\Lambda \ , \tag{1.14}$$

where $\ln\Lambda$ is called the **Coulomb logarithm**, and is given by $\ln\Lambda \equiv \ln(R/b_{\rm min}) \approx \ln N$.

Finally, $n_{\rm relax}$, which is the number of times a particle will cross the system before its velocity changes by an order of itself is:

$$n_{\rm relax} = \frac{\mathrm{d}v^2}{v^2} = \frac{10 \ln N}{N} \ , \tag{1.15}$$

and the relaxation time is given by

$$t_{\rm relax} = \frac{0.1N}{\ln(N)} t_{\rm cross} \ . \tag{1.16}$$

An important concept in N-body simulations is **numerical relaxation**. Since N-body simulations use massive point particles that are meant to sample a smooth continuous density field, this results in numerical artifacts from two-body interactions. This can be characterized by a size scale, $r_{\rm relax}$,

$$r_{\rm relax} = \left(\frac{t \ln N}{0.1N}\right)^{2/3} (Gm)^{1/3} \ ; \tag{1.17}$$

structure on scales smaller than this will be affected by two-body relaxation. To resolve smaller structures, the number of particles in the simulation needs to be increased.

1.3.3 Analyzing Simulations

Another important technical aspect of numerical simulations is how to extract information. There is a large amount of literature on how to identify which particles belong to which haloes (e.g. Knebe et al., 2013; Behroozi et al., 2015). Additionally, extensive work has been done on how to robustly measure density profiles (e.g. Vera-Ciro et al., 2013; Klypin et al., 2016), the 3D shape (e.g. Bailin & Steinmetz, 2005; Zemp et al., 2011), and concentration of individual simulated haloes (e.g. Prada et al., 2012; Dutton & Macciò, 2014; Klypin et al., 2016). In this thesis, all of these quantities will be measured, and detailed descriptions of our methods can be found in the relevant chapters.

1.4 Dark Matter Haloes as a Probe for Cosmology

The aim of this thesis is to show how the structural properties of dark matter haloes can be used to advance the understanding of cosmology. This section first briefly outlines the current cosmological model, gives an overview of the main types of astronomical observations and then describes some of the ways in which dark matter haloes are used to study cosmology.

1.4.1 The Cosmological Model

The Friedmann equation, introduced in Section 1.2.1, has a number of free parameters, including the Hubble parameter at the current time (H_0) and the mass–energy content of the universe. Additionally, to describe the characteristic density fluctuations in the universe, an additional two parameters are needed (such as σ_8 and n_s, as defined in Section 1.2.2).

The current favored model of the universe is known as the **ΛCDM model**. Λ refers to the fact that dark energy is described by a cosmological constant (with an equation of state parameter of $w = -1$), and CDM indicates that the dark matter component is almost entirely cold. Overall, ΛCDM can be described by six parameters; the amount of dark energy, dark matter and baryonic matter in the universe, as well as H_0, σ_8 and n_s. From the most recent CMB constraints, baryonic matter makes up 5% of the mass–energy content of the universe, and dark matter and dark energy make up the remaining 26% and 69%, while values for H_0, σ_8 and n_s are approximately $68\,\mathrm{km\,s^{-1}\,Mpc^{-1}}$, 0.81 and 0.97, respectively (Planck Collaboration et al., 2018).

While the ΛCDM model is largely successful, there are currently tensions in H_0 and σ_8 values, with different methods for measuring the parameters giving conflicting values. To reconcile these results, possible extensions to ΛCDM have been proposed including $w \neq -1$, more exotic forms of dark matter, and modifications to gravity.

1.4.2 Types of Observations of Individual Haloes

Since studies of cosmology typically require astronomical observations, it is important to understand the main types of observations used to study dark matter haloes. First, **optical observations** measure the luminous matter contained within astronomical structures; the movement of this visible structure should depend on the total mass of the system, including dark matter. Traditional detections of dark matter were from optical results: e.g. galaxy

rotation curves, and measurements of the velocity dispersion of galaxies within clusters. These studies often use assumptions about the dynamical state of the system, i.e., they assume the system is in dynamical equilibrium to calculate the total mass.

Secondly, **X-ray surveys** image the hot gas in the centre of galaxy clusters, which reside in the largest dark matter haloes. Since clusters are the only extended X-ray source in the universe, they are very easy to detect, and these clusters reside within the largest dark matter haloes in the universe. The main advantages to X-ray studies of clusters are that they suffer from minimal projection effects, since X-ray emission scales as density squared, and also that clusters follow well-defined scaling relations between their X-ray properties and properties at other wavelengths. One of the main disadvantages is that X-ray surveys have to be conducted from space, and are thus very expensive. In general, masses inferred from X-ray observations assume hydrostatic equilibrium, and neglect magnetic fields, turbulence, and cosmic rays.

At the millimeter wavelength, the **Sunyaev-Zel'dovich (SZ) effect** provides another method to detect hot gas in clusters. The SZ effect is from the inverse Compton scattering of photons from the CMB as they pass through the hot gas in galaxy clusters. This causes a shift in the blackbody spectrum, which is proportional to the integrated electron pressure along the line of sight (Sunyaev & Zeldovich, 1970). The main advantage to SZ surveys is that they are nearly redshift independent; since the signal is coming from the CMB, there is no cosmological dimming. Additionally, SZ-based mass estimates are less sensitive to the details of gas dynamics than ones based on X-ray emission (Motl et al., 2005; Nagai, 2006). Challenges in SZ studies are understanding the mass–observable relation, and quantifying how much results are impacted by radio and IR sources (Sehgal et al., 2010). Also, the SZ signal is linear in density, so it is more sensitive to projection effects (Shaw et al., 2008).

Finally, gravitational lensing is the bending of light rays by massive objects, as described in Section 1.1.2. If there is a massive object located between the observer and a background source, its mass distribution can be inferred through its lensing effect. Gravitational lensing can be classified as strong or weak; in **strong lensing** the effect is strong enough to split an object into multiple images, while in **weak lensing** there are coherent distortions of background galaxies that can be stacked and analyzed statistically to determine the underlying mass distribution. The main advantage to lensing techniques are that they measure the mass of the dark matter directly, requiring no assumptions about how baryonic matter traces dark matter. Additionally, these measurements do not require any assumptions about the dynamical state of the system.

1.4.3 Cosmological Tests

Small Scale Structure

Small scale structure may be the best place to test the nature of dark matter. For example, warm dark matter will disrupt low mass subhaloes (e.g. Knebe et al., 2008) while self-interacting dark matter will produce constant-density cores, with lower central densities (e.g. Burkert, 2000). While numerical simulations match observed large scale structure very well, there are some discrepancies on small scales (below $\sim$1 Mpc) which challenge the ΛCDM paradigm.

Overall, there are three main potential small-scale structure problems, commonly referred to as (1) the "missing satellites" problem (2) the "core–cusp" problem, and (3) the "too–big–to–fail" problem. The **missing satellite problem** refers to the fact that there are many more subhaloes predicted in numerical simulations than observed dwarf galaxies in the Milky Way (Klypin et al., 1999; Moore et al., 1999). The **core-cusp problem** is that numerical simulations predict a steep inner slope in the density profile (cusp), while many observed dark matter dominated galaxies seem to have constant density cores (Moore, 1994). Finally, the **too–big–to–fail problem** is that the most massive subhaloes in simulations are much too dense to correspond to the most-massive satellites in the Milky Way (Flores & Primack, 1994; Boylan-Kolchin et al., 2011).

While there have been a number of suggested solutions to all these problems, it is likely they can all be solved by including baryonic feedback in simulations (for a recent, comprehensive review see Bullock & Boylan-Kolchin (2017)). However, it is important to understand the origins for these discrepancies to develop concrete predictions for how substructure varies with different types of dark matter particles.

Indirect Dark Matter Searches

As discussed in Section 1.1.3, one potential way to detect dark matter is through indirect detection, i.e. detecting Standard Model products that arise from dark matter annihilation or decay. **Dark matter annihilation** is proportional to the density of dark matter squared and is therefore sensitive to the inhomogeneity of the particle distribution; e.g. substructure in a halo will contribute greatly to the overall signal. **Dark matter decay**, on the other hand, scales linearly with density, and therefore the contribution from substructure is negligible. Indirect searches have already ruled out some candidates (e.g. Di Mauro et al., 2019); however, these types of studies require accurate predictions of how dark matter is distributed.

Cluster Counts

Since the expansion of the universe as well as the characteristics of the density fluctuations in the early universe are linked to the underlying cosmological model, dark matter halo abundances should reflect the cosmological parameters. Ultimately, the **halo mass function**, $n(z)$, which describes the number of haloes per unit comoving volume, depends on a combination of cosmological parameters, which is best expressed as $\sigma_8 f(z) \approx \sigma_8 \Omega_m^\gamma$, where $f(z)$ is the growth factor and γ is the growth index. The first effort to predict dark matter halo mass functions analytically is the work of Press & Schechter (1974), with later extensions from Bond et al. (1991) and Sheth et al. (2001). However, since these analytic approaches make a number of simplifying assumptions, more recent work derives estimates of the mass function using N-body simulations (e.g. Tinker et al., 2008; Watson et al., 2013).

1.5 Outline of Thesis

The main goal of this thesis is to develop models for the structural evolution of dark matter haloes in both minor and major mergers. First, in Chapter 2 we introduce a model for tidally-stripped dark matter haloes, based on truncating the distribution function, and compare it to isolated minor merger simulations. We explore this model further in Chapter 3, by comparing to other models in the literature, and examining some of the assumptions in more detail; further, we test universality and examine implications for the annihilation boost factor. The next two chapters focus on dark matter halo evolution in major mergers. In Chapter 4, we present a large suite of isolated, binary, equal-mass mergers and explore changes in halo spin, size, and shape. Then, in Chapter 5, we examine how the density profile and concentration parameter of major merger remnants depend on the parameters of the merger, as well as implications to the annihilation boost factor. Finally, in Chapter 6, we summarize the main findings and introduce a potential cosmological test, using halo properties in combination with cluster counts to constrain σ_8.

Chapter 2

The Phase-Space Structure of Tidally Stripped Haloes

2.1 Introduction

On large scales, a number of independent and complementary tests, including the spectrum of fluctuations in the microwave background (e.g. Planck Collaboration et al., 2016), galaxy clustering (e.g. Alam et al., 2017), and weak gravitational lensing (e.g. Kitching et al., 2014), provide overwhelming support for the existence of dark matter. This component dominates over regular matter by a factor of ~ 5 (Planck Collaboration et al., 2016), and collapsed, virialized dark matter haloes are thought to be the site of all galaxy formation (see Frenk & White, 2012, for a review).

On smaller scales, observational tests including galaxy kinematics (e.g. Ouellette et al., 2017; Battaglia et al., 2013)), satellite kinematics (e.g. Prada et al., 2003; Guo et al., 2012), and weak or strong gravitational lensing (e.g. Okabe et al., 2013; Umetsu et al., 2016), amongst others, are beginning to probe the structure of individual dark matter haloes, placing direct constraints on their density profile and velocity structure, as well as central concentration, shape, and substructure. For the moment, however, most of our knowledge of these non-linear scales comes from numerical simulations, which have studied the formation and evolution of haloes at ever increasing resolution (e.g. Diemand et al., 2007; Springel et al., 2008; Diemand et al., 2008; Stadel et al., 2009; Gao et al., 2012).

One of the main results of these simulations has been the observation that haloes have a universal density profile (UDP), when averaged spherically. The classic approximation

to this profile is from the work of (Navarro et al., 1996, 1997)—NFW hereafter:

$$\rho(r) = \frac{\rho_0}{r/r_{\rm s}(1+r/r_{\rm s})^2} \quad , \tag{2.1}$$

where ρ_0 is a characteristic density and $r_{\rm s}$ is the scale radius, corresponding to the point where the logarithmic slope is $\mathrm{d}\ln\rho/\mathrm{d}\ln\mathrm{r} = -2$. This profile has no outer limit *a priori*; as r goes to infinity the central potential remains finite but the mass diverges. In a cosmological context, haloes are usually considered out to the virial radius, the radius within which they are in approximate virial equilibrium. In practice, the virial radius can be defined by one of several overdensity criteria, or it can be specified in terms of the concentration parameter $c \equiv r_{\rm vir}/r_{\rm s}$.

More recent work at higher resolution has determined that haloes differ slightly but systematically from the original NFW fit, and that a better approximation is the Einasto profile (Navarro et al., 2004; Merritt et al., 2006; Gao et al., 2008):

$$\rho(r) = \rho_{-2} \exp\left(-\frac{2}{\alpha}\left[\left(\frac{r}{r_{-2}}\right)^{\alpha} - 1\right]\right) \quad , \tag{2.2}$$

which contains an extra shape parameter α that seems to vary systematically with mass and redshift (Gao et al., 2008; Dutton & Macciò, 2014; Klypin et al., 2016). In this chapter we will consider only the simpler NFW model, although our results are easily extended to an Einasto profile, and our initial condition code, described in the Appendix, includes the Einasto profile as an option.

Since the discovery of the universal density profile, there has been extensive work characterizing halo properties such as shape, concentration, spin, and substructure (see Taylor 2011 for older references, or Klypin et al. 2016 for more recent references). Average values for properties such as concentration are now well determined as a function of mass, redshift, and cosmology. On the other hand, given the complexity of halo growth through hierarchical merging in a cosmological context, idealized, isolated simulations of mergers between pairs of haloes may be better suited to determining the physical mechanisms by which these average trends are established. For this work, it is convenient to be able to construct models whose density is truncated at a finite radius and/or whose mass converges to a finite value. Prior work (e.g. Moore et al., 2004; Kazantzidis et al., 2004) has used models with exponentially truncated NFW profiles, but there is no particular theoretical motivation for this choice. Our initial goal at the outset of this work was to provide a better motivated model for the initial conditions for simulations of isolated, truncated systems.

The standard theory of cosmological structure formation also predicts that haloes should grow through repeated, hierarchical mergers, and that the cores of smaller merging

systems should survive as tidally-stripped, self-bound substructure within galaxy, group, and cluster haloes. In previous work, Hayashi et al. (2003) studied the evolution of halo substructure by simulating the tidal stripping of a smaller satellite halo by a larger host halo. They found that, independent of orbit, the density profile of the satellite halo changed in a predictable way. This change could be described by an empirical model which only required one additional parameter, equivalent to a tidal radius $r_{\rm t}$. Though this paper did a thorough job of describing the profile of tidally stripped haloes, it did not determine the exact mechanisms behind the changes. Subsequent work by Kampakoglou & Benson (2007) showed that tidal forces acting on individual particles may explain some of the form of the density profile of stripped systems, while Choi et al. (2009) showed that particles become unbound based more on their energy than on their angular momentum. Despite this work, the net effect of tidal forces on the full distribution function remains somewhat unclear.

Observational tests of these theoretical predictions based on lensing (e.g. Grillo et al., 2015; Jauzac et al., 2016) or internal kinematics (e.g. Ouellette et al., 2017) are still in their infancy, but show promise given forthcoming datasets from very large surveys. Other substructure calculations, such as the boost factor for dark matter annihilation (e.g. Anderhalden & Diemand, 2013; Sánchez-Conde & Prada, 2014, and references therein), depend not only on the density profile, but also on the full distribution function (DF) of dark matter in stripped systems. For these applications, and in order to understand the mechanisms of tidal stripping fully, it would be useful to have a simple analytic model for the DF of a tidally stripped system.

In our experiments with the truncation of distribution functions (DFs) in energy space, we have found a simple method for realizing spatially truncated haloes whose central regions resemble NFW profiles. In this chapter we describe the method, but also show that the truncated systems it produces closely resemble tidally stripped subhaloes orbiting within a larger potential. Thus our model can be used to represent either stable, isolated systems with a finite extent (e.g. for merger simulations) or tidally stripped systems (e.g. for substructure calculations).

The outline of this chapter is as follows: in Section 2, we describe an iterative algorithm for generating the ICs for an isolated, spatially truncated NFW profile. In Section 2.3, we compare this approach to an analytic model where the NFW DF is truncated in energy and shifted, analogously to a King model. In Section 2.4 we describe our simulations of tidal stripping of haloes on various orbits, and in Section 2.5 we compare the properties of the stripped remnants to the analytic truncated models. Finally, in Section 2.6 we discuss the implications of our results and summarize our main conclusions.

2.2 Creating Truncated Initial Conditions

To simulate how a spherical dark matter halo evolves in isolation, we require a method for generating initial conditions (ICs) for particles which collectively form a stable self-gravitating system. Given an analytic expression for the density profile, we can integrate this to obtain the normalized cumulative mass distribution $M(< r)/M_{\rm tot}$, and select particles randomly from this distribution, mapping enclosed mass fraction to radius. Clearly, profiles whose total mass $M_{\rm tot}$ diverges at large radii need to be truncated in some way. The most common solution for cosmological haloes (e.g. Kazantzidis et al., 2004; Moore et al., 2004; Kazantzidis et al., 2006; Peñarrubia et al., 2010) is to use the exponentially truncated NFW profile first introduced by Springel & White (1999), although this form is motivated more by mathematical convenience than by any physical argument.

There are two approaches to determining particle velocities (assumed in the simplest case to be spherically symmetric and isotropic in velocity space). We can either calculate the velocity dispersion at each radius from the Jeans equation, making the approximation that the velocity distribution is Maxwellian (e.g. Hernquist, 1993) or, for a more accurate model, we can draw particle energies from the full DF (e.g. Kazantzidis et al., 2004) and convert these to velocities. We review the latter approach below, before introducing and testing our truncation method.

2.2.1 Generating Initial Conditions from the Distribution Function

We will briefly review the main properties of the DF; a more detailed explanation can be found in Binney & Tremaine (1987). The DF, f, describes the mass per phase-space volume. For a spherical, isotropic, self-gravitating system, it can be written as a function of a single variable, say a relative energy $\mathcal{E}$. Given a potential Φ, we will define the (potential and total) relative energies as $\Psi = -\Phi + \Phi_0$ and $\mathcal{E} = \Psi - v^2/2$. The parameter Φ_0 is free, and is generally set to the value of the potential at the outer boundary of the system, such that the $f > 0$ only when $\mathcal{E} > 0$, while $f = 0$ when $\mathcal{E} \leq 0$.

A relationship between the density profile of a system and the DF can be found by integrating $f(\mathcal{E})$ over all velocities. For a spherically symmetric system:

$$\rho(r) = 4\pi \int_0^{\Psi(r)} f(\mathcal{E}) \sqrt{2(\Psi(r) - \mathcal{E})} \mathrm{d}\mathcal{E} \ . \tag{2.3}$$

Equation (2.3) can be inverted (Eddington, 1916), and thus the DF can be expressed in terms of the density:

$$f(\mathcal{E}) = \frac{1}{\sqrt{8}\pi^2}\left[\int_0^{\mathcal{E}} \frac{1}{\sqrt{\mathcal{E}-\Psi}}\frac{\mathrm{d}^2\rho}{\mathrm{d}\Psi^2}\mathrm{d}\Psi + \frac{1}{\sqrt{\mathcal{E}}}\left(\frac{\mathrm{d}\rho}{\mathrm{d}\Psi}\right)_{\Psi=0}\right] \quad . \tag{2.4}$$

A particle at radius r then has energy $\mathcal{E} \in (0, \Psi(r))$ with a probability proportional to $f(\mathcal{E})\sqrt{\Psi(r) - \mathcal{E}}$.

Given a density profile ρ, the relative potential $\Psi(r)$ can be calculated using Poisson's equation, and the derivatives $\mathrm{d}\rho/\mathrm{d}\Psi$ and $\mathrm{d}^2\rho/\mathrm{d}\Psi^2$ can be evaluated analytically or numerically. The distribution function $f(\mathcal{E})$ can than be calculated for a given relative energy $\mathcal{E}$ using Equation (2.4). To generate a model halo, a radius and a relative energy are selected at random for each particle, in such a way as to reproduce the correct density profile and distribution function. Once the radius and relative energy have been assigned, the norm of the velocity of each particle can be calculated as $v = \sqrt{2(\Psi(r) - \mathcal{E})}$. Finally, 3D position and velocity components can be chosen at random assuming (spatial) spherical symmetry, and isotropy in velocity space, respectively. Although these techniques are well known, for convenience we review them in Appendix A.

2.2.2 Truncating the NFW Profile at a Finite Radius

The exponentially truncated NFW profile was first described in Springel & White (1999), and is identical to the NFW profile within the virial radius, $r_{\rm vir}$, but is truncated exponentially beyond that. How fast this decay occurs depends on the parameter r_d:

$$\rho(r) = \begin{cases} \dfrac{\rho_0 r_{\rm s}^3}{r(r_{\rm s}+r)^2} & \text{if } r < r_{\rm vir} \\ \dfrac{\rho_0}{c(1+c)^2}\left(\dfrac{r}{r_{\rm vir}}\right)^{\epsilon}\exp\left(-\dfrac{r-r_{\rm vir}}{r_{\rm d}}\right) & \text{if } r > r_{\rm vir} \end{cases} , \tag{2.5}$$

where the constants ρ_0 and $r_{\rm s}$ are as in Equation (2.1). Additionally, to ensure that the logarithmic slope at $r_{\rm vir}$ is continuous, there is the constraint:

$$\epsilon = -\frac{r_{\rm s} + 3r_{\rm vir}}{r_{\rm s} + r_{\rm vir}} + \frac{r_{\rm vir}}{r_{\rm d}} \quad . \tag{2.6}$$

Not only does this solution have little physical motivation, however, but it is also discontinuous in the second derivative of $\rho(r)$. Since Equation (2.4) depends on this second

derivative through the $\mathrm{d}^2\rho/\mathrm{d}\Psi^2$ term, the DF may not be monotonically increasing for certain choices of r_d, resulting in unphysical behaviour. [1]

Instead, we propose a different modification to the NFW profile. Our solution is to consider particles as if they were sampled from an infinitely extended NFW profile, but only choose those within some radius r_cut. Particle energies are initially assigned from the DF corresponding to the full (infinitely extended) NFW profile, as described in Section 2.2.1. We then iteratively remove any unbound particles, using at each step of the iteration the potential defined by the set of particles remaining.[2] For a halo with $r_\mathrm{cut} = 10\,r_\mathrm{s}$, this process converges within 10 iterations or fewer, leaving approximately 65 per cent of the mass within r_cut bound. The final result is a system with a density profile that matches NFW at small radii, but drops off more steeply at large radii, reaching zero density at r_cut. While this truncated profile is instantaneously self-bound, its long term stability is unclear. We will consider this point in the next section.

2.2.3 Stability Tests

Before we test the stability of our truncated profile, we need to estimate the possible contribution from collisional effects. These can complicate the interpretation of any N-body simulation. Our method for determining particle ICs assumes that the particles exist in a smooth continuous potential; each particle can be considered a Monte Carlo sampling of this potential. However, individual particle-particle interactions lead to a gradual loss of the initial structure, most noticeably in the dense center of the halo.

There are two time scales on which collisional effects are important. The first, the relaxation time scale, t_rel, corresponds to the time which it takes a typical particle's velocity to change by an order of itself. The second, slower timescale is the evaporation time, t_evap, the amount of time it takes a typical particle to reach escape speed, and thus 'evaporate' from the system. Following the arguments from Binney & Tremaine (1987), we calculate:

$$\begin{aligned} t_\mathrm{rel}(r) &\approx 0.1 \frac{\sqrt{N(<r)}}{\ln N(<r)} \sqrt{\frac{r^3}{Gm}} \quad , \text{ and} \\ t_\mathrm{evap}(r) &\approx 136\, t_\mathrm{rel}(r) \quad , \end{aligned} \tag{2.7}$$

[1] One of the stability criteria for spherical, isotropic systems is that the DF increases monotonically with $\mathcal{E}$ (Antonov, 1961); for certain choices of r_d, the sign of $\mathrm{d}^2\rho/\mathrm{d}\Psi^2$ changes at the discontinuity, resulting in a non-mononotonic DF.

[2] Note Choi et al. (2007) propose an alternative, but more complicated method, truncating the initial density profile, calculating a distribution function via Eddington inversion, recalculating the resulting density profile, and iterating over these steps until convergence.

where $N(< r)$ is the number of particles within radius r. Using these formulae, we can define a '(central) relaxation radius', $r_{\rm rel}(t)$, and a '(central) evaporation radius', $r_{\rm evap}(t)$, such that $t_{\rm rel}(r_{\rm rel}) = t$ and $t_{\rm evap}(r_{\rm evap}) = t$ respectively, within which relaxation and evaporation are important.

To verify the stability of our initial satellite halo, we evolve it in isolation with the N-body code GADGET-2 (Springel, 2005). We generate an initial NFW system with 2×10^6 particles within a radius $r_{\rm cut} = 10\, r_{\rm s}$. After iteratively removing unbound particles (as described in Section 2.2.2), the final number of particles in the truncated system is $N = 1286991$. We then assign each particle a mass m such that the total satellite has mass $M_{\rm sat}$. We simulate the evolution of the system using the softening length proposed in van Kampen (2000), $\epsilon = 0.5 r_{\rm h} N^{-1/3}$, where $r_{\rm h}$ is the half-mass radius. For our ICs, $\epsilon = 0.01\, r_{\rm s}$.

Fig. 2.1 shows the evolution of the density profile with time. The outer part of the profile appears to be completely stable, with any systematic changes invisible on the scale of the figure. The only visible change is in the region interior to $r_{\rm evap}$. This is consistent with the results of Hayashi et al. (2003), who found that the internal structure evolves at radii where the evaporation time is close to t. (We have also confirmed the predicted scaling of $r_{\rm evap}$ with particle number using lower resolution simulations.) We conclude that this central change is a collisional effect due to finite resolution, and that our ICs are otherwise extremely stable.

One disadvantage of our iterative unbinding method is that the resulting truncated DF does not have a simple expression, even for cases where the original, un-truncated DF is simple. Thus, in the next section we will consider a slightly different analytic approach, and show that it produces remarkably similar results.

2.3 An Analytic Model for the Truncated Distribution Function

Our goal is to derive an analytic approximation for the DF of a truncated system with a NFW or UDP-like central density profile. We will take an approach similar to the derivation of the King model (King, 1966), truncating and lowering the DF in energy space, as described below. For the NFW profile, this approach has been proposed previously by Widrow & Dubinski (2005), who showed that it leads to sharply truncated density profiles (see their Figure 1).

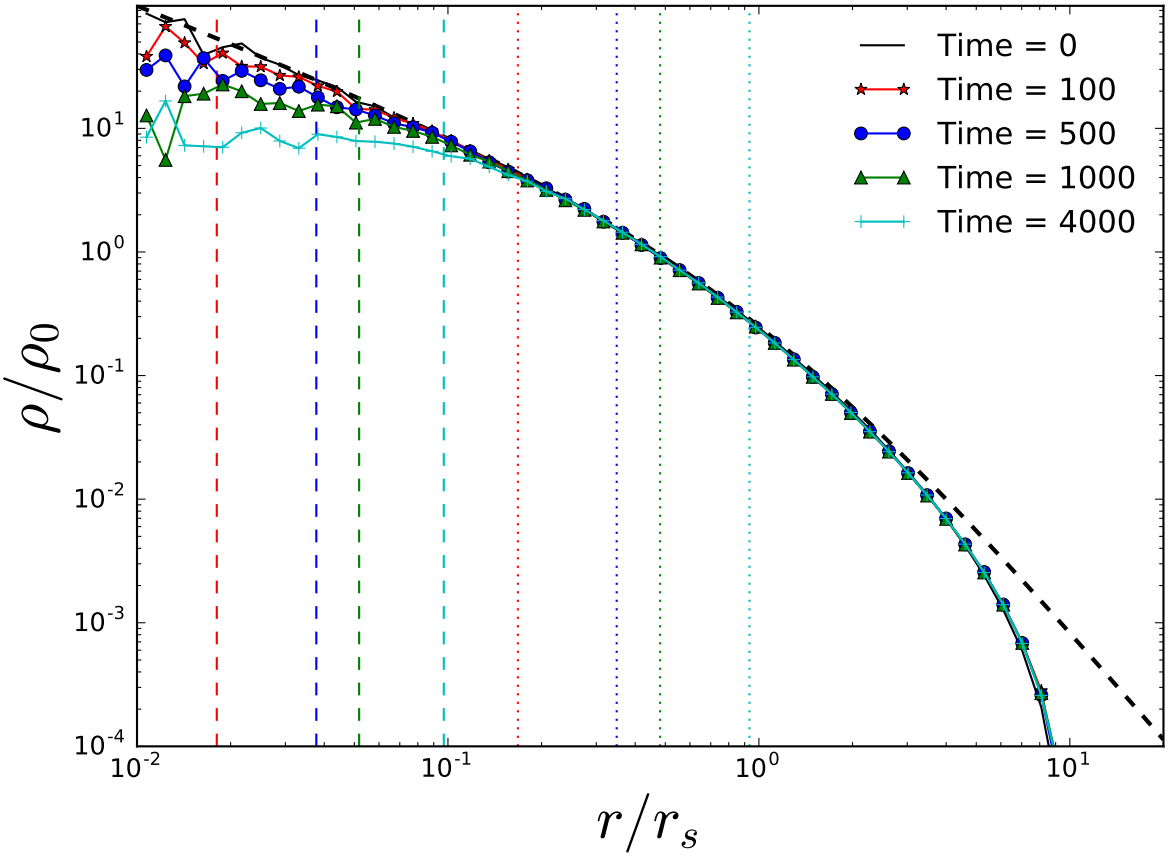

Figure 2.1: Evolution of the density profile simulated in isolation. The black dashed line shows a (non-truncated) NFW profile, and the solid black line shows the profile of our ICs at $t = 0$. The coloured lines show the density profile at subsequent times, as labeled. Radii $r_{\rm rel}$ and $r_{\rm evap}$ at which relaxation and evaporation effects become important are shown with vertical dotted and dashed lines, respectively. The truncated profile is completely stable outside $r_{\rm evap}$. Time is in units of $\sqrt{r_{\rm s}^3/GM_{\rm sat}}$, where $r_{\rm s}$ is the scale radius, and $M_{\rm sat}$ is the mass of the halo.

2.3.1 Review of the King Model

The King model is a lowered isothermal model based on the (infinitely extended) isothermal sphere, but with a lowered relative energy $\mathcal{E}$. Additionally, it subtracts a constant term to ensure that the DF is continuous at this truncation energy. This last step results in a more extended profile (Hunter, 1977), and presumably increases the stability of the model (e.g. Guo & Li, 2008).

As previously, we will define relative energies $\Psi = -\Phi + \Phi_0$ and $\mathcal{E} = \Psi - v^2/2$. Suppose initially we choose $\Phi_0 = 0$. The DF for an isothermal sphere of velocity dispersion σ can be written:

$$F_{\rm iso}(Z) = F_0 \exp[Z] \ , \tag{2.8}$$

where $Z = \mathcal{E}/\sigma^2$ is a dimensionless, scaled version of the relative energy. As with the NFW profile, this DF corresponds to a profile that extends to infinity and has infinite mass.

A solution to the infinite mass problem of the isothermal sphere is to lower the relative energy, letting $Z \rightarrow Z - Z_{\rm t}$ (Woolley, 1954). This produces a truncated DF of the form:

$$F_{\rm Wooley}(Z) = \begin{cases} F_{\rm iso}(Z - Z_{\rm t}) & Z \geq Z_{\rm t} \\ 0 & Z \leq Z_{\rm t} \ . \end{cases} \tag{2.9}$$

If one uses the freedom of Φ_0 to express F in terms of $Z' = Z - Z_{\rm t}$, the DF has the same form as that of the infinitely extended isothermal sphere, but the density now drops to zero at a finite radius.

This form of the DF introduces a new complication, however, as it is now discontinuous at $F(Z_{\rm t})$. A solution to this problem is to subtract a constant term. DFs of this form are known as King models (Michie & Bodenheimer, 1963; King, 1966):

$$F_{\rm King}(Z) = \begin{cases} F_{\rm iso}(Z - Z_{\rm t}) - F_{\rm iso}(0) & Z \geq Z_{\rm t} \\ 0 & Z \leq Z_{\rm t} \ . \end{cases} \tag{2.10}$$

2.3.2 Energy Truncation of a NFW Distribution Function

For mathematical convenience, we introduce the following dimensionless variables; $R = r/r_{\rm s}$, $p = \rho/\rho_0$, $P = \Psi/(4\pi G \rho_0 r_{\rm s}^2)$, $Z = \mathcal{E}/(4\pi G \rho_0 r_{\rm s}^2)$ and $F = (4\pi G)^{3/2} r_{\rm s}^3 \rho_0^{1/2} f$, where $\Psi(r) = -\Phi(r) + \Phi_0$ and $\mathcal{E} = \Psi(r) - v^2/2$, as above. Here, the energies have been normalized by the magnitude of the central potential of a NFW profile $|\Phi_{\rm NFW}(r = 0)| = 4\pi G \rho_0 r_{\rm s}^2$.

The DF for the NFW profile can be determined numerically from Equation (2.4). However, in practice, we use the analytic approximation proposed by Widrow (2000):

$$F_{\rm NFW}(Z) = F_0 Z^{3/2}(1-Z)^{-5/2}\left(-\frac{\ln Z}{1-Z}\right)^q \times \exp(p_1 Z + p_2 Z^2 + p_3 Z^3 + p_4 Z^4) \ , \quad (2.11)$$

where $q = -2.7419$, $p_1 = 0.3620$, $p_2 = -0.5639$, $p_3 = -0.0859$, $p_4 = -0.4912$ and $F_0 = 0.091968$. We find that this approximation agrees with the numerically calculated DF to within 2 per cent.

We wish to truncate the NFW DF at some truncation energy $\mathcal{E}_{\rm t}$, or in dimensionless form $Z_{\rm t} = \mathcal{E}_{\rm t}/(4\pi G\rho_0 r_{\rm s}^2)$. The modified DF is then given by:

$$F(Z) = \begin{cases} F_{\rm NFW}(Z) - F_{\rm NFW}(Z_{\rm t}) & Z \geq Z_{\rm t} \\ 0 & Z \leq Z_{\rm t} \ . \end{cases} \quad (2.12)$$

We can exploit the freedom of Φ_0, picking a new value such that the relative energy is zero on the boundary. Given this new value of Φ_0, and denoting the new relative energy variable $Z' = Z - Z_{\rm t}$, the DF then becomes:

$$F(Z') = \begin{cases} F_{\rm NFW}(Z' + Z_{\rm t}) - F_{\rm NFW}(Z_{\rm t}) & Z' \geq 0 \\ 0 & Z' \leq 0 \ , \end{cases} \quad (2.13)$$

where $Z_{\rm t}$ the truncation energy defined using the original value of Φ_0.

Note that this derivation is slightly different from that of the lowered isothermal sphere model outlined in Section 2.3.1. Comparing Equations (2.10) and (2.13), we find that applying the latter to the isothermal sphere will recover the King model, but multiplied by a constant term $e^{Z_{\rm t}}$.

It can be shown that the relative energy of the energy-truncated NFW profile has a maximum value $Z = 1 - Z_{\rm t}$; this corresponds to the central relative potential $P(0)$ of the truncated system. The final system has a finite radius, $r_{\rm t}$. Increasing the truncation energy will decrease the central potential, the truncation radius, and the total mass of the system.

We need two more equations to describe this system. The density profile can be recovered from Equation (2.3), and the relative potential can be determined from Poisson's equation:

$$\frac{{\rm d}^2\Psi}{{\rm d}r^2} + \frac{2}{r}\frac{{\rm d}\Psi}{{\rm d}r} = -4\pi G\rho(\Psi) \ , \quad (2.14)$$

or, re-expressed in the dimensionless parameters:

$$\frac{\mathrm{d}^2 P}{\mathrm{d}R^2} + \frac{2}{R}\frac{\mathrm{d}P}{\mathrm{d}R} = -p(P) = -4\pi \int_0^P F(Z)\sqrt{2(P-Z)}\mathrm{d}Z \ . \tag{2.15}$$

The initial conditions are $P(0) = 1 - Z_\mathrm{t}$ and $\mathrm{d}P(0)/\mathrm{d}R = 0$. Equation (2.15) can be integrated numerically until $P(R_\mathrm{t}) = 0$.

Putting all this together, the density of the truncated halo at radius R can be determined using the following steps:

1. Specify the dimensionless truncation energy $Z_\mathrm{t} \in (0, 1)$.
2. Given the distribution function, calculate the potential at radius R by numerically integrating Poisson's equation (Equation (2.15)) with initial conditions $P(0) = 1 - Z_\mathrm{t}$, $\mathrm{d}P(0)/\mathrm{d}R = 0$.
3. Find the density by numerically integrating Equation (2.3).

The potential $\Phi(r) = -\Psi(r) + \Phi_0$ can be recovered once the truncation radius has been determined, since $\Phi_0 = -GM(r_\mathrm{t})/r_\mathrm{t}$.

Finally, we note that although we have discussed the energy-truncation method specifically for an NFW profile, it can be used for any density profile with a known or calculable DF, including an Einasto profile, and could also be extended to the various theoretically motivated models of the intrinsic halo DF (e.g. Hjorth & Williams, 2010; Pontzen & Governato, 2013; Beraldo e Silva et al., 2014). For cored density profiles, energy truncation will generally reduce the central density of the system significantly as the outer radius decreases, as discussed by Widrow & Dubinski (2005) and Peñarrubia et al. (2010).

2.3.3 Properties of the Truncated Model

As we increase the truncation energy, the mass and extent of the NFW profile will decrease progressively. Fig. 2.2 shows how the density profile changes as a function of the dimensionless truncation energy Z_t, relative to the original NFW profile. Note that by definition, the density drops to zero outside the truncation radius (indicated by the vertical dashed lines).

The relationships between the truncation energy, Z_t, and the total bound mass and truncation radius are shown in Fig. 2.3. Both the mass and the truncation radius are

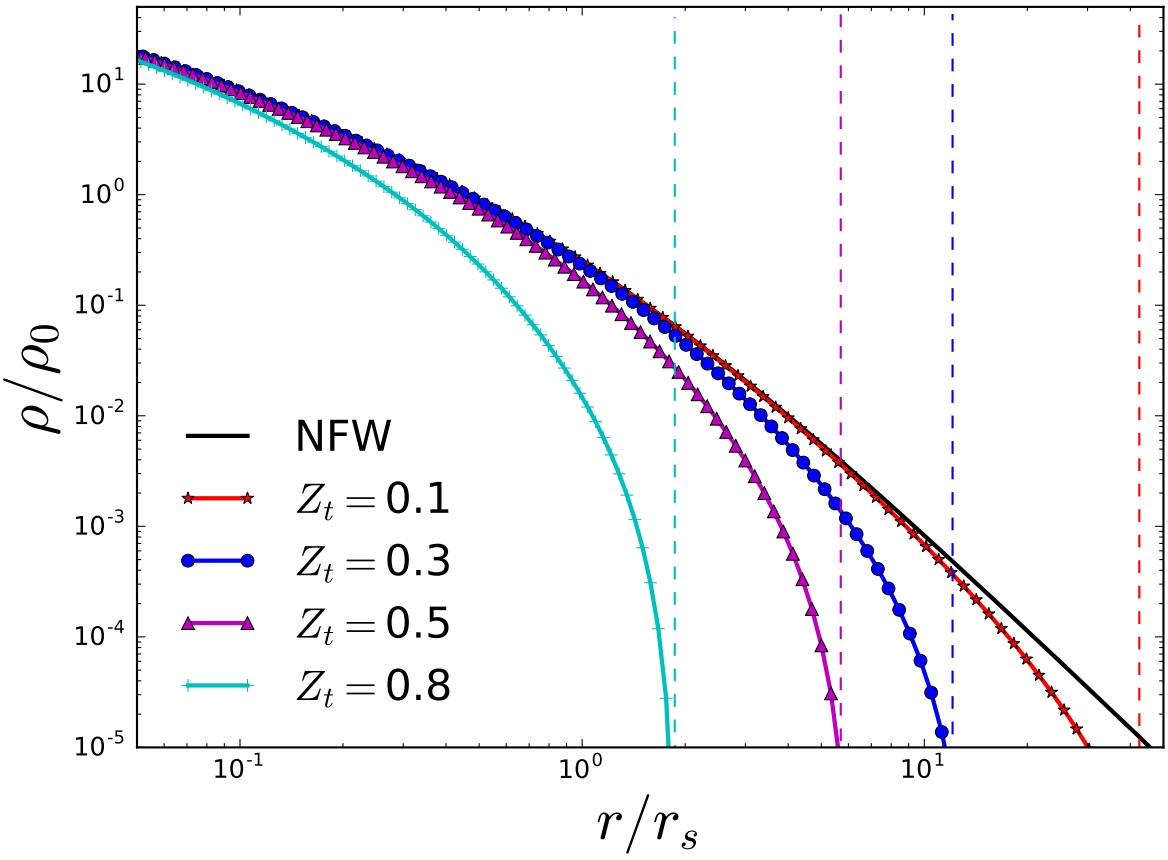

Figure 2.2: Density profile of an energy-truncated NFW profile. The truncation energy, $Z_{\rm t}$, is the dimensionless relative energy, $Z_{\rm t} = \mathcal{E}_{\rm t}/4\pi G\rho_0 r_{\rm s}^2$. Vertical dashed lines indicate the truncation radius, $r_{\rm t}$.

smooth, decreasing functions of the truncation energy, as expected. The polynomial fits to the data shown (and valid over the range of the plot) are $M_f \equiv M(r < r_\mathrm{t})/M_\mathrm{NFW}(r < r_\mathrm{t}) = 0.35Z_\mathrm{t}^2 - 1.14Z_\mathrm{t} + 0.83$ and $r_f \equiv \log_{10}(r_\mathrm{t}/r_\mathrm{s}) = -3.70Z_\mathrm{t}^3 + 5.93Z_\mathrm{t}^2 - 4.56Z_\mathrm{t} + 2.01$. We can also fit the inverse relations: $Z_\mathrm{t} = 0.6M_f^2 - 1.7M_f + 1.02$ and $Z_\mathrm{t} = 0.2r_f^3 - 0.4r_f^2 - 0.39r_f + 0.94$.

Finally, we return to our original goal, to establish an analytic approximation to the DF produced by the iterative unbinding procedure we introduced in Section 2.2. In Fig. 2.4, we show how the ICs derived in Section 2.2 compare to the analytic energy-truncated NFW model developed in this section. The histogram shows the ICs, the lower dashed curve shows the result of truncating the NFW DF at the energy $\mathcal{E}_\mathrm{t}$ (i.e. $f(\mathcal{E}) = f_\mathrm{NFW}(\mathcal{E} + \mathcal{E}_\mathrm{t})$), while the upper dotted curve shows the full model, including the shift to make f continuous at zero: $f(\mathcal{E}) = f_\mathrm{NFW}(\mathcal{E} + \mathcal{E}_\mathrm{t}) - f_\mathrm{NFW}(\mathcal{E}_\mathrm{t})$. As before, the solid line shows the original untruncated profile. Both models provide a good match to the density profile of the ICs. As with the King model, subtracting the constant term $f_\mathrm{NFW}(\mathcal{E}_\mathrm{t})$ produces a more extended profile. We will adopt this version as our final analytic model for the DF, on the assumption that it is slightly more stable than the model where f is discontinuous at zero. Overall, these results suggest that an energy-truncated DF comes close to describing ICs obtained using the method outlined in Section 2.2. In principle, ICs could therefore be generated directly from the energy-truncated DF, although in practice our code implements the iterative unbinding procedure.

2.4 Simulating Tidally Stripped Haloes

The very similar truncated profiles derived either by iterative unbinding in Section 2.2, or analytically in Section 2.3, were designed to represent isolated systems of finite mass and radial extent. We note, however, that they also look very similar to the density profiles of tidally stripped haloes orbiting within the potential of a larger system (e.g. Hayashi et al., 2003). To pursue this analogy, we will compare our truncated models directly to tidally stripped haloes taken from simulations of satellite mass loss. We describe the simulations and basic analysis below, and then compare the simulated systems to our models in Section 2.5.

2.4.1 Simulation Parameters

Simulations of a smaller 'satellite' halo orbiting within the potential of a larger static 'host' halo were performed using the N-body code GADGET-2 (Springel, 2005). This code was

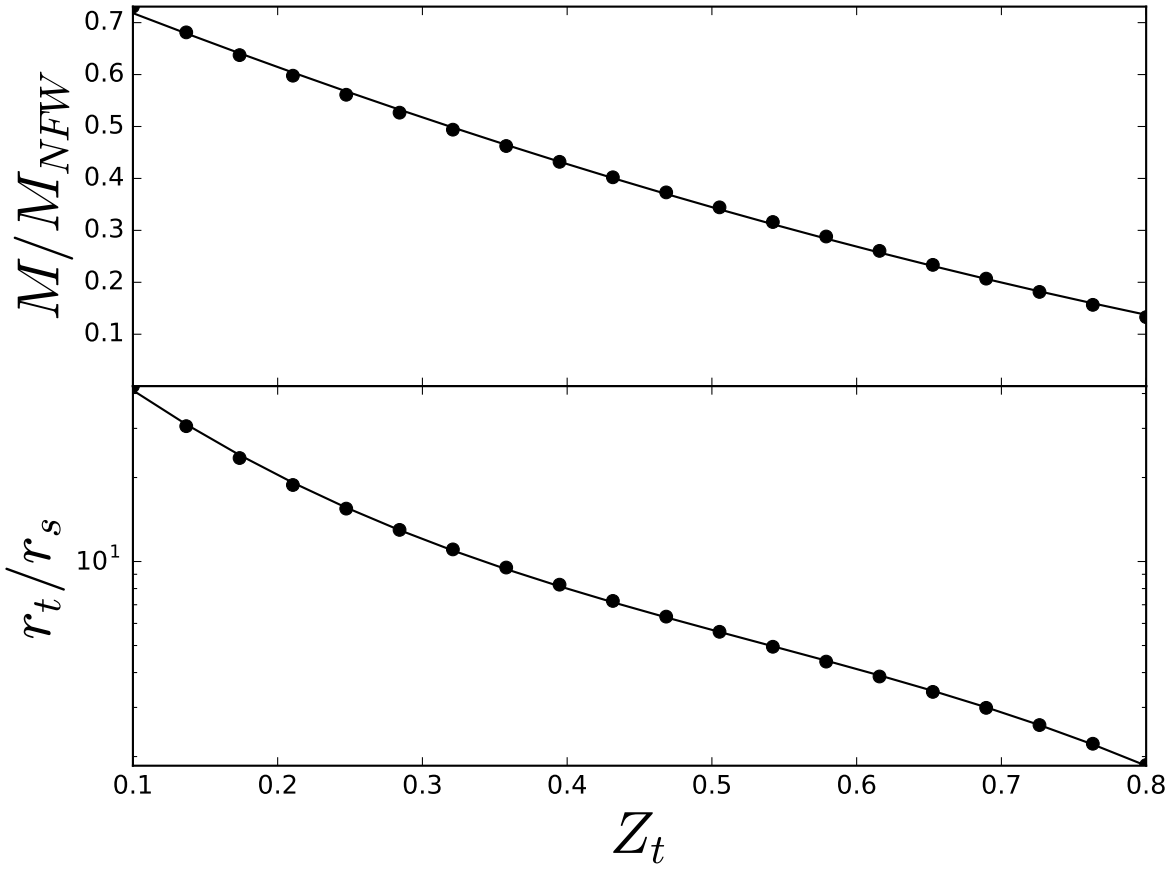

Figure 2.3: How the bound mass fraction (top) and truncation radius (bottom) change as a function of the dimensionless truncation energy, $Z_{\rm t} = \mathcal{E}_{\rm t}/4\pi G\rho_0 r_{\rm s}^2$. The bound mass fraction is defined as the total mass within the truncation radius divided by the mass of an untruncated NFW profile within the same radius. Polynomial fits are given in the text.

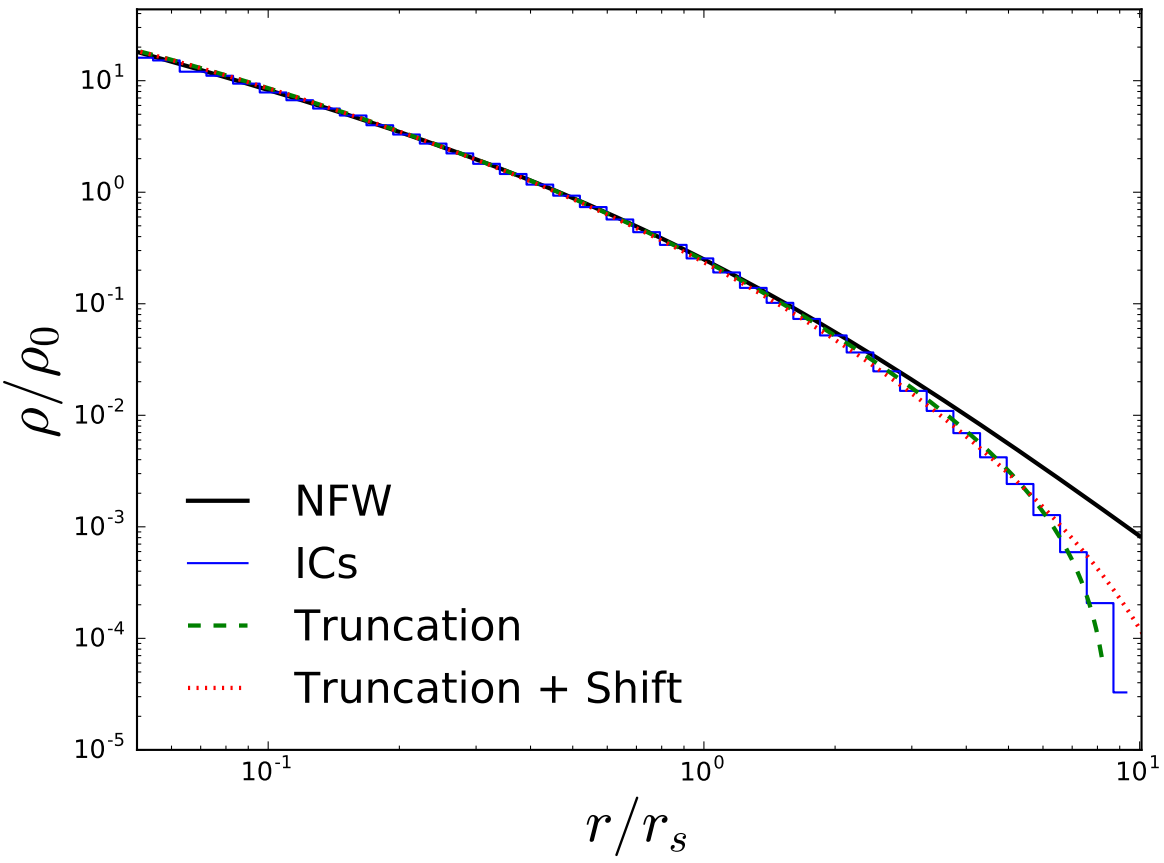

Figure 2.4: Analytic models for the truncated profile, compared to ICs generated using the iterative method (histogram). The lower dashed curve shows the result of an energy truncation alone, such that $f(\mathcal{E}) = f_{\rm NFW}(\mathcal{E}+\mathcal{E}_{\rm t})$. The upper dotted curve shows the result of a truncation plus a shift to make the DF continuous at zero: $f(\mathcal{E}) = f_{\rm NFW}(\mathcal{E}+\mathcal{E}_{\rm t}) - f_{\rm NFW}(\mathcal{E}_{\rm t})$. The solid line shows the untruncated NFW profile.

modified to contain a fixed background potential corresponding to a host halo with an NFW profile. We use the mass and scale radius of the satellite halo ($M_{\rm sat}$ and $r_{\rm s}$) as the mass and distance units. Time is given in units $t_{\rm unit} = \sqrt{r_{\rm s}^3/GM_{\rm sat}}$, and velocity in units of $v_{\rm unit} = \sqrt{GM_{\rm sat}/r_{\rm s}}$. The host and satellite haloes were assumed to have the same initial density within their outer, or 'virial' radii, as would be the case for a merger between two cosmological haloes at a fixed redshift. We generated initial conditions for the satellite using our iterative unbinding algorithm with $r_{\rm cut} = r_{\rm vir} = 10\,r_{\rm s}$, as described in Section 2.2. The virial radius of the main halo scales as $(M_{\rm host}/M_{\rm sat})^{1/3}$, while the scale radius of the host was set assuming $c_{\rm host} = 10$.

The orbital parameters of infalling satellite haloes have been studied extensively in simulations (Tormen, 1997; Ghigna et al., 1998; Vitvitska et al., 2002; Benson, 2005; Wang et al., 2005; Zentner et al., 2005; Khochfar & Burkert, 2006; Wetzel, 2011; Jiang et al., 2015). The parameters used in this chapter (see Table 2.1) cover the full range of energy and angular momentum expected for cosmological mergers (e.g. Jiang et al., 2015), with the exception of Simulations 5 and 6 which have unusually low and high energies, respectively. This allows us to test our tidal-stripping model not only for cosmological orbits, but also for a few more extreme cases.

We considered four different host/satellite mass ratios, $M_{\rm host}/M_{\rm sat} = 300$, 100, 50 and 10. Since the host halo was modelled as a fixed background potential, the satellite is not subject to dynamical friction in our simulations, and we expect its specific energy and angular momentum to be roughly conserved, even as it loses mass. The assumption that the host halo is static becomes less physically valid for low mass ratios, where dynamical friction plays a larger role. Nonetheless, we run a few cases at smaller mass ratios to test the effect of a larger satellite on the evolution of the density profile. At large mass ratios, where the satellite is small compared to the scale of the background potential, we expect satellite evolution to become independent of mass ratio. We chose a limiting value of $M_{\rm host}/M_{\rm sat} = 300$ for practical reasons, as the ratio of the simulation time step to the orbital period is becoming very long at this point.

2.4.2 Locating the Satellite Remnant

We identified the satellite remnant at any given time using a method similar to the one outlined in Tormen et al. (1997, 1998). This is also the method used in Hayashi et al. (2003). There are two steps to this method; first the highest density peak of the particles is located approximately by iteratively decreasing the radius R of a sphere, and re-centering it at each step on the center of mass of the particles contained within the sphere. We decreased the

Table 2.1: Summary of simulation parameters. Columns give (1) the simulation number (2) the mass ratio between the host and satellite halo (3) the virial radius of the host (4) the apocentric distance (5) the pericentric distance (6) the tangential velocity at apocenter (7) the (radial) orbital period, (8) the circularity of the orbit, (9) the relative energy (defined as the energy divided by the energy of a circular orbit at the virial radius) (10) the radius of a circular orbit with the same energy divided by the virial radius.

Sim	$M_{\rm host}/M_{\rm sat}$	$R_{\rm vir}/r_{\rm s}$	$r_a/r_{\rm s}$	$r_{\rm p}/r_{\rm s}$	$v_{\rm a}/v_{\rm unit}$	$t_{\rm orb}/t_{\rm unit}$	ϵ_c	η	$R_c/R_{\rm vir}$
1	100	46.4	100	10	0.34	206.8	0.42	0.85	1.26
2	100	46.4	100	50	0.90	299.4	0.92	0.71	1.63
3	300	66.9	100	10	0.51	129.7	0.40	1.09	0.88
4	300	66.9	100	50	1.42	185.4	0.92	0.92	1.13
5	100	46.4	500	50	0.23	1778.5	0.47	0.24	6.14
6	300	66.9	25	10	1.50	31.48	0.82	2.29	0.26
7	50	36.8	80	5	0.19	201.6	0.30	0.86	1.24
8	50	36.8	90	15	0.37	259.7	0.58	0.76	1.48
9	10	21.5	40	10	0.30	196.8	0.71	0.88	1.19
10	10	21.5	25	10	0.42	123.2	0.85	1.14	0.82

sphere by $0.9\,R$ on each iteration, and repeated until there were fewer than 100 particles within the sphere. We expect our results to be insensitive to this choice of final particle number, as discussed in Tormen et al. (1997). The velocity of the satellite frame was then calculated as the average velocity of all satellite particles within a sphere of radius $r_{\rm cut}$ (the original truncation radius of the satellite) centered on the highest density peak. The second step of this process was to identify which subset of particles was self-bound in this frame. This was calculated by iteratively removing unbound particles in the rest frame of the satellite until the algorithm converged.

Finally, we found that in a few cases where the algorithm had trouble locating a self-bound remnant (particularly at late times in Simulation 6), we were able to improve the algorithm by first approximating the location of the satellite remnant by integrating forward from the previous snapshot (assuming the satellite was a point mass orbiting in the potential of the host), and then only considering particles within $2\,r_{\rm cut}$ of this predicted location.

Fig. 2.5 shows how the recovered satellite mass decreases with time for the ten simulations. Given a bound remnant and associated satellite reference frame in each step, we then fit the remnant's profile to the analytic model from Section 2.3, as described below.

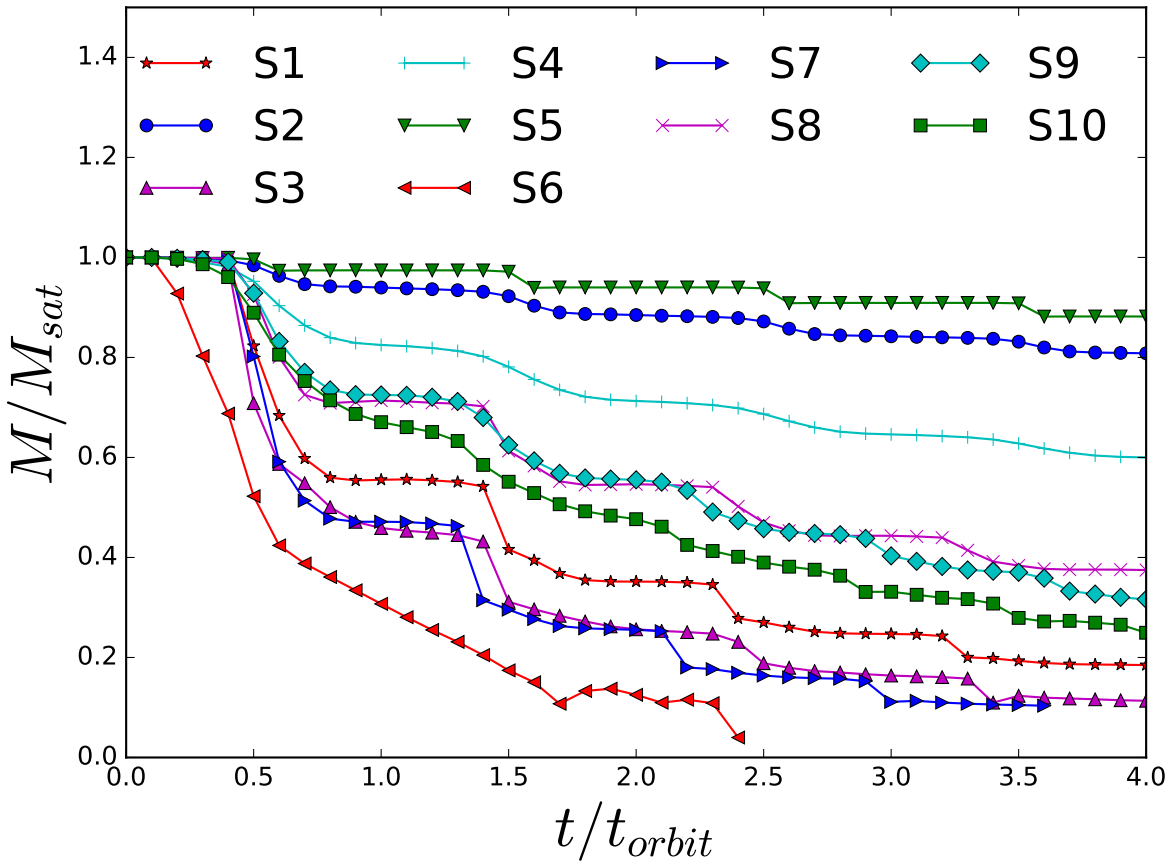

Figure 2.5: Bound mass fraction as a function of time (in units of the orbital period).

2.5 Results

2.5.1 Fitting Criteria

To compare our tidally stripped satellites to the energy truncated DF model, we need a way of determining the free parameter, $Z_{\rm t}$. We do this by normalizing our DF models, such that their scale radii and central densities before truncation match those of the original NFW profile from which the ICs for the simulations were derived by the iterative method. This accounts for the fact that the initial conditions in the simulations are already truncated at a finite radius. $Z_{\rm t}$ is then chosen so that both the simulations and the models have the same mass. We compare the analytic model to the simulations at apocenter on successive orbits, since these are the times when we expect the satellite to be closest to equilibrium.

2.5.2 Density Profiles, Enclosed Mass, and Circular Velocity Profiles

The top panels of Fig. 2.6 show a comparison of the satellite density profiles from simulations (points) with the energy-truncated model (solid curves), where $Z_{\rm t}$ has been fixed as described above. The thick dashed curve shows an untruncated NFW profile. We demonstrate how the profile changes in time for Simulations 4 and 3 in the two left-most panels, as well as how the different simulations compare in the two right-most panels. Note that Simulation 4 and Simulations 2, 5, 8 and 9 are the orbits with the slowest mass loss, and therefore the ones we might expect to be the most successfully described by our model. The bottom panels of Fig. 2.6 show the relative residuals in density, $(\rho_{\rm sim}/\rho_{\rm model} - 1)$. These are generally less than 10 per cent for the orbits with slower mass loss, or less than 20 per cent for orbits with faster mass loss. They are largest for Simulation 6, which loses mass extremely rapidly (see Fig. 2.5), or at late times for Simulation 3. The residuals are generally slightly larger at large radii, where an excess relative to the model is also visible in the top panels. Previous authors (e.g. Peñarrubia et al., 2008b, 2009, 2010, and earlier references therein) have noted a distinct population of particles in the outer parts of tidally stripped systems, at radii too large to have crossed the satellite in the time since last pericentric passage. This may account for some of the excess seen here.

Fig. 2.7 and Fig. 2.8 show a comparison of the enclosed mass and circular velocity profiles, respectively. Linestyles are as in Fig. 2.6. Here too, residuals are generally at the 10–20 per cent level or less. The largest deviations occur in Simulation 6, which loses mass the fastest. It should also be noted that Simulation 6 corresponds to an extreme,

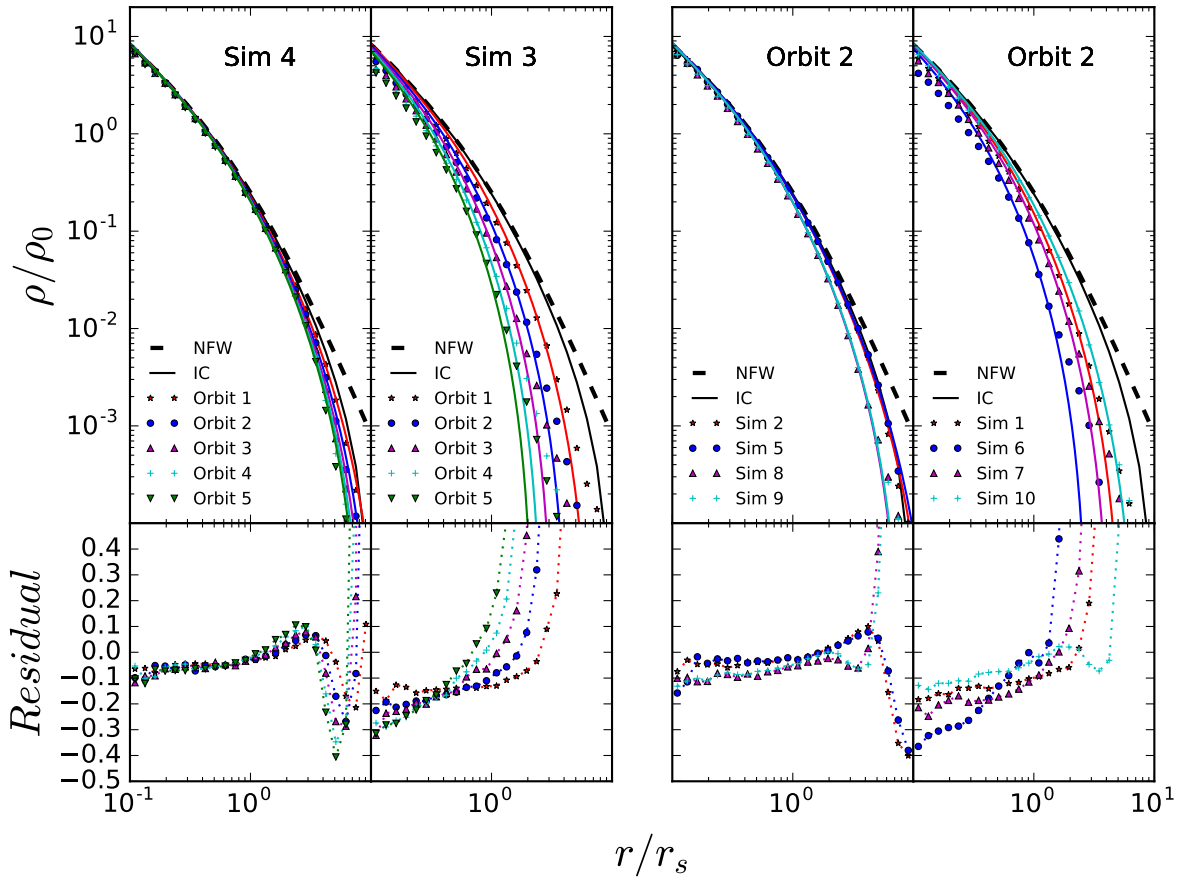

Figure 2.6: (Top panels) Density profiles of the bound satellite remnant. Simulation results are shown with points, and the best-fit energy-truncated model is shown with lines. The thick dashed curve shows an untruncated NFW profile, while the solid black curve shows the initial conditions at the start of the simulation. The two left panels show the first four orbits of Simulation 4 and Simulation 3. The two panels on the right show the profiles after two orbits for the simulations indicated. (Bottom panels) Relative residuals in density, $(\rho_{\rm sim} - \rho_{\rm model})/\rho_{\rm model}$.

uncosmological orbit, with unusually large energy and extremely rapid mass loss, so it is less representative of realistic halo mergers. We also note that our mass profiles and circular velocity profiles are constrained by the condition that the stripped mass fraction in the simulations matches the corresponding fraction in the models; a slightly different choice of $Z_{\rm t}$ would have improved the agreement at some radii (e.g. near the peak of the circular velocity curve in Simulation 1), at the expense of a slightly worse fit close to $r_{\rm cut}$.

In general, the radius at which evaporation becomes important is not visible on the scales of Figs. 2.6–2.8. The exception is Simulation 5, which has a very long orbital time scale. Thus, the deficit of mass at small radii for this simulation can be attributed to collisional effects.

2.5.3 Distribution Function and Moments of the Phase-Space Distribution

Finally, we can attempt to compare the full DF of our simulated systems to the analytic energy-truncated model. We note that the construction of the DF requires a frame in which to define velocities, and a set of particles to integrate over when calculating the potential. Thus the 'distribution function' of a subsystem within a larger halo is a slightly problematic concept, relative to the usual definition for an isolated system. Here, to be concrete, we define velocities in the mean center-of-mass frame of the self-bound remnant, and calculate potential energies summing only over those particles that are bound.

Given this convention, the DFs for the first four orbits of Simulation 4 are shown in Fig. 2.9. Each point represents the number of particles in a bin of normalized relative energy Z. This was found by binning the particles in 500 equally sized bins in both radius and velocity. The phase-space density of each bin was then calculated as the number of particles divided by $16\pi^2 r^2 v^2 {\rm drdv}$. As usual, the relative energy is $\mathcal{E} = \Psi(r) - v^2/2$, where $\Psi(r) = -\Phi(r) + \Phi(r_{\rm max})$, and $r_{\rm max}$ is the radius of the remnant. Only bins with phase-space volume greater than 10^{-5} were plotted, to avoid numerical errors resulting from dividing by small numbers.

The solid lines show the prediction of the analytic model from Section 2.3 for comparison, while the dashed line shows the original (untruncated) NFW DF. Generally speaking, there is good agreement between the tidally stripped DFs and the analytic models for low relative energies, though it is difficult to compare the simulation to the model for large values of Z (corresponding to particles at small radii and/or low energies), since the phase-space volume becomes very small in this limit.

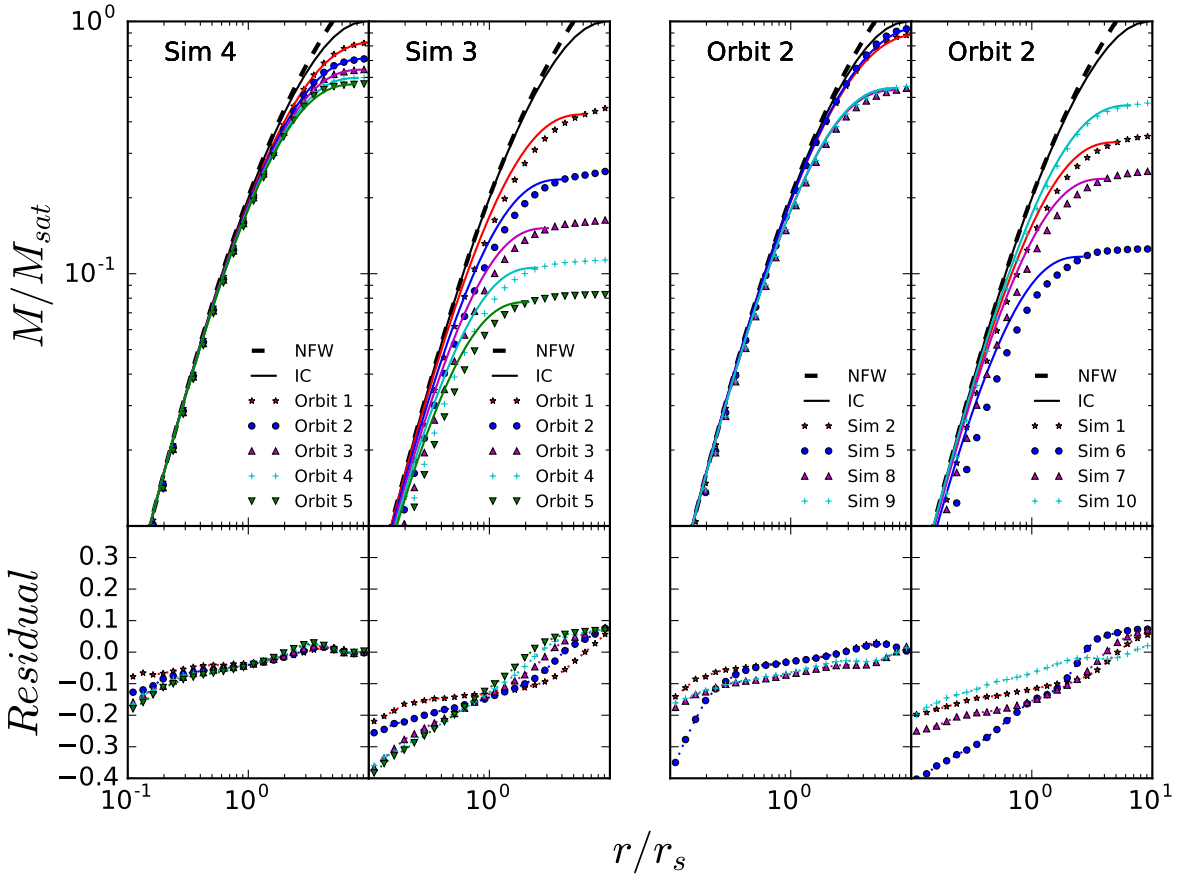

Figure 2.7: (Top panels) Cumulative mass profiles of the bound satellite remnant. Simulation results are shown with points, and the best-fit energy-truncated model is shown with lines. The thick dashed curve shows an untruncated NFW profile, while the solid black curve shows the initial conditions at the start of the simulation. The two left panels show the first four orbits of Simulation 4 and Simulation 3. The two panels on the right show the profiles after two orbits for the simulations indicated. (Bottom panels) Relative residuals in mass, $(M_{\rm sim} - M_{\rm model})/M_{\rm model}$.

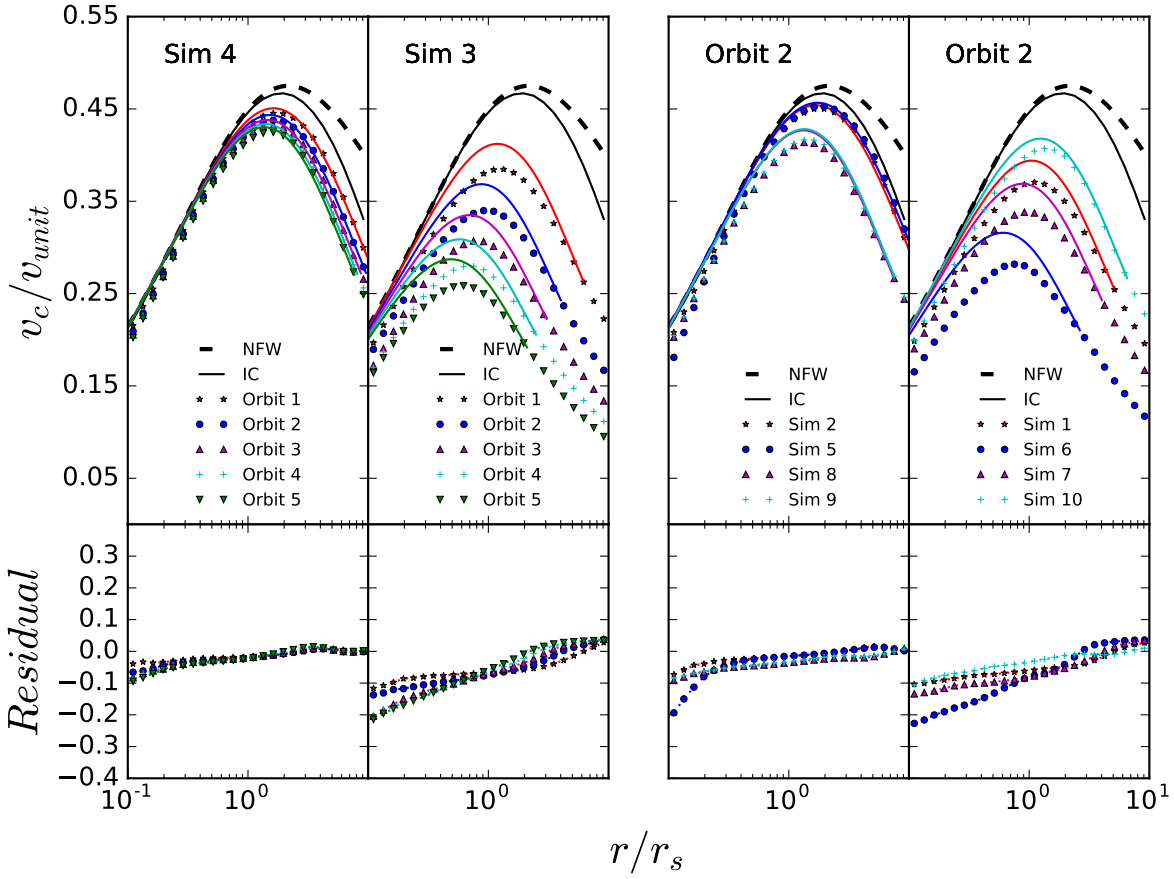

Figure 2.8: (Top panel) Circular velocity of the bound satellite remnant as a function of radius. Simulation results are shown with points, and the best-fit energy-truncated model is shown with lines. The thick dashed curve shows an untruncated NFW profile, while the solid black curve shows the initial conditions at the start of the simulation. The two left panels show the first four orbits of Simulation 4 and Simulation 3. The two panels on the right show the profiles after two orbits for the simulations indicated. (Bottom panels) Relative residuals $(v_{\rm sim} - v_{\rm model})/v_{\rm model}$.

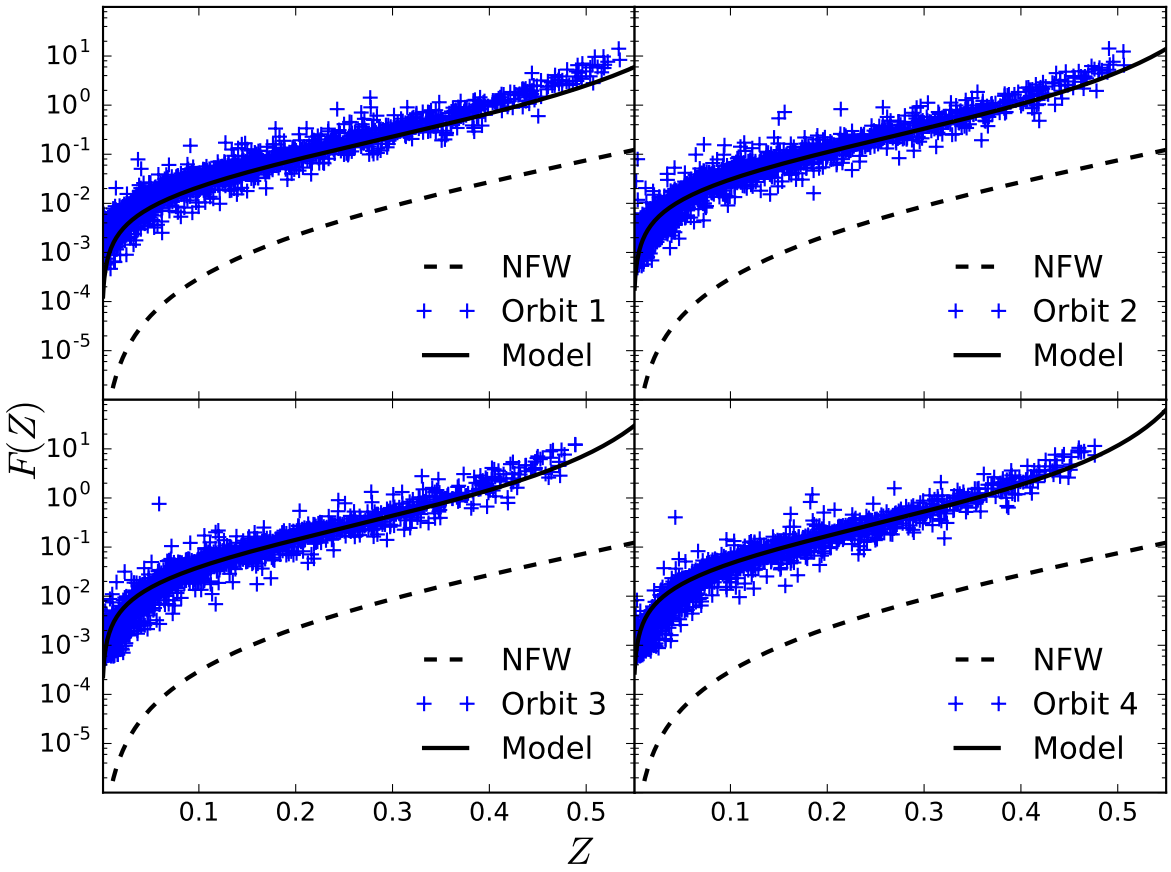

Figure 2.9: The DF as a function of the dimensionless relative energy Z, for the first four orbits of Simulation 4. The simulation results, binned in phase-space, are shown as crosses, while the predictions of the energy-truncated model are shown as solid curves. The dashed curves show the DF for an infinitely extended NFW profile.

In Fig. 2.10 we also show the evolution of the pseudo-phase-space density for Simulations 3 and 4 (top panel). As first noted by Taylor & Navarro (2001), the spherically averaged pseudo-phase-space density, ρ/σ^3, of isotropic, cosmological haloes appears to follow a simple power law as a function of radius. The dashed line shows this power-law for an infinitely extended NFW profile. For the truncated analytic models (solid lines), we can calculate the velocity dispersion from the probability distribution function for velocities, $P(v) \propto f(\mathcal{E})v^2/\rho(r)$. The analytic models also follow a power law out to around the truncation radius, but with a flatter slope. The relative increase in pseudo-phase-space density at large radii is expected, since energy truncation reduces the number of particles with large velocities, and thus the velocity dispersion, in these regions. A similar flattening of the slope has also been seen in tidally truncated subhaloes from self-consistent cosmological simulations (Vera-Ciro et al., 2014).

Interestingly, while the simulation results (points) match the analytic models extremely well at small radii, they deviate from them systematically at large radii. The bottom panel shows the likely reason for this discrepancy: the tidally stripped simulations are not isotropic in their outer regions. Plotting the anisotropy parameter $\beta = 1-(\sigma_\theta^2+\sigma_\phi^2)/2\sigma_r^2$ as a function of radius, we see that the analytic model and simulation results in the top panel begin to differ at radii where β is becoming significantly different from zero, suggesting that our analytic model fails to match the outer parts of the simulations primarily because the assumption of isotropy is no longer valid there.

To get a better sense of where the simulations differ from the models in the full phase space, we can also bin the DF in radius and (total) velocity. Fig. 2.11 shows this 2-D distribution for the first three orbits of Simulation 4 (top three panels), the corresponding analytic models (middle panels), and the differences between the two (lower panels). Generally speaking, there is good agreement between the models and the simulations in this projection of the full phase space. The tidally stripped satellites show a slight excess of particles at large radii and large velocities, and this excess may even have a caustic-like structure to it. It seems likely that this is related to the excess component at large radii noted by earlier authors and discussed in the previous section. Peñarrubia et al. (2009) found that this outer material, while still bound, is on its way out of the system and is mostly lost on the next orbit. Such non-equilibrium effects would not be captured by our analytic truncation model. There is also a slight deficit of particles at small radii and low velocities. Here, relaxation may play a role in scattering particle energies, and depleting the lowest-energy orbits.

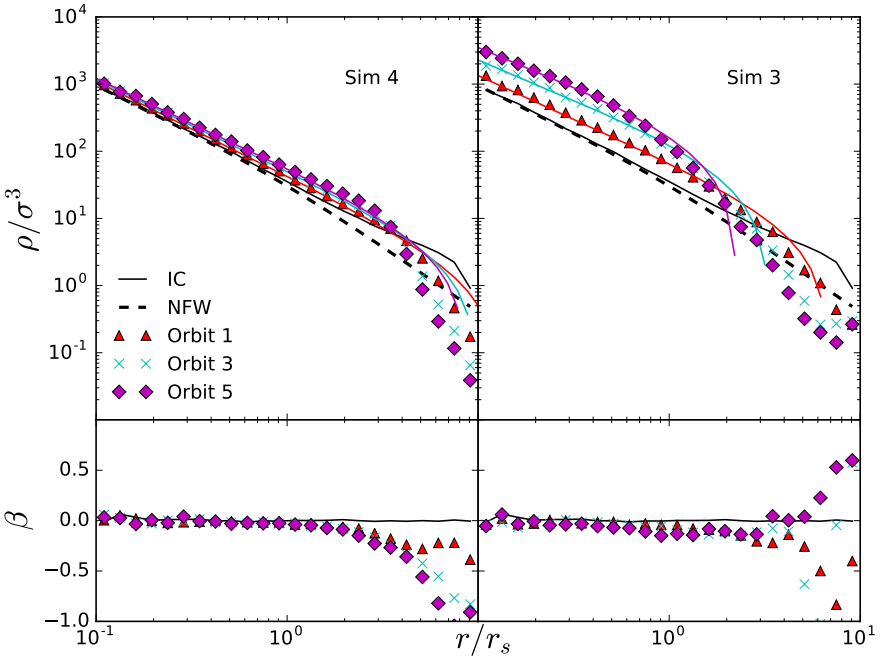

Figure 2.10: The pseudo-phase-space density (top) and anisotropy parameter (bottom) as a function of radius for Simulations 4 (left) and 3 (right). Density is in units ρ_0, and the velocity in units $v_{\rm unit} = \sqrt{GM_{\rm sat}/r_{\rm s}}$. The thick dashed curve shows an untruncated NFW profile, while the solid black curve shows the initial conditions at the start of the simulation. Simulation results are shown with points, and the analytic model with lines.

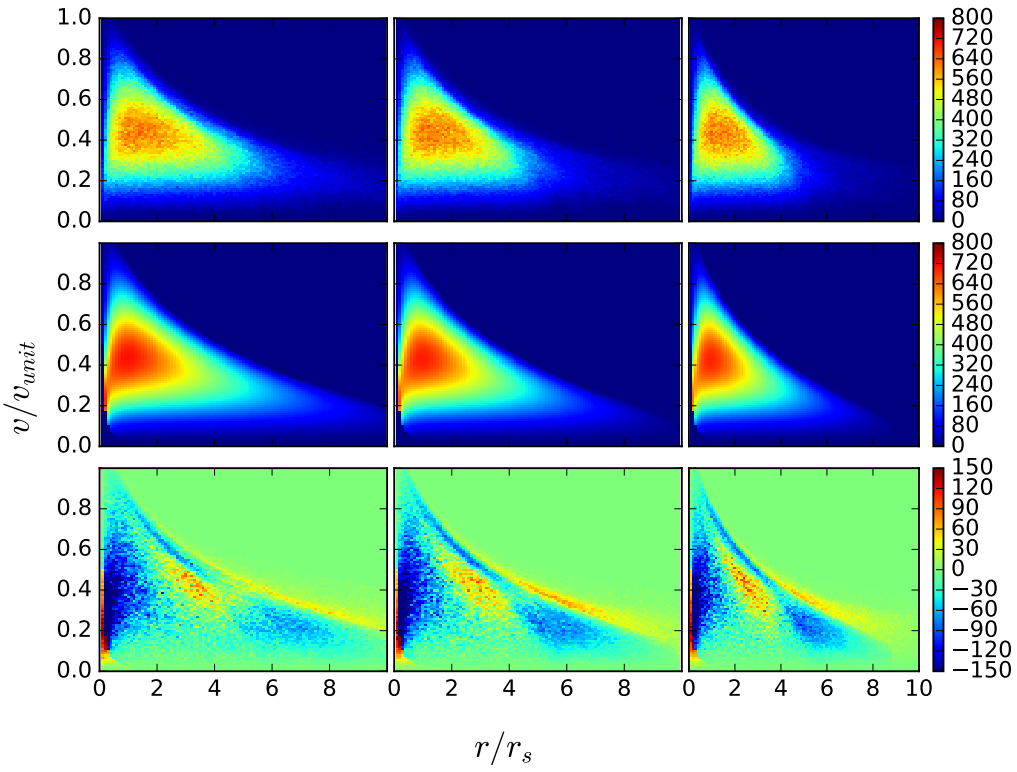

Figure 2.11: Number of particles as a function of radius and total velocity. The Simulation 4 results (top row), the analytic model (middle row), and the difference between the two (bottom row), at each of the first three apocentric passages (three columns).

2.6 Discussion and Conclusions

Dark matter haloes play a central role in the current picture of cosmological structure formation, and their properties and evolution determine many of the broad trends in the properties of galaxies, galaxy groups and galaxy clusters. Our understanding of halo formation and evolution is still limited, however; many basic questions, such as the origin of the universal density profile or the concentration-mass relation, have not yet been answered fully. Progress in understanding halo properties will come from a combination of fully realistic, large-volume cosmological simulations, together with simpler, idealized simulations of individual haloes. Our original goal, in this work, was to develop a better algorithm for generating initial conditions for the latter.

We have found through experimentation that two different approaches yield similar results: either truncating an NFW profile abruptly at some radius $r_{\rm cut}$, and then iteratively removing unbound particles until convergence is reached, or using an analytic NFW distribution function truncated at some energy and shifted such that the resulting distribution function is continuous at $\mathcal{E} = 0$. The latter technique, inspired by the King model (King, 1966) and proposed previously by Widrow & Dubinski (2005), produces almost the same density profile as the former, and allows us to construct simple analytic models for spatially finite systems whose central regions resemble NFW profiles. For generating initial conditions in practice, we have used the first method; our tests show that these models are extremely stable, and thus well suited to the study of isolated systems.

For either of these solutions, the density profile drops off steeply, reaching zero at a finite truncation radius. This behaviour is familiar from numerical studies of tidally stripped haloes, starting with (Hayashi et al., 2003). Pursuing the suggestion of a connection between the two, we have simulated the tidal evolution of satellite subhaloes in the potential of a larger system. We find that the resulting tidally stripped remnants match our theoretical models at the 10–20 per cent level or better in density profile, enclosed mass and/or circular velocity profile. In phase space they also look similar, particularly when we plot phase-space density projected in terms of radius and total velocity. Some of the minor differences may relate to the presence of unrelaxed material close to the outer edge of the system, as discussed by Peñarrubia et al. (2009), or to relaxation effects near its centre. The origin and full significance of these differences will require further work to clarify. Nonetheless, overall our analytic model provides a good first approximation to the detailed distribution function of tidally stripped systems.

This result is actually slightly surprising. Tidal mass loss is a complex process, and has been investigated by many authors previously, using different approaches and approximations. Taylor & Babul (2001), for instance, developed a 1-D model for tidal stripping,

calculating the average effects of tidal heating and expansion, as well as adiabatic cooling, within spherical shells, and removing the mass outside an instantaneous tidal limit over a timescale equal to the instantaneous (angular) orbital period, $t_{\rm orb} = 2\pi/\omega$. A limitation of this model, in the present context, is that it did not specify the actual density profile of the satellite at any one time, but only the net effect of heating and cooling on mass loss. Benson et al. (2002) considered a similar model, but with several corrections, notably using the shorter of the angular orbital period and the radial infall time R/v_R as the timescale for mass loss. They found this gives better agreement with mass loss rates from simulations for very radial orbits. Analytic models of a type similar have also been developed by several other groups (e.g. Zentner & Bullock, 2003; Oguri & Lee, 2004; van den Bosch et al., 2005; Zentner et al., 2005).

Kampakoglou & Benson (2007) considered the problem of mass loss in more detail, calculating the effects of heating on circular orbits more precisely using particles to sample the distribution function in energy and angular momentum, as well as for particle orbits of different inclination. They found that by successively heating and removing unbound particles, they predicted a profile similar to the one seen in their simulations, at least in the limit of weak tidal fields. This may provide the first hint that modelling mass loss in energy space can naturally explain the profile of tidally stripped cosmological haloes.

Given that they were trying to establish simpler, semi-analytic prescriptions for tidal mass loss, none of these approaches considered the full complexity of the problem. In reality, the tidal boundary is non-spherical even for a spherical system on a circular orbit; for a general orbit it is also time-varying, and the timescales for relaxation and mass removal in the outer parts of the satellite are unfortunately very close to the orbital timescales. Furthermore, real haloes are usually triaxial, and may have their spin partly coupled to their orbital angular momentum. Thus a general, predictive and highly accurate model for tidal mass loss seems a distant prospect.

Nonetheless, some simple patterns do emerge. Hayashi et al. (2003) first pointed out that all tidally truncated NFW profiles look the same, and can be fit by a single additional parameter; they showed that mass loss in their simulations is essentially a 1-dimensional sequence, a result later confirmed for a wider range of profiles by Peñarrubia et al. (2010). Our results now connect this stripping sequence to a simple cutoff and shift in the underlying distribution function, parameterized by an increasing truncation energy $\mathcal{E}_{\rm t}$. Exactly how heating, relaxation, and unbinding conspire to produce this simple result is unclear. A hint comes from the work of Choi et al. (2009), who show that individual particles in tidally stripped systems do or don't become unbound based primarily on their energy, rather than their angular momentum. Thus, a simple cut in energy may provide a fairly accurate description of the mass-loss process.

Producing a more detailed description of tidal mass loss will be the focus of future work. In the interim, the models presented here provide a new, physically motivated way of generating initial conditions for isolated haloes or tidally truncated subhaloes. Applications include studies of tidal stream formation (e.g. Amorisco, 2015, and references therein), disk heating (e.g. Moetazedian & Just, 2016, and references therein), mergers (e.g. Carucci et al., 2014, and references therein), and dwarf galaxy evolution (e.g. Tomozeiu et al., 2016, and references therein). A python code for generating ICs using our iterative method is available on-line. Its use is described in the appendix.

Finally, we note several limitations to this work. We have studied the tidal evolution of idealized, spherical, isotropic haloes, with an NFW density profile and corresponding DF. Haloes in self-consistent cosmological simulations differ from this idealized case in a number of ways. It is tempting to look to self-consistent simulations to try to understand tidal mass loss in a more realistic situation; Springel et al. (2008), for instance, show the density profiles of tidally truncated subhaloes resolved in the Aquarius simulations with $10^5 - 10^6$ particles or more. Broadly speaking they resemble our models, with a profile similar to field haloes (i.e. close to an NFW or Einasto profile) in the inner parts, and truncated abruptly in the outer parts. Unfortunately, in self-consistent simulations the exact profile and distribution function of a subhalo will depend on the group-finder used. Group-finders use various different criteria for defining the boundary of a subhalo, producing slightly different results (e.g. Muldrew et al. 2011; see Onions et al. 2012 for a general review). Establishing precisely which particles are or aren't associated with a subhalo, in a region dominated by the background potential of the main system, is essentially impossible. Thus, the idealized simulations presented here actually provide more reliable information about the behaviour of stripped systems close to the tidal boundary, and may even help to evaluate different group-finding schemes in realistic simulations.

The isotropic NFW models considered in this work do not necessarily provide the most accurate description of cosmological haloes, either. The highest-resolution simulations indicate that an Einasto profile is a better fit to the density profile (e.g. Navarro et al., 2010; Klypin et al., 2016), but real haloes are also anisotropic, triaxial, and have more complicated correlations between shape and anisotropy (e.g. Wojtak et al., 2013). There are also several proposed models for the 'true' DF of dark matter haloes, based on maximizing entropy under various constraints, or other arguments (e.g. Hjorth & Williams 2010; Pontzen & Governato 2013; Beraldo e Silva et al. 2014; see Halle et al. 2019 for a discussion). Our focus here is not on which of these theoretical models is correct, but on the generic effects of tidal mass loss on any DF. Our analysis is general and may be applied to these theoretical models, or to any other model with an explicit DF.

Many real systems of interest also have a separate baryonic component that is impor-

tant, if only as a tracer of dynamics and mass loss. Various authors have considered the density profiles and/or phase-space distributions of luminous stars within a surrounding, tidally limited dark matter potential, and their evolution through tidal interactions (e.g. Mashchenko & Sills, 2004, 2005a,b; Peñarrubia et al., 2008b; Sales et al., 2010; Kazantzidis et al., 2011; Amorisco & Evans, 2011). Our focus here is simply on understanding the phase-space evolution of the dark matter particles themselves. We leave further discussion of the evolution of self-consistent, two-component systems to future work.

Chapter 3

An Energy-Based Model for the Evolution of Tidally Stripped Systems; Universality and Applications

3.1 Introduction

The standard theory of structure formation predicts that dark matter haloes grow through "hierarchical" merging, in which small structures merge to form progressively larger ones. As smaller systems merge with larger ones, they evolve through dynamical friction, mass loss and tidal heating, and survive as self-bound structures within galaxy, group, and cluster haloes. Isolated dark matter haloes have a nearly universal density profile (UDP), which is commonly described in terms of the Navarro-Frenk-White (NFW) profile (Navarro et al., 1996, 1997):

$$\rho(r) = \frac{\rho_0 r_{\rm s}^3}{r(r+r_{\rm s})^2} \ , \tag{3.1}$$

where ρ_0 is a characteristic density and $r_{\rm s}$ is the scale radius, describing the point where the logarithmic slope is $\mathrm{d}\ln\rho/\mathrm{d}\ln\mathrm{r} = -2$.

Most of the understanding of dark matter haloes comes from cosmological simulations, though to understand the detailed physical processes involved in halo mergers, isolated simulations are often used. Tidal stripping in minor mergers, for instance, is frequently

studied using simulations of a satellite halo evolving within a static host halo (e.g. Hayashi et al., 2003; Kazantzidis et al., 2004; Boylan-Kolchin & Ma, 2007; Kampakoglou & Benson, 2007; Peñarrubia et al., 2008a,b, 2009; Choi et al., 2009; Peñarrubia et al., 2010; Drakos et al., 2017). These idealized simulations provide a way to test the physical processes which govern subhalo evolution.

The fate of the central density of these haloes is particularly important, since visible structures, such as galaxies, trace the central regions of haloes. Additionally, the inner density of dark matter haloes has implications to dark matter annihilation surveys, since the annihilation signal scales as density squared. For instance, there is some work on the inner slopes of the earliest haloes (e.g. Ishiyama, 2014; Angulo et al., 2017; Ogiya & Hahn, 2018; Sten Delos et al., 2019), that suggests that the first objects are cuspy, with an inner slope $r^{-1.3}$. This could enhance the dark matter annihilation significantly, but it is unclear whether these high density central regions survive merging and tidal stripping. Since the innermost parts of haloes are difficult to resolve in simulations due to gravitational softening, this is beyond the dynamic range of simulations. For this reason, it is important to have a theoretical understanding of how suhaloes evolve.

Classical approaches to modelling tidally stripped haloes generally remove mass outside of some tidal radius (e.g. Taylor & Babul, 2001; Peñarrubia et al., 2004; Just & Peñarrubia, 2005; Benson, 2005), though more detailed models of subhalo evolution also take into account individual particle energies and angular momenta (e.g. Kampakoglou & Benson, 2007). As first pointed out by Choi et al. (2009), tidal stripping may be best described by an outside-in process in energy space. Following this, in Chapter 2, we described a physical model that is based on an energy truncation of a halo's distribution function. When applying the model to isolated simulations of NFW subhaloes, we found it matches the stripped profile as well as the phase-space distribution quite well.

The aim of this chapter is to further examine the assumptions in our energy-truncation model. Additionally, since our model can be applied to any collisionless system, we apply it to other profile models to test whether it may be used as a universal model for tidally stripped systems, and calculate its implications for the dark matter annihilation boost factor. The structure of this chapter is as follows: in Section 3.2 we review the model presented in Chapter 2, and then in Section 3.3 compare it to other models in the literature. In Section 3.4 we apply the model to an NFW profile as in Chapter 2, and explore the limitations of the model, and the validity of model assumptions. In Section 3.5 we apply the model to a number of other profiles, to examine its universality. In Section 3.6 we explore the implications of this model to the annihilation boost factor. Finally, we summarize the findings of this chapter in Section 3.7.

3.2 Review of Energy-Truncation Model

In Chapter 2, we outlined a method for truncating a spherically symmetric profile in energy space, which we will review here. First, we provide a brief summary of the distribution function (DF) and its properties; a more detailed description can be found in Binney & Tremaine (1987).

3.2.1 Distribution Function

The DF, $f(r, v)$, describes the mass per phase-space volume $dr^3 dv^3$. For spherically symmetric, isotropic systems, the DF is only a function of the relative energy $\mathcal{E} = \Psi(r) - v^2/2$; i.e. $f(r, v) = f(\mathcal{E})$. The relative potential energy, $\Psi(r)$ is defined as $\Psi = -(\Phi + \Phi_0)$, where Φ_0 is usually defined at the outer boundary of the system, such that $f > 0$ when $\mathcal{E} > 0$, and $f = 0$ otherwise. The DF is related to the density profile, $\rho(r)$, as follows:

$$\rho(r) = 4\pi \int_0^{\Psi(r)} f(\mathcal{E}) \sqrt{2(\Psi(r) - \mathcal{E})} \mathrm{d}\mathcal{E} \quad . \tag{3.2}$$

This relationship can be inverted, and the DF expressed in terms of the density profile by using Eddington's inversion method (Eddington, 1916):

$$f(\mathcal{E}) = \frac{1}{\sqrt{8}\pi^2} \left[\int_0^{\mathcal{E}} \frac{1}{\sqrt{\mathcal{E} - \Psi}} \frac{\mathrm{d}^2\rho}{\mathrm{d}\Psi^2} \mathrm{d}\Psi + \frac{1}{\sqrt{\mathcal{E}}} \left(\frac{\mathrm{d}\rho}{\mathrm{d}\Psi} \right)_{\Psi=0} \right] \quad . \tag{3.3}$$

3.2.2 The Model

The model presented in Chapter 2 is created by lowering the original DF of the subhalo and then recovering the modified density profile, analogous to how the King Model is created by lowering the DF of an isothermal sphere (King, 1966). This method was originally proposed in Widrow (2000) as a method to truncate NFW profiles to use as initial conditions (ICs) in isolated simulations. In Chapter 2, we showed that it also worked well as a description for tidally stripped haloes.

First, given the DF of the original system $f_0(\mathcal{E})$, the new DF is expressed as:

$$f(\mathcal{E}) = \begin{cases} f_0(\mathcal{E} + \mathcal{E}_\mathrm{T}) - f_0(\mathcal{E}_\mathrm{T}) & \mathcal{E} \geq 0 \\ 0 & \mathcal{E} \leq 0 \end{cases} , \tag{3.4}$$

where $\mathcal{E}_{\rm T}$ is the truncation or tidal energy. Then, the relative potential of the truncated system can be found by solving Poisson's equation:

$$\begin{aligned} &\frac{\mathrm{d}^2\Psi}{\mathrm{d}r^2} + \frac{2}{r}\frac{\mathrm{d}\Psi}{\mathrm{d}r} = \\ &-16\pi^2 G \int_0^{\Psi(r)} (f_0(\mathcal{E}+\mathcal{E}_{\rm T}) - f_0(\mathcal{E}_{\rm T}))\sqrt{2(\Psi(r)-\mathcal{E})}\mathrm{d}\mathcal{E} \end{aligned} \tag{3.5}$$

$$\begin{aligned} \Psi(0) &= \Psi_0(0) - \mathcal{E}_{\rm T} \\ \frac{\mathrm{d}\Psi(0)}{\mathrm{d}r} &= 0 \ , \end{aligned}$$

Where Ψ_0 is the relative potential of the original, un-truncated system. Once Ψ has been calculated, the truncation radius, $r_{\rm t}$, is given by $\Psi(r_{\rm t}) = 0$, and the density profile can be found from Equation (3.2).

3.3 Model Comparisons

3.3.1 Simulations

In Chapter 2 we found that our model works well for haloes which lose mass slowly, and less well for subhaloes that are being rapidly stripped. We will use Simulations 3 and 4 from Chapter 2, which are representative of simulations which lose mass quickly and slowly, and refer to them as the "Fast Sim" and "Slow Sim", respectively. These simulations were performed using the N-body code GADGET-2 (Springel, 2005), which was modified to contain a fixed background potential corresponding to the host halo. The satellite halo was created using the publicly available code ICICLE (Drakos et al., 2017). Since the mass of NFW profiles diverges with increasing radius, particles were generated within a specified radius, $r_{\rm cut}$, and then unbound particles were iteratively removed. The resulting satellite is a truncated NFW profile with $N = 1286991$ particles, with a maximum radius of $r_{\rm cut} = 10\,r_{\rm s}$, where r_s is the scale radius of the satellite. The host halo had a mass $M_{\rm host}/m_{\rm sat} = 300$ and a concentration of $c_{\rm host} = 10$. The orbits in the Slow and Fast Sims have an apocenter of $r_{\rm a} = 300\,r_{\rm unit}$, and pericentres of $r_{\rm p} = 50\,r_{\rm unit}$ and $10\,r_{\rm unit}$, respectively, where the radial unit $r_{\rm unit} = r_{\rm s}$. We summarize these simulations in Table 3.1.

The bound satellite was defined as in Chapter 2. First, the centre of the satellite was found by calculating the centre of mass in increasingly smaller spheres, as originally described in Tormen et al. (1997). The sphere was decreased by $0.9\,r/r_{\rm s}$ at each iteration,

Table 3.1: Summary of orbital parameters. Columns give (1) the simulation name (2) the mass ratio between the host and satellite halo (3) concentration of the host halo (4) the apocentric distance (5) the pericentric distance (6) the tangential velocity at apocenter (7) the (radial) orbital period

Simulation	$M_{\rm host}/M_{\rm sat}$	$c_{\rm host}$	$r_{\rm a}/r_{\rm unit}$	$r_{\rm p}/r_{\rm unit}$	$v_a/v_{\rm unit}$	$t_{\rm orb}/t_{\rm unit}$
Slow Sim	300	10	100	50	1.42	185.4
Fast Sim	300	10	100	10	0.51	129.7

until there were fewer than 100 particles in the sphere. The velocity frame was calculated as the average particle velocity within $r_{\rm cut}$. Finally, the energy of each particle was then calculated in this frame (assuming a spherical potential), and unbound particles were iteratively removed until convergence. The resulting mass loss curves for these two simulations are shown in Fig. 3.1, with the apocenter indicated with a vertical dashed line (calculated as the apocenter of a point mass orbiting within the same potential). Both the Slow Sim and Fast Sim lose most of their mass at pericentric passages.

3.3.2 Model Comparison

Here we compare our model for the effect of mass loss on the density profile to other models in the literature; detailed descriptions of each of these models are given in Appendix B. First, Hayashi et al. (2003) proposed a simple empirical model for tidally stripped NFW profiles, that could be described by one parameter, the bound mass fraction. A slightly more complicated empirical model was proposed by Peñarrubia et al. (2010), which again only depends on the bound mass fraction. While the model proposed in Peñarrubia et al. (2010) is more complicated than that in Hayashi et al. (2003), it is more general, and can be used for any profile of the form:

$$\rho(r) = \frac{\rho_0}{(r/r_{\rm s})^{\gamma}[1+(r/r_{\rm s})^{\alpha}]^{(\beta-\gamma)/\alpha}} \quad . \tag{3.6}$$

Like the models proposed in Hayashi et al. (2003) and Peñarrubia et al. (2010), our model is also dependent on one parameter (the tidal energy, $\mathcal{E}_{\rm T}$, but which can be alternatively expressed in terms of the bound mass). However, our model has the advantages that it is physically motivated (the tidal energy, $\mathcal{E}_{\rm T}$, being interpreted as the maximum energy of any bound particle in the frame of the satellite), and that it can potentially be applied to any collisionless system. The universality of the model will be explored further in Section 3.5.

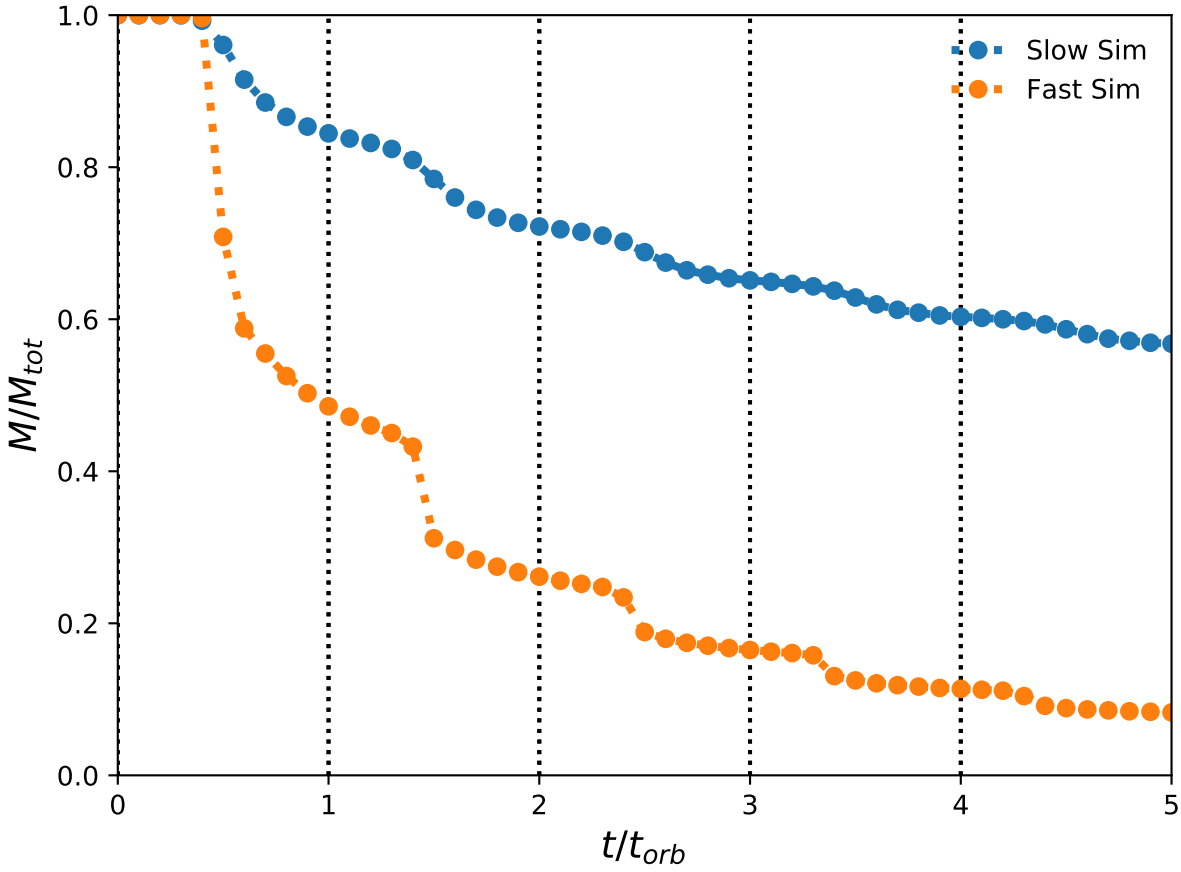

Figure 3.1: Bound mass fraction as a function of time. Vertical dotted lines indicate apocenteric passages.

To compare how well our model describes the density profile of the subhalo remnant compared to other models, we fit the bound subhalo remnant after one orbit, at apocenter. Apocenter was chosen since the subhalo should be roughly in equilibrium at this point; similar results can be found in subsequent orbits (see Chapter 2). The tidal energy for our model was calculated as in Chapter 2, by requiring that the total mass of the bound halo was equal to that of the model. The other two models were calculated as described in Appendix B. In all three cases, the fits were dependent on a single parameter, the bound mass.

Fig. 3.2 shows how the tidally stripped halo simulations compare to our model, as well as to the models presented in Hayashi et al. (2003) and Peñarrubia et al. (2010). Residuals of the model fits are shown for the density, mass and circular velocity profiles, calculated as $(y_{\rm model} - y_{\rm simulation})/y_{\rm simulation}$. As in Chapter 2, our model is better at describing the remnant from the Slow Sim compared to the Fast Sim. In the case of the Slow Sim, our model performs very well, and agrees with the profiles better than the other two models. For the Fast Sim, our model over-predicts the mass and density in the centre of the halo, though the magnitude of the residuals are comparable with the other two models. The model from Hayashi et al. (2003) tends to under-predict the central mass and density of the central halo; this could be because in their simulations they used the local Maxwellian approximation to generate their ICs, which can lead to artificial relaxation in the centre of the subhalo (Kazantzidis et al., 2004). Overall, it appears that our model is at least comparable to, if not more accurate than the models presented in Hayashi et al. (2003) and Peñarrubia et al. (2010).

We note that since all three of these methods are dependent on the bound mass, they are sensitive to the method used for defining bound particles. Also, bound mass calculations include mass which is only temporarily bound, but is leaving the system. Since most of this temporarily-bound mass is at larger radii, a more accurate fitting criteria may be to fit the radius enclosing some fraction of the mass, or to fit the peak circular velocity. Clearly, the details of mass loss are important, and will be the focus of future work.

3.4 Model Assumptions

Overall, our model describes the density, mass and velocity profiles of the subhalo remnants quite well, as shown in the previous section. This suggests that subhalo evolution is primarily an energy-based process, as proposed by Choi et al. (2009). However, we wish to examine the physical reasons as to why this model works better in the cases where subhaloes

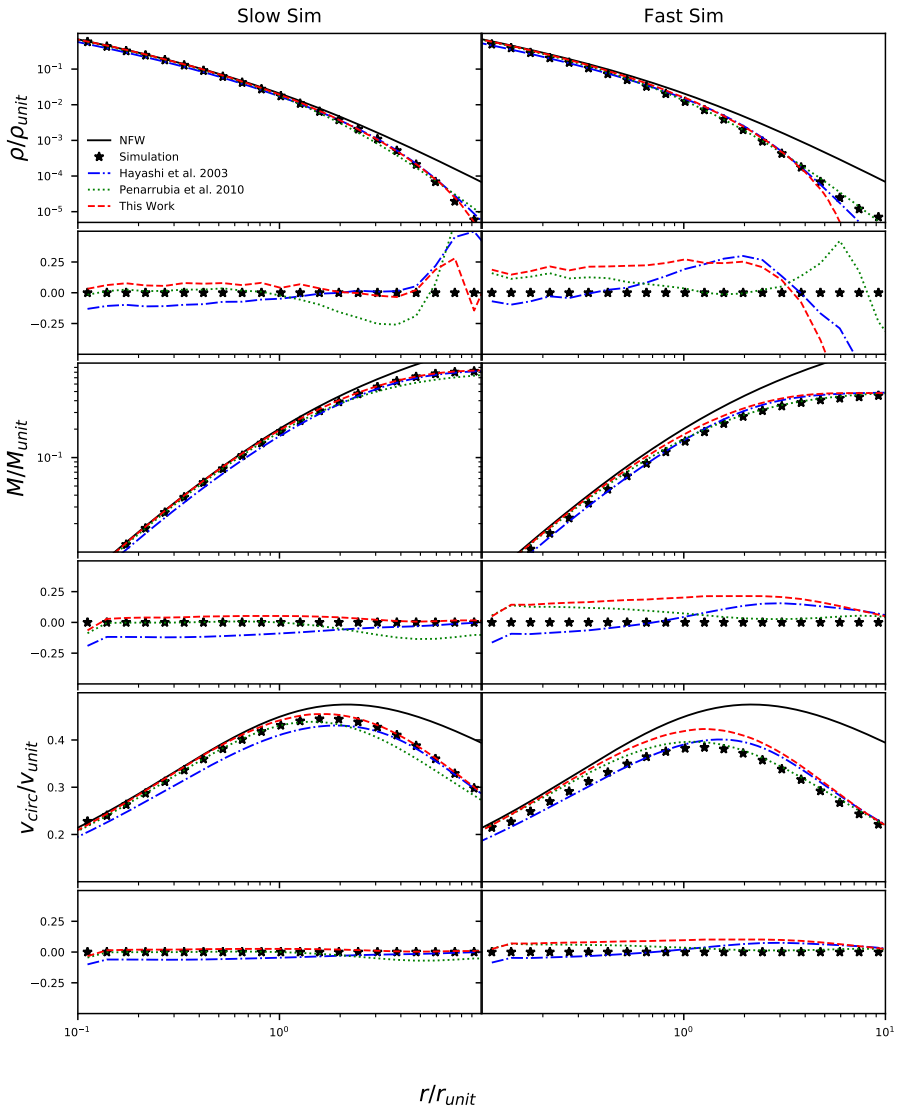

Figure 3.2: Comparison of density, mass and velocity profiles of the bound satellite remnant after one orbit to different models for the Slow Sim (left) and Fast Sim (right). Simulation results are shown with points, and the models are shown with lines. The thick dashed curve shows the original, untruncated NFW profile. The residuals in the fits are calculated as $(y_{\rm model}/y_{\rm simulation} - 1)$, where y is the density, mass or circular velocity profile. Our model from Chapter 2 is described in Section 3.2, and the other models in Appendix B.

lose mass gradually. To do this, we first identify four main simplifying assumptions in our model:

1. The remnant is in equilibrium.
2. The remnant is spherical.
3. The remnant is isotropic.
4. The truncation is purely energy based.

This section will focus on the "Fast" and "Slow" simulations described in 3.3.1. Our goal is to understand why the model fits the latter better than the former, by considering each of the model assumptions in turn.

3.4.1 Equilibrium

One assumption of our model is that the subhalo is in equilibrium at apocenter. To test this, we identify the bound subhalo remnant at $t = 2\,t_{\rm orb}$, and evolve it in isolation using GADGET-2 for an additional $t = 2\,t_{\rm orb}$. We compare the initial subhalo to the final subhalo in Fig. 3.3. For both the Fast and Slow simulations there is very little evolution, except at large radii. Since differences between the Fast Sim and our model can be seen at all radii, this suggests that the equilibrium assumption is not the reason for discrepancies between the simulations and model.

3.4.2 Spherical Symmetry

Another assumption of our model is that the haloes are spherically symmetric. The shape of the subhaloes were calculated as in (Dubinski & Carlberg, 1991; Drakos et al., 2019); beginning with axis ratios $s = b/a = 1$ and $q = c/a = 1$ (where $a > b > c$ are the principal axes sizes), the dimensionless inertia tensor was calculated as $I_{ij} = \sum x_i x_j / d^2$, where $d = x_i^2 + (x_j/s)^2 + (x_k/q)^2$ is the ellipsoidal coordinate. The coordinates of each particle were rotated using the eigenvectors of and the principal axis ratios s and q were recalculated. This process was repeated until convergence, which was defined as when $s = b/a$ and $q = c/a$ both had a percentage change of less than 10^{-3}.

Fig. 3.4 shows how the shape of the subhaloes evolve in time. In both the Fast and Slow Sims the remnants are roughly spherical at apocenter. At pericenter, the shapes become

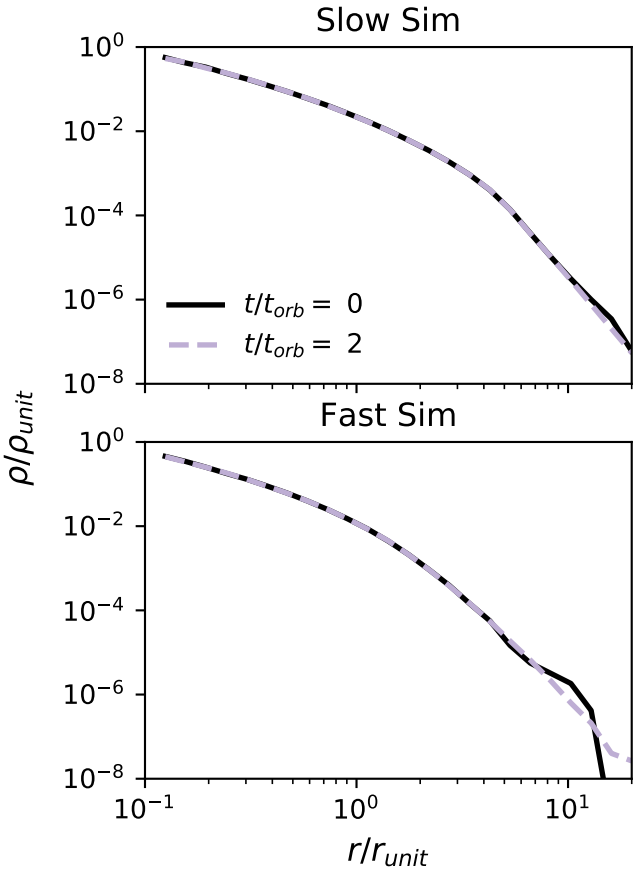

Figure 3.3: Evolution of subhalo density profile when removed from the fixed background potential. The initial haloes (solid black lines) are from the subhalo after two orbits in a fixed potential. The final profiles (dashed purple lines) are after the haloes are allowed to evolve for an additional $t = 2\,t_{\rm orb}$ in isolation.

more prolate ($a > b \approx c$), particularly for the Fast Sim. Since pericenter is the point at where the majority of mass is loss, the difference between the Fast and Slow Sim might be the subhalo shape at pericenter. For instance, Moore et al. (2004) showed prolate haloes can lose mass at a rate several times higher than an isotropic spherical halo with the same density profile, and conclude this is because particles on radial orbits are more vulnerable to being stripped.

3.4.3 Isotropy

Our model also assumes that haloes are isotropic, and thus the distribution function is only a function of the energy, $\mathcal{E}$. Fig. 3.5 shows the anisotropy parameter, $\beta = 1-(\sigma_\theta^2+\sigma_\phi^2)/2\sigma_r^2$ for the Fast and Slow Sims. The ICs ($t/t_{\rm orb} = 0$) are isotropic by construction. As time progresses, the remnants become more anisotropic, particularly at large radii. While the Fast Sim does show more anisotropy than the Slow Sim, this is time dependent; for instance, Slow Sim at $t/t_{\rm orb} = 5$ is very similar to the Fast Sim at $t/t_{\rm orb} = 1$. Since the residuals in the model fits do not depend on the orbit number (see Chapter 2), it seems unlikely that this is the reason for the difference between the two situations.

3.4.4 Truncation

Finally, our model assumes that particles are removes strictly based on their energy, but, as suggested in Choi et al. (2009), there may also be a dependence on the angular momentum of the particle. This is because particles that are on more radial orbits are more vulnerable to being stripped when they are at apocenter.

As in Choi et al. (2009), we calculate the initial relative energy, $\mathcal{E}$ and circularity, η, for each particle as $\mathcal{E} = \Psi(r) - v^2/2$ and $\eta = L/L_{\rm max}$. To calculate $L_{\rm max}$, we first determined the radius of a circular orbit with the same energy, $r_\mathcal{E}$ from $\mathcal{E} = \Psi(r_\mathcal{E}) - v_c(r_\mathcal{E})^2/2$, where v_c is the circular velocity, and then $L_{\rm max} = \sqrt{GM(r_\mathcal{E})r_\mathcal{E}}$. Fig. 3.6 shows the fraction of particles remaining in η–$\mathcal{E}$ space, according to their original energy and angular momentum.

From Fig. 3.6, it seems that there is a very slight angular momenta dependence, as in Choi et al. (2009). Additionally, there may be a less abrupt truncation in the Fast Sim case; to examine this further, we plot the histogram of original energies and of angular momentums removed at each time step in Fig. 3.7. The slope of the histograms become less steep at each successive orbit, but the fractional range of energies removed is roughly constant (approximately 10 per cent for the Slow Sim, and 30 per cent for the Fast Sim).

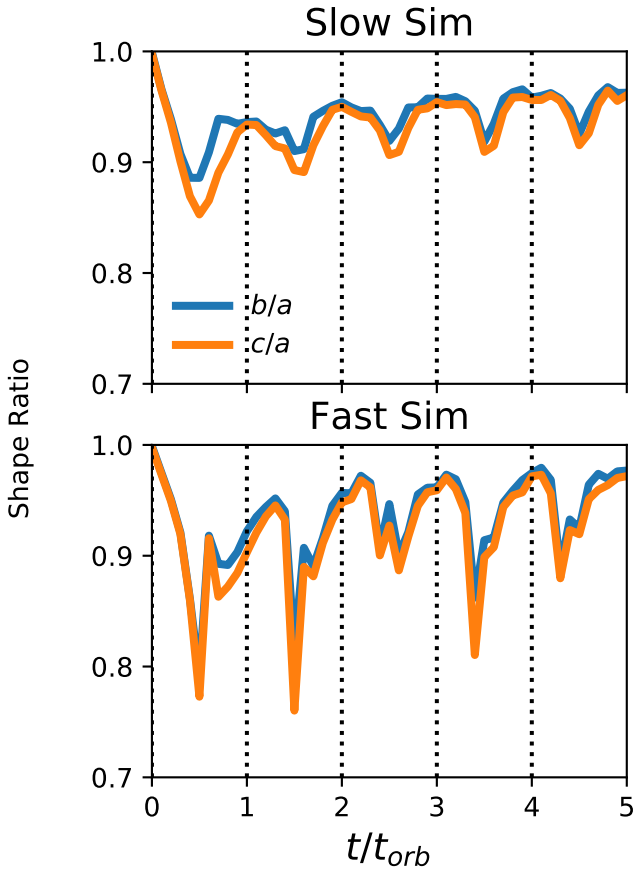

Figure 3.4: Subhalo shape ratios as a function of time. Dotted lines indicate where the subhaloes are at apocenter.

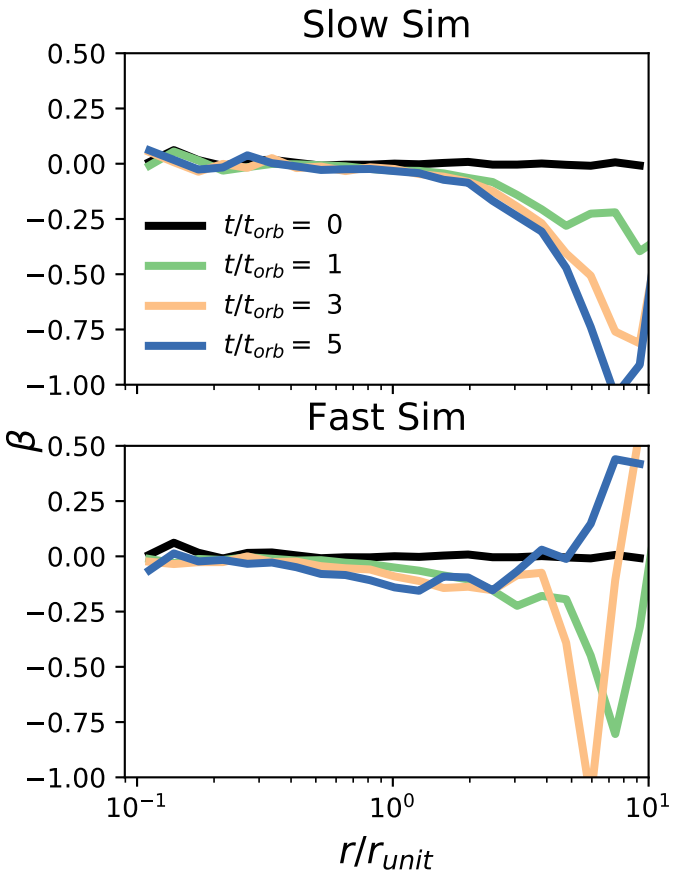

Figure 3.5: Anistropy, $\beta = 1 - (\sigma_\theta^2 + \sigma_\phi^2)/2\sigma_r^2$ of Slow (top) and Fast (bottom) Sims.

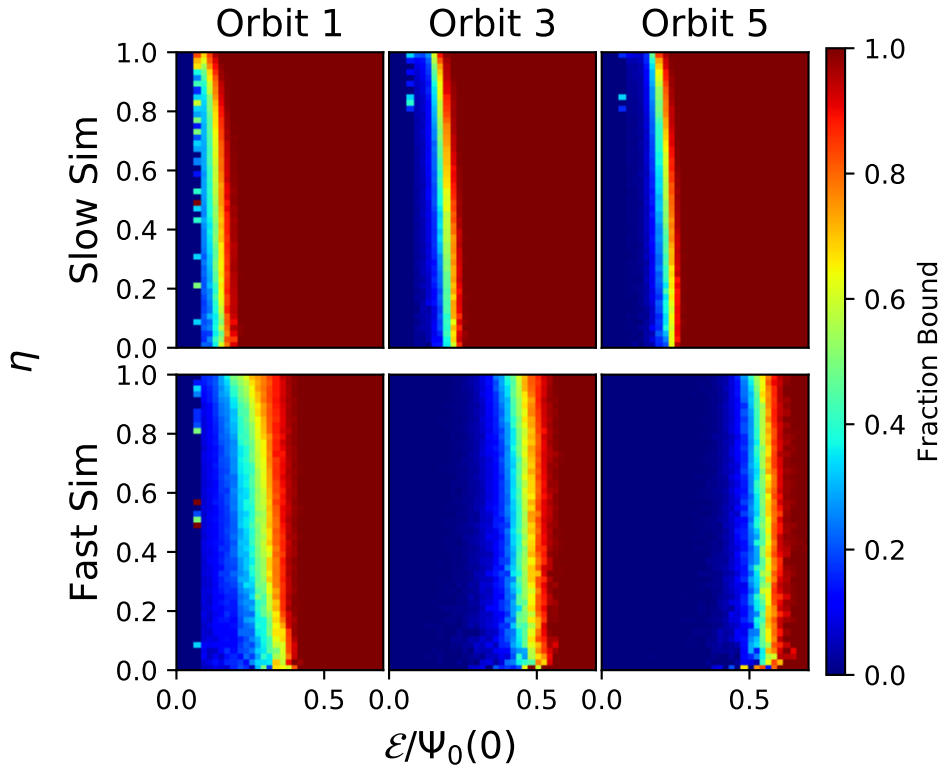

Figure 3.6: Fraction of remaining particles as a function of the particles' initial circularity, η, and relative energy, $\mathcal{E}$, for the Slow (top) and Fast (bottom) Sims. Each column corresponds to the number of orbits the subhalo has undergone, measured at apocenter.

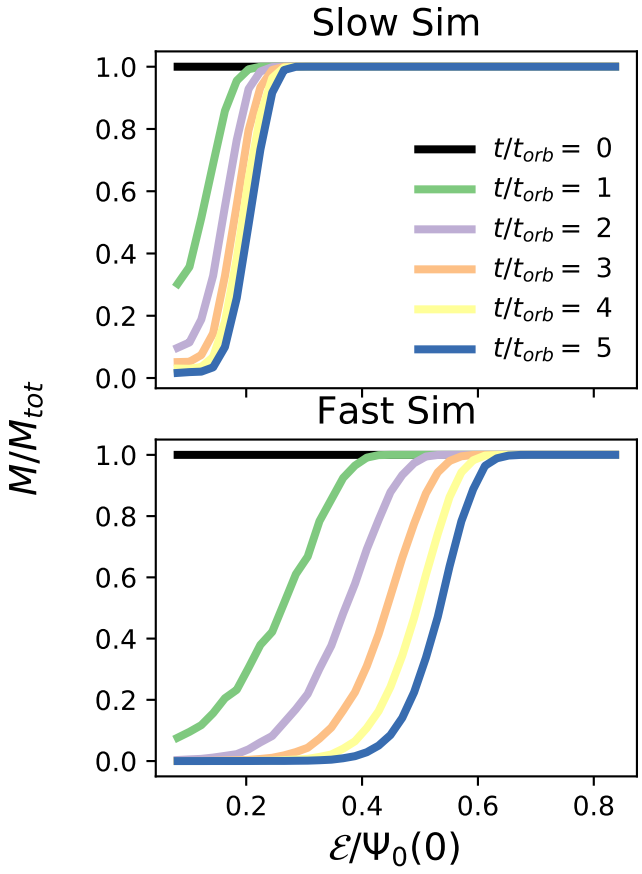

Figure 3.7: The fraction of particles remaining bound as a function of relative binding energy, $\mathcal{E}$, measured at each apocentric passage.

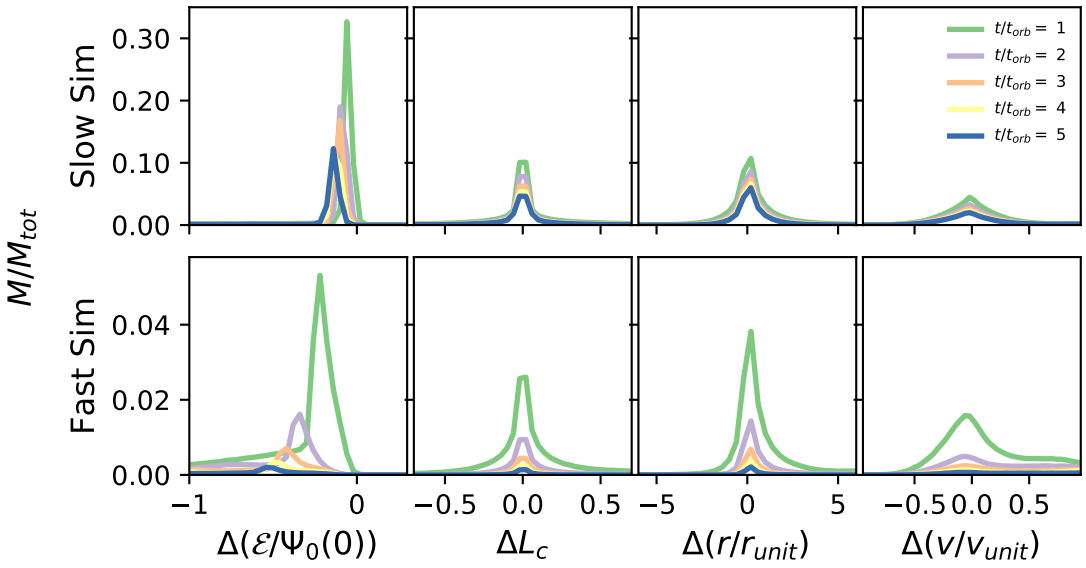

Figure 3.8: Distribution in the change in energy, angular momentum, radius and velocity of individual particles for the Slow Sim (top) and Fast Sim (bottom).

It should be noted that so far we have labeled particles by their *initial* energy and angular momentum, which assumes there is no energy or momentum exchange between particles. Therefore, in Fig. 3.8 we show the change in individual particle energies, angular momenta, radii and velocities. Angular momenta and radii changes are roughly symmetric about zero. The binding energy, $\mathcal{E}$ decreases with each orbit; this is because the mass, and thus the total potential energy, in system is decreasing. For velocity can see two populations in the fast simulation (i.e. there is an extra bump around $\Delta v = 0.6$) these are likely particles that are temporarily still bound but are leaving system. Overall, the Fast Sim has wider distributions, indicating that there is more mixing in this case.

Fig. 3.9 shows the fraction of particles removed in η–$\mathcal{E}$ space, but instead of only considering the initial energy/circularity of each particle, we recalculate these values at each orbit. For both the Slow (top) and Fast (bottom) Sims, particles are removed mainly based on energy, as shown previously. Each successive row then shows where these particles were in η–$\mathcal{E}$ space at an orbital time earlier. Interestingly, there is still a fairly discrete slice in each case; the removed particles simply seem to shift in $\mathcal{E}$ (this is due to the system losing mass and thus potential energy), though there is a slight amount of mixing, particularly for the Fast Sim case. Overall, Fig. 3.9 shows that tidal stripping can mainly be described

by removing particles based on their initial energies.

3.4.5 Conclusions

While comparing the Fast and Slow Sim, we found that the Fast Sim remnants are more prolate at pericenter, and more anisotropic than the Slow Sim remnants. Both remnants do seem to be roughly in equilibrium at apocenter, except for a small number of particles at large radii. The largest difference between the two simulations is that the energy truncation is less sharp (i.e. the histogram becomes less steep, as shown in Fig. 3.7). Since the majority of particles are removed during their pericentric passage (particularly for the Fast Sims), mixing during an orbit will result in a less abrupt energy truncation since the instantaneous particle energies may be altered. Therefore, deviations due to mixing are likely the main cause of discrepancies between the energy-truncation model and simulations of rapid mass-loss systems.

3.5 Universality

Thus far we have only applied our model to NFW systems. The purpose of this section is to see how successful the energy truncation model is in describing the tidal evolution of other collisionless systems. We will look at three additional profile models: Hernquist, Einasto, and King.

3.5.1 The Profiles

Hernquist

The Hernquist profile (Hernquist, 1990) was originally used to describe spherical galaxies, however it is also a good approximation of cosmological dark matter halo profiles. The density profile is given by:

$$\rho(r) = \frac{M_{\rm tot}}{2\pi} \frac{a}{r(r+a)^3} \quad , \tag{3.7}$$

where $M_{\rm tot}$ is the total mass and a is a characteristic radius (the radius at which the enclosed mass is $M_{\rm tot}/4$) .

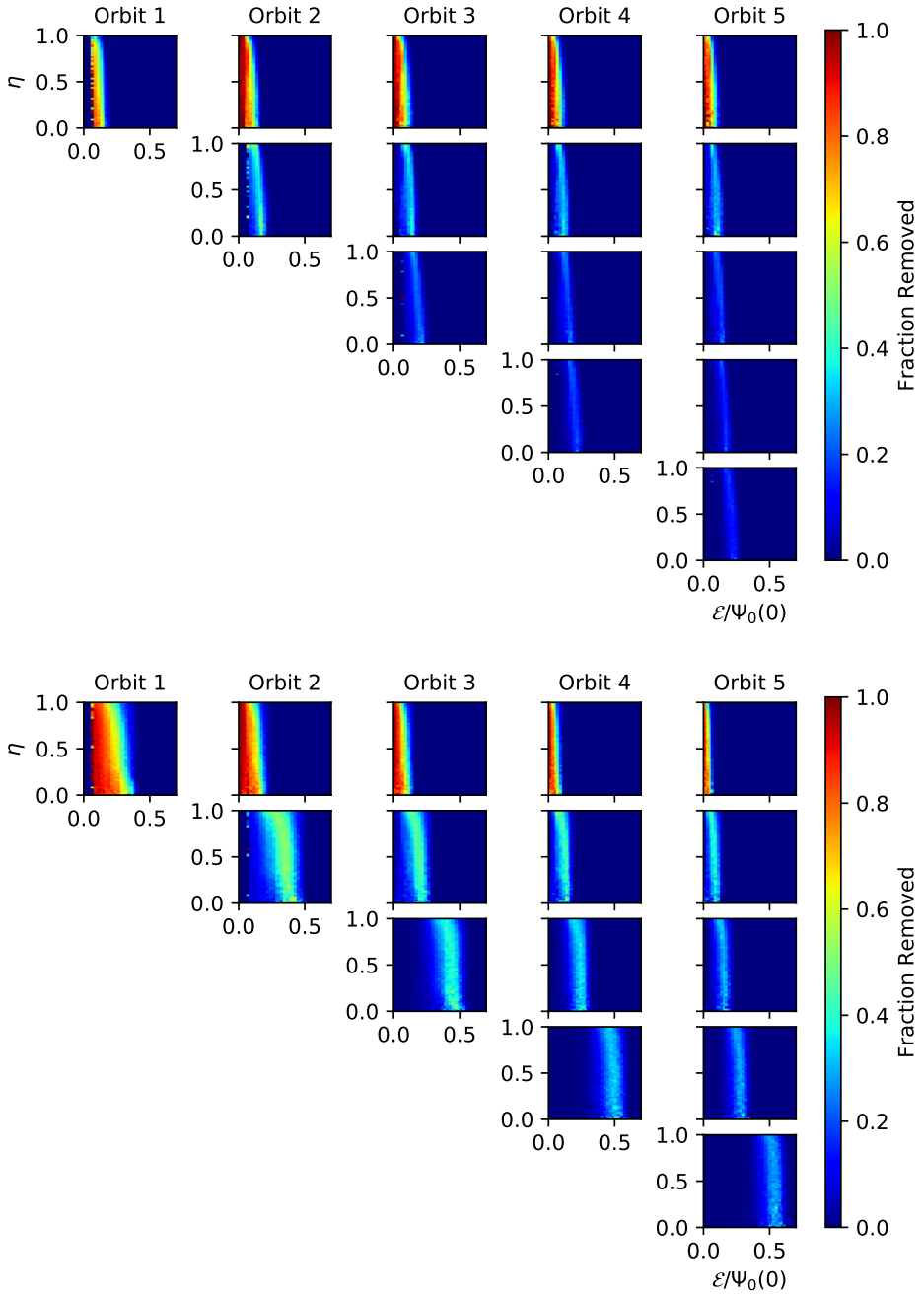

Figure 3.9: The fraction of particles removed in η–$\mathcal{E}$ space for the Slow Sim (top) and Fast Sim (bottom). In each $n = 1$–5 row, the particles are labeled by their angular momentum and energy n orbits earlier.

The advantage to this model is that it has simple analytic expressions for many of its properties, including its DF:

$$f(\mathcal{E}) = \frac{M}{8\sqrt{2}\pi^3 a^3 v_g^3} \frac{1}{(1-q^2)^{5/2}} \times \left(3\sin^{-1} q + q(1-q^2)^{1/2}(1-2q^2)(8q^4-8q^2-3)\right) \tag{3.8a}$$

$$q = \sqrt{\frac{a\mathcal{E}}{GM}} \tag{3.8b}$$

$$v_g = \left(\frac{GM}{a}\right)^{1/2} \quad . \tag{3.8c}$$

Einasto

The Einasto profile was first used to describe star counts in the Milky Way (Einasto, 1965). However, it has since been argued that it is a better description of cosmological profiles than the well-known NFW profile (e.g. Navarro et al., 2004; Gao et al., 2008; Klypin et al., 2016). The Einasto profile has the following form:

$$\rho(r) = \rho_{-2} \exp\left(-\frac{2}{\alpha}\left[\left(\frac{r}{r_{-2}}\right)^{\alpha} - 1\right]\right) \quad , \tag{3.9}$$

where α is the Einasto shape parameter and r_{-2} is the radius where the logarithmic slope is -2. Compared to the NFW profile, the Einasto profile has an extra parameter, α, which controls the inner slope of the density profile, and reflects the mass accretion history of the halo.

King

The King model resembles an isothermal sphere at small radii, and has a finite mass within a well-defined tidal radius. This model is typically used to describe globular clusters or elliptical galaxies (King, 1966). The King model is derived by lowering the DF of an isothermal sphere:

$$f(\mathcal{E}) = \rho_1 (2\pi\sigma^2)^{-3/2} (e^{\mathcal{E}/\sigma^2} - 1) \quad , \tag{3.10}$$

where σ is the velocity dispersion, ρ_1 is a characteristic density.

The density profile of the King model can then be calculated from the DF using Equation (3.2), which gives:

$$\rho(\Psi) = \rho_1 \left[e^{\Psi/\sigma^2} \mathrm{erf}\left(\frac{\sqrt{\Psi}}{\sigma}\right) - \sqrt{\frac{4\Psi}{\pi\sigma^2}}\left(1 + \frac{2\Psi}{3\sigma^2}\right)\right] \quad . \tag{3.11}$$

To relate the relative potential energy, to the radius of the profile, $\Psi(r)$ can be solved numerically using Poisson's Equation (Equation (3.5)). There are many possible parameterizations of the King model, but it can be uniquely defined by the total mass, tidal radius, r_t, and a dimensionless central potential, $P_0 = \Psi(0)/\sigma^2$.

King models can also be characterized by a concentration parameter, c_K, which depends on the King radius r_0. These quantities are defined as:

$$\begin{aligned} c_K &= \log_{10}\left(\frac{r_\mathrm{t}}{r_0}\right) \\ r_0 &= \sqrt{\frac{9\sigma^2}{4\pi G \rho_0}} \quad . \end{aligned} \tag{3.12}$$

where ρ_0 is the central density of the halo.

3.5.2 Initial Halo Models

The ICs were created using ICICLE. As before, we define the mass unit to be the mass of the satellite, $m_\mathrm{unit} = M_\mathrm{sat}$. We define the distance unit to be $r_\mathrm{unit} = a$ for the Hernquist model, r_{-2} for the Einasto models, and $0.1\,r_\mathrm{t}$ for the King models. Then the density, time and energy units are $\rho_\mathrm{unit} = m_\mathrm{unit} r_\mathrm{unit}^{-3}$, $t_\mathrm{unit} = \sqrt{r_\mathrm{unit}^3/G m_\mathrm{unit}}$ and $E_\mathrm{unit} = GM_\mathrm{sat}/r_\mathrm{unit}$, respectively. For the Einasto models, there is one free parameter, α; we chose values of $\alpha = 0.15$ and 0.3, as these are representative of the range found in simulations (Gao et al., 2008). The King models also have one free parameter (this could be chosen as r_0, P_0 or c). We used $P_0 = 3$ and $P_0 = 12$, which correspond to concentrations of $c_K = 0.7$ and $c_K = 2.7$. These concentrations are typical of globular clusters and elliptical galaxies, respectively (Binney & Tremaine, 1987). Additionally, we calculated the softening length for each profile as $\epsilon = 0.5 r_h N^{-1/3}$, as in van Kampen (2000). A summary of the IC properties are given in Table 3.2. To check the stability of the ICs, they were evolved for in isolation using GADGET-2, as shown in Fig. 3.10; all four profiles are stable outside $r_\mathrm{unit} = 0.1$ at $t = 1000\,t_\mathrm{unit}$.

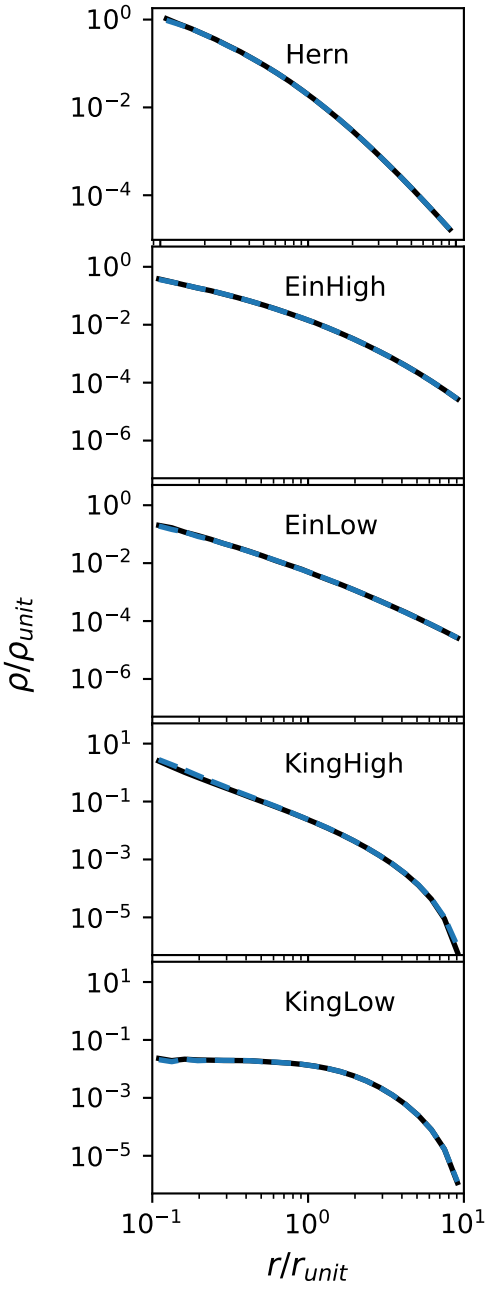

Figure 3.10: Stability of ICs. Dashed lines are measured at $t = 0\,t_{\rm unit}$, and solid lines at $t = 1000\,t_{\rm unit}$.

Table 3.2: Summary of the parameters used for the ICs; all satellites have a mass of $M_{\rm sat} = 1$. The columns list (1) the name of the ICs, (2) the number of particles N, (3) the radial unit, (4) specified profile parameters, (5) derived profile parameters, and (6) the softening length.

Profile Name	N	$r_{\rm unit}$	IC Parameters	Derived Parameters	$\epsilon/r_{\rm unit}$
NFWT	$\approx 1.3 \times 10^6$	$r_{\rm s}$	$r_{\rm cut} = 10\, r_{\rm unit}$	$\rho_0 = 0.08\, \rho_{\rm unit}$	0.01
Hernquist	10^6	a	—	—	0.01
EinHigh	10^6	r_{-2}	$\alpha_E = 0.3$	$\rho_{-2} = 0.01\, \rho_{\rm unit}$	0.02
EinLow	10^6	r_{-2}	$\alpha_E = 0.15$	$\rho_{-2} = 0.005\, \rho_{\rm unit}$	0.07
KingHigh	10^6	$r_{\rm t}/10$	$P_0 = 3$	$\rho_1 = 0.003\, \rho_{\rm unit}$, $r_0 = 0.02\, r_{\rm unit}$, $c_K = 0.7$	0.01
KingLow	10^6	$r_{\rm t}/10$	$P_0 = 12$	$\rho_1 = 0.001\, \rho_{\rm unit}$, $r_0 = 2.13\, r_{\rm unit}$, $c_K = 2.7$	0.01

3.5.3 Truncated Profiles

The Hernquist, Einasto and King models were truncated as described in Section 3.2.2. We note that applying our model to a King model simply results in another King model, with its parameters mapped as follows:

$$\begin{aligned} P_{0,\rm T} &= P_0 - \mathcal{E}_{\rm T}/\sigma^2 \\ \rho_{1,\rm T} &= \rho_1 \exp(\mathcal{E}_{\rm T}/\sigma^2) \\ r_{0,\rm T} &= r_0 \sqrt{\frac{\rho(P_0)}{\rho_T(P_{0,\rm T})}} \quad . \end{aligned} \tag{3.13}$$

We show the truncated profiles in Fig. 3.11, coloured by the tidal energy $\mathcal{E}_{\rm T}/\Psi(0)$. For most of the halo models, the density profiles show a decrease in in density at all radii, though most of this decrease is at large radii. An exception is the KingLow models; interestingly the tidal radius, $r_{\rm t}$, *increases* for large values of $\mathcal{E}_{\rm T}/\Psi(0)$. Additionally, when the density profile is very flat (as in the centre of the King models), the central density decreases a lot, while for the cuspier profiles, the density is more conserved. This is consistent with the results from (Peñarrubia et al., 2010). We also find that the scale radius of the Hernquist and Einasto profiles (given by the peak of ρr^2) decreases as the halo becomes tidally stripped; this may relate to an increase in concentration, though the virial radius is also decreasing. Further, the peak of the circular velocity curve decreases with $\mathcal{E}/\Psi(0)$ for all profiles except KingLow.

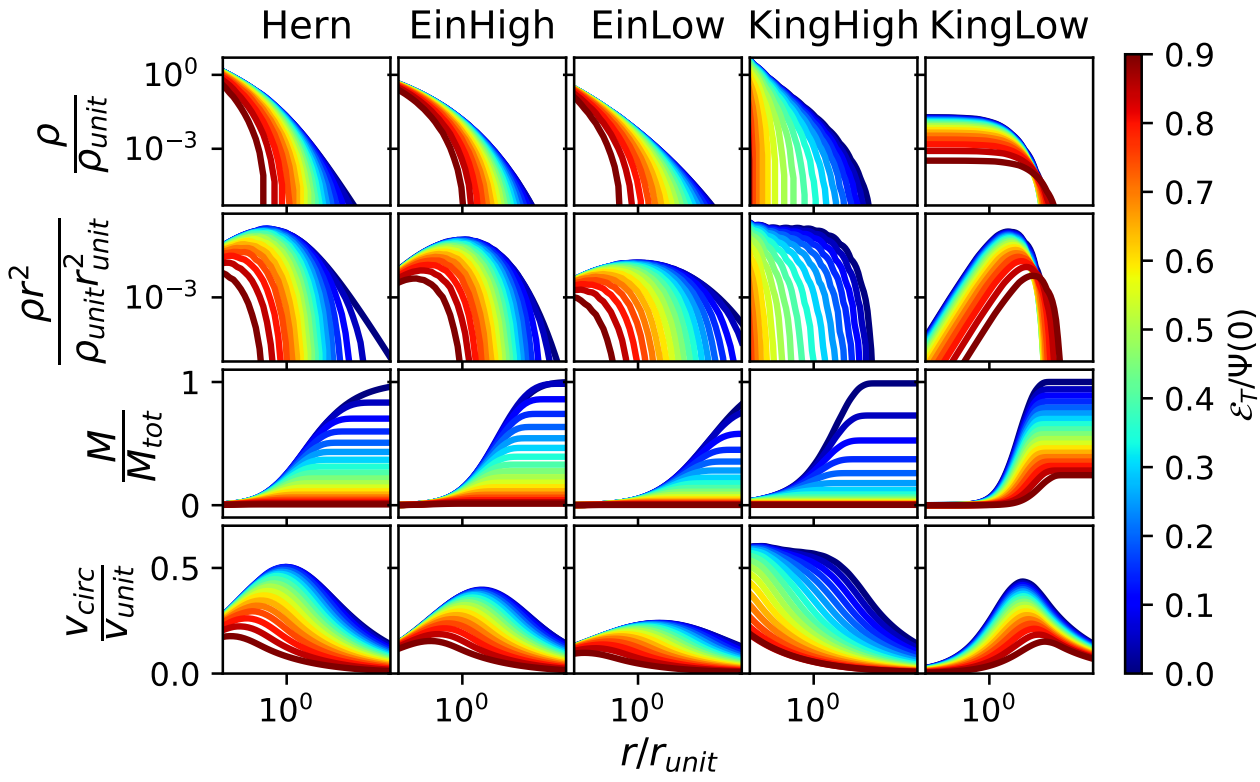

Figure 3.11: Energy truncation model described in Section 3.2.2 applied to different initial density profiles. EinLow and EinHigh have α values of $\alpha = 0.15$ and 0.3, respectively, while KingHigh and KingLow profiles have central potentials of $P_0 = 12$ and 3, respectively. The relative energy, $\mathcal{E}$ is normalized by the relative potential of the untruncated profile at $r = 0$.

3.5.4 Simulation Results

To test whether this model captures the behaviour found in simulations, we compare it to isolated simulations of subhalo evolution. We use the same host potential and subhalo orbits as in for the Fast and Slow Sims, as described in Section 3.3.1, and summarized in Table 3.1. The softening lengths were assigned according to the subhalo model, as given in Table 3.2. Additionally subhalo centres and bound particles were identified as described in Section 3.3.1. The model was fit using the fitting criteria that the bound mass of the simulated halo was equal to the total mass in the truncated model.

The evolution of bound mass, and tidal radii are shown in Fig. 3.12. We also include the NFWT simulations from Section 3.3.1; since these ICs were truncated, we fit them to the model as well. We find that the tidal energy, $\mathcal{E}_{\rm T}$, is different for all the profiles, even though they are on the same orbit. This is likely because the profiles have different radial extents, and thus probing different regions of the tidal field.

We show how the density, mass and circular velocity profiles of the Slow Sim results compare to the energy-truncated model in Fig. 3.13, at $t = 1\,t_{\rm orb}$ and $5\,t_{\rm orb}$. The model and simulation results match very well, though there are some discrepancies at large radii; this could be due to material that is not in equilibrium. Peñarrubia et al. (2009) found similar trends in simulations of subhalo evolution at large radii, and concluded that though this material is still bound, it is mostly lost on the next orbit. There is also a slight disagreement in the circular velocity curves of the KingHigh profiles at small radii. This could be because the inner part of this profile is sensitive to the best-fit $\mathcal{E}_{\rm T}$, or because of numerical issues in integrating the mass profile at small radii.

Overall, other than slight deviations at large radii, we find that our model matches all profiles very well, supporting our assertion that the energy-truncation is universal. Interestingly, the truncation energy, $\mathcal{E}_{\rm T}$ depends not only on the satellite orbit, but also on the satellite model. Future work will focus on predicting how $\mathcal{E}_{\rm T}$ evolves with orbit; this would also give a theoretical prediction of mass loss.

3.6 Applications to the Boost Factor

One potential technique for determining the identity of dark matter particles is through dark matter annhilation. To place constraints on particle masses and interaction cross-sections, it is important to have accurate predictions of the distribution of dark matter within subhaloes, since dark matter annihilation signals depend not only on the host halo, but also on substructure within the halo.

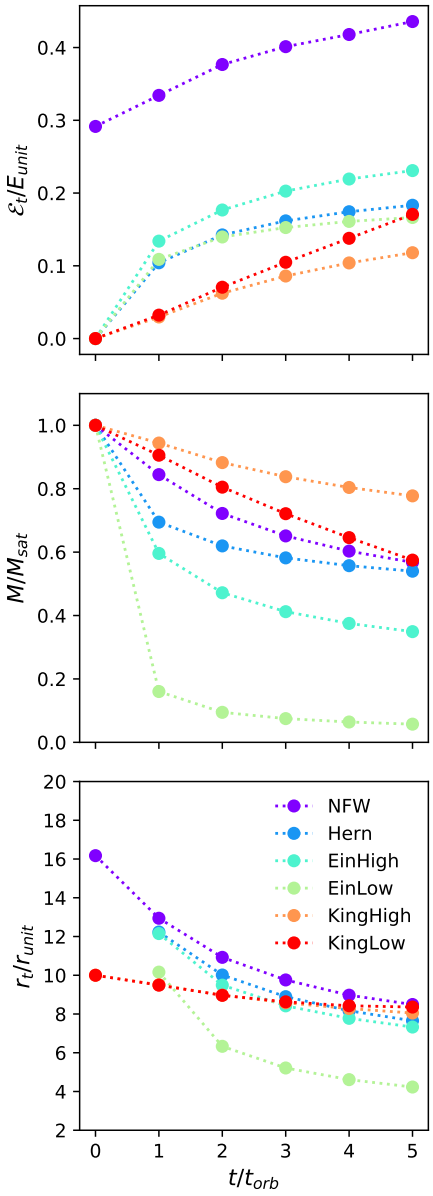

Figure 3.12: The tidal energy (top), mass fraction (middle) and tidal radius (bottom) as a function of time for the best fit models. The tidal energy and tidal radius are defined in Section 3.2.

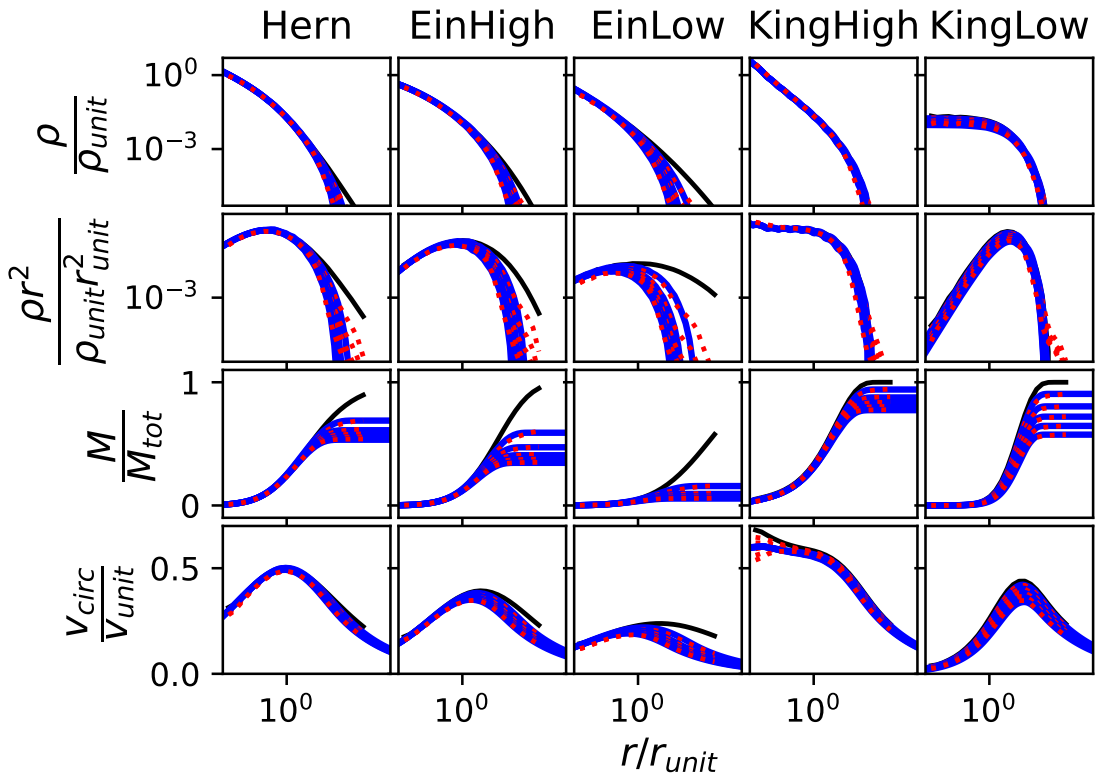

Figure 3.13: Comparison of simulation results (red dotted lines) and truncation model (solid blue lines). The profiles are shown at $t = 1\,t_{\rm orb}$ and $t = 5\,t_{\rm orb}$. The initial models are shown with the solid black line.

Assuming the dark matter particles are Majorana WIMPs (weakly interacting massive particles), the rate at which they will annihilate is given by:

$$R = \frac{\langle \sigma v \rangle}{2m^2} \int_V \rho^2 \mathrm{d}V \ , \tag{3.14}$$

where $\langle \sigma v \rangle$ is the velocity-averaged annihilation cross section, m is mass of the dark matter particle, ρ is the density and V is a volume.

This rate can be separated into two factors: one which depends on the particles' fundamental properties, and one on the spatial distribution of particles. The particle distribution is often described using a dimensionless quantity known as the boost factor,

$$B = \frac{1}{\bar{\rho}^2 V} \int \rho^2 \mathrm{d}V \ , \tag{3.15}$$

which characterizes the inhomogeneity of the particle distribution.

One common method to predict the expected observed boost factor is by considering the boost from individual subhaloes, and then drawing from distributions of radius, infall mass, etc. to calculate the total boost factor (e.g. Bartels & Ando, 2015; Han et al., 2016; Okoli et al., 2018; Hütten et al., 2019). Since this method depends on the model used for individual subhalo boost factors, we will examine how predictions from our model for tidally stripped haloes varies from simply truncating the original profile abruptly.

Using the energy-truncation model, we calculated how the boost factor within the tidal radius evolves for each profile; the top panel of Fig. 3.14 shows how the subhalo boost factor, B evolves for each subhalo. Note that the Einasto and Hernquist profiles are initially infinitely extended, so the boost factor is infinite for these at time zero. The boost factor decreases with time for all the simulations, though remains fairly constant.

The boost factor, B, evolves due to both a change in the tidal radius (since the integration volume changes), as well as from changes in the density profile. Therefore, we also show the ratio B/B_0, where B_0 is the initial un-truncated profile within the same tidal radius (bottom panel of Fig. 3.14). Taylor & Silk (2003) showed that using fitting the subhalo remnants with Equation (B.1) gives $B = 1.3\, B_0$, which we show as a solid black line. We find that using our model typically results in much higher values of B/B_0—overall, B is very sensitive to the density profile; accounting for mass loss within the tidal radius can make a factor of 10 difference between an abrupt truncation.

Compared to the Hayashi et al. (2003) value of $B/B_0 = 1.3$ for NFW profiles, our energy-truncation model predicts $B/B_0 \approx 3$. A possible explanation for this is that the

model from Hayashi et al. (2003) is fitting the artificial drop in central density due to numerical effects from the method used to generate their ICs (Kazantzidis et al., 2004), resulting in a decrease in central density. In contrast, our model predicts very little mass loss at small radii.

Overall, this demonstrates how sensitive boost factor calculations are to the assumed subhalo mass profile. We find that there can be up to an order of magnitude increase in boost factor predictions from our model compared to truncating the profile abruptly at a fixed radii. Since the boost factor is dominated by the inner parts of the profiles, which are not resolved in simulations, it is important to have physically motivated models such as the one presented in this chapter.

3.7 Conclusions

Recently, in Chapter 2, we proposed an energy-truncation model to describe the evolution of tidally stripped haloes, and showed it matched results from isolated simulations of NFW subhalo evolution. In this chapter, we explored the universality and limitations of this model. Overall, it has similar or better accuracy at predicting halo profile evolution compared to empirical models (e.g. Hayashi et al., 2003; Peñarrubia et al., 2010), but has the advantage of being physically motivated, allowing for a theoretical prediction of density evolution at very small radii. Looking at the model assumptions in more detail, we have found that most of the assumptions are justified, but there is a some mixing in energy space, particularly in cases of rapid mass loss. It is possible that slight modifications to the energy truncation model could account for some of this effect (e.g. allowing for a more gradual energy cut-off).

The distinction between bound and unbound particles is another factor that could affect how well our model describes the simulations. In this work, we simply remove all unbound particles in a method similar to what is used in halo finders. This, however, includes particles that are only temporarily bound. It would be interesting to explore a more detailed model of mass loss, that could determine the timescale at which particles are removed, and how to identify transient particles.

We also examined the universality of the energy truncation model by testing it on various other theoretical profiles. Overall, the model does a very good job at describing the density, mass and velocity profile evolution in all the tested cases. Additionally, our model naturally captures the effect that more cuspy profiles conserve central density, while cored profiles have a large decrease in central density, as described in Peñarrubia et al. (2010).

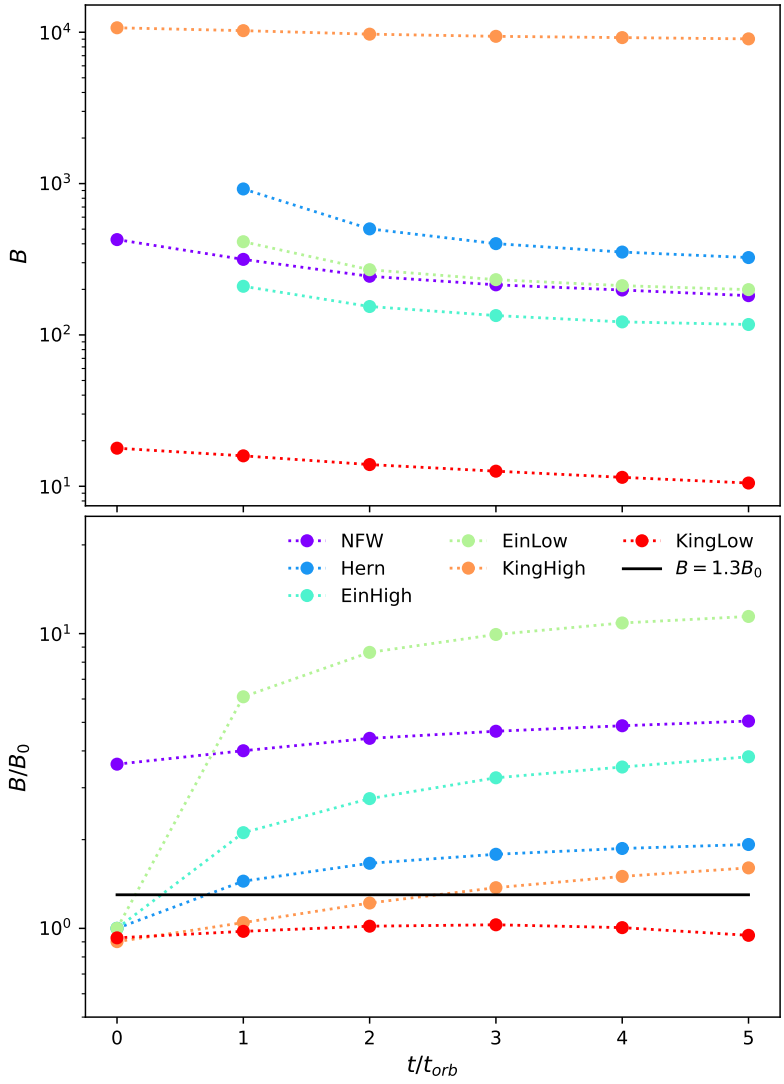

Figure 3.14: Boost factor, B versus time (top), as well as the ratio between B and the untruncated profile model calculated within the same tidal radius, B_0 (bottom).

Finally, we showed the implications to the annihilation boost factor. Overall, we found that the boost factor (measured within the evolving tidal radius) remains fairly constant. A surprising result was that the boost factor is very sensitive to how the subhalo profile is modeled; different models can result in boost factor values that differ by an order of magnitude. For this reason, physically based models for subhalo evolution are critical for correctly predicting density profile evolution at small radii, as these regions dominate the signal but cannot be resolved in simulations.

While we demonstrated that subhalo evolution can be described fairly accurately by a single parameter (such as the tidal energy, $\mathcal{E}_{\rm T}$), it is currently unclear what determines the value of this parameter. Likely, $\mathcal{E}_{\rm T}$ is dependent on the strength of the tidal field, as well as the size and mass of the subhalo; predicting this parameter would also allow for a prediction of the mass loss of the system. Subhalo mass evolution is a complicated process, and it is often difficult to determine whether mass loss is due to physical processes or numerical artifacts (e.g. van den Bosch et al., 2018; van den Bosch & Ogiya, 2018). For this reason, it would be useful to have a physically based model for how mass evolves with time, and this will be explored in future studies.

Overall, we showed that the energy-truncation model proposed in Chapter 2 works well to describe the evolution of a wide range of collisionless models undergoing tidal stripping. This allows for a physically based model of how density profiles evolve, which is important for predictions of dark matter annihilation. Particularly, we showed that our model can increase predictions of the dark matter annihilation boost factor by an order of magnitude. Further work needs to be done to determine the effects of mixing and shape on subhalo evolution, as well as to understand the details of mass loss.

Chapter 4

Major Mergers Between Dark Matter Haloes – I. Predictions for Size, Shape, and Spin

4.1 Introduction

There is now compelling evidence for the existence of dark matter over a vast range of scales, from the horizon scales probed by the Cosmic Microwave Background (e.g. Planck Collaboration et al., 2018), to the galactic and sub-galactic scales probed by local dwarf galaxies (see e.g. McConnachie, 2012, and references therein). On large scales, dark matter clusters into sheets and filaments; where filaments intersect, they form higher density, roughly spherical structures termed 'haloes'. Dark matter haloes are the exclusive sites of galaxy, group, and cluster formation. Thus, understanding their structure and evolution is of fundamental importance in cosmology.

Our information about halo structure and evolution comes mainly from simulations. These have established that some halo properties, such as the spherically averaged density profile, are approximately universal (Navarro et al., 1996, 1997), while other properties such as shape, central concentration, or the presence of substructure, vary from system to system. Since observational information from galaxy kinematics (e.g. Ouellette et al., 2017), satellite kinematics (e.g. Guo et al., 2012), and weak and/or strong gravitational lensing (e.g. Umetsu et al., 2016) is beginning to fix or constrain these individual properties for large samples of haloes, the time is ripe to consider what the structure of individual haloes can teach us.

It is clear that the structure of individual haloes is closely related to their merger history. Shape changes, for instance, have been linked to the parameters of the last major merger (e.g. Despali et al., 2017), the remnant being elongated along the merger axis (e.g. Macciò et al., 2007; Vera-Ciro et al., 2011). Concentration is correlated with the overall age of a halo (e.g. Wechsler et al., 2002; Zhao et al., 2009; Wong & Taylor, 2012); the density in the central regions reflects the background density of the universe at the time of formation (Navarro et al., 1996, 1997; Bullock et al., 2001a), or possibly at the end of the rapid, major-merger dominated phase of halo growth (e.g. Zhao et al., 2003). Finally, substructure is formed from the tidally stripped cores of infalling subhaloes, and is thus mainly determined by the recent merger history (e.g. Taylor & Babul, 2005).

Measuring the shape, concentration, and substructure of haloes may therefore provide an opportunity to learn about individual growth histories, and the connection between growth history and the properties of the visible galaxy or galaxies that reside within a halo. Given a quantitative understanding of the connection between history and structure, measurements of structural properties for large, well-defined samples may also provide new cosmological tests (see e.g. Taylor, 2011, for a discussion). So far, observations of cluster shape (e.g. Oguri et al., 2010) and concentration (e.g. Sereno et al., 2018) have been shown to be consistent with the concordance cosmology established by other tests. Both observational systematics and theoretical predictions need to be refined, however, before these methods can be used to improve our knowledge of the cosmological parameters.

Halo growth occurs through accretion of material from the surrounding density field, both smoothly and in a series of violent, stochastic mergers. To understand the smooth part of the process requires cosmological simulations, in order to capture the statistics of the density and velocity fields around the peaks where haloes form. There have been extensive theoretical studies of halo structure in this cosmological context, though many focus on mean trends, rather than individual cases (e.g. Navarro et al., 1997; Bullock et al., 2001a; Zhao et al., 2003; Butsky et al., 2016; Klypin et al., 2016; Despali et al., 2017). Mergers complicate the picture, however; sufficiently so that they have often been studied in simpler, idealized simulations with controlled ICs (ICs; e.g. Fulton & Barnes, 2001; Boylan-Kolchin & Ma, 2004; Moore et al., 2004; McMillan et al., 2007; Vass et al., 2009; Ogiya et al., 2016).

Even when studying major mergers using isolated simulations, there are still many degrees of freedom (halo profile, mass ratio, shape, orbit) that can obscure which essential parameters determine the properties of the final remnant. Therefore, in this chapter we will start by considering the simplest case: an equal-mass merger between two isolated, identical spherical systems, given one of various realistic density profiles, and placed on a variety of initial orbits. This work is the first in a series; in this chapter we will introduce

our major merger simulations and examine how the ICs determine the shape and spin of the final remnant. In subsequent work, we will examine how other properties, such as concentration and the detailed form of the density profile, depend on the ICs of the merger.

The outline of this chapter is as follows. In Section 4.2 we describe the initial halo models, and verify their stability in isolation. In Section 4.3 we describe the set-up and analysis of the merger simulations. In Section 4.4 we present our main results on shape and spin. Finally, in Section 4.5 we discuss our conclusions, the limitations of this study, and future work.

4.2 Halo Models

Each of our simulations follows the merger of two identical haloes. To investigate the effect of the halo model on the shape and spin of the remnant, we consider several different initial models, as described below.

4.2.1 Initial Conditions

We consider initial halo models with NFW (Navarro et al., 1996, 1997) and Einasto (Einasto, 1965) profiles. The ICs (ICs) were created using the code ICICLE (Drakos et al., 2017). Since the mass of an NFW profile diverges at large radii, the ICs need to be truncated in order to be realized with a finite number of particles. One common approach is to use an exponentially truncated NFW profile (hereafter denoted "NFWX"), which is NFW within the virial radius, $r_{\rm vir}$, and then decays exponentially outside the virial radius (Springel & White, 1999). An additional parameter $r_{\rm d}$ sets how fast the decay occurs with radius. An alternative approach to truncating an NFW profile is to generate the part of the profile interior to some tidal radius, r_t, and then iteratively remove any particles that are unbound, given the escape speed of the truncated system. As the tidal radius approaches infinity, systems generated in this way are equivalent to an infinitely extended NFW profile. It has been shown that the profiles resulting from this second approach are stable, and resemble tidally stripped NFW profiles (Drakos et al., 2017), and thus we denote them "NFWT" profiles.

Overall, we considered six different initial profiles. Four of these profiles are NFW, but truncated in different ways (two are NFWT and two are NFWX profiles). Two are Einasto profiles, with α_E values representative of the range found in simulations (Gao et al., 2008):

Table 4.1: Summary of the parameters used for the ICs. The profiles are shown in Fig. 4.1. The columns list (1) the name of the ICs, (2) the number of particles N, (3) the parameters used to construct the ICs, (4) the relaxation time evaluated at the peak radius, $t_{\rm relax}(r_{\rm peak})$ and (5) the total internal energy of the halo, E_0.

Initial conditions name	N	Parameters	$t_{\rm relax}(r_{\rm peak})/t_{\rm unit}$	$E_0/E_{\rm unit}$
EinLow	5×10^5	$\alpha_E = 0.15$	610	-2.2
EinHigh	5×10^5	$\alpha_E = 0.3$	1300	-1.2
NFWT10	$\sim 3.2 \times 10^5$	$r_{\rm cut} = 10$	1100	-1.0
NFWT15	$\sim 3.5 \times 10^5$	$r_{\rm cut} = 15$	1000	-1.3
NFWXSlow	5×10^5	$r_{\rm vir} = 10$, $r_{\rm d} = 2\,r_{\rm s}$	1100	-1.6
NFWXFast	5×10^5	$r_{\rm vir} = 10$, $r_{\rm d} = 0.2\,r_{\rm s}$	1200	-1.5

to explore how the inner slope affects the simulations we use an Einasto profile with a low α_E value of 0.15, and also a profile with a high α_E value of 0.3.

The simulation units were chosen so that the gravitational constant, G, the peak circular velocity, $v_{\rm peak}$, and the radius at which the circular velocity peaks, $r_{\rm peak}$, are all unity. Setting $G = M_{\rm peak} = r_{\rm peak} = 1$ produces a time unit $t_{\rm unit} = \sqrt{r^3_{\rm peak}/GM_{\rm peak}}$, a density unit $\rho_{\rm unit} = M_{\rm peak}/r^3_{\rm peak}$ and an energy unit $E_{\rm unit} = GM^2_{\rm peak}/r_{\rm peak}$. All the haloes were constructed initially using 5×10^5 particles; after removing unbound particles, the resulting NFWT profiles then have fewer particles. The IC profiles are compared in Fig. 4.1, and the IC parameters and properties are summarized in Table 4.1.

4.2.2 Internal Energies

The internal energy of each halo, E_0, was calculated as follows:

$$E_0 = P_0 + K_0 \ , \tag{4.1}$$

where P_0 and K_0 are the potential and kinetic energy of the halo, respectively. These are most generally expressed as

$$\begin{aligned} K_0 &= \sum_{i=1}^{N} m v_i^2 \\ P_0 &= -\frac{1}{2} \sum_{i,j=1}^{N} \frac{Gm^2}{r_{ij}} \ , \end{aligned} \tag{4.2}$$

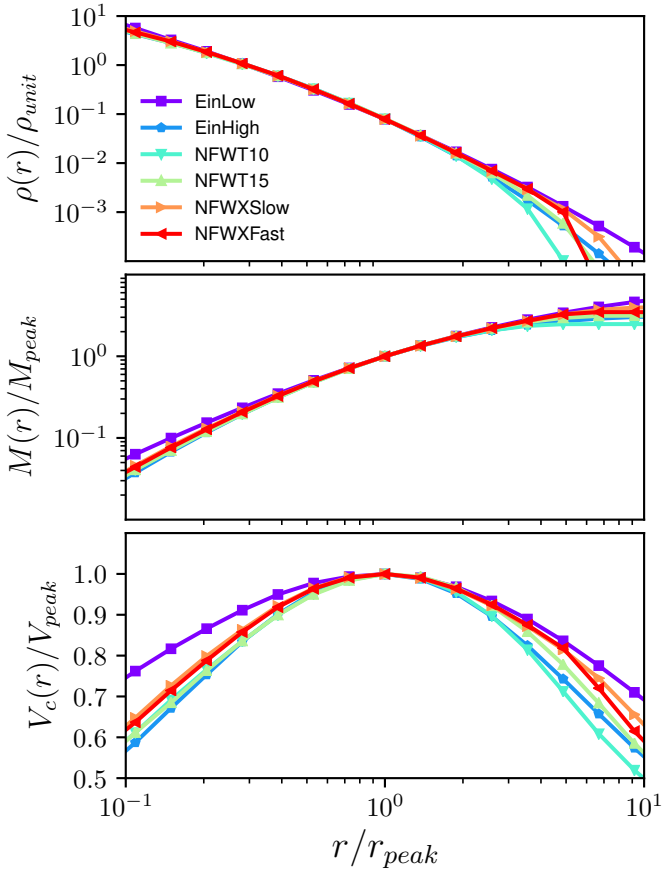

Figure 4.1: Comparison of the density (top), enclosed mass (middle), and circular velocity (bottom) profiles of the initial models.

where m is the mass of each particle and r_{ij} is the distance between particles i and j. Since the ICs are spherically symmetric, however, at least to within the discreteness noise of the individual particles, we can treat the mass of each particle i as being distributed over a shell of radius r_i, and write:

$$P_0 \approx -\frac{Gm^2}{2} \sum_{i=1}^{N} \left(\frac{N(< r_i)}{r_i} + \sum_{j=1, r_j > r_i}^{N} \frac{1}{r_j} \right) , \tag{4.3}$$

where the two terms in parentheses give the contributions interior to and exterior to the position of each particle i, respectively. The internal energy for each of the halo models is listed in Table 4.1.

4.2.3 IC Stability

To verify the stability of the ICs, they were evolved in isolation using GADGET-2 (Springel, 2005), with a softening length of $\epsilon = 0.02\, r_{\rm peak}$. The stability of the ICs will be limited by relaxation due to the limited number of particles. The characteristic relaxation time for each profile was calculated as follows:

$$t_{\rm rel}(r) = 0.1 \frac{\sqrt{N(< r)}}{\ln N(< r)} \sqrt{\frac{r^3}{GM(< r)}} , \tag{4.4}$$

as in Binney & Tremaine (1987), and is included in Table 4.1. Fig. 4.2 illustrates the stability of the host haloes over a time-scale of $t = 300\ t_{\rm unit}$. We also tested the sensitivity of these results to time step size and the error in the force calculations by increasing and decreasing the GADGET-2 parameters ErrTolIntAccurac and ErrTolForceAcc by a factor of 3, but found that this did not make a noticeable difference in the stability of the ICs.

4.3 Merger Simulations

The merger simulations were run in GADGET-2 using $N = 5 \times 10^5$ particles per halo and a softening length of $\epsilon = 0.02\, r_{\rm peak}$. The centre of the remnant halo was found by calculating the centre of mass within increasingly smaller spheres; as in (Moore et al., 2004), we found that this was roughly equivalent to tracking the most bound particle.

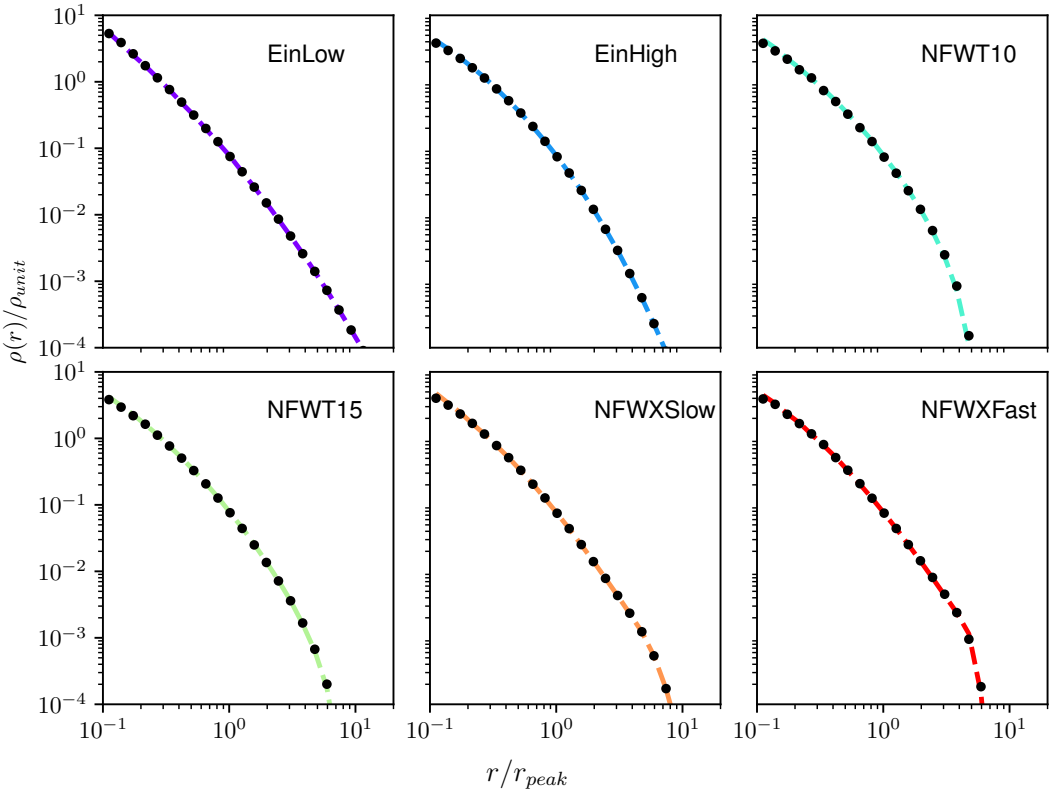

Figure 4.2: Stability of the ICs. The dashed line shows the initial profile, while black circles show the profile at the time $t = 300\ t_{\rm unit}$.

4.3.1 Orbital Parameters

For each of the six models, we performed 30 equal-mass binary merger simulations, for a total of 180 simulations. Simulations were analyzed in the rest frame of the first halo, the second halo being given an initial position and velocity in this frame. We considered three different radial separations, $r_{\rm sep} = 2, 5$ or $10\, r_{\rm peak}$. The initial velocity was either purely tangential or purely radial, with magnitude $v_0 = 0.1$, 0.2, 0.6, 0.8 or $1.2\, v_{\rm esc}$, where $v_{\rm esc}$ is the escape velocity of a point mass located at $r_{\rm sep}$.

Each orbit can be described by its energy and angular momentum. The orbital energy, $E_{\rm orb}$, was calculated as the total energy of the system minus the internal energy of the individual haloes, i.e.,

$$E_{\rm orb} = P + K - 2E_0 \ , \tag{4.5}$$

where the internal energy of each halo, E_0, was calculated as described in Section 4.2, and the total potential and kinetic energies of the system were calculated as described in Bett et al. (2010):

$$\begin{aligned} K &= \frac{1}{2}\sum_{i=1}^{N} m{\mathbf{v_i}}^2 \ , \\ P &= \left(\frac{N^2 - N}{N_{\rm sel}^2 - N_{\rm sel}}\right)\left(\frac{-Gm^2}{\epsilon}\right)\sum_{i=1}^{N_{\rm sel}-1}\sum_{j=i+1}^{N_{\rm sel}} -W(r_{ij}/\epsilon)\,. \end{aligned} \tag{4.6}$$

Here $N_{\rm sel}$ is the number of randomly selected particles, used to approximate the entire distribution; after experimentation we found that 5000 particles from each halo were sufficient to calculate P accurately. W is the smoothing kernel used for force calculations in GADGET-2 (Springel et al., 2001),

$$W(x) = \begin{cases} \frac{16}{3}x^2 - \frac{48}{5}x^4 + \frac{32}{5}x^5 - \frac{14}{5}, & 0 \le x \le \frac{1}{2} \\ \frac{1}{15x} + \frac{32}{3}x^2 - 16x^2 + \frac{48}{5}x^4 & \\ -\frac{32}{15}x^5 - \frac{16}{5}, & \frac{1}{2} \le x \le 1 \\ -\frac{1}{x}, & x \ge 1 \ . \end{cases} \tag{4.7}$$

Finally, the orbital angular momentum was calculated as follows:

$$\mathbf{J} = \sum_i m\mathbf{r}_i \times \mathbf{v}_i \ , \tag{4.8}$$

which was found to be equivalent to $\mathbf{J} = M\mathbf{r}_{\rm sep} \times \mathbf{v_0}$ to within 0.5 per cent. The energy and angular momenta used in our simulations are shown in Fig. 4.3.

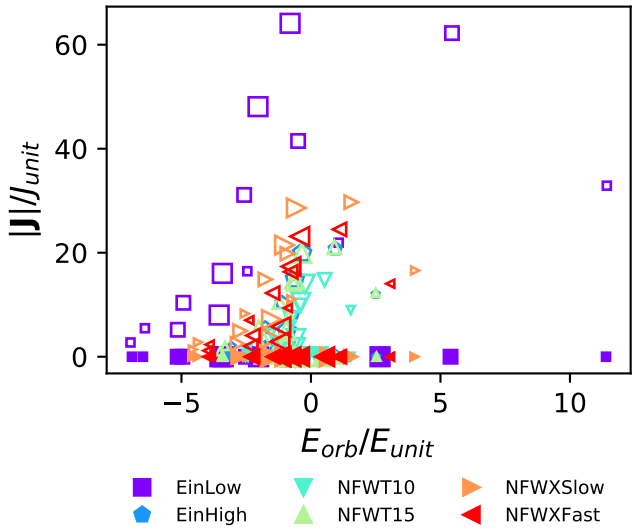

Figure 4.3: The range of orbital energies $E_{\rm orb}$ and angular momenta J used in the simulations. Colours and symbols are as in Fig. 4.1. Open points indicate tangential initial velocities, and filled points denote radial initial velocities. The size of the symbols indicates the initial radial separation, $r_{\rm sep}$.

In cosmological simulations, orbital energy is often expressed in units of the energy of a circular orbit at the virial radius, and angular momentum is expressed in terms of the circularity, ϵ, defined as the angular momentum divided by the angular momentum of a circular orbit with the same energy, $\epsilon = J/J_C(E)$ (Lacey & Cole, 1993). Neither of these quantities is well defined in this context, however, since the virial radius does not have a clear definition for isolated, non-cosmological simulations, and the definition of circularity requires that the orbit be bound.

Overall, our simulations cover a wider range of energy and angular momentum than would be expected in a cosmological scenario. Typically, subhaloes merging into galaxy- or cluster-sized haloes have a broad distribution of orbital circularity with a mean of $\epsilon \approx 0.5$ (although primordial haloes may merge on more radial orbits; Ogiya et al. (2016)) while the energies of cosmological orbits are typically close to that of a circular orbit at the virial radius (e.g. Khochfar & Burkert, 2006; Wetzel, 2011; Jiang et al., 2015). In contrast, the orbits in our simulations are chosen to sample the full range of physical possibilities, in order to determine how orbital parameters affect the outcome of a merger generally. Thus we include completely radial and completely tangential orbits, and also a broad range of possible energies, from almost unbound to extremely tightly bound.

4.3.2 Merger Time-scale

Fig. 4.4 shows the radial separation between the merging haloes as a function of time. At the highest relative velocity, haloes on tangential orbits had not merged by the time $t = 100\, t_{\rm unit}$, and thus were excluded from this study, such that only 174 simulations are analyzed. For the majority of the simulations, the haloes merged very quickly (i.e. in less than one orbit). This is broadly consistent with predicted orbital decay times due to dynamical friction (Colpi et al., 1999):

$$\tau_{\rm DF} = 1.2 \frac{J_{\rm circ} r_{\rm circ}}{(G M_{\rm sat}/e) \log(M_{\rm halo}/M_{\rm sat})} \epsilon^{0.4} \quad , \tag{4.9}$$

where $J_{\rm circ}$ is the angular momentum of a circular orbit with the same energy, ϵ is the circularity (i.e. the angular momentum divided by the angular momentum of a circular orbit of the same energy), and $r_{\rm circ}$ is the radius of a circular orbit with the same energy. $M_{\rm sat}$ and $M_{\rm halo}$ are the masses of the satellite halo and the main system, respectively. Although this equation cannot be applied directly to the majority of our simulations (since many of our orbits are unbound, and because this estimate is not applicable to completely radial orbits), it predicts decay times of less than an orbital period as the mass ratio approaches unity.

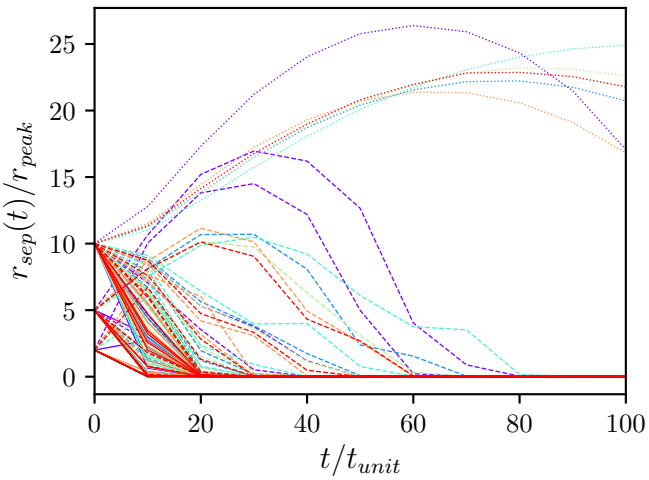

Figure 4.4: Radial separation between the halo centres, as a function of time. The six cases that did not merge by $t = 100\,t_{\rm unit}$ (dotted lines) were excluded from subsequent analysis. Colours indicate the initial profile model, as in Fig. 4.1. Dashed lines indicate tangential initial velocities, and solid lines denote radial initial velocities.

We also determined how long it took for the remnant to reach virial equilibrium, after the merger. At every time step the potential and kinetic energy, P and K, were calculated in the frame of the first halo, using Equation (4.6). Fig. 4.5 shows an example of the time evolution of these energies, the virial ratio, and the separation between the halo centres, in a simulation with EinLow ICs, with orbital parameters $r_{\rm sep} = 10\,r_{\rm peak}$ and a radial velocity of $v_0 = 0.8\,v_{\rm esc}$. For this simulation, the haloes merge by $t = 20\,t_{\rm unit}$, which is less than one period of the initial orbit. The potential and kinetic energy remain constant after the halo has merged, with a virial ratio of $-P/2K \approx 1$ to good approximation. Although we only demonstrate that virial equilibrium is reached when $r_{\rm sep} \approx 0$ for one case, this result holds for all the simulations in this work.

4.3.3 Shape Measurement

A halo is, in general, triaxial, with principal axes $a > b > c$. Prolate haloes will have one long and two short axes, while oblate haloes will have two long and one short axes. Following Moore et al. (2004), we calculated principal axis ratios $s = b/a$ and $q = c/a$ using the iterative method described in Dubinski & Carlberg (1991). Beginning with $a = b = c =$

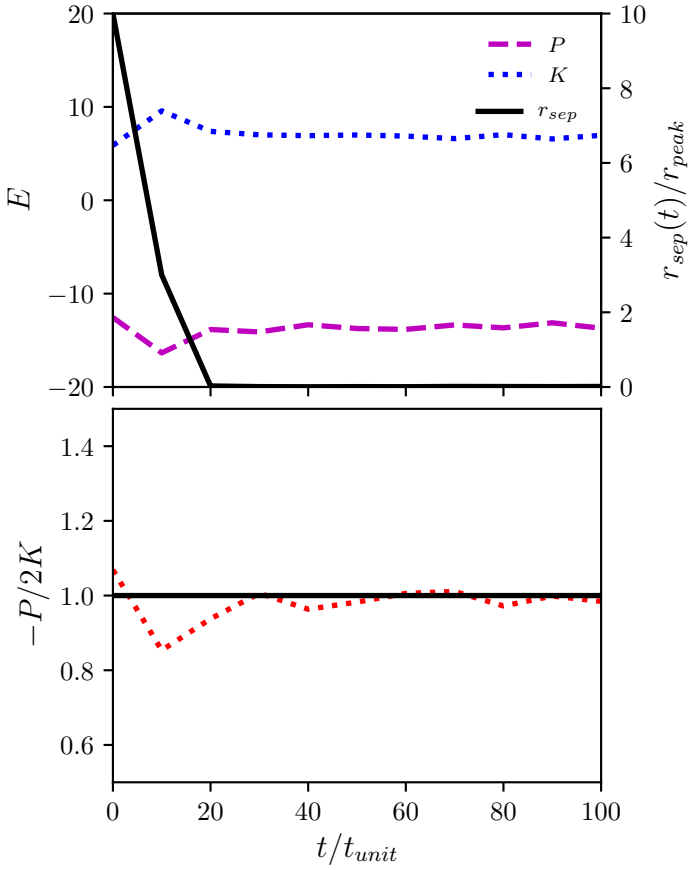

Figure 4.5: Evolution towards equilibrium with time. The top panel shows the radial separation between the halo centres (solid black line), as well as the potential and kinetic energy of the entire system. The bottom panel shows the virial ratio $-P/2K$ (dotted red line), which should be 1 for a virialized system (solid black line).

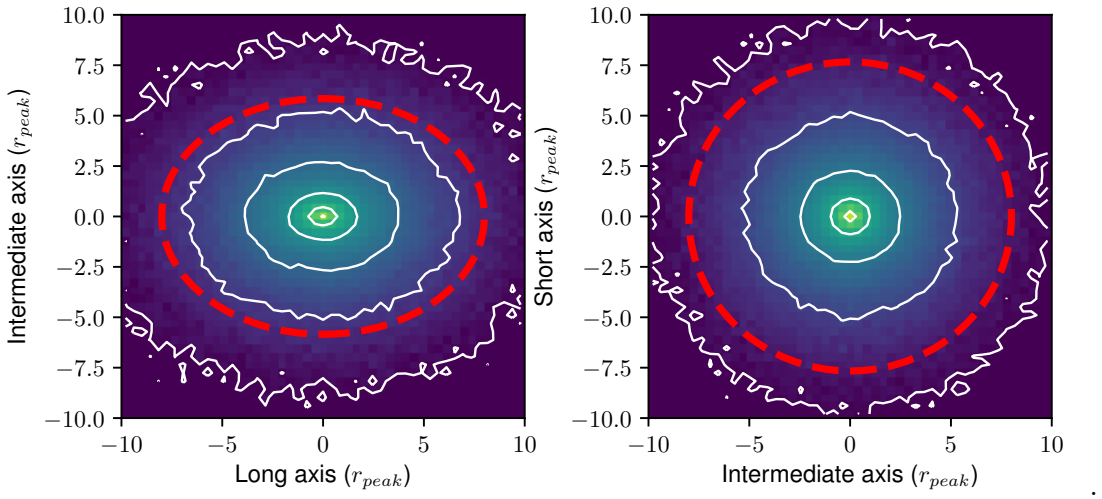

Figure 4.6: Projected isodensity contours (white lines) of the halo remnant. The measured shape ratio is shown as by the red dashed line.

1, the eigenvalues $w_1 = a^2$, $w_2 = b^2$ and $w_3 = c^2$ were found from the dimensionless inertia tensor $I_{ij} = \sum x_i x_j / d^2$, where $d = x_i^2 + (x_j/s)^2 + (x_k/q)^2$ is the ellipsoidal coordinate. The coordinates of each particle were then rotated using the eigenvectors of the new principal axis, and the principal axis ratios were recalculated. This process was repeated until convergence, which was defined as when s and q both had a relative change of less than 10^{-5}.

In Fig. 4.6 we compare the shape measurement to the isodensity contours of the remnant halo for a radial merger between two haloes with EinLow profiles. The haloes were initially separated by $r_{\rm sep} = 10\, r_{\rm peak}$, and the second halo was given an initial velocity of $v_0 \approx 0.9\, v_{\rm peak}$ (this corresponds to 80 per cent of the escape speed of a point mass located at $r_{\rm sep}$). The shape measurement agrees well with the isodensity contours. We note that since our shapes are measured using all the halo particles, we will not catch radial variations in halo shape, but at least in this case, radial variations do not appear to be significant.

We investigated the effect of numerical resolution on our shape measurements by considering haloes with various numbers of particles, ranging from $N = 5 \times 10^3$ to $N = 5 \times 10^5$. The original softening length of $\epsilon = 0.02\, r_{\rm peak}$ for the $N = 5 \times 10^5$ profile was scaled as $N^{-1/3}$. As above, we considered the case of a merger between two EinLow profiles, since this profile has the shortest relaxation time.

We compared shape parameters c/a and c/b, as well as the values of $r_{\rm peak}$ and $v_{\rm peak}$. Fig. 4.7 shows how these properties change as a function of time at each resolution. While there are significant fluctuations in the values over time at low resolution, at the resolution of our main set of simulations, the structural parameters are stable between $t = 100$ and $300\,t_{\rm unit}$.

The net effect of resolution on the final measurements (averaged over 10 snapshots between $t = 200\,t_{\rm unit}$ and $300\,t_{\rm unit}$) is shown in Fig. 4.8. For each point, five different realizations were simulated, using different random seeds to generate the ICs. Low resolutions tend to predict more circular haloes, but at the resolution of 5×10^5 particles per halo, the shape parameters are determined to within 1 per cent or better. The maximum of the circular velocity, $v_{\rm peak}$ has similar accuracy, while $r_{\rm peak}$ is more sensitive to relaxation, and has an uncertainty of 6 per cent. We note that there is a transient period before the haloes merge in which c/a is very small; this is because the algorithm we use for calculating shapes takes into account the particles of both (un-merged) haloes.

We conclude that a resolution of 5×10^5 particles per halo is sufficient to study the properties of the merger remnant. At lower resolution, numerical relaxation can artificially increase the location of $r_{\rm peak}$. We found that this effect could be somewhat alleviated by decreasing the time-stepping parameter (ErrTolIntAccuracy in gadget-2), at the cost of much slower run times. For the simulations shown in this chapter, the value ErrTolIntAccuracy= 0.02 was used.

4.3.4 Halo Rotation

Finally, we check to see whether the halo remnants are in solid-body rotation. In the previous section, we showed that the axis ratios stayed approximately constant with time, after an initial transient period. This result holds for all the simulations performed in this work. Since the merger remnants from tangential encounters should rotate due to conservation of the initial angular momentum, we are also interested in whether they rotate differentially, or as a solid body. We considered cases in which the remnant is prolate ($b/a < 0.8$), such that the major axis has a well-defined direction, and measured rotation by tracking changes in the orientation of the major axis.

In Fig. 4.9 we show two sample cases, chosen such that the mergers have similar energies and angular momenta. The first is a merger between two EinHigh profiles with orbital parameters $r_{\rm sep} = 5\,r_{\rm peak}$ and $v_0 = 0.2\,v_{\rm esc}$. The second case consists of two EinLow profiles with orbital parameters $r_{\rm sep} = 2\,r_{\rm peak}$ and $v_0 = 0.8\,v_{\rm esc}$. The top two panels show the axis ratios, while the bottom panel shows the normalized x-component of the major

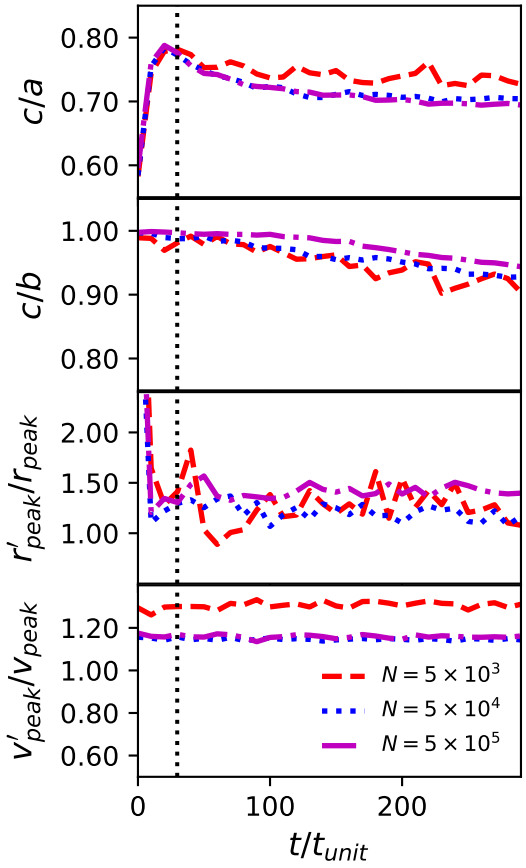

Figure 4.7: The axis ratios c/a and c/b and the structural parameters $r'_{\rm peak}$ and $v'_{\rm peak}$ relative to their original values $r_{\rm peak}$ and $v_{\rm peak}$, as a function of time, for different resolutions. The vertical dotted lines show the time by which the two haloes had completely merged.

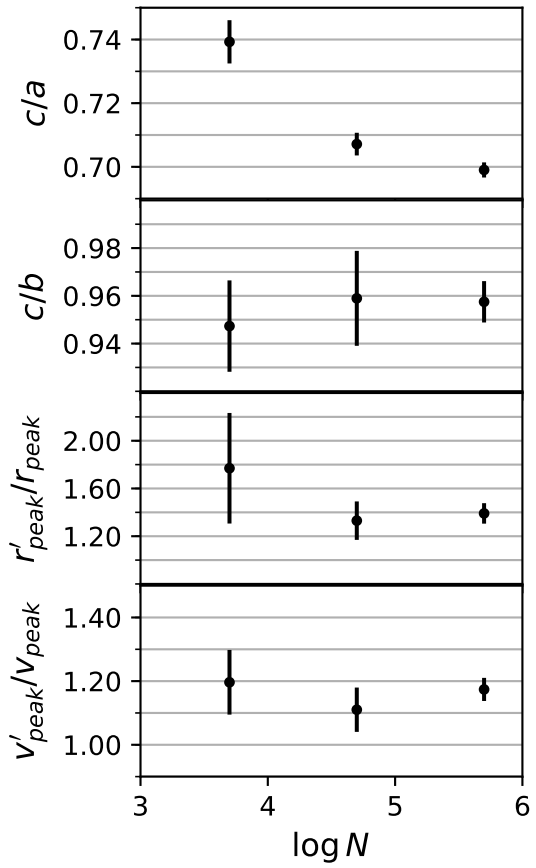

Figure 4.8: The axis ratios c/a and c/b and the structural parameters $r'_{\rm peak}$ and $v'_{\rm peak}$ relative to their original values $r_{\rm peak}$ and $v_{\rm peak}$, as a function of resolution. Each point is averaged over five realizations, while error bars show the r.m.s..

principal axis, $a_x/|\mathbf{a}|$, as a measure of orientation. As in Fig. 4.7, c/a is very small in the transient period before the haloes merge since our algorithm calculates shape based on all the particles from both haloes.

In the first case, the halo appears to be rotating as a solid body, and there may be some slight change in the shape ratio c/b, though the change is within the uncertainty of the shape measurements. In the second case, there is no clear rotation. The main difference between these two cases is that the EinLow profile is very extended, with a lot of mass at large radii; it is possible that in this case the envelope is decoupled from the core, explaining the irregular variation in the orientation of the major principal axis. We conclude that the rotation of the remnants can be complicated, including both differential and solid-body rotation. In either of the two cases, however, the long-term shape of the remnants is well defined. We will proceed to study how this shape depends on halo profiles and orbital parameters.

4.4 Results

Fig. 4.10 shows sample results from four different merger simulations. The top panels show the resulting remnants (using a random subset of 10^3 particles), the middle panels show the density profiles, and the bottom panels show the cumulative mass profiles. In general, we find that the remnants are non-spherical in shape, with the radial and tangential orbits producing prolate and oblate systems, respectively. We can compare the final density and mass profiles (solid black lines) to those of the initial haloes (dotted green lines), scaling the mass by a factor of 2 and the radius by a factor of $2^{1/3}$, as expected if the remnant has the same mean density as the ICs. We see some differences between the remnant and scaled ICs; specifically, the density profile changes slightly in curvature, and there appears to be some mass rearrangement. In general the remnant profile appears to be more extended than the ICs, but there is also a slight increase in central density. The density profiles of the remnants will be considered in detail in Chapter 5.

4.4.1 Scaled Energy and Angular Momentum

Changes in halo structure should presumably depend not on the total orbital energy, but on the fraction of this energy that is available as internal energy, given momentum conservation requires some bulk motion of the remnant. Before the merger, the total energy of the system

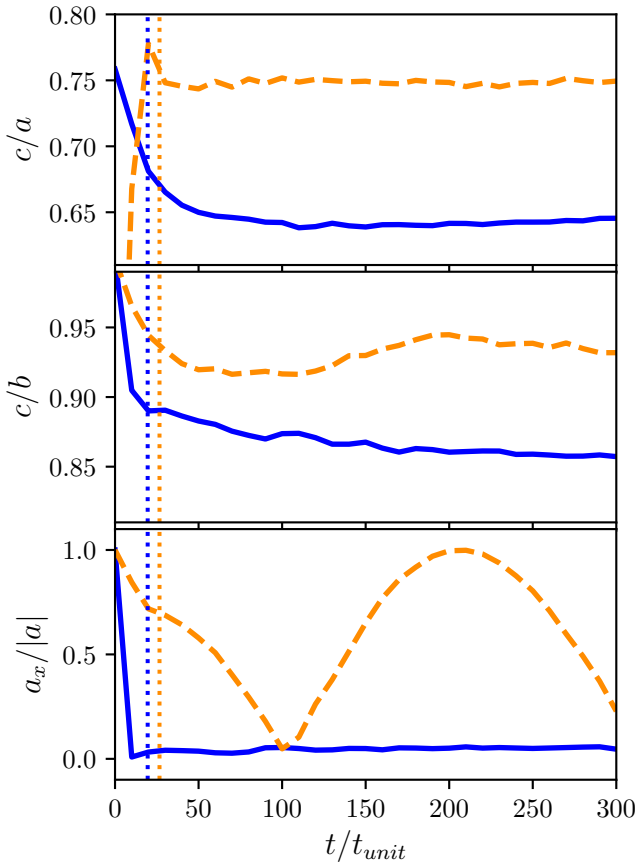

Figure 4.9: The time evolution in the shape ratios c/a and c/b (top and middle panels), as well as the x-component of the normalized major axis (bottom panel). The two examples are mergers between two EinHigh profiles (orange dashed lines) and two EinLow profiles (blue solid lines), chosen because they have comparable energies and angular momenta. The vertical dotted lines show the time by which the two haloes had completely merged.

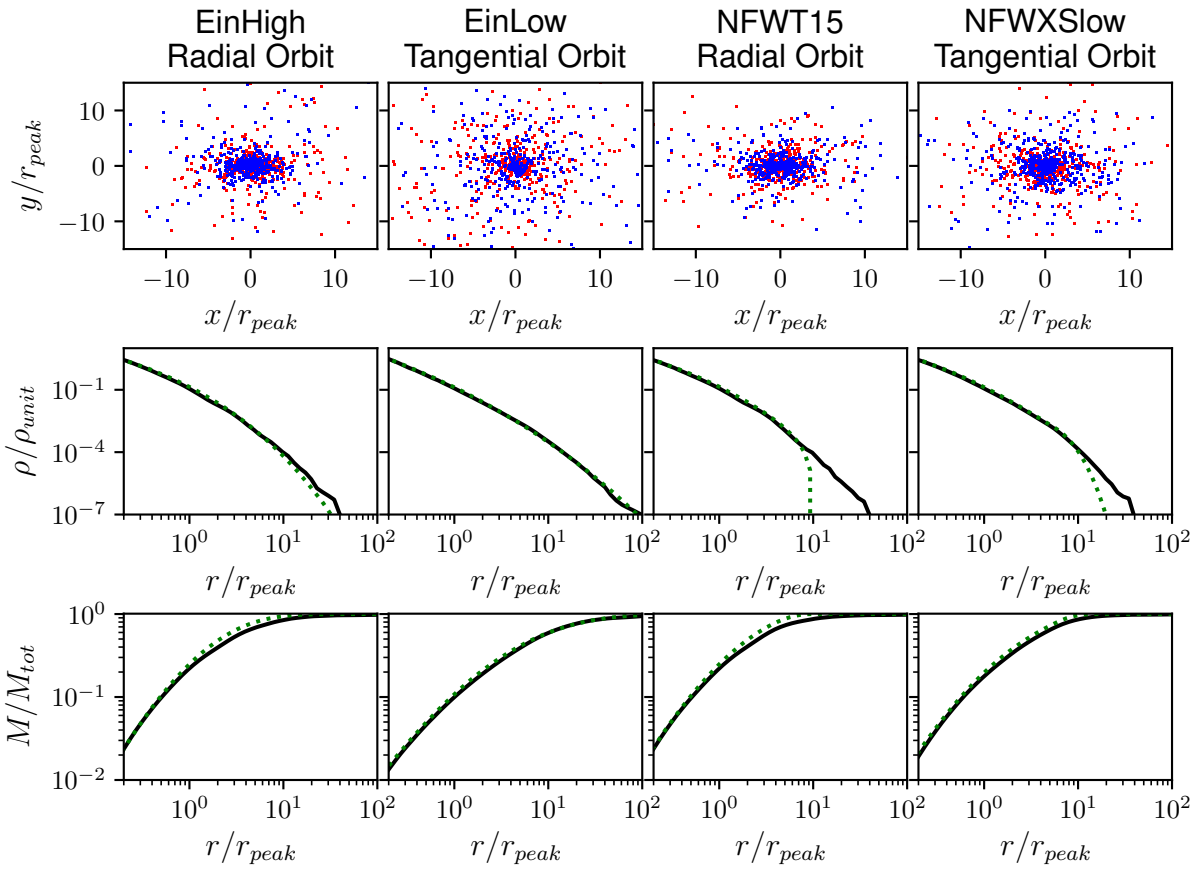

Figure 4.10: Sample results from four merger simulations. The top row of panels shows the state of the remnant at $t = 300\,t_{\rm unit}$ (in this plot we show only 10^3 randomly selected particles). The particles are coloured either red or blue, depending on their initial halo. The middle row of panels shows the density profiles, and the bottom row shows the mass profiles. The scaled ICs and remnants are shown with dotted green lines and solid black lines, respectively. All haloes were initially separated by $r_{\rm sep} = 10$, and given either a radial or tangential velocity of $v_0 = 0.8\,v_{\rm esc}$, where $v_{\rm esc}$ is the escape speed of a point mass in the potential of the initial halo.

is equal to the internal energy of the two initial haloes, plus the initial orbital energy:

$$E_{\rm tot} = 2E_0 + E_{\rm orb}\,. \tag{4.10}$$

After the merger, the remnant will have internal energy E_0', plus some net kinetic energy, $K_{\rm orb}'$; $E_{\rm tot}' = E_0' + K_{\rm orb}'$. The net orbital kinetic energy, $K_{\rm orb}'$, can be calculated from conservation of momentum, $K_{\rm orb}' = K_{\rm orb}M/M'$, where $K_{\rm orb}$ is the initial (orbital) kinetic energy, M is the mass of the initial halo, and M' is the mass of the remnant. For an equal mass merger, $K_{\rm orb} = Mv_0^2/2$, and $M/M' = 1/2$. Thus, since $E_{\rm tot} = E_{\rm tot}'$, the internal energy of the remnant halo will be:

$$E_0' = E_{\rm orb} + 2E_0 - \frac{1}{4}Mv_0^2\ . \tag{4.11}$$

We found that calculating E_0' in this way agrees to within 2 per cent with a direct calculation of the internal energy of the remnant using Equation (4.6).

In a cosmological context, encounters between haloes may be close to parabolic, with $E_{\rm orb} \sim 0$ in the centre-of-mass frame. In this case, the total energy of the remnant is then just twice the energy of the initial haloes. If the form of the density profile is conserved, from the scaling of potential energy we expect that the size of the remnant will increase linearly with mass, i.e. by a factor of 2 (Farouki et al., 1983). As a result, the density of the remnant will be lower than that of the initial haloes. This evolution at constant specific energy has been considered the baseline in previous studies of mergers (e.g. Navarro, 1989). On the other hand, we are interested in following the evolution of shape and concentration in mergers partly to determine how the mean density of structures evolves with time, for instance in order to calculate the boost factor for dark matter annihilation (e.g. Okoli et al., 2018), which scales as $\int \rho\,{\rm d}m$. Thus, we will consider the baseline case one in which the *overall density distribution* is conserved. We define 'self-similar evolution' to be evolution where the relative mass fraction at any given density in a structure remains constant, and thus the mean density and boost factor do not change.

In the case of self-similar evolution, $r \sim M^{1/3}$ and thus $E_0 \propto M^{5/3}$. Thus in the self-similar case for equal-mass mergers, the internal energy of the halo should increase by $2^{5/3}$. More generally, we can define a new parameter, the change in internal energy relative to the change expected in self-similar evolution:

$$\kappa \equiv \frac{E_0'}{E_0}\left(\frac{M}{M'}\right)^{5/3}\ , \tag{4.12}$$

This parameter provides a convenient dimensionless measure of the change in internal energy of the halo; a value of $\kappa = 1$ corresponds to a self-similar change in energy. If

$\kappa < 1$, then the remnant is less bound than the progenitor, while if $\kappa > 1$ the remnant is more bound.

We can also express angular momentum using a dimensionless spin parameter. The spin parameter was originally defined by Peebles (1971) as

$$\lambda = \frac{\sqrt{|E_0|}|\mathbf{J}|}{GM^{5/2}} \ , \tag{4.13}$$

while an alternative definition commonly used in the literature was proposed by Bullock et al. (2001b):

$$\lambda_{\rm B} = \frac{|\mathbf{J}|}{\sqrt{2}M_{\rm vir}r_{\rm vir}v_{\rm vir}} \ . \tag{4.14}$$

The second definition, $\lambda_{\rm B}$, is equivalent to λ under the assumption of virialization and an isothermal profile, and is often preferred in the literature since calculating mass is much easier than calculating the full energy. However, these assumptions lead to scatter in the expected spin (Ahn et al., 2014). Additionally, $\lambda_{\rm B}$ is not well-defined in non-cosmological simulations, and therefore we will use λ as defined in Equation (4.13).

The expected spin parameter of the remnant can be predicted from the ICs, using Equations (4.8) and (4.11). Comparing this to a direct calculation of the spin parameter of the remnant, we find the two agree to within 1 per cent. The orbital parameters κ and λ for all our simulations are shown in Fig. 4.11. We note that there are restrictions in this parameter space in low-κ/high-λ as well as in high-κ/high-λ regions. The former is because orbits become unbound as κ increases, while the latter is due to the amount of free energy available.

Since ϵ and λ are both measures of the angular momentum of the initial orbit, they will clearly be correlated. Fig. 4.12 compares the value of the two parameters, to clarify this relationship. Circularities are calculated assuming the orbital energy of the second halo is that of a point mass orbiting in the potential of the first halo. Note that circularity cannot be calculated for the higher energy orbits (since there is no bound circular orbit with the same energy), and therefore this plot contains only a subset of the simulations. Although ϵ and λ are (positively) correlated, there is also an energy dependence in both definitions; for the same angular momentum, spin increases with kinetic energy (and thus decreases with increasing κ).

4.4.2 Halo Alignment

Fig. 4.13 shows the final alignment of the halo remnants. Haloes were initially separated along the x-axis, and given an initial velocity in the x-axis (radial orbits) or in the y-axis

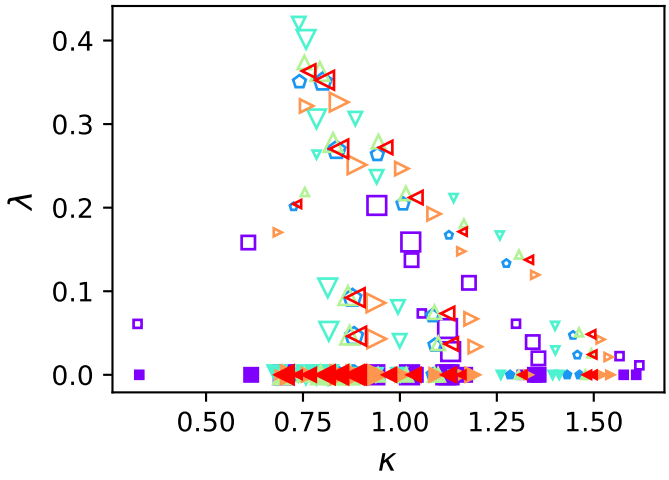

Figure 4.11: Dimensionless energy and spin parameters κ and λ, for the full set of simulations. Symbols are as in Fig. 4.3.

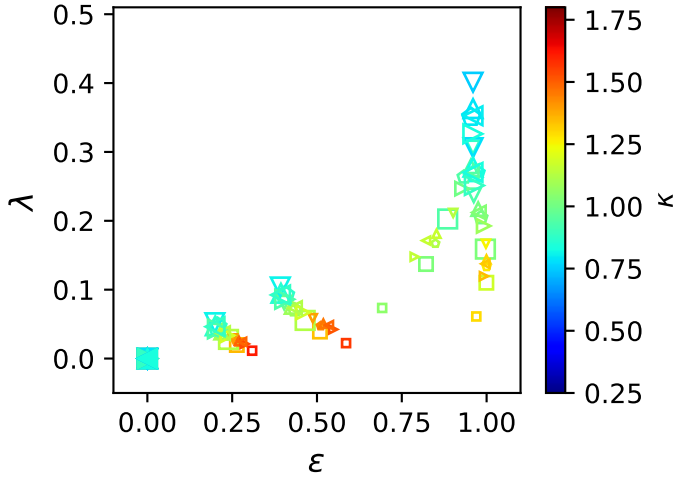

Figure 4.12: Spin parameter of the merger remnant, λ, versus the circularity of the initial orbit, ϵ. Symbols are as in Fig. 4.3.

(tangential orbits). Fig. 4.13 demonstrates that haloes on radial orbits have their major axis, a, aligned along the axis of the merger, x. The two other axes, b and c, lie in the y–z plane. On the other hand, for tangential orbits, axes a and b lie in the x–y plane, while the minor axis c points in the z direction. Clearly, the shape of the remnant is aligned with the direction of the merger as expected from previous works (e.g. Macciò et al., 2007; Vera-Ciro et al., 2011). Since it has been suggested that radial orbits produce prolate haloes, while tangential orbitals produce oblate haloes (e.g. Moore et al., 2004), there seems to be a link between halo orientation and shape. The effects of orbital parameters on halo shape will be explored further in Section 4.4.4.

4.4.3 Net Change in Halo Size

After the merger, we expect the remnant to be larger than either of the initial haloes, and possibly also elongated in the merger direction, at least in the case of more radial mergers. As a profile-independent measure of size, we define the 'radial extent' of a system (either the merger remnant, or an initial halo) to be the mean distance of all particles in the halo from the centre of the system, where the latter was determined as discussed in Section 4.3. Extents along the principal axes are defined similarly, as the mean distance projected on each axis. In Fig. 4.14 we show the radial extent of the merger relative to the radial extent of the ICs, as a function of κ. The size of the remnant, relative to the ICs, depends mainly on κ, though there is also a small dependence on the initial halo model. The EinLow simulations (squares) do not increase in size as much as the other initial halo models for high-energy (low κ) orbits. This may be because the EinLow ICs are very extended compared to the other models. The results go through the self-similar expectation for an equal mass merger, $\bar{r}/\bar{r}_0 = 2^{1/3}$ when $\kappa = 1$. If $\kappa > 1$ (more bound remnants), the remnant is smaller than expected in the self-similar case, and may even have a radial extent smaller than that of the initial haloes. If $\kappa < 1$ (less bound remnants), the remnant is larger than expected from self-similar scaling. There is little or no dependence on whether the orbit is radial or tangential, nor on the parameter $r_{\rm sep}$.

For $\kappa < 1$, we find that $\bar{r}/\bar{r}_0 \approx 2^{1/3}\kappa^{-5}$; this might be expected since the energy of a virialized self-similar halo scales as $M^2/r \sim r^5$, and therefore the change in halo radius scales as κ^{-5}. However, as the size of the halo decreases, the dependence on κ weakens; this may be because for these very low-energy orbits, the halo remnant is not self-similar to the ICs. The EinLow simulations also have a weaker dependence on κ, and this may once again indicate departures from self-similarity. We will explore the self-similarity between initial halo models and final remnants in Chapter 5.

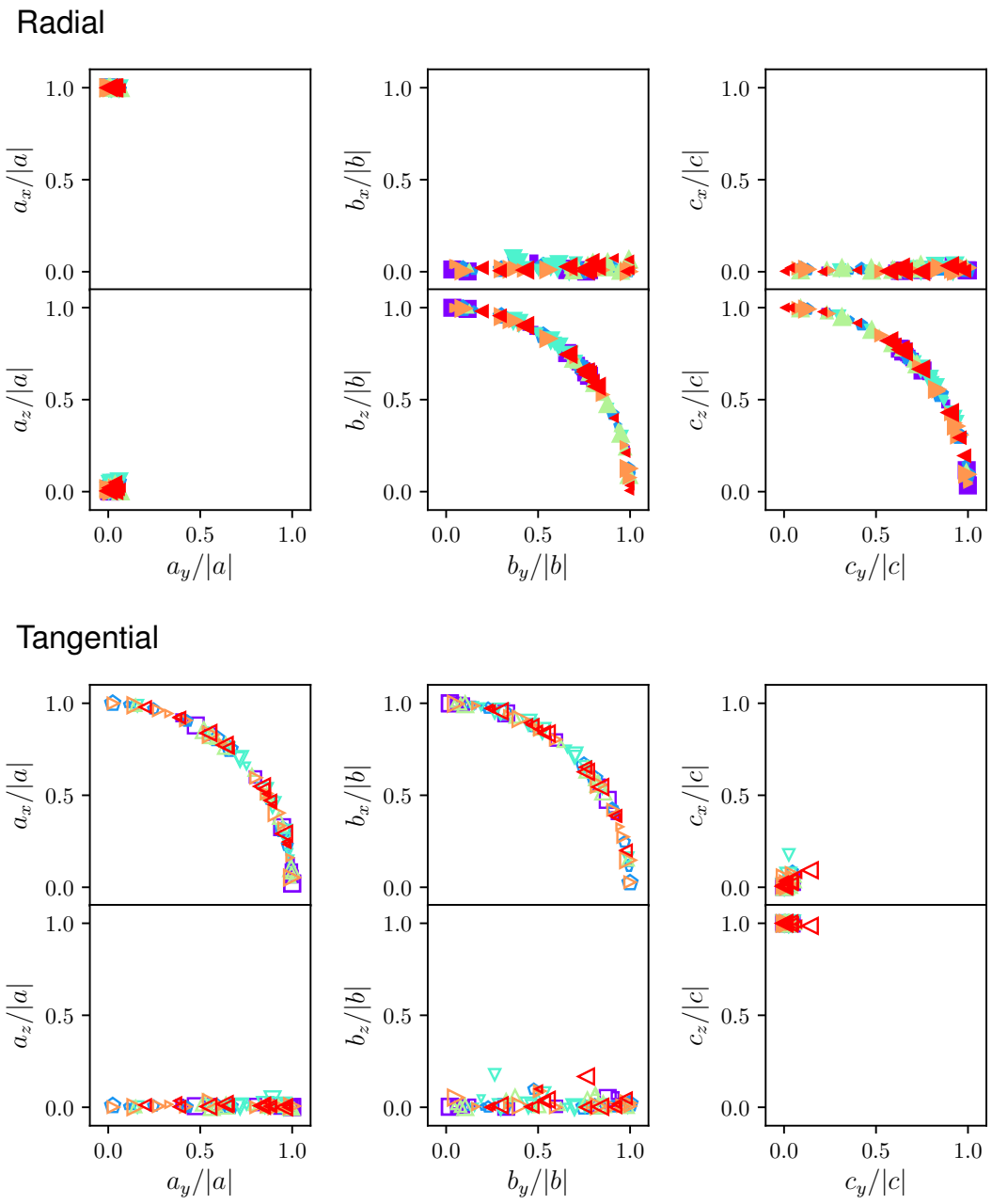

Figure 4.13: Normalized x, y and z-components of the normalized principal axes a, b and c of the remnants of halo mergers with either (top) radial or (bottom) tangential initial velocity, at the final time. Colours and symbols are as in Fig. 4.3.

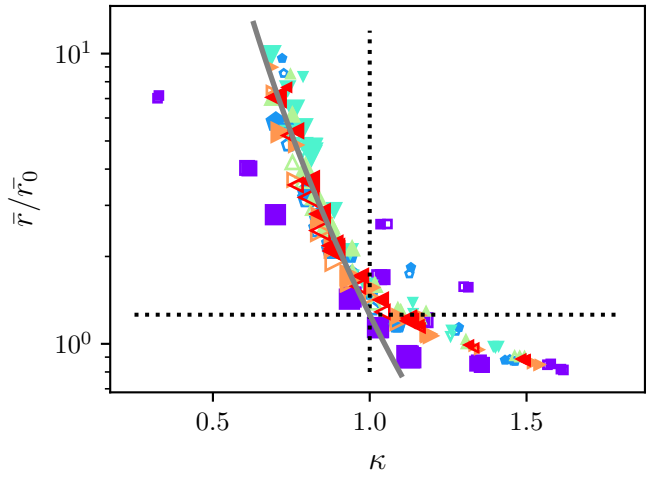

Figure 4.14: The mean radial extent of the remnant, $\bar{r}$, relative to the mean radial extent the initial halo models, $\bar{r}_0$, versus the energy parameter κ. The self-similar expectations are shown with dotted black lines. The solid gray line is when $\bar{r}/\bar{r}_0 = 2^{1/3}\kappa^{-5}$. Symbols and colours are as in Fig. 4.3.

Similar trends can be found when comparing the mean extent of the remnant projected along each of the principal axes (Fig. 4.15). Relative to the initial halo models, the size of the remnant is largest along the major principal axis a by definition. The extent of the halo along this axis increases slightly more than expected from self-similar scaling when $\kappa = 1$. We might expect the intermediate axis of the remnant, b, to be larger for tangential orbits than for radial orbits, because the orbit lies in the a–b plane; it seems, however, that b changes by roughly the same amount in radial and tangential cases, but that the minor axis c (perpendicular to the orbital plane) is smaller in tangential cases compared to radial cases.

We can derive a simple theoretical prediction for the expected size of the remnants along the major axis. In the spherical collapse model, when a cosmological overdensity collapses and virializes, the final radius of each shell is equal to half its radius at turnaround, as a consequence of energy conservation and the (scalar) virial theorem. By analogy, if the merger remnants in our simulations were to conserve the virial tensor component-wise, we might expect their extent along the major axis to be half the turnaround radius of the initial two-halo system, $r_{\rm TA}$. Since the virial radius should also increase by a factor of $2^{1/3}$ due to the extra mass in the system, however, we expect the virial radius along the longest axis to be $r_{\rm vir} \approx (r_{\rm TA}/2)2^{1/3} = r_{\rm TA}/2^{2/3}$.

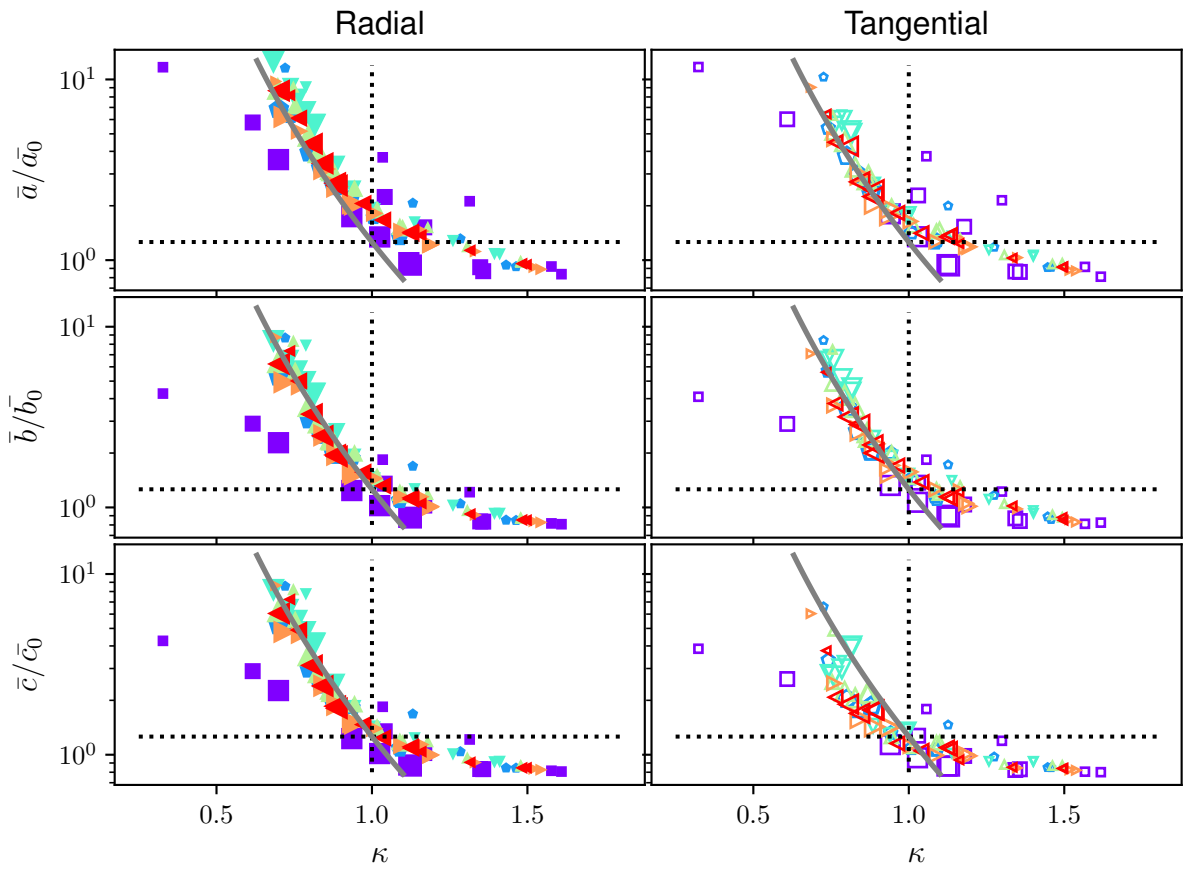

Figure 4.15: The change in the mean extent along the three principal axes, a, b and c, versus κ. The solid gray line is when the change in the mean extent is equal to $2^{1/3}\kappa^{-5}$. The self-similar expectations are shown with the dotted black lines. Symbols and colours are as in Fig. 4.3. The left- and right-hand panels are simulations with radial and tangential initial velocities, respectively.

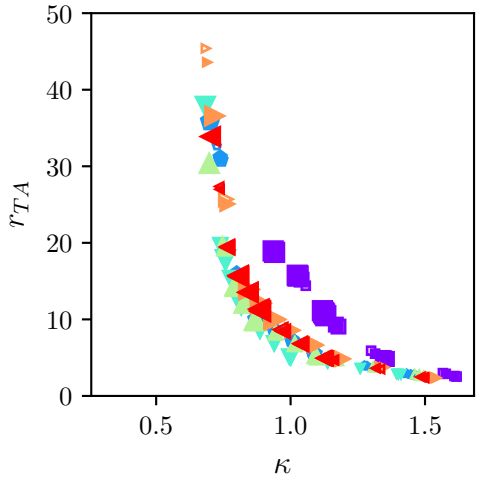

Figure 4.16: Turnaround radius as a function of κ. Symbols and colours are as in Fig. 4.3.

To determine the turnaround radius, we calculated $P_{\rm orb}(r)$ for each set of ICs by placing the two initial haloes a distance of r apart and calculating $P_{\rm orb} = P - 2P_0$, where the total potential P and internal potential energy of each halo, P_0, were calculated from Equations (4.6) and (4.3), respectively. The turnaround radius is then the radius such that $E_{\rm orb} = P_{\rm orb}(r_{\rm TA})$; i.e. the radius at which there is no kinetic orbital energy. This was determined by first smoothing $P_{\rm orb}(r)$, using a Gaussian filter, and then interpolating this smoothed potential to find $r_{\rm TA}$. Fig. 4.16 shows the turnaround radius as a function of κ. For high-energy orbits with small κ the turnaround radius is very large, but then it goes to zero for large κ.

To test the prediction that $r'_{\rm vir} \approx r_{\rm TA}/2^{2/3}$ along the largest axis, we assume that the virial radius scales as the average particle distance in the ICs, $\bar{r}_0$, and propose:

$$\frac{\bar{a}}{\bar{a}_0} = 2^{-2/3}\frac{r_{\rm TA}}{\bar{r}_0} \quad . \tag{4.15}$$

We compare the change in all three principal axes in Fig. 4.17. We find the extent along the largest axis, $\bar{a}$, does indeed scale as predicted, albeit with considerable scatter for large values of $r_{\rm TA}$. Since $r_{\rm TA}$ decreases exponentially with κ, the larger $r_{\rm TA}$ values are more sensitive to the interpolation used to estimate them, so this effect may be purely numerical. For the low-energy orbits (high κ, low $r_{\rm TA}$), the extents along the other axes b and c behave similarly to a, but for higher energy orbits, the change is smaller than our prediction.

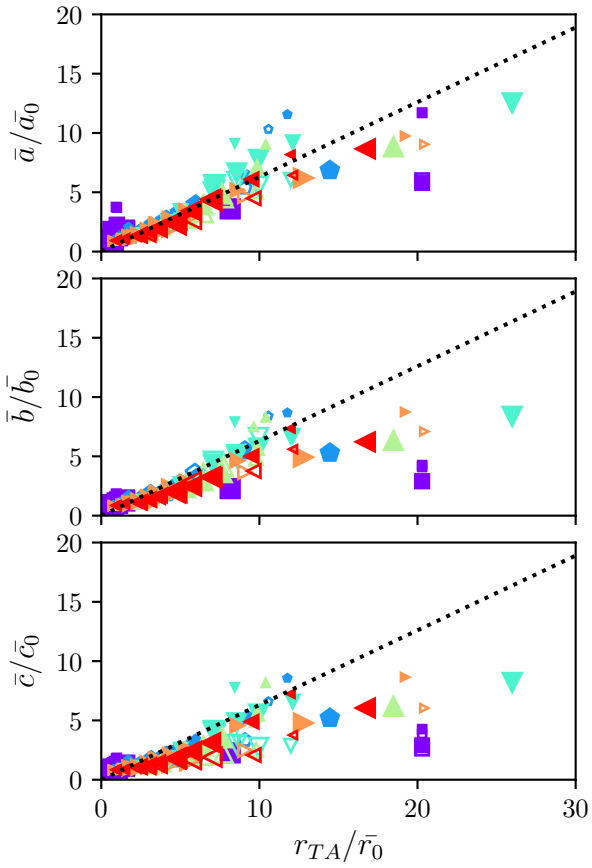

Figure 4.17: The size of the remnant versus the turnaround radius of the initial orbit. The size of the remnant is measured by the mean extent along the three principal axes, a, b and c, and the turnaround radius is normalized by the average radial extent of the initial halo. Dotted lines are the prediction from Equation (4.15). Symbols and colours are as in Fig. 4.3.

4.4.4 Net Change in Halo Shape

The axis ratios of the merger remnants were calculated as in Section 4.3.3 and are shown in Fig. 4.18. We emphasize that these measurements of principal axes sizes, a, b, and c are not the same as the extent, $\bar{a}$, $\bar{b}$, and $\bar{c}$, discussed in the previous section, which were calculated as the mean particle distance projected along the principal axes. The top and bottom panels of Fig. 4.18 are coloured by the relative energy parameter κ and spin parameter λ, respectively. Generally speaking, more bound remnants are also more spherical. The shape ratio c/a depends mainly on energy, and is smaller when κ is smaller (less bound haloes). The parameter c/b depends mainly on λ, and b/a depends on both κ and λ. There is little or no dependence on the IC models or on the parameter $r_{\rm sep}$ on the final shape of the remnant. Spin dictates whether the final remnant is prolate or oblate in shape; mergers on (low-spin) radial orbits produce prolate haloes with $c/b \approx 1$, while mergers on tangential (high-spin) orbits produce oblate haloes with $c/b \approx c/a$. For the largest spin values considered here, $c/b \approx c/a \approx 0.6$. Overall, these results are consistent with the two cases considered in Moore et al. (2004).

Fig. 4.19 shows the final shape parameters, c/a (top) and c/b (bottom) of the halo remnants as a function of κ and λ, respectively. We also show fits to the main trends:

$$c/a = 0.24\kappa + 0.47 \tag{4.16a}$$
$$c/b = -0.90\lambda + 0.96 \ . \tag{4.16b}$$

Alternatively, we could fit the inverse ratios a/c and b/c, since the axis c generally grows less than a or b after the merger. Fig. 4.20 shows these ratios, along with the fits:

$$a/c = -0.50\kappa + 1.91 \tag{4.17a}$$
$$b/c = 1.32\lambda + 1.03 \ . \tag{4.17b}$$

In the bottom panel of Fig. 4.19, it is a bit surprising that $c/b \neq 1$ in some cases, even when $\lambda = 0$. As discussed previously, by symmetry, one would expect $c = b$ for mergers on purely radial orbits. It seems likely that $c \neq b$ in practice for numerical reasons arising from the fact that the ICs are not perfectly symmetric. We expect this to be particularly true at high energies, where the simulation is sensitive to the direction of the initial velocity. Any noise or uncertainty in the shape measurement will result in an underestimate of c/b, since by definition $c < b$, and thus $c/b < 1$.

One implication of Equation (4.16a) is that for a self-similar change in energy, $c/a \approx 0.7$. To understand this, we can consider a self-similar radial merger between two spherical,

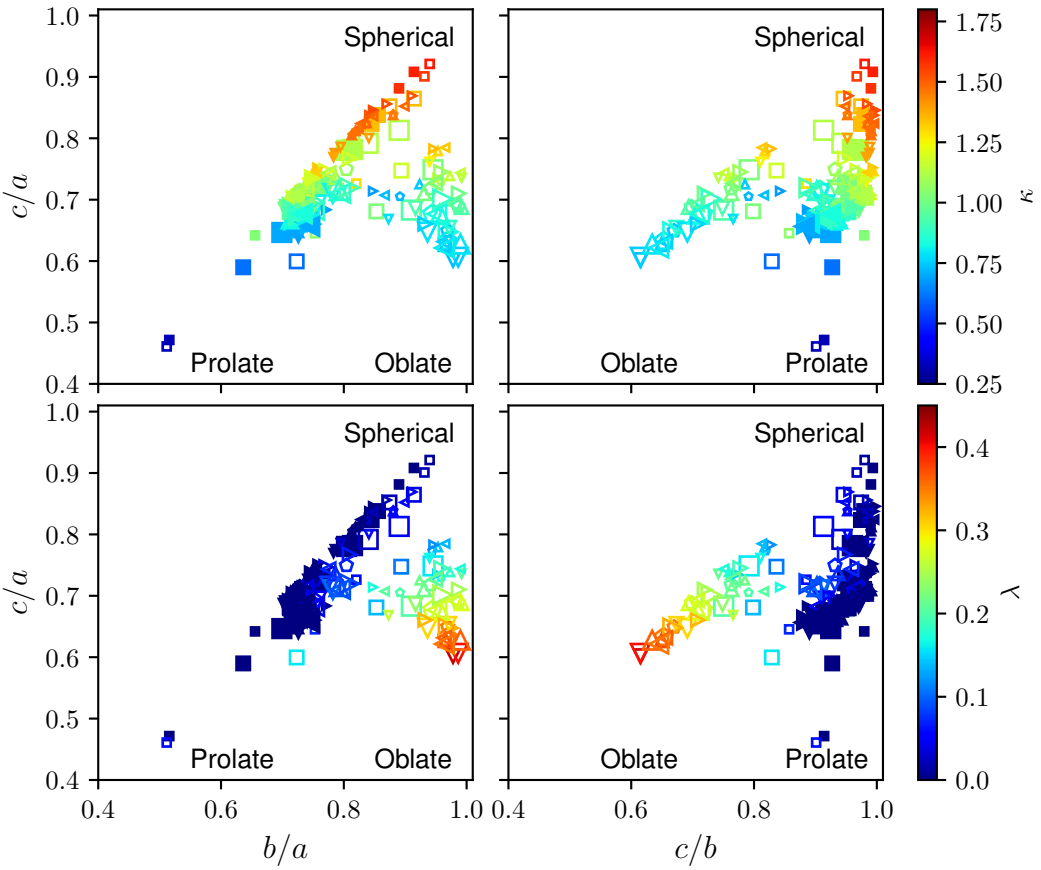

Figure 4.18: Remnant axis ratios c/a versus b/a (left) and c/a versus c/b (right), where $a > b > c$. Regions of parameter space corresponding to spherical, prolate and oblate haloes are labeled. The top panels are coloured by the relative energy parameter κ, and the bottom panels by the spin parameter, λ. Symbols are as in Fig. 4.3.

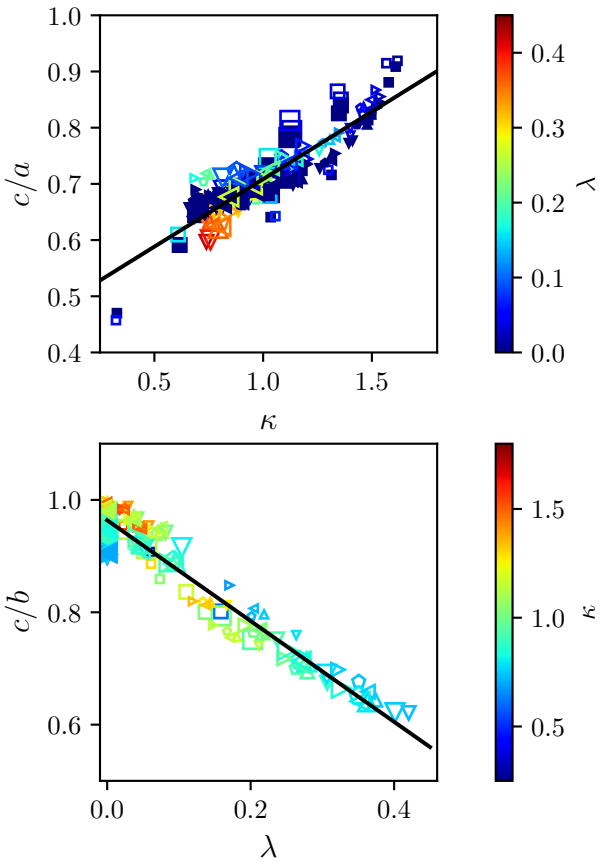

Figure 4.19: Remnant axis ratios c/a (top) and c/b (bottom) as a function of the relative energy parameter κ, and the spin parameter, λ, respectively. Symbols are as in Fig. 4.3. Fits to the average trends are given in the text; the RMS scatter with respect to each is approximately 0.03.

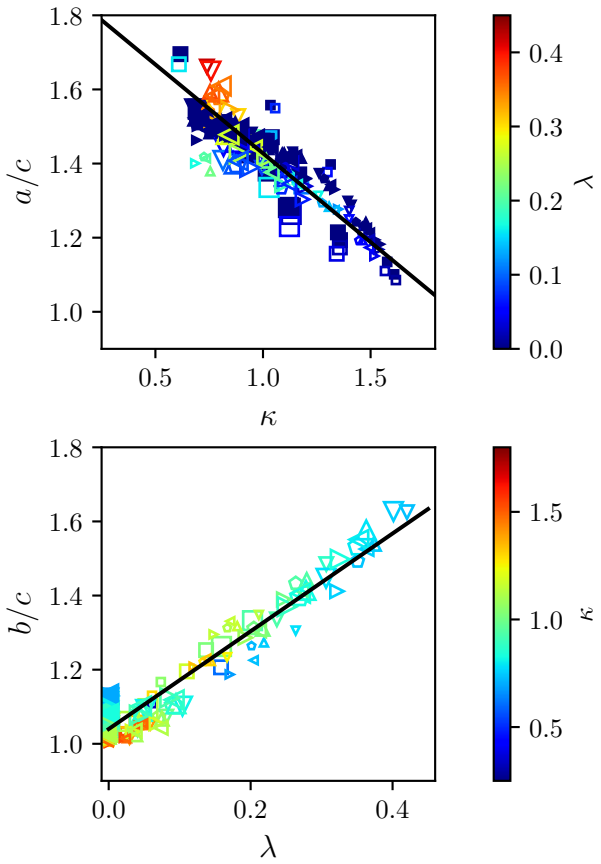

Figure 4.20: Remnant axis ratios a/c (top) and b/c (bottom) as a function of the relative energy parameter κ, and the spin parameter, λ, respectively. Symbols are as in Fig. 4.3. Fits to the average trends are given in the text; the RMS scatter with respect to each is approximately 0.07 (top) and 0.04 (bottom).

equal-mass haloes. In the self-similar case, the radius of the remnant should scale as $r'/r = 2^{1/3}$. Further, we will assume that the original size of the halo is x_0 along any of the principal axes, and that only the a axis increases in size, such that $a' = \beta x_0$, $b' = x_0$ and $c' = x_0$. Then,

$$\begin{aligned} \frac{r'}{r} = 2^{1/3} &= \sqrt{\frac{a'^2 + b'^2 + c'^2}{a^2 + b^2 + c^2}} \\ \Leftrightarrow 2^{2/3} &= \frac{\beta^2 + 2}{3}. \end{aligned} \tag{4.18}$$

Solving, we find $\beta \sim 1.66$, and thus $c/a = 1/\beta \approx 0.6$.

This predicts an axis ratio c/a slightly smaller than the one found; on the other hand, in the preceding derivation we assumed that all of the change in size occurred along the major axis, whereas the previous section showed that all axes grow to some degree, not just those in the plane of the merger.

Overall, for the range of orbital parameters we have tested, the axis ratios c/a and c/b scale roughly linearly with κ and λ. This simple result suggests that shape changes are relatively easy to understand, and that the details of the initial density profiles are not important, provided the internal energies of the initial haloes are appropriately accounted for.

4.5 Conclusions

We have performed a large number of idealized simulations of mergers between isolated haloes with realistic density profiles, to determine what dictates the structure of the remnant in major halo mergers. In this chapter, we describe our IC generation and convergence tests, and then consider the size and shape of the final remnant, which we find is reasonably well described by a triaxial ellipsoid with axes $a > b > c$. The shape of the remnant is mainly determined by the orbital parameters of the merger, the energy and angular momentum of the orbit controlling the axis ratios c/a and c/b, respectively. The size of the remnant depends mainly on the energy of the orbit, although there is some dependence on the initial halo profile as well. The overall spin of the remnant is also determined by the orbit, through conservation of angular momentum, though the remnant does not generally rotate as a solid body. The radial separation, $r_{\rm sep}$, and the initial velocity, v_0, do not have a direct effect on the size or shape of the final halo remnants.

We can interpret our results most simply in terms of the scaled energy parameter κ and the dimensionless spin parameter λ. The former is the net internal energy available

to the remnant, relative to its initial energy, and normalized by the overall scaling factor expected if the mean density is conserved while the mass doubles (cf. Equation (4.12)). The latter follows the usual cosmological definition (Equation (4.13)). In terms of these variables, we find that the minor-to-major axis ratio c/a scales roughly linearly with relative energy κ. Mergers with less (negative) total energy (i.e. low values of κ, equivalent to merging from large initial separations) produce more elongated remnants, while mergers from smaller initial separations produce rounder remnants. For the 'scale invariant' value $\kappa = 1$, mergers produce remnants with $c/a \sim 0.7$, as expected from a simple analysis of the energy available along each axis.

The minor-to-intermediate axis ratio c/b depends mainly on the angular momentum of the original encounter, scaling roughly linearly with the spin parameter λ. High spin mergers produce oblate, disky remnants that are almost axially symmetric. As the spin parameter decreases, the remnants become progressively more prolate, eventually becoming non-rotating, elongated objects in the limit of radial encounters.

These results are consistent with the previous study of Moore et al. (2004), which found that a radial merger produced a prolate remnant, while a more circular encounter produced a disky remnant, although we extend these results to a much wider range of ICs. Similarily, (McMillan et al., 2007) found that more radial orbits resulted in more prolate remnants. We find that the shape of the final remnant does not depend on the detailed density profile of the initial halo models; this is somewhat contrary to what was found by Fulton & Barnes (2001) and McMillan et al. (2007), who both suggest that shallow cusps produce prolate remnants, and steep cusps produce oblate remnants. This discrepancy is likely because even at fixed orbital energy, the scaled energy parameter κ will be different for different ICs if they have different internal energies. We suspect that comparing their results at the same value of κ would show no dependence of shape on the initial profile.

Interestingly, we have found that binary equal-mass mergers between spherical haloes rarely result in remnants with shape ratios less than 0.6, while cosmological haloes typically have shape ratio $c/a < 0.7$ (e.g. Jing & Suto, 2002; Allgood et al., 2006; Despali et al., 2014; Bonamigo et al., 2015). This could be because of the intrinsic initial shape of the density perturbations, or because multiple successive mergers often occur along the same filament. We wish to explore this further by considering mergers between two non-spherical haloes along their major axes. Since generating isolated ICs for non-spherical haloes is not straightforward, we can use the remnants from the binary mergers presented in this work as the new ICs, as proposed by Moore et al. (2004).

It should be emphasized that this work only considers equal-mass mergers, which are relatively rare. The rate of mergers per halo decreases with mass ratio, and 1:1 mergers are

expected to occur at a rate of approximately 0.1 mergers per unit redshift (Fakhouri et al., 2010); non-equal-mass mergers are thus much more common. It is therefore interesting to discuss briefly how our results are expected to extend to non-equal-mass mergers (this will also be the focus of a future study). The parameters λ and κ defined in this work can also be calculated for non-equal-mass mergers. Overall, we expect that the qualitative results found here will extend to non-equal-mass major mergers. Size should scale inversely with κ, c/a should scale with κ, and c/b should scale with λ. Additionally, the relations derived for the change in the size a in Equation (4.15), and the prediction for $c/a\,(\kappa = 1)$ in Equation (4.18) can be extended to non-equal-mass mergers. This implies, however, that the exact relationship between c/a and κ is dependent on the mass ratio of the merger. In the limit of a very large mass ratio, the larger halo will remain unaffected by the merger, and thus $c/a \approx 1$ when $\kappa = 1$.

Overall, there are several caveats to our conclusions. The first is that our ICs represent a great simplification of the typical cosmological situation. In a cosmological setting, haloes are almost never completely isolated, and major mergers between single pairs of haloes are rare. After initial experiments analyzing realistic mergers directly in their cosmological context, we reduced our study to the simplest possible configuration, finding that even simple mergers are complex enough to warrant separate treatment. In future work, we will consider how these results extend to more complicated merger situations such as multiple mergers, or smooth but anisotropic accretion, with the goal of understanding fully the dependence of halo shape on mass and environment that has been measured in cosmological simulations (e.g. Jing & Suto, 2002; Allgood et al., 2006; Maulbetsch et al., 2007; Despali et al., 2014; Lee et al., 2017; Vega-Ferrero et al., 2017).

Further, to apply our results to observations, we must also account for baryonic effects. These have been studied before in isolated mergers (Aceves & Velázquez, 2006; Kazantzidis et al., 2006). These authors found that the shape of the final merger remnant within the virial radius was similar, whether the merger was simulated using dark matter only, or in full hydrodynamic simulations including baryons. More generally, some hydrodynamic simulations find that baryons make haloes rounder at small radii (e.g. Butsky et al., 2016), while others find that they have less effect, at least on cluster scales (e.g. Sereno et al., 2018), so further work on this subject is needed.

Since observations are beginning to place constraints on the shapes of individual galaxy clusters, this is an obvious area in which to pursue the development of next-generation cosmological tests based on structural properties. It would also be interesting to split cluster samples by projected or 3D shape, and compare their mean galaxy content and substructure, to establish a connection between final states and past merger history, for large numbers of systems. Shape and internal structure may also be relevant in understanding

the X-ray scaling relations, using the offset from the mean relations versus shape as a probe of how cluster thermodynamics evolve after a major merger (e.g. Poole et al., 2007). Finally, in the longer term, the structural properties of individual haloes may be used to probe the statistics of the surrounding density field, including both the spatial anisotropy of the region around the local density peak, and the angular momentum distribution of this region. These properties of the density field should in turn be sensitive to non-Gaussianity and other more subtle aspects of structure formation.

The results presented in this chapter should form the basis for a full model of how a halo's shape changes as it grows through mergers and accretion. Such a model may in turn allow semi-analytic predictions of the full distribution of halo shapes as a function of cosmological parameters. In the shorter term, we will use the ICs and analysis tools established here to study the evolution of the density profile and the concentration parameter in major halo mergers. This will be the subject of Chapter 5.

Chapter 5

Major Mergers Between Dark matter Haloes – II. Profile and Concentration Changes

5.1 Introduction

Dark matter haloes play a central role in our current understanding of cosmological structure formation, being the site of all visible galaxy formation. While observational tests including galaxy kinematics (e.g. Ouellette et al., 2017), satellite kinematics (e.g. Guo et al., 2012) and weak and strong gravitational lensing (e.g. Umetsu et al., 2016) place important constraints on halo properties, most of our detailed knowledge of halo structure comes from numerical simulations. A remarkable property of dark matter haloes discovered in cosmological simulations is the existence of a nearly universal density profile, regardless of mass or cosmological model (Navarro et al., 1996, 1997), commonly approximated by the Navarro–Frenk–White (NFW) form,

$$\rho(r) = \frac{\rho_0 r_\mathrm{s}^3}{r(r+r_\mathrm{s})^2} \quad , \tag{5.1}$$

where ρ_0 is a characteristic density and r_s is the scale radius, describing the point where the logarithmic slope is $\mathrm{d}\ln\rho/\mathrm{d}\ln r = -2$. Though NFW profiles are still commonly used in the literature, dark matter halo density profiles are slightly better described by Einasto profiles (e.g. Navarro et al., 2004; Gao et al., 2008; Klypin et al., 2016), which can be

expressed as:

$$\rho(r) = \rho_{-2} \exp\left(-\frac{2}{\alpha_E}\left[\left(\frac{r}{r_{-2}}\right)^{\alpha_E} - 1\right]\right) \quad , \tag{5.2}$$

where α_E is the Einasto shape parameter and r_{-2} is the radius where the logarithmic slope is -2.

The mean density of dark matter haloes within their outer, virial boundary scales with the mean or critical background density at the epoch at which they are observed, but is the same for all haloes at that epoch, independent of mass or growth history. On the other hand, the central densities of haloes at any one epoch can vary considerably, depending on their concentration. The concentration parameter c was originally defined in terms of the NFW density profile as $c = r_{\rm vir}/r_{\rm s}$, where $r_{\rm vir}$ is the virial radius. This definition can be extended to the Einasto profile by taking $r_{\rm s} = r_{-2}$; this definition does not capture the effects of α_E on the central density of the halo (Klypin et al., 2016), however. An alternative, profile independent, definition of concentration is based on the ratio of the maximum circular velocity to the virial velocity $v_{\rm peak}/v_{\rm vir}$ (Prada et al., 2012; Klypin et al., 2016), which is monotonically related to the original definition of c.

For an individual halo, the evolution of the concentration parameter is linked to the halo's merger history (e.g. Navarro et al., 1997; Bullock et al., 2001a; van den Bosch, 2002; Zhao et al., 2009; Wong & Taylor, 2012; Klypin et al., 2016). These previous studies have established that haloes undergo two main phases of mass accretion. In the first, rapid phase, the concentration parameter remains roughly constant, with a value of $c \approx 3$. In the second, slow phase, the concentration parameter grows as the virial radius increases while the scale radius remains fixed. The increase in mass and concentration during this second phase is mainly due to the decreasing reference density, and is therefore sometimes referred to as pseudo-evolution (e.g. Diemer et al., 2013). Averaged over many systems, these patterns give rise to the mean concentration–mass–redshift relation, in which concentration generally decreases with increasing mass (e.g. Navarro et al., 1996, 1997; Jing, 2000; Bullock et al., 2001a), except at the largest masses, where velocity-based definitions can increase again (e.g. Klypin et al., 2016).

An important implication of previous measurements of the concentration–mass–redshift relation is that the inner scale radius must increase as haloes grow. In cosmological simulations, the median concentration of haloes of a given mass evolves with redshift as $c \sim c_0(1+z)^{-1}$, as first demonstrated by Bullock et al. (2001a), or possibly as $c \sim c_0 \rho_c^{-1/3}$, (where ρ_c is the critical density of the universe), as pointed out by Pilipenko et al. (2017). This would correspond to the scaling of the virial radius for an object whose mass did not increase with redshift, that is for an isolated system surrounded by a void. Haloes never

exist in complete isolation, however; as the virial radius increases, it will enclose more matter, increasing both the total mass and the virial radius further. Thus, the net growth will go as $r_{\rm vir} \propto (M_{\rm vir}/\rho_c)^{1/3}$. For concentration to scale as $c \propto \rho_c^{-1/3}$, the scale radius must therefore increase as $M_{\rm vir}^{1/3}$ as well. A similar conclusion was reached by Zhao et al. (2003), who showed directly that $r_{\rm s}$ increases during the period of rapid accretion. Provided $r_{\rm s}$ increases as $M_{\rm vir}^{1/3}$, the density at or within one scale radius will remain constant, while the density within a *fixed physical* radius increases.

This prediction seems puzzling given several other pieces of evidence that central density must decrease as haloes grow. The first was discovered by Nusser & Sheth (1999), who showed that in the absence of any rearrangement of the pre-existing material, accretion onto the outside of a halo would produce a structure with a central density much higher than that of haloes in cosmological simulations. A second piece of evidence comes from simulations of the first haloes by Ishiyama (2014). Evolving these down to a final redshift of $z = 32$, he found central densities that were once again much higher at fixed physical radius than expected from extrapolations of the low-redshift concentration–mass–redshift relations; if these densities are conserved, they would increase estimates of the boost factor by up to two orders of magnitude (Okoli et al., 2018). From both these studies, the implication is that there must be some mechanism that rearranges the central parts of haloes, causing the mass distribution to expand, and decreasing the central density. Given the work of Nusser & Sheth (1999), this mechanism must be distinct from slow accretion and associated with periods of rapid growth; thus major mergers seem an obvious candidate.

Isolated major mergers between otherwise undisturbed systems are rare in a cosmological context, and thus the effects of major mergers are best studied through controlled simulations of isolated systems (e.g. Boylan-Kolchin & Ma, 2004; Aceves & Velázquez, 2006; Kazantzidis et al., 2006; McMillan et al., 2007; Zemp et al., 2008; Vass et al., 2009; Ogiya et al., 2016; Drakos et al., 2019). Most authors find that haloes are robust to major mergers; in particular, it appears that the slope of the steepest density profile is preserved (Boylan-Kolchin & Ma, 2004; Aceves & Velázquez, 2006; Kazantzidis et al., 2006; Zemp et al., 2008; Vass et al., 2009), and there is also some suggestion that concentration does not change (Kazantzidis et al., 2006). However, the simulations of Moore et al. (2004) suggest that concentration can decrease in major mergers, provided the initial encounter has sufficient angular momentum. Furthermore, the simulations of Ogiya et al. (2016) suggest that if the inner slopes of the dark matter haloes are particularly steep (as in the case of primordial haloes), major mergers can also cause a decrease in the inner slope (again with some orbital dependence).

In Chapter 4, we performed a large number of isolated major merger simulations, covering a wide range of initial halo models and orbital parameters to study how the spin,

size, and 3D shape of merger remnants depend on the initial conditions (ICs) and the orbital parameters describing the encounter. We showed that the spin and shape of merger remnants depend mainly on the angular momentum and energy of the merger. In this chapter, we will consider how the characteristic radii, density profile, and concentration parameter depend on orbital properties and ICs. Our main goal is to determine whether major mergers are a viable mechanism for increasing scale radius and/or decreasing central density, and if so, under which conditions.

The outline of the chapter is as follows: in Section 5.2, we briefly review our method for generating ICs, and the merger simulations from Chapter 4. In Section 5.3, we examine the overall behaviour of the density profile and various characteristic radii. In Section 5.4, we show the results of fitting analytic density profiles to the remnants, and in Section 5.5, we consider the implications for the concentration parameter. We summarize and discuss our results in Section 5.6.

5.2 Simulations

In this section we briefly outline the merger simulations. For a more detailed explanation of the simulations, see Chapter 4.

5.2.1 Initial Profile Models

The halo ICs (ICs) were created using the public code ICICLE (Drakos et al., 2017). We considered six different halo models. Two were NFW models truncated using an exponential cut-off (NFWX), and two were NFW models truncated by iteratively removing unbound particles outside a specified radius (NFWT). The last two models were Einasto profiles (Ein), one with a low shape parameter $\alpha_E = 0.15$, and one with a high shape parameter $\alpha_E = 0.3$. These values of α_E span the range found in cosmological simulations by Gao et al. (2008). The Einasto profiles were not truncated, as the total mass converges to a finite value with increasing radius. The properties of the profiles are summarized in Table 5.1. The simulation units were chosen so that the gravitational constant G, the peak circular velocity, $v_{\rm peak}$, and the radius at which the circular velocity peaks, $r_{\rm peak}$, are all unity. Setting $G = M_{\rm peak} = r_{\rm peak} = 1$ produces a time unit $t_{\rm unit} = \sqrt{r_{\rm peak}^3/GM_{\rm peak}}$, a density unit $\rho_{\rm unit} = M_{\rm peak}/r_{\rm peak}^3$, and an energy unit $E_{\rm unit} = GM_{\rm peak}^2/r_{\rm peak}$.

Table 5.1: Summary of IC properties. The columns list (1) the name of the IC, (2) the number of particles N, (3) the parameters used to construct the IC, and (4) the total internal energy of the IC, E_0.

Initial condition name	N	Parameters	$E_0/E_{\rm unit}$
EinLow	5×10^5	$\alpha_E = 0.15$	-2.2
EinHigh	5×10^5	$\alpha_E = 0.3$	-1.2
NFWT10	$\sim 3.2 \times 10^5$	$r_{\rm cut} = 10$	-1.0
NFWT15	$\sim 3.5 \times 10^5$	$r_{\rm cut} = 15$	-1.3
NFWXSlow	5×10^5	$r_{\rm vir} = 10$, $r_{\rm d} = 2\,r_{\rm s}$	-1.6
NFWXFast	5×10^5	$r_{\rm vir} = 10$, $r_{\rm d} = 0.2\,r_{\rm s}$	-1.5

5.2.2 Orbits

For each of the six density profiles, we simulated encounters between two identical haloes with that profile, the first initially at rest and the second on a specific initial orbit. We considered 29 different orbits: 15 with a purely radial (R), and 14 with a purely tangential (T) initial velocity in the frame of the first halo. The haloes had an initial separation of $r_{\rm sep} = 2$, 5, or $10\,r_{\rm peak}$ and an initial velocity of $v_0 = 0.1$, 0.2, 0.6, 0.8 , or $1.2\,v_{\rm esc}$, where $v_{\rm esc}$ is the escape speed of a point mass located at $r_{\rm sep}$. For $v_0 = 1.2\,v_{\rm esc}$, tangential orbits do not produce a bound remnant, so we did not simulate tangential orbits with this highest velocity. As described in Chapter 4, the merger simulations were run in GADGET-2 (Springel, 2005) using a softening length of $\epsilon = 0.02\,r_{\rm peak}$. The centre of the remnant halo was found by calculating the centre of mass within increasingly smaller spheres.

In Chapter 4, we found that the 3D shape of the final merger remnant depends on the energy and angular momentum of the initial orbit. The dependence is simplest when expressed in terms of dimensionless energy and spin parameters κ and λ:

$$\begin{aligned} \kappa &= \frac{E_0'}{E_0}\left(\frac{M}{M'}\right)^{5/3} \\ \lambda &= \frac{\sqrt{|E_0'|}}{GM'^{5/2}}|\mathbf{J}'| \quad . \end{aligned} \tag{5.3}$$

Here E_0' and E_0 are the internal energies of the remnant and of the initial halo, while M' and M are their respective masses. The definition of the energy parameter includes the factor $(M/M')^{5/3}$, since the energy scales as $E_0 \propto M^2/r \propto M^{5/3}$ for 'self-similar' growth, that is growth that conserves the mean density and the form of the density profile, as explained in Chapter 4. Given this definition, $\kappa = 1$ corresponds to a final remnant that is

self-similar to the ICs, $\kappa < 1$ indicates that the remnant is less bound than the progenitor, and $\kappa > 1$ indicates it is more bound. The dimensionless spin parameter follows the definition of Peebles (1969), as discussed in Chapter 4.

The range of κ and λ used is shown in Fig. 5.1. In this space, there is a natural restriction on the spin parameter for both small and large values of κ. For small values of κ, orbits with larger λ values become unbound, while large κ simulations correspond to tightly bound orbits with small radial separations and velocities, so the range of λ is also limited.

Conveniently, both κ and λ can be calculated directly from the ICs using conservation laws. Specifically, the angular momentum $\mathbf{J}'$ and internal energy E_0' of the remnant can be calculated given the radial separation $r_{\rm sep}$, the initial velocity v_0, the orbital energy $E_{\rm orb}$, the internal energy of the initial halo E_0 and the mass of the initial halo M:

$$\begin{aligned} \mathbf{J}' &= M\mathbf{r}_{\rm sep} \times \mathbf{v_0} \ , \\ E_0' &= E_{\rm orb} + 2E_0 - \frac{1}{4}Mv_0^2 \ . \end{aligned} \tag{5.4}$$

In Chapter 4, it was found that E_0' and J' calculated in this manner agreed to a direct calculation to within 2 per cent and 0.5 per cent, respectively.

5.3 Net Change in the Mass Distribution

In this section, we explore how the density profile changes going from the IC to the final remnant. As in Chapter 4, the properties of the final remnant are measured at time $300\,t_{\rm unit}$, by which time it has fully relaxed.

5.3.1 General Results

In Fig. 5.2 we show the final density profiles of the remnants, compared to the initial halo models (dashed grey lines). The density increases at any given radius for all remnants, which is perhaps not surprising given the total mass of the system has doubled. We also show the initial profiles with the radii scaled by $2^{1/3}$ (dotted black lines); this is the scaling expected for self-similar evolution in an equal-mass merger, since it will conserve the mean density as the mass doubles.

The final remnants have been coloured by the relative energy parameter, κ. At small radii, the changes in the profile compared to the scaled ICs are subtle, and the inner

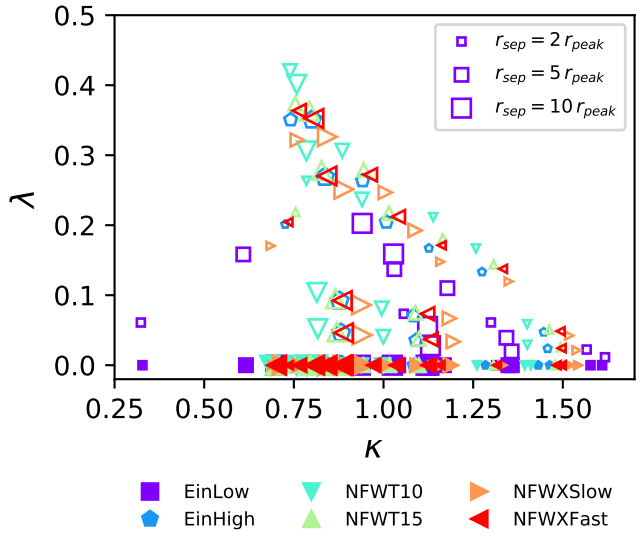

Figure 5.1: The range of orbital parameters used in the simulations. The orbital parameters are the energy parameter κ (which expresses the change in internal energy from the ICs to the final remnant, relative to the self-similar value for a binary merger), and the spin parameter, λ. Open points indicate tangential initial velocities, and filled points denote radial initial velocities. The size of the symbols corresponds to the initial radial separation, $r_{\rm sep}$.

slope is roughly conserved, in agreement with previous studies (Boylan-Kolchin & Ma, 2004; Aceves & Velázquez, 2006; Kazantzidis et al., 2006; Zemp et al., 2008; Vass et al., 2009). At large radii, the changes in the density profile are more obvious, as mass has moved outwards, relative to the scaled ICs. (Admittedly, some of this is likely due to the artificially truncated nature of the ICs.) The panels have been divided into orbits with radial (R) or tangential (T) initial velocities; as shown in Chapter 4, these orbits should produce remnants with different 3D shapes. Interestingly, orbital angular momentum has little effect on the spherically averaged density profile. There does, however, seem to be a systematic change in the density profile with κ; remnants of low κ encounters have more power-law like profiles (low Einasto alpha parameters), whereas remnants of high κ encounters have more sharply truncated profiles (high Einasto alpha parameters).

Since the change in the density profile is difficult to see, particularly at small radii, in Fig. 5.3 we also plot the enclosed mass fraction within a given radius versus the mean density within that radius. Note that the direction of the x-axis has been reversed here, since large densities correspond to small radii. In this plot it is clear that the mass distribution changes even at small radii. The remnants evolve in a monotonic sequence with κ, with higher κ values producing denser remnants at all mass fractions. Again, we find little dependence on the angular momentum of the orbit. Comparing to the ICs, the final remnant curves lie roughly either inside or outside the IC curve, with the divide occurring at the self-similar energy, $\kappa = 1$. Sharply truncated profiles, such as NFWXFast, produce remnants with more diffuse outer regions, even for $\kappa = 1$. In a few instances, the remnant curves also cross over the ICs, or over curves of higher or lower κ, but it is not clear whether this behaviour is robust to changes in resolution.

Overall, it appears that the density profiles of the haloes evolve in a straightforward way that is mainly dependent on κ. In general, some mass is ejected to large radii, but the central density does not decrease significantly compared to predictions from self-similar scaling. Surprisingly, there is little difference between the remnants produced by radial and tangential encounters. One implication is that the spherically averaged density profile of a remnant is unrelated to its 3D shape, as we showed in Chapter 4 that the shape of the halo *does* vary with the angular momentum of the encounter.

5.3.2 Evolution of Structural Parameters

Haloes do not typically have sharp boundaries, and therefore their sizes are not well defined. One convenient measure of the size of extended systems is the gravitational radius, which

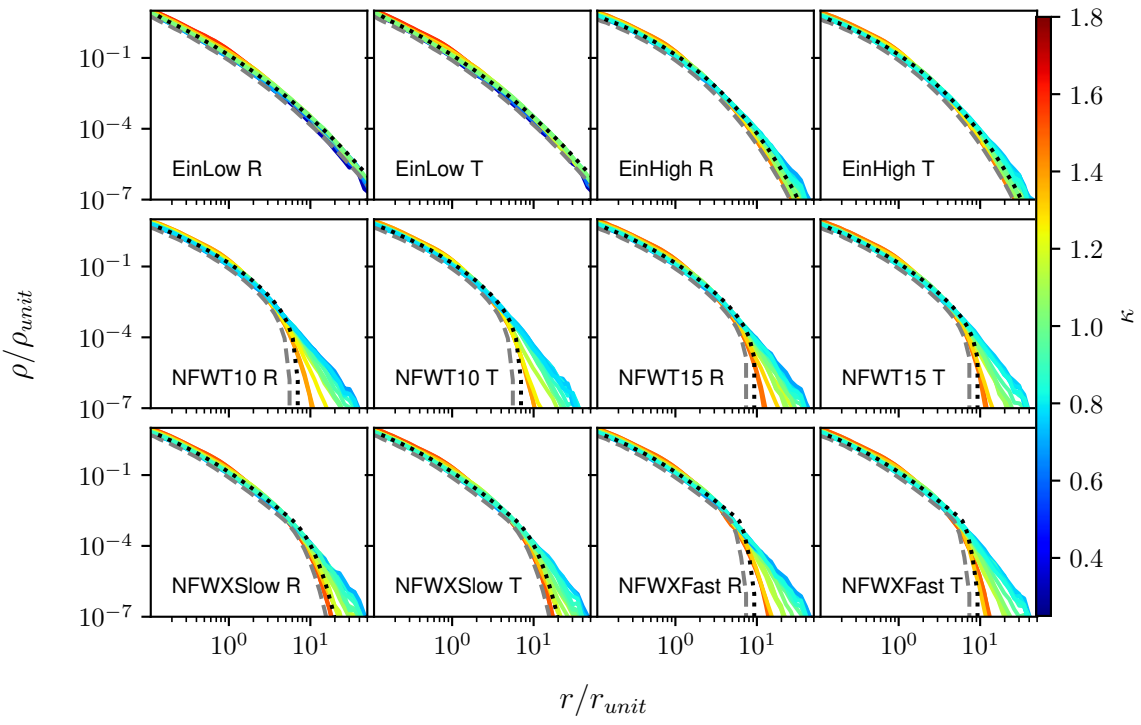

Figure 5.2: Density profiles of the halo remnants. The dashed grey lines show the initial halo models, and the dotted black lines are the ICs with the radius rescaled by a factor of $2^{1/3}$, as expected for a self-similar equal-mass merger. The labels indicate the initial halo models, as well as whether the initial velocity was tangential (T) or radial (R). The remnants are coloured by the relative energy change, κ.

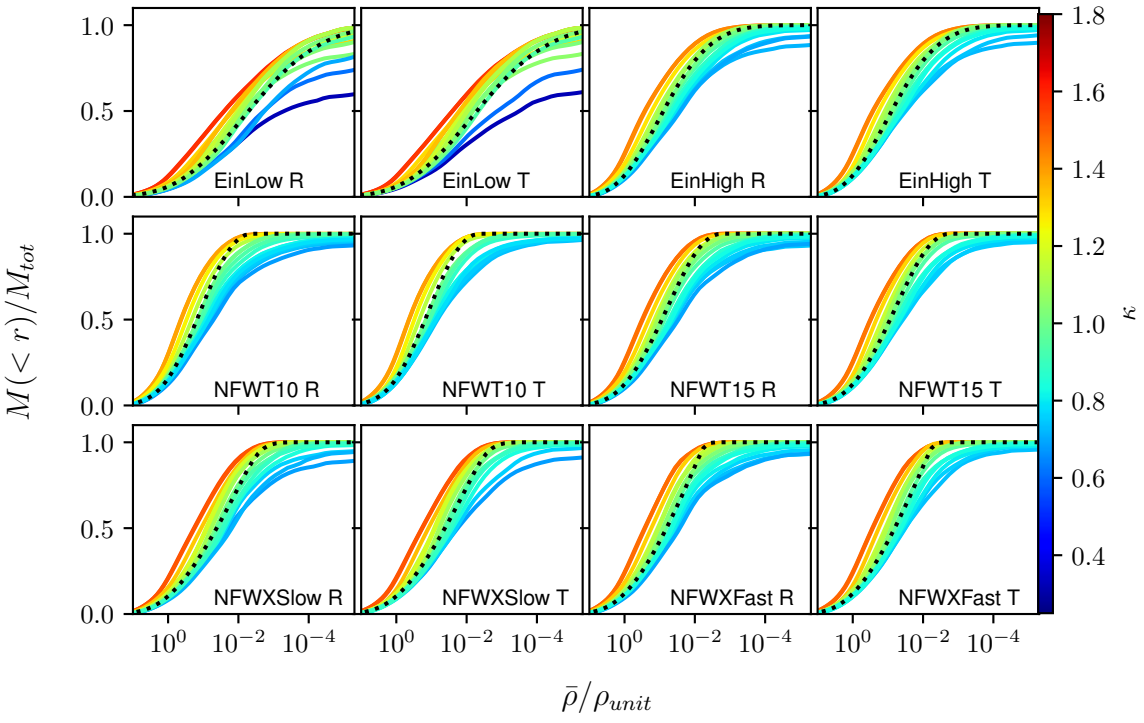

Figure 5.3: The enclosed mass fraction within a given radius in the merger remnant, versus the enclosed mean density within that radius. The initial haloes are shown with dotted black lines. Labels indicate the IC model, and whether the initial velocity was purely tangential (T) or purely radial (R). The curves are coloured by the relative energy change κ, which indicates the change in internal energy relative to scaled ICs. Note that density increases to the left on the horizontal axis, to match the orientation of Fig. 5.2, with larger radii to the right.

is defined as:

$$r_{\rm g} \equiv \frac{GM^2}{|P|} \ , \tag{5.5}$$

where P is the potential energy of the system. For a virialized halo, $\langle v^2 \rangle = GM/r_{\rm g}$. In practice, however, the potential energy is difficult to measure. Therefore, the half-mass radius, $r_{1/2}$, the radius enclosing half the mass of the halo, is a more convenient quantity to characterize halo size. As discussed in Binney & Tremaine (1987), $r_{1/2}$ is typically proportional to $r_{\rm g}$, and $r_{1/2}/r_{\rm g}$ can range from about 0.4 to 0.5 depending on the system's density profile; thus in general we can estimate that $r_{1/2}/r_{\rm g} \approx 0.45$ to good approximation.

For the work presented here, $r_{\rm g}$ is a useful quantity since it is closely related to the relative energy change, κ. For a virialized halo, $P = 2E_0$, and thus $r_{\rm g} \propto M^2/E_0$. Given our previous definition of the relative energy change,

$$\kappa = \frac{E_0'}{E_0} \left(\frac{M}{M'} \right)^{5/3} \ , \tag{5.6}$$

and the fact that the initial and final haloes are in virial equilibrium, we have:

$$\frac{r_{\rm g}'}{r_{\rm g}} = \frac{1}{\kappa} \left(\frac{M'}{M} \right)^{1/3} = \frac{2^{1/3}}{\kappa} \ . \tag{5.7}$$

We verify this prediction in the left-hand panel of Fig. 5.4 by calculating the gravitational radius directly from Equation (5.5), and find that it does indeed scale with $1/\kappa$ as expected. This relationship shows that larger values of κ (mergers between more highly bound pairs, where the total energy is more negative) result in less diffuse structures. The middle panel of Fig. 5.4 shows how the change in half-mass radius varies as a function of κ. There is a monotonically decreasing relationship between κ and $r_{1/2}'/r_{1/2}$, though it shows more scatter than the relationship between $r_{\rm g}'/r_{\rm g}$ and κ. The dotted lines show where $r_{1/2}'/r_{1/2} = 2^{1/3}$, as expected for self-similar evolution. The prediction from Equation (5.7), assuming $r_{1/2}$ is proportional to $r_{\rm g}$, is also shown (red dashed line). The solid black line is a fit to the data, $r_{1/2}'/r_{1/2} = 1.2\kappa^2 - 3.9\kappa + 3.9$; the RMS scatter with respect to this fit is 0.06.

We see that the simulation results go through the self-similar expectation at $\kappa = 1$. They also agree with the prediction from Equation (5.7), except at low κ (less bound mergers). To see why this is, in the right-hand panel of Fig. 5.4 we show $r_{1/2}'$ vs r_g'. The dotted line corresponds to $r_{1/2} \approx 0.45 r_{\rm g}$. For the most part, the remnants obey the expected relationship, with the exception of two points, corresponding to the simulations

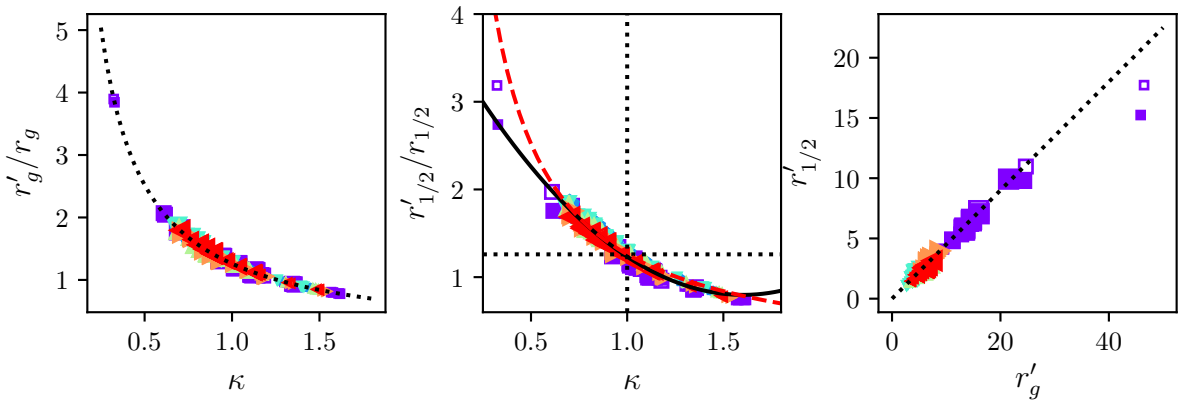

Figure 5.4: (Left) The gravitational radius as a function of the relative energy change κ. The dotted black line is the theoretical expectation, $r_{\rm g} \propto 1/\kappa$. (Middle) The relative change in the half-mass radius, $r'_{1/2}/r_{1/2}$, as a function of the relative energy change κ. The black dotted lines show the expected values for self-similar evolution of the density profile. The red dashed curve is the theoretical expectation if $r_{1/2}$ is proportional to $r_{\rm g}$. The solid black line is a fit to the data, $r'_{1/2}/r_{1/2} = 1.2\kappa^2 - 3.9\kappa + 3.9$. (Right) The half-mass radius versus the gravitational radius. The dotted line corresponds to $r_{1/2} = 0.45\, r_{\rm g}$. Colours and symbols are as in Fig. 5.1.

with the lowest κ values. This deviation from the expected relationship may indicate a departure from self-similarity.

While $r_{\rm g}$ and $r_{1/2}$ are useful for describing how the size of a halo changes in a major merger, concentration measurements typically depend on a characteristic scale radius, r_{-2} and the virial radius, $r_{\rm vir}$, or possibly on the peak of the circular velocity curve, $v_{\rm peak}$ and the circular velocity at the virial radius, $v_{\rm vir}$. The scale radius, r_{-2} (the radius at which the logarithmic slope of the density profile is -2), is difficult to measure accurately, since it requires numerical differentiation; to help with this, we apply a Gaussian smoothing kernel with a $\sigma = 0.1 \ln r_{\rm peak}$ to the derivative of the profile $\mathrm{d}\ln\rho/\mathrm{d}\ln r$. We note, however, that the resulting value of r_{-2} is somewhat sensitive to the degree of smoothing, and thus we expect some scatter in the results. In the next section, we will also measure r_{-2} using the more commonly employed method of profile fitting, and compare the results to those obtained here in Appendix D.

Despite the greater scatter in the measurements, Fig. 5.5 shows a clear trend in the scale radius with κ. Unlike $r_{\rm g}$ or $r_{1/2}$, however, changes in r_{-2} generally *increase* with increasing κ, matching the self-similar prediction at $\kappa = 1$ (black dotted lines). The solid black line is a fit to the simulation results, $r'_{-2}/r_{-2} = 0.80\kappa + 0.38$. This fit has an RMS scatter of 0.3, although the scatter is smaller for $\kappa < 1$ and much larger for $\kappa > 1$. Interestingly, the lower κ mergers seem to leave the scale radius, r_{-2}, unchanged, or even decrease it slightly. This is surprising, since these correspond to more 'violent' encounters with more initial kinetic energy. Naively, these mergers might be expected to heat up the central parts of the haloes, producing a remnant with lower central density and a larger scale radius. Fig. 5.3 shows that while the profile of the remnant has expanded relative to the self-similar prediction, the resulting density change is much larger at large radii than at small radii. As a result, the scale radius does not necessarily increase, and can even decrease.

To understand why the scale radius increases with κ, while other radii decrease, in Fig. 5.6 we plot ρr^2 versus radius. The peak of the curve indicates the radius at which $r = r_{-2}$. We note several interesting features. First, the profiles become more sharply peaked (i.e. they have higher Einasto alpha parameters) for larger values of κ. Second, the curves are not completely smooth, but have several small variations relative to the scaled ICs. These might appear to be noise in the density profiles, but the fact that they reoccur at similar radii in simulations with different κ values (e.g. in the NFWT15 R or NFWXSlow R panels) suggests that they are real features in the remnants. Similar variations can be seen in merger remnants from e.g. McMillan et al. (2007). For very flat profiles, such as the EinLow simulations, these features make the scale radius hard to measure and add scatter to the measured values.

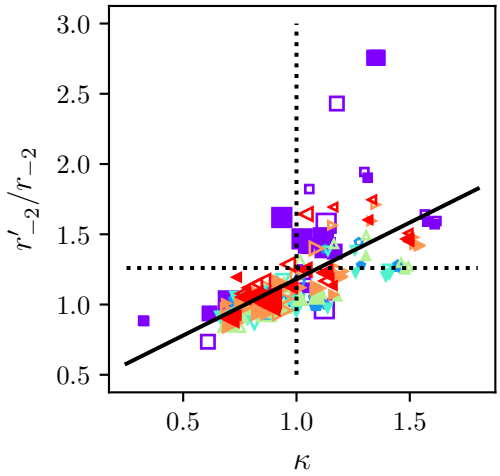

Figure 5.5: The change in the scale radius, r'_{-2}/r_{-2}, as a function of the relative energy change, κ. The dotted lines are the expectations for self-similar evolution of the density profile. Colours and symbols are as in Fig. 5.1. The solid black line is a fit to the data, $r'_{-2}/r_{-2} = 0.80\kappa + 0.38$.

Third, if we consider the difference between the scaled ICs (dotted black lines) and the final remnants, we see that the largest changes in density are at, or past, the scale radius. At small radii, the density changes less, and only ever drops $\sim$10 per cent below the corresponding value for the scaled ICs. The net effect of the density changes being larger at large radii is that while low κ simulations produce more extended profiles (see Fig. 5.2), they actually have *smaller* scale radii. Conversely, very bound (high κ) remnants have large scale radii, but are then truncated abruptly beyond this radius.

Next, we consider the virial radius, $r_{\rm vir}$. For cosmological haloes, this is formally the radius within which the system is in virial equilibrium. Strictly speaking, this definition only applies to systems that are accreting continuously from the surrounding density field; there is no clear analogue of this quantity in our isolated simulations. In practice, however, the virial radius in cosmological simulations is usually defined as the radius within which the mean density of the halo exceeds a reference background density $\rho_{\rm ref}$ by a factor Δ. A common choice is $\rho_{\rm ref} = \rho_{\rm c}$, the critical density, and $\Delta = 200$ (Navarro et al., 1996, 1997). By analogy, we will consider two 'virial radii' that enclose mean densities $\bar{\rho} = 0.1\,\rho_{\rm unit}$ and $0.008\,\rho_{\rm unit}$. Given our choice of units, for an NFW profile these would correspond to 3 and 10 times the scale radius, respectively (or concentration parameters of $c = 3$ and $c = 10$), in our ICs. (Given these definitions, we also note that the 'virial mass' within each of these

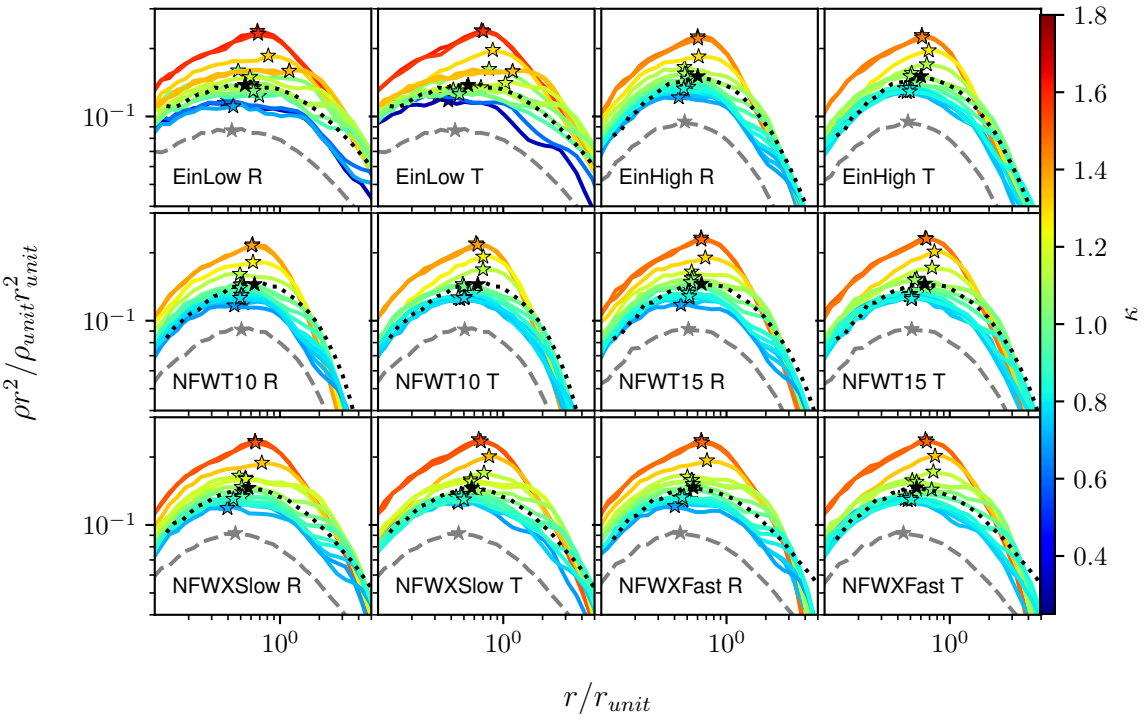

Figure 5.6: ρr^2 versus radius for the halo remnants, coloured by the relative energy change, κ. Scale radii, r_{-2}, are indicated with stars. The dashed grey lines show the initial halo models, and the dotted black lines are the ICs with the radius rescaled by a factor of $2^{1/3}$, as expected for a self-similar equal-mass merger.

radii will scale as $M_{\rm vir} \propto r_{\rm vir}^3$.) Fig. 5.7 shows the change in these radii as a function of κ. The solid lines are fits to the data, $r'_{\rm vir}/r_{\rm vir} = 0.39\kappa + 0.87$ (top) and $r'_{\rm vir}/r_{\rm vir} = 0.22\kappa + 1.02$ (bottom), with an RMS scatter of 0.03 for both. Overall, the relationship between $r_{\rm vir}$ and κ is monotonic, and fairly tight, with some possible dependence on the initial profile. As with the scale radius, the change in the virial radius *increases* with κ. Thus, while the remnants produced by more energetic encounters are larger and more diffuse, a virial radius defined in terms of enclosed density is actually smaller for these systems. We note, however, that the slopes of the virial radius–κ relations (0.39 and 0.22, for the two density thresholds) are both shallower than the relation for the scale radius (0.8). Thus, although the density change relative to self-similar scaling is larger in the outer parts of the remnant (as shown in Fig. 5.3), the relative change in size is smaller at larger radii than at smaller radii.

Finally, we examine how the peak circular velocity, $v_{\rm peak}$, and the corresponding radius, $r_{\rm peak}$, vary from the ICs to the final remnant. Fig. 5.8 shows the relative changes in $r_{\rm peak}$ (top) and $v_{\rm peak}$ (bottom) as a function of the relative energy change, κ. The solid black lines are fits to the data $r'_{\rm peak}/r_{\rm peak} = 0.29\kappa + 0.95$ (top) and $v'_{\rm peak}/v_{\rm peak} = 0.46\kappa + 0.81$ (bottom); the RMS scatter with respect to these are 0.2 and 0.04, respectively. The relative change in peak velocity increases approximately linearly with κ. The relationship between $r_{\rm peak}$ and κ is more complicated; here the points follow two trends. The low-energy simulations generally produce remnants with peak radii close to those of the ICs, that is to say smaller than the self-similar expectation, while for the high-energy simulations $r_{\rm peak}$ generally increases linearly with κ, passing through the self-similar value at $\kappa = 1$. There are a number of exceptions to these trends, however, notably the simulations with EinLow profiles.

In Chapter 4, we found that the size of haloes, measured as the average particle distance from the halo centre, decreased with κ as κ^{-5}. The results in this chapter indicate that while the radii $r_{\rm g}$ and $r_{1/2}$ also decrease (albeit as κ^{-1}), the characteristic radii r_{-2}, $r_{\rm vir}$, and $r_{\rm peak}$ all *increase* roughly linearly with κ. Clearly the changes in the profile are complicated and non-self-similar, suggesting that the behaviour of the concentration parameter may be complicated. Finally, since there is a considerable literature investigating how the inner slope of halo profiles evolve in mergers, we have also included a discussion of this point in Appendix C.

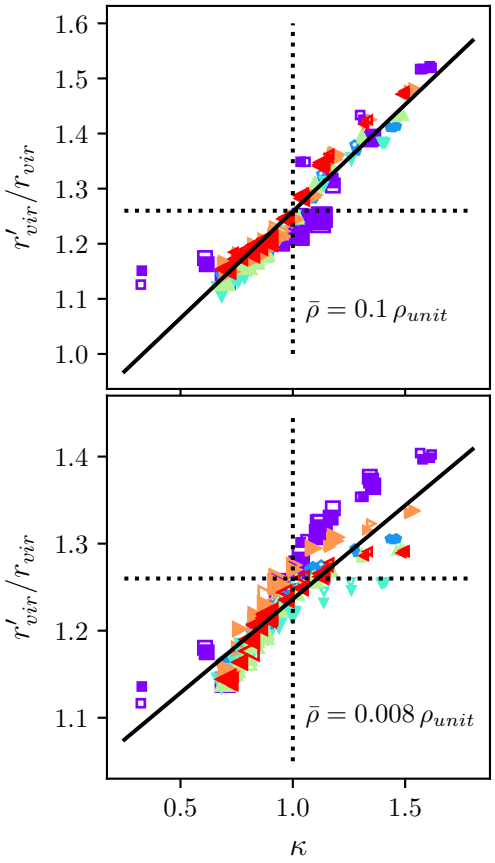

Figure 5.7: The change in virial radius, $r'_{\rm vir}/r_{\rm vir}$, as a function of the relative energy change, κ. The two virial radii are defined in terms of enclosed mean density, as described in the text, for densities of $\bar{\rho} = 0.1\,\rho_{\rm unit}$ (top) and $0.008\,\rho_{\rm unit}$ (bottom). The dotted lines show the expected values for self-similar scaling of the density profile. Colours and symbols are as in Fig. 5.1. The solid lines are fits to the data, $r'_{\rm vir}/r_{\rm vir} = 0.39\kappa + 0.87$ (top) and $r'_{\rm vir}/r_{\rm vir} = 0.22\kappa + 1.02$ (bottom).

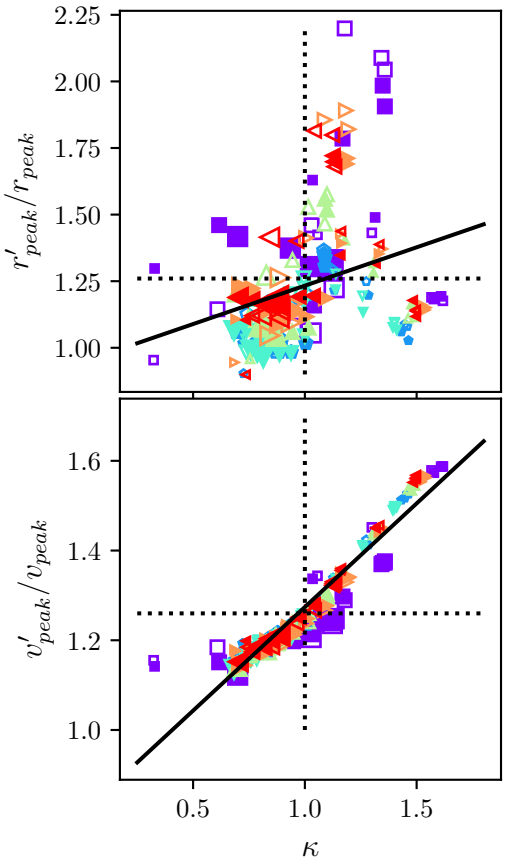

Figure 5.8: Changes in $r_{\rm peak}$ (top) and $v_{\rm peak}$ (bottom) as a function of the relative energy change, κ. The dotted lines show the values for self-similar scaling. Colours and symbols are as in Fig. 5.1. The solid black lines are fits to the data $r'_{\rm peak}/r_{\rm peak} = 0.29\kappa + 0.95$ (top) and $v'_{\rm peak}/v_{\rm peak} = 0.46\kappa + 0.81$ (bottom).

5.4 Profile Fitting

In the previous section, we examined how the overall mass distribution and the characteristic radii evolve in major mergers. In this section, we fit analytic NFW and Einasto profiles to the remnants, and discuss how well these analytic forms describe the remnants.

5.4.1 Methods

To determine the NFW parameters (r_s, ρ_0) or the Einasto parameters $(r_{-2}, \rho_{-2}, \alpha_E)$, we fit the circular velocity profiles using a χ^2 minimization procedure. Though previous studies generally fit the density profile directly (e.g. Neto et al., 2007; Duffy et al., 2008; Dutton & Macciò, 2014; Meneghetti et al., 2014), fitting the circular velocity is less susceptible to noise, as discussed in Vera-Ciro et al. (2013).

The data were binned in logarithmic radial bins, with each bin centred on $\ln r_i$. As in Vera-Ciro et al. (2013, 2014), we fit the profiles by minimizing

$$\chi^2 = \frac{1}{N_\mathrm{bins}} \sum_{i=1}^{N_\mathrm{bins}} (\ln v_c^2 - \ln v_{c,i}^2)^2 \ , \tag{5.8}$$

where N_bins is the number of bins, v_c is the circular velocity of the fitted profile at radius r_i, and $v_{c,i}$ is the circular velocity of the simulated halo at r_i. The fit was performed between three times the softening length and the radius at which the mean enclosed density was $\bar{\rho} = 0.01\,\rho_\mathrm{unit}$. Though we present both NFW and Einasto fits, it has been shown that concentrations from Einasto fits are more robust to variations in fitting details, such as the radial range (Gao et al., 2008).

5.4.2 Fits to Individual Remnants

Fig. 5.9 shows the merger remnants of radial mergers with EinHigh (left) and NFWXSlow ICs (right). Einasto profiles provide a much better description of the remnants in both cases. This may not be surprising, given that the ICs had either Einasto or truncated profiles. Even for the Einasto profile, however, there is a change in the α_E parameter. These results demonstrate that the profiles of the remnants are not, in general, NFW, nor are they self-similar to the ICs.

To assess how well the haloes are fit by NFW and Einasto profiles, we show the residuals in Fig. 5.10, in the range that the velocity profiles were fit. The remnants are coloured

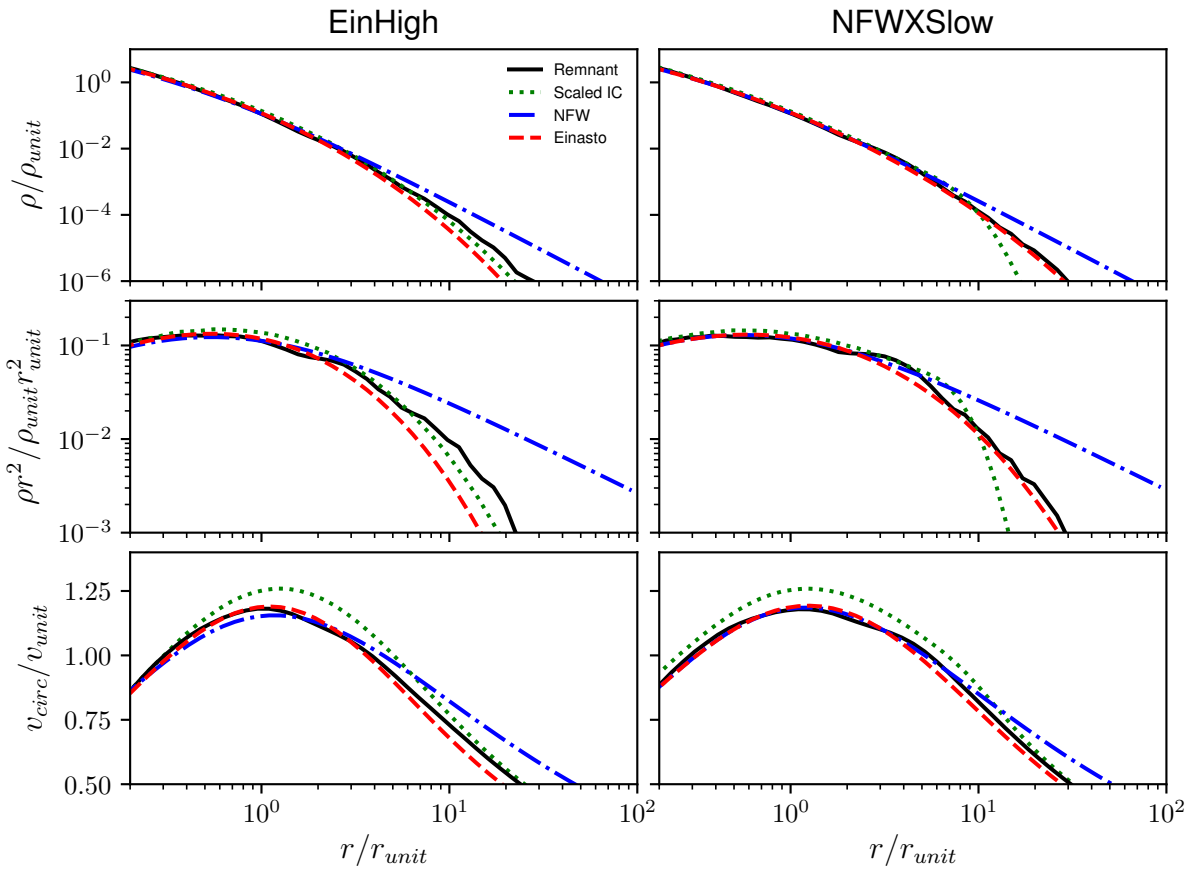

Figure 5.9: Density profile, ρ (top), ρr^2 (middle), and the circular velocity curve $v_{\rm circ}$ (bottom) for two example remnants. The initial ICs were either EinHigh (left) or NFWXSlow (right), and merged on a radial orbit at a separation of $10\,r_{\rm peak}$ with an initial velocity of $0.8\,v_{\rm esc}$. The remnant and ICs are shown with solid black and dotted green lines, respectively. The ICs have been scaled as expected for self-similar evolution in an equal-mass merger; i.e., the radii and velocities have been scaled by $2^{1/3}$. The best-fitting NFW (blue dash-dotted line) and Einasto (red dashed line) profiles are also shown.

by their relative energy parameter (where redder lines correspond to higher κ values), and fits to the ICs are shown in black. Overall, the residual of the remnant fits are more consistent with zero for the Einasto fits when compared to the NFW fits. The residuals look very similar for a given relative energy for all the ICs, with the exception of the EinLow simulations. The high-κ simulations show different trends in their residuals compared to the low-κ simulations. Comparing the ICs to the profile fits, we can see that the Einasto profiles are well fit with Einasto profiles, and NFWX profiles by NFW profiles, as expected. Interestingly, the NFWT ICs have very low residuals when fit with an Einasto profile; since these profiles resemble tidally stripped systems (Drakos et al., 2017), this shows that Einasto profiles are a reasonable description of tidally stripped NFW profiles.

Fig. 5.11 shows the changes in the NFW parameters, ρ_0 and r_s, as a function of κ. The density parameter, ρ_0, has little dependence on κ, with the exception of the high-κ simulations. The change in the scale radius, $r'_\mathrm{s}/r_\mathrm{s}$, generally increases with increasing κ, as was found previously from direct fitting (cf. Fig. 5.5). Both parameters roughly match the self-similar prediction for $\kappa = 1$ (where the dotted lines intersect). At high energies (low-κ), it is generally found that $r'_\mathrm{s}/r_\mathrm{s} < 2^{1/3}$, i.e. r_s is smaller than expected from self-similar evolution. We also note that there appears to be some systematic dependence on the initial halo model in both sets of results (as indicated by the point colour).

The lowest energy simulations (high κ values) appear to behave slightly differently from the other simulations; the density increases more than for the other simulations, while the trend in r_s with κ is reversed at these energies. This change in behaviour may indicate that these remnants are no longer well fit by NFW profiles. In what follows, we will generally distinguish three groups of simulations with somewhat distinct behaviour: the EinLow simulations, the lowest energy (highest κ) simulations, and the rest of the simulations, which follow a simpler trend.

Similarly, the variations in the three Einasto parameters α_E, ρ_{-2} and r_{-2} are shown in Fig. 5.12. The variations in α_E and ρ_{-2} are roughly independent of κ, although, as with the NFW parameters, the high-κ simulations differ considerably from the others, producing remnants with higher α_E and ρ_{-2} values. Variations in r_{-2} have a stronger dependence on κ; r_{-2} generally increases more for larger values of κ, though once again the high-κ simulations deviate from the main pattern. As with the NFW profile, for all three Einasto parameters, the main trends only roughly match the prediction for self-similar scaling when $\kappa = 1$. This could be because the profile is not perfectly described by an Einasto model, especially in the outer regions, and the parameter values are very sensitive to the exact profile fit.

In summary, we find that the remnants of equal-mass binary mergers are not self-similar

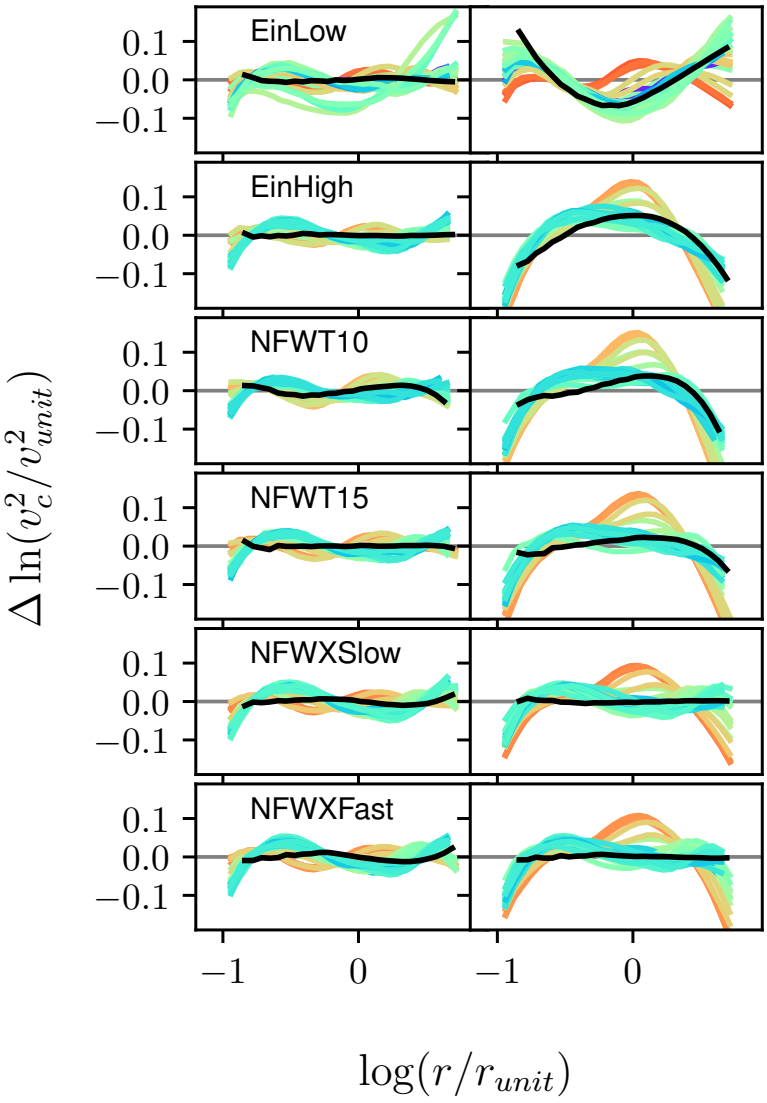

Figure 5.10: Residuals in the Einasto (left) and NFW (right) fits to the individual remnants. The residuals are measured as the difference in $\ln v_c^2$ between the remnant and the fits. The halo remnants are coloured by the relative energy change, κ. Residuals in the fits to the ICs are shown in black.

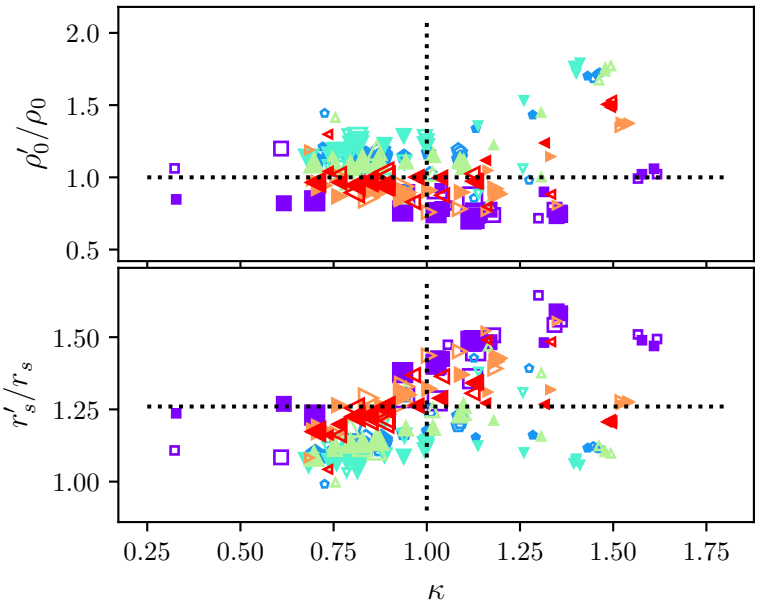

Figure 5.11: The change in the best-fitting NFW parameters r_{-2} and ρ_0 as a function of the relative energy change, κ. The dotted lines are the expectations for self-similar evolution of the density profile. Colours and symbols are as in Fig. 5.1.

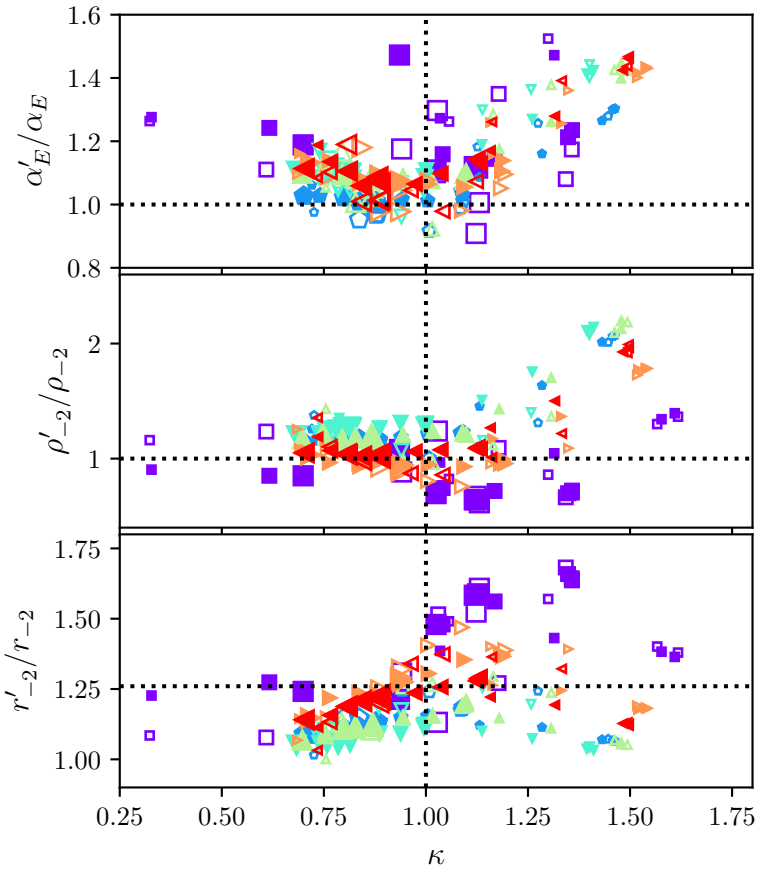

Figure 5.12: The change in the best-fitting Einasto parameters, α_E, ρ_{-2}, and r_{-2}, as a function of the relative energy change, κ. The dotted lines are the expectations for self-similar evolution of the density profile. Colours and symbols are as in Fig. 5.1.

to their ICs, but are fairly well described by Einasto profiles. Changes in the halo profile depend mainly on the relative change in internal energy, κ, though there is also some dependence on the initial model of the halo. Interestingly, the Einasto shape parameter $\alpha_{\rm E}$ typically increases in mergers. High peaks in the density field, and/or rapidly forming haloes, have higher values of α_E (Gao et al., 2008; Ogiya et al., 2016); it is possible that mergers have a role in producing these profiles.

5.4.3 Analytic Model of Profile Changes

Ultimately, we would like a synthetic prediction for how the profile of the remnant will differ from that of the ICs. We can specify the relationship fully by determining the changes in the three Einasto parameters, α_E, ρ_{-2}, and r_{-2}, as a function of the ICs and/or merger parameters. Clearly, we need three independent equations to predict the changes in these three parameters. Ideally, we would use the equations for $r_{1/2}$, $v_{\rm peak}$, and $r_{\rm vir}$ derived in Section 5.3.2, since they have little dependence on the initial halo model. In practice, however, we have found that this method does not work well, as the Einasto parameters are very sensitive to small variations in these equations. Instead, we determine the three Einasto parameters from profile fits to the merger remnants, and fit directly for the dependence on κ and E_0. We assume that the dependence is at most quadratic in both variables. The resulting fits are:

$$\alpha'_E = (0.03\kappa^2 - 0.06\kappa + 0.06)\times \left(0.37\frac{E_0^2}{E_{\rm unit}^2} + 4.72\frac{E_0}{E_{\rm unit}} + 13.2\right) \tag{5.9a}$$

$$\frac{\rho'_{-2}}{\rho_{\rm unit}} = (0.96\kappa^2 - 1.75\kappa + 1.19)\times \left(0.46\frac{E_0^2}{E_{\rm unit}^2} + 1.87\frac{E_0}{E_{\rm unit}} + 2.68\right) \tag{5.9b}$$

$$\frac{r'_{-2}}{r_{\rm peak}} = (-0.11\kappa^2 + 0.25\kappa + 0.06)\times \left(-0.75\frac{E_0^2}{E_{\rm unit}^2} - 2.79\frac{E_0}{E_{\rm unit}} + 0.57\right) \quad . \tag{5.9c}$$

Fig. 5.13 shows how the predicted Einasto parameters compare to those derived from profile fits to the individual remnants. The RMS scatter with respect to the fit is 0.02,

0.06, and 0.03 for the top, middle, and bottom panels, respectively. In general, the scatter is fairly small, except for the EinLow profiles (squares). Remnants from EinLow ICs have low α_E parameters, and most have fairly flat logarithmic slopes to their density profile, as illustrated in Fig. 5.6; overall, these are the most massive, extended profiles with a large fraction of their mass at large radii, possibly explaining the deviations from the general trend. Overall, we conclude that Equations (5.9a)-(5.9c) provide a good description of the final remnant, as a function of the ICs and the orbital parameters (specifically κ).

5.5 Implications for Concentration Changes

Having described how the profile of the remnant depends on the ICs and the merger parameters, we will now consider the implications for the evolution of the concentration parameter.

5.5.1 Definitions of Concentration

There are several methods for measuring concentration in simulated haloes; most commonly concentration is defined as $c = r_{\rm vir}/r_{-2}$, where r_{-2} is determined through profile fitting and $r_{\rm vir}$ is defined in terms of the enclosed mean density. However, concentration can also be determined indirectly by measuring other properties, such as the peak circular velocity (Prada et al., 2012; Klypin et al., 2016) or the mean density profile (Alam et al., 2002; Diemand et al., 2007), and inverting the relationship between these properties and the usual concentration parameter, given an assumed theoretical profile. These different methods should all agree for NFW profiles, but can give different answers when the density profile is not NFW.

As discussed in Prada et al. (2012) and Klypin et al. (2016), determining the concentration from the ratio of the peak circular velocity to the circular velocity at the virial radius,

$$R = v_{\rm peak}/v_{\rm vir} \ , \tag{5.10}$$

may be more justified than profile fitting, since it accounts for differences in the Einasto shape parameter, α_E, that affect the central concentration of the mass distribution. Additionally, calculating R does not require any assumption about the profile.

Since R is monotonically related to $c = r_{\rm vir}/r_{-2}$, to convert from R to the concentration,

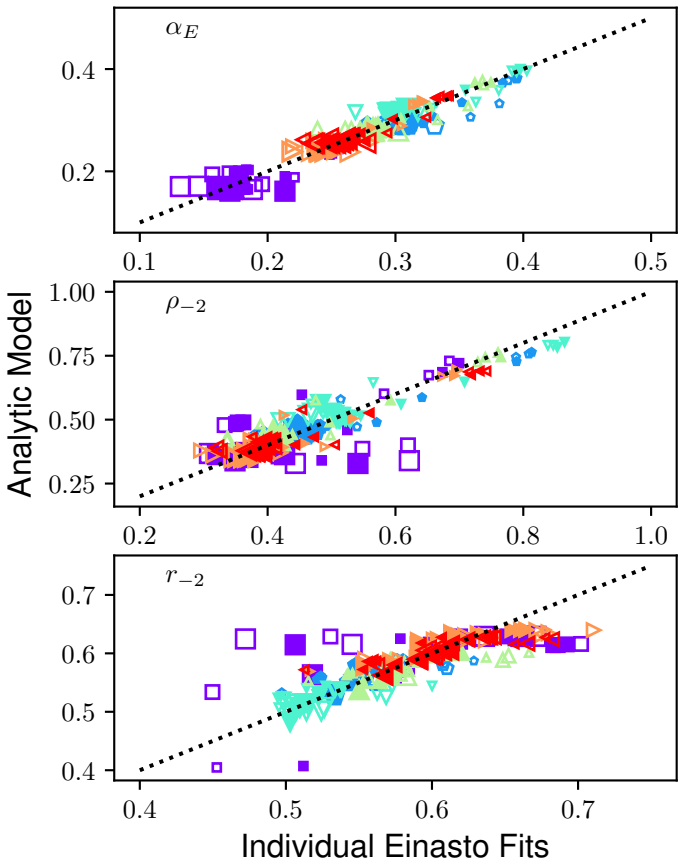

Figure 5.13: Einasto parameters α_E, ρ_{-2} and r_{-2} predicted by our fits (Equations (5.9a)-(5.9c)), versus the parameters values measured from the best-fitting profile to each remnant halo.

$c_{\rm R}$, one can assume a profile (e.g. NFW or Einasto), and use the formula:

$$R = \sqrt{\frac{c_{\rm R} f(x_{\rm peak})}{x_{\rm peak} f(c_{\rm R})}} \ , \tag{5.11}$$

where $f(x)$ is the mass profile corresponding to the specified density profile and $x_{\rm peak} \equiv r_{\rm peak}/r_{-2}$ (Klypin et al., 2016). For convenience, we show how R and c_R are related in Appendix D.

None of the usual methods for calculating c are well defined in non-cosmological simulations, however, as they use a virial radius defined in terms of a mean background density. One approach to measuring relative *changes* in concentration, without needing to define a virial radius, is to scale the profiles so that they have the same $v_{\rm peak}$, and then scale $r_{\rm peak}$ by the same factor (Moore et al., 2004). The concentration change can then be inferred from ratio of the intial $r_{\rm peak}$ to the shifted remnant $r'_{\rm peak}$. Mathematically, this can be expressed as:

$$\frac{c'_M}{c_M} = \frac{r_{\rm peak}}{r'_{\rm peak}} \frac{v'_{\rm peak}}{v_{\rm peak}} \ , \tag{5.12}$$

where c'_M is the concentration of the remnant, and c_M is the concentration of the original halo. For self-similar haloes with the same concentration, scaling the radii of the haloes so they have the same peak circular velocity ensures they have the same virial radius (since it accounts for the increase in mass). The radius at the peak circular velocity, $r_{\rm peak}$ then scales as r_{-2} if the profile remains the same. The disadvantage to this method is that it assumes the remnant is self-similar to the initial profile, and that the background density remains constant. Since this definition is strongly dependent on the assumption of self-similar evolution, and we have demonstrated major mergers are not, in general, self-similar to the ICs, we will not use this definition to calculate concentration. However, for completeness, we present results using this definition in Appendix D.

5.5.2 Concentration Changes

In this work, we track the net change in concentration from the ICs to the final remnant in three ways:

1. using $c = r_{\rm vir}/r_{-2}$, with r_{-2} measured directly from the logarithmic derivative of the density profile of the remnant, as the point where $\mathrm{d}\ln\rho/\mathrm{d}\ln r = -2$, smoothing with a Gaussian kernel of width $\sigma = 0.1$, while $r_{\rm vir}$ is defined based on the enclosed density, as explained in Section 5.3.2.

2. using $c_{\rm Ein} = r_{\rm vir}/r_{-2}$, with values of r_{-2} and $r_{\rm vir}$ determined by fitting an Einasto profile to the individual merger remnant, as described in Sections 5.4.1–5.4.2.

3. using $R = v_{\rm peak}/v_{\rm vir}$ with $v_{\rm peak}$ and $v_{\rm vir}$ determined directly from the density profile of the individual remnant, as in Section 5.3.2.

Since the remnants are better described by Einasto profiles, we will not consider the concentration measured from the NFW fit, $c_{\rm NFW}$, however, we provide a comparison between $c_{\rm Ein}$ and $c_{\rm NFW}$ in Appendix D.

In Fig. 5.14 we show how the concentration parameters c (method i), $c_{\rm Ein}$ (method ii), or R (method iii) change with energy. As with the changes in the Einasto parameters, there appears to be a dependence on the initial halo model, particularly for $c_{\rm Ein}$. Individual concentration measurements, c, which are based on direct measurements of r_{-2} show that concentration changes decrease with κ; high-energy (low-κ) mergers cause an *increase* in concentration, while low-energy (high-κ) mergers decrease concentration. The trends in $c'_{\rm Ein}/c_{\rm Ein}$ and R'/R are more similar to the expected result, with little change in concentration at low-κ, and increasing at high-κ encounters . The ratio c'/c obtained from direct measurements of the scale radius does not show the same increase in concentration at high κ values as the ratio derived from the Einasto fits; this could be because the haloes produced by mergers of very bound pairs are not as well approximated by the Einasto profile. From this plot, however, it appears that the profile-independent measurement of R'/R shows a similar increase in concentration for high-κ simulations, so it is more likely due to the numerical difficulty with measuring c'/c directly. Finally, we note that R can be mapped on to an equivalent (radial) concentration parameter $c_{\rm R}$; testing this inversion, we find that while $c_{\rm Ein}$ and $c_{\rm R}$ agree roughly, there is considerable ($\sim$20 per cent) scatter between the two.

Overall, the pattern of concentration changes is complicated, depending on both κ and the initial halo model. Concentration measurements are very sensitive to the method used, and there is considerable scatter from one method to another. Regardless of the method used, however, we find that concentration usually *increases* in major mergers, except in the case of mergers between very bound pairs and/or between haloes with low α_E parameters. It is surprising to find that high-energy major mergers rarely decrease concentration. This is somewhat contrary to the results by Moore et al. (2004), who found that two NFW haloes merging on a high-energy orbit with a tangential velocity produced a remnant that was less concentrated than its progenitors. On the other hand, it is more consistent with the results of Kazantzidis et al. (2006), as discussed further in Section 5.6.

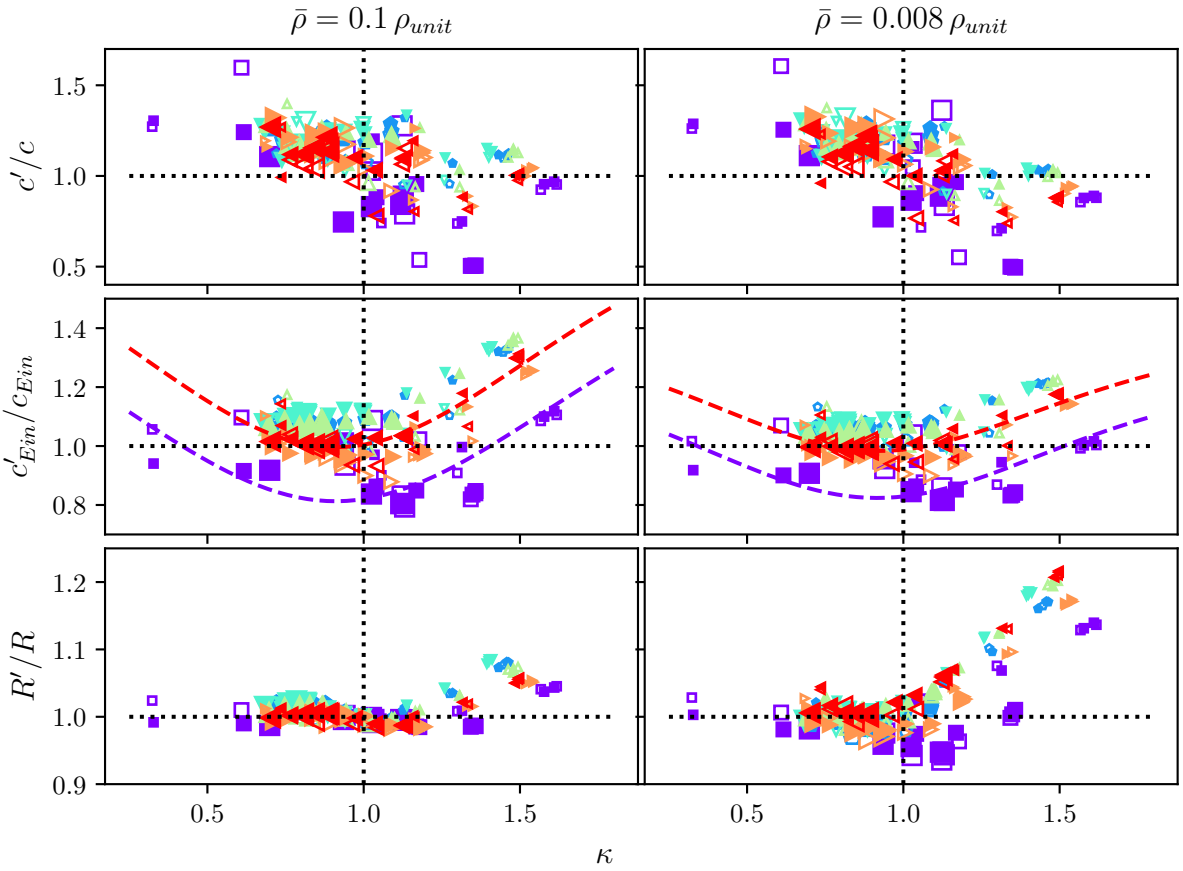

Figure 5.14: Net concentration change as a function of the relative energy change, κ. The concentrations are determined using either scale radii measured directly for individual profiles (top row), from the Einasto parameters determined from profile fitting (middle row), or derived from the velocity ratio $R = v_{\rm peak}/v_{\rm vir}$ measured directly from the profile (bottom row). The virial radii were calculated using overdensities $\bar{\rho} = 0.1\,\rho_{\rm unit}$ (left) and $0.008\,\rho_{\rm unit}$ (right). The dashed curves indicate $c' = c_{\rm analytic}$ recovered from the fits given in the text (Equations (5.9a)–(5.9c)), for two values of E_0, as described in the following section. Colours and symbols are as in Fig. 5.1.

5.5.3 Analytic Model for Concentration Changes

Ultimately, we wish to predict how concentration will change in major mergers. Our results indicate that the remnants of binary mergers are not, in general, self-similar to the ICs, but have properties that vary systematically with the energy of the system. Rather than determine concentration changes from direct fits to r_{-2}, together with some arbitrary choice of virial radius, we will use the analytic model from Section 5.4.3 to estimate how the profile will change, and then use that to calculate the corresponding change in concentration.

Given the initial haloes, and the orbital parameters of the merger, a prediction for the resulting Einasto remnant can be determined from the analytic predictions for the Einasto parameters. Then, the virial radius can be calculated from solving $\Delta_{\rm vir}\rho_b = \bar{\rho}(r_{\rm vir})$, where $\bar{\rho}$ is the mean enclosed density of the Einasto profile. The radius of the peak circular velocity can be found from the approximation $r_{\rm peak} \approx 3.15\exp\left(-0.64\alpha_E^{1/3}\right)r_{-2}$ (Klypin et al., 2016), and $v_{\rm peak}$ and $v_{\rm vir}$ from from the circular velocity profile $v_{\rm circ} = \sqrt{GM/r}$. In what follows, we refer to concentrations predicted by this analytic model as $c_{\rm analytic} = r_{\rm vir}/r_{-2}$ or $R_{\rm analytic} = v_{\rm peak}/v_{\rm vir}$.

Fig. 5.15 compares concentration values derived from the predicted profile changes using Equations (5.9a)-(5.9c) to concentrations measured from Einasto fits to individual profiles, for two choices of the virial radius. On the whole the two values agree fairly well; the RMS scatter between results and fit are 0.2 (top left), 0.5 (top right), 0.01 (bottom left), and 0.03 (bottom right), although once again much of this comes from the EinLow (square) simulations. From this plot it appears that the R' prediction, $R'_{\rm analytic}$, is more successful than the c' prediction, $c'_{\rm analytic}$. However, once the R values are mapped back to c (a mapping that is sensitive to the predicted profile), this is no longer the case. Overall, the concentration predictions presented here are accurate to within approximately 10 per cent.

5.5.4 Implications for the Boost Factor

Concentration changes have important consequences for the central densities of haloes, and therefore the dark matter annihilation boost factor. The boost factor within a volume V is defined as:

$$B = \frac{1}{\bar{\rho}^2 V}\int \rho^2 dV \quad , \tag{5.13}$$

where ρ is the density of the halo; (see, e.g., Okoli et al., 2018, for a discussion).

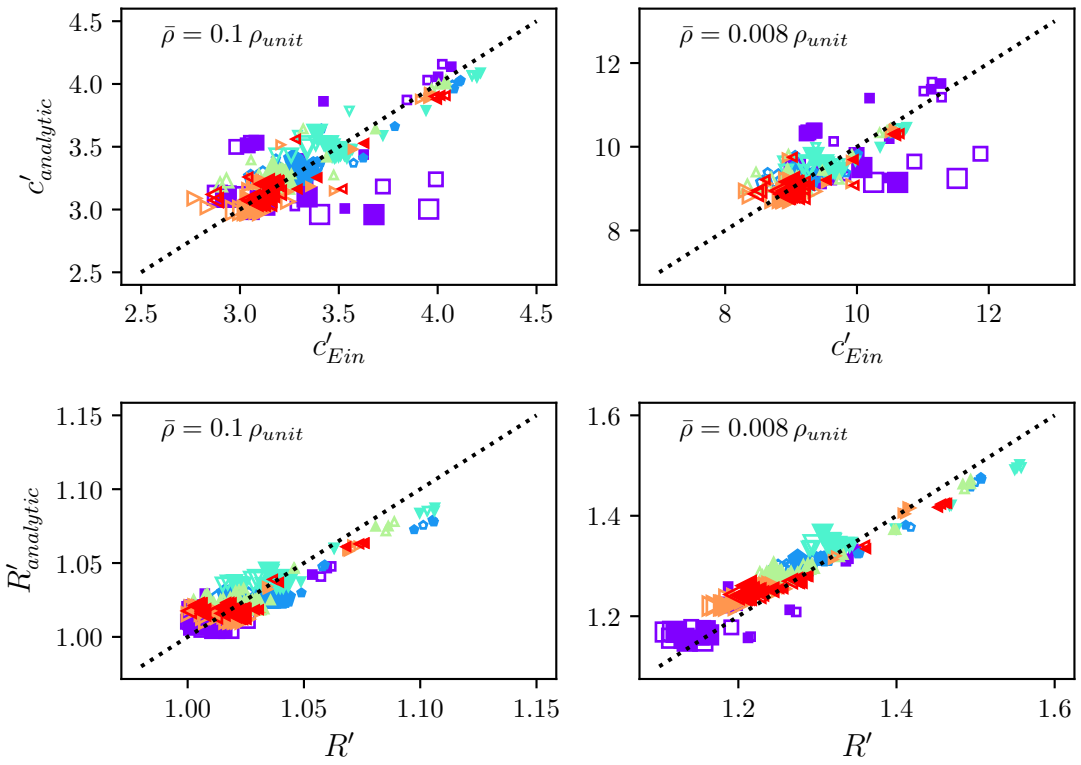

Figure 5.15: Predictions for concentration parameter (top) and velocity ratio R (bottom) derived from our analytic fit (Equations (5.9a)-(5.9c)), versus values measured from individual profiles. The virial radii were calculated using overdensities $\bar{\rho} = 0.1\,\rho_{\rm unit}$ (left) and $0.008\,\rho_{\rm unit}$ (right). Colours and symbols are as in Fig. 5.1.

Since this calculation can be sensitive to the inner regions of the profile, we calculate the boost factor within the virial radius from the best-fitting Einasto profile, assuming spherical symmetry in the remnant. Fig. 5.16 shows that the change in boost factor is correlated with the change in concentration, as expected. We have compared these direct calculations of the boost factor to the values obtained assuming our scaling relations for the Einasto parameters, and find that they agree to within approximately 5 per cent .

5.6 Discussion

A number of lines of evidence suggest that major mergers play an important role in determining the properties of dark matter haloes. In this chapter, we have performed over a hundred simulations of major mergers between identical, isolated haloes with various density profiles and initial orbits, and have tracked how the density profile of the remnant differs from that of the initial haloes. The differences are subtle, but indicate that the evolution from the initial to the final state is not self-similar, although the remnants are well described by Einasto profiles. Relative to scaled ICs, the mass distributions of the haloes are rearranged in a systematic way, with low-energy (high κ) mergers resulting in the mass moving inwards to higher density, while high-energy (low κ) mergers result in more extended haloes. Some halo properties depend mainly on κ (particularly the half-mass radius and the peak circular velocity), while others also depend on the initial halo model (e.g. the Einasto parameters α_E, r_{-2}, and ρ_{-2}).

A surprising result of our study is that while energetic mergers produce more extended mass distributions, they do not generally reduce the concentration parameter significantly, and they result in an increased central density, even compared to the expectation from self-similar scaling. In addition, although the scale radius generally increases after mergers, it does not increase as much as expected from self-similar evolution (e.g. Fig. 5.12). This suggests that major mergers do not fully explain the evolution of the central density or scale radius of haloes as they grow.

Considering the evolution of the halo mass profiles in detail, we find significant rearrangement of the mass distribution. If we define a virial radius corresponding to the density contour $\bar{\rho} = 0.008\,\rho_{\rm unit}$, for instance, we find that the final virial mass ranges from 1.3 to 4.1 times that of the ICs, where the expected value for self-similar evolution is 2. Previous studies of isolated major mergers have found that about 20-50 per cent of the mass lies outside the virial radius (e.g. Kazantzidis et al., 2006; Valluri et al., 2007; Vass et al., 2009). Our results are consistent with these previous ones, but we have tested a much larger range of orbital parameters, including unrealistically low-energy mergers in which

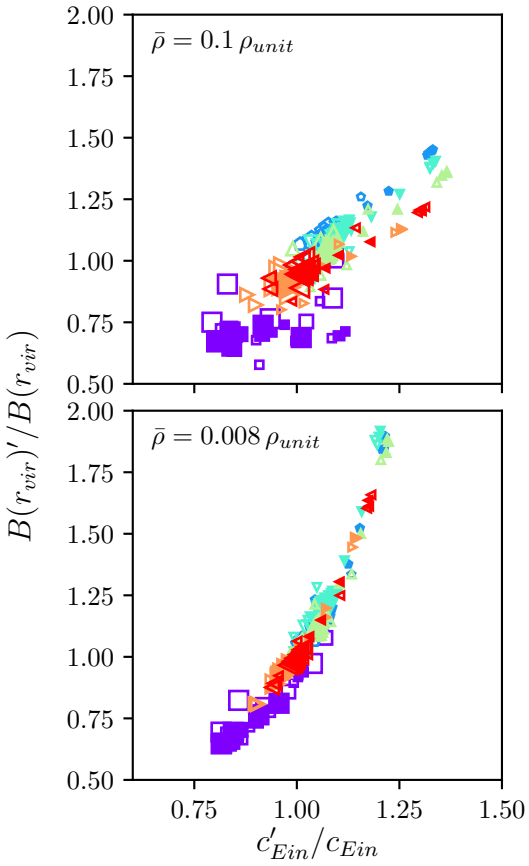

Figure 5.16: Relation between the change in boost factor and the change in concentration calculated as $c = r_{\rm vir}/r_{-2}$ from the best Einasto fit. The virial radii were calculated using overdensities $\bar{\rho} = 0.1\,\rho_{\rm unit}$ (top) and $0.008\,\rho_{\rm unit}$ (bottom). Colours and symbols are as in Fig. 5.1.

the virial mass increases more than expected from self-similar evolution. The fact that virial mass is not additive in halo mergers has important implications for semi-analytic models of galaxy formation, as discussed in Kazantzidis et al. (2006) and Valluri et al. (2007). Similarly, as pointed out in Okoli et al. (2018), boost factor calculations often assume that the virial mass is additive; relaxing this assumption would affect boost factor predictions considerably.

One of our original goals was to produce a prediction for how halo concentration changes in major mergers. Using fits to the evolution of the three Einasto parameters shown in Equations (5.9a)-(5.9c), we have produced predictions that match our simulation results to 10 per cent on average. Overall, it seems that while major mergers can cause systematic departures from self-similar evolution and corresponding changes in concentration, the pattern is opposite to what one might naively expect, in that energetic mergers (low κ values) *increase the concentration* while low-energy (tightly bound) mergers decrease it. This is in contrast to Moore et al. (2004), who concluded (from a single example) that high-energy mergers resulting in oblate haloes may decrease halo concentration. This could be because they assumed self-similar evolution in their concentration measurement. Our results are more consistent with Kazantzidis et al. (2006), who concluded that haloes are robust to major mergers. Though they also found that the profile changes resulting from major mergers are subtle, their fig. 8 suggests that mass moves inwards for haloes with lower central densities, but outwards for haloes with high central density compared to the scaled initial models. This is similar to our results, where the high-central density EinLow haloes tended to produce remnants with decreased concentrations.

Given our results, if the central density in haloes does drop as they grow, the mechanism for this remains unclear. This could be because we have only considered the simplest model for major mergers; binary, equal-mass mergers of identical haloes that are spherical, non-rotating, and lack substructure. How these results extend to more realistic mergers in a cosmological context is also unclear; cosmological conditions are different because equal-mass and/or isolated binary mergers are rare. Given the merger remnant takes an orbital period or two to settle into virial equilibrium, multiple mergers staggered by some fraction of an orbital period might lead to a decrease in central density, or substructure left by an earlier merger may affect the evolution of a later one. We will consider the effect of multiple mergers in future work.

In conclusion, we have explored how the density profiles and concentrations of dark matter haloes change in equal-mass mergers. These mergers do not generally decrease the central density or the concentration parameter, and often cause remnants to become more concentrated. This is a puzzle, given previous results suggesting the central density must drop as haloes grow. Therefore mergers seem unlikely to cause the evolution of halo central

density needed to explain results from cosmological simulations, as pointed out by Okoli et al. (2018). Our future work will explore more complicated and more realistic merger scenarios, to see if the trends found in this chapter still hold in a cosmological setting.

Chapter 6

Future Work

6.1 Summary of Thesis Work

The work presented in this thesis focuses on how dark matter halo properties evolve in mergers. Dark matter haloes can be described in a number of ways, including their spherically averaged density profile, concentration, 3D shape and amount of substructure. These properties are strongly linked to the merger histories of haloes. Although the mean trends in the evolution of halo properties are well understood, it is less clear how individual haloes evolve during mergers.

6.1.1 Minor Mergers

In minor mergers, smaller dark matter haloes fall into larger host haloes and lose mass through tidal stripping; the remaining bound material may survive indefinitely as distinct substructure within the host halo. From earlier work, such as that by Hayashi et al. (2003), it is known how density profiles evolve during tidal stripping; material at large radii is preferentially lost, but there is also a decrease in central density. While Hayashi et al. (2003) showed empirically how density profiles evolve, the physical explanation for their results was unclear. In Chapter 2 we presented a simple model for the effect of tidal stripping on the structure of haloes, based on truncating the distribution function at a specified energy. Overall, our model is generally more accurate at describing the halo remnant compared to other models in the literature, and is physically motivated, rather than empirical. Additionally, it allows for a simple description of the evolution of the full

distribution function (i.e. both the spatial and velocity distributions) of subhaloes. This is useful for calculations that depend upon the distribution function, such as the boost factor for dark matter annihilation.

In Chapter 3, we examined this model further to understand the underlying physical mechanisms, and to validate many of the assumptions in the model. Additionally, we showed that the model appears to be universal, in that it can be applied to any collisionless system. Density profile evolution is often modeled as a sharp truncation at the tidal radius, with no central mass loss, or using an empirical fit to simulation data, such as from Hayashi et al. (2003). While we found that the boost factor does not evolve much for an individual subhalo (as calculated within the tidal radius), the method used to determine the profile evolution can greatly effect the boost factor—in some cases by an order of magnitude. This is because the boost factor depends strongly on the density at very small radii that cannot easily be probed by N-body simulations.

In the work presented in this thesis, we estimated the truncation energy empirically by fitting to the simulations. In future work, it would be useful to have a prediction for how the truncation energy evolves with time, based on the initial subhalo and orbital properties. Also, determining which particles are considered part of the subhalo is a complicated problem, so looking at mass loss in more detail, and being able to determine which particles are only transiently bound would better allow for a comparison between our model and simulations. In the future, it would be also be interesting to apply our model to two-component systems (such as stars embedded within a dark matter halo), and test how well it agrees with numerical simulations.

6.1.2 Major Mergers

In addition to minor mergers, we also examined halo evolution in major mergers. Work by, e.g. Moore et al. (2004), suggests that halo properties such as halo shape, spin and concentration are influenced by major mergers. We investigated this in Chapters 4 and 5, and found that the shape, spin, size, and overall profile of binary merger remnants do reflect the merger orbit, with the final outcome of the halo depending strongly on the change in energy and the halo spin parameter.

One question is how the central density of haloes evolves during mergers. Results from cosmological simulations suggest that halo central density should decrease as a halo grows; this in turn implies there must be a mechanism to heat haloes, and major mergers seem an obvious explanation. However, in Chapter 5 we found that major mergers are *not* effective at decreasing the central density of haloes, and thus mechanisms for the evolution of halo

central densities remains unclear. One possibility may be that more complicated merger scenarios are needed to produce the expected decrease in central density with time.

Overall, this work provides predictions for how size, shape, spin, density profiles and concentration of haloes change in major mergers; these predictions can then be used in semi-analytic models of halo structural evolution. While we looked at a large range of initial halo models and orbits, we only considered the simplest merger scenario of binary equal-mass mergers. In future work, we wish to extend this to more complicated merger scenarios, such as how haloes change in unequal mass mergers between non-spherical and/or non-isotropic systems. Further, non-binary mergers may be needed to reproduce the trends found in cosmological simulations.

6.1.3 Significance

Overall, this work has provided new understanding into how haloes evolve in mergers; this has applications to studying small-scale structure problems in CDM, dark matter detection techniques, and the development of semi-analytic models of halo evolution. Particularly, the detection of a dark matter annihilation signal would definitively establish the existence of dark matter. Given that the boost factor for dark matter annihilation is sensitive to the density profiles of both the host halo and subhaloes, our work suggests that predictions of the dark matter annihilation signal need to be revised. Additionally, given the size and accuracy of forthcoming datasets, new cosmological tests are needed to make significant progress on cosmological constraints. One potential application of semi-analytic models of structural evolution is to create predictions on how halo properties vary with the amplitude of matter fluctuations in the present-day universe, σ_8; this idea will be outlined in the following section.

6.2 A Potential Application

6.2.1 Tension in σ_8

One of the most pressing questions for the ΛCDM paradigm is the origin of the tension in measurements of the cosmological parameters H_0 and σ_8. The tension in σ_8 is between large-scale-structure (LSS) measurements (from e.g., cluster counts, galaxy clustering, cosmic shear or redshift space distortions) and Cosmic Microwave Background (CMB) measurements, as summarized in Fig. 6.1. CMB results favor a higher value of σ_8 compared

to LSS measurements (0.83 versus 0.79). This tension could be due to unknown systematics in the LSS or CMB measurements, or due to the standard cosmological model being incorrect.

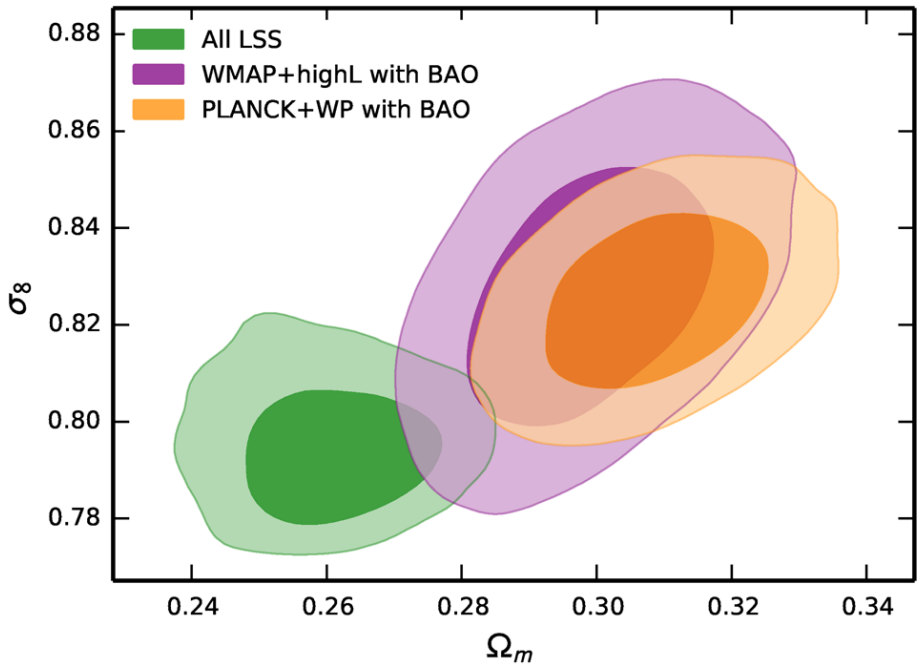

Figure 6.1: Summary of the σ_8 tension. Green contours show the constraints from LSS studies. Purple and orange contours show constraints from CMB measurements combined with Baryon Acoustic Oscillations (BAO) measurements. Figure is adapted from Battye et al. (2015).

Clearly this tension must be resolved to accurately constrain σ_8, and determine whether ΛCDM is an adequate description of our universe. To this end, it is important to have many independent methods for measuring σ_8, to account for unknown systematics. One potential method for constraining σ_8 that will become viable with the advances in observations is through the measurement of structural properties of galaxy clusters.

6.2.2 Halo Properties Break Degeneracy

Though there is a degeneracy in cluster numbers between low-Ω_m/high-σ_8 and high-Ω_m/low-σ_8 cosmologies, in the former case, dark matter haloes form earlier and thus are older on average (Taylor, 2011). Typically, older haloes tend to be more concentrated, have less substructure and are rounder compared to younger haloes. Since properties of dark matter haloes are strongly linked to their age and merger history, this means that the degeneracy in cluster counts may be broken by considering halo properties.

Information about halo structure and evolution comes mainly from N-body simulations. These have established that some halo properties, such as the spherically averaged density profile, are approximately universal (Navarro et al., 1996, 1997), while other properties such as 3D shape, concentration parameter, spin, or the amount of substructure, vary between systems. The relationship between halo age and halo properties was studied thoroughly in (Wong & Taylor, 2012) using principal component analysis. The authors found that halo concentration is the property that is most strongly correlated with halo age.

There have been some preliminary attempts to compare halo shape and concentration to predictions from ΛCDM. In Oguri et al. (2010), the authors measured the halo shapes of 18 clusters using weak-lensing results, and found that the mean halo ellipticity is in good agreement with predictions from Jing & Suto (2002). The authors also showed how predictions in halo shape distributions change as a function of σ_8. These predictions and their results are shown in Fig. 6.2. More recently, Sereno et al. (2018) measured halo concentration and shape in 16 CLASH clusters using a combination of strong lensing, weak lensing, X-ray photometry, X-ray spectroscopy, and Sunyaev-Zel'dovich (SZ) signal. Again, this study showed that observed halo shapes and concentrations are broadly consistent to ΛCDM predictions. Overall, though measured halo properties are in agreement with ΛCDM, neither predictions or the observations are precise enough to make constraints.

6.2.3 Initial Tests

While it is clear that halo properties should vary systematically between "late" (low-σ_8/high-Ω_m) and "early" (high-σ_8/low-Ω_m) cosmologies, it is not clear which properties will give the clearest measurement, or whether observations have enough signal to differentiate between the two cases. Therefore, we performed initial tests on numerical simulations to determine whether this idea is feasible.

There are many candidate properties that are known to correlate with halo age, such as concentration, shape, spin, and amount of substructure. It must also be determined

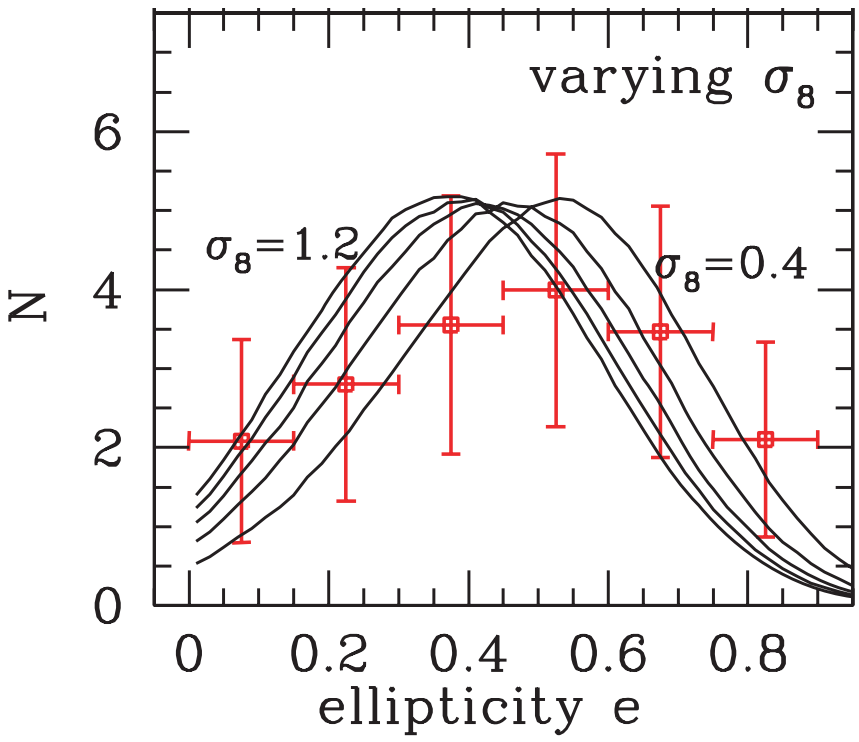

Figure 6.2: Halo ellipticity distribution measured from 18 cluster sized haloes (red boxes), compared to ΛCDM predictions with σ_8 varied from 0.4 to 1.2 in intervals of 0.2. Figure is adapted from Oguri et al. (2010).

which redshift, mass range, and environment should be used for cluster selection. Since high-resolution simulations are computationally costly, it is not feasible to sample the full parameter space through cosmological simulations. Therefore, the strategy of these initial tests is to run a limited number of simulations to calibrate the relation between structure, growth history and cosmology in a few cases, and then build semi-analytic extensions to this.

In previous work, Wong & Taylor (2012) compared the age of haloes to various halo properties. They measured age as z_x, where $x = M(z)/M_0$ is the fraction of the halo mass formed by redshift z. They found that concentration is the best halo age indicator, but correlates most strongly with $z_{0.2}$. How this relates to the concentration of a halo observed at redshift $z = 0$ remains unclear. On the other hand, halo elongation (a measure of halo shape, where a value of 1 corresponds to spherical haloes) also correlates with age, and is less sensitive to x. Additionally, the authors found that spin has a weak anti-correlation with halo age, again with little x sensitivity. In addition to halo concentration, shape and spin, the amount of halo substructure should also correlate with halo age. To examine this, in Taylor (2011), the author generated semi-analytic models in "late" and "early" cosmologies, where structure formed earlier or later respectively, and found a difference in substructure fractions.

As a preliminary step, we have compared two cosmological simulations run in GADGET-2 (Springel, 2005). The "late" cosmology had $\Omega_M = 0.3$ and $\sigma_8 = 0.8$, and the "early" cosmology had parameters $\Omega_M = 0.25$ and $\sigma_8 = 0.9$. Each simulation was run with 512^3 particles. Considering only haloes with masses above $5 \times 10^{13} M_\odot$ (as these were deemed to be resolved enough to measure accurate halo properties, and correspond to cluster-sized haloes), halo concentration, elongation and spin were measured at redshift $z = 0$ using the halo finder AHF (Gill et al., 2004; Knollmann & Knebe, 2009). We only see a significant difference in the elongation parameter (a two sample K-S test gives a difference of 10 per cent with a p-value of 0.03), whose distribution is shown in Fig. 6.3. This preliminary test indicates that elongation may be the best way to differentiate between "early" and "late" cosmologies, though we have only looked at redshift $z = 0$.

6.2.4 Upcoming Surveys

Given accurate semi-analytic models of halo evolution as a function of σ_8, these models can be applied to cluster observations, notably lensing results from *Euclid* and WFIRST, but also potentially X-ray and SZ observations, to constrain σ_8 and Ω_m. Though individual cluster shape measurements have large errors due to their 2D projection, averaging over many objects allows an accurate measurement of the mean elongation of haloes.

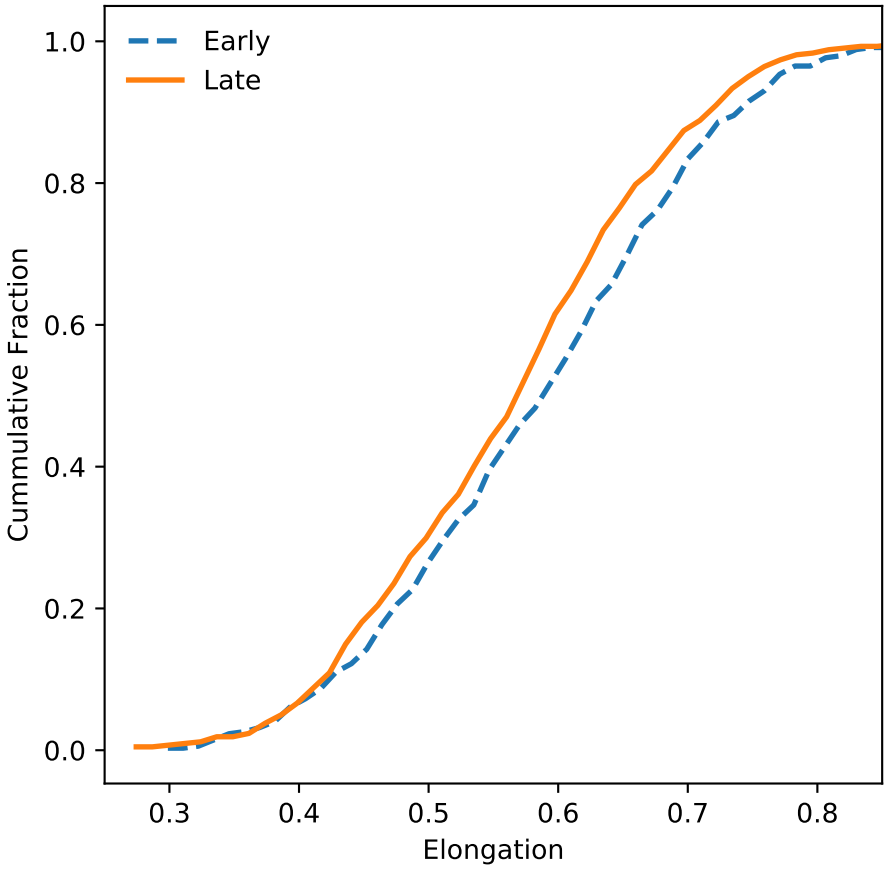

Figure 6.3: Preliminary results on how the distribution of halo elongation varies between "early" (low-Ω_m/high-σ_8) and "late" (high-Ω_m/low-σ_8) cosmologies.

Preliminary tests shown here indicate that distributions of halo elongation measured at $z = 0$ differ by approximately 10 per cent in "early" and "late" cosmologies. However, these cosmologies assumed σ_8 ranged from 0.8 to 0.9. If we want *independent* constraints that can detect a 0.05 difference in σ_8, that means we need to be able to detect a 5 per cent difference in elongations (distributions should vary roughly linearly with σ_8—see Fig. 6.2). In practice, observations can usually only measure projected, 2D elongation on the plane of the sky. Uncertainties in 3D shape estimates will be largely dominated by this effect, and we therefore expect individual elongation measurements to have uncertainties of around 50 per cent. Errors in the mean shape measurement will then equal $0.5/\sqrt{N}$, where N is the number of shape measurements. Therefore, to measure differences in σ_8 of 0.05 at the 5σ level, we will require approximately 2500 clusters.

To obtain a shape measurement, the cluster needs to be detected with signal-to-noise ratio, SNR$\geq$ 5. *Euclid* is projected to detect over 2×10^5 clusters at this significance (Sartoris et al., 2016), which is more than enough to constrain σ_8 to within 0.05 at the 5σ level, and could potentially constrain σ_8 to the 0.01 level or better. Therefore, this survey is ideal for using halo shapes to constrain cosmology.

Although we have specifically focused on constraints from lensing, multi-probe techniques, as used in, e.g. Sereno et al. (2018), may be more powerful in placing constraints on halo shapes, as they can constrain intrinsic shape and orientation without having to make dynamical assumptions such as hydrostatic equilibrium. LSST in particular should help provide more robust shape and mass estimates of clusters when combined with *Euclid* (Rhodes et al., 2017). Further, the upcoming CMB-S4 experiment should obtain SZ signal for approximately 10^5 clusters, which can be combined with *Euclid* weak lensing results (Abazajian et al., 2016). With the large number of *Euclid* clusters, and the complementary data from other surveys, we will likely be able to use this method to measure 0.01 differences in σ_8. Additionally, this approach could also be used to measure the dark energy equation of state parameter, w, since the age of haloes also depends on w. Though upcoming results from WFIRST (Wide Field Infrared Survey Telescope) will detect fewer haloes then *Euclid*, they will be detected at a much higher redshift (Doré et al., 2019), and thus WFIRST may be useful to look for potential time variations in w.

References

Abazajian K. N., et al., 2016, arXiv e-prints, p. arXiv:1610.02743

Aceves H., Velázquez H., 2006, Rev. Mex. Astron. Astrofis., 42, 41

Ahn J., Kim J., Shin J., Kim S. S., Choi Y.-Y., 2014, Journal of Korean Astronomical Society, 47, 77

Alam S. M. K., Bullock J. S., Weinberg D. H., 2002, ApJ, 572, 34

Alam S., et al., 2017, MNRAS, 470, 2617

Allgood B., Flores R. A., Primack J. R., Kravtsov A. V., Wechsler R. H., Faltenbacher A., Bullock J. S., 2006, MNRAS, 367, 1781

Amorisco N. C., 2015, MNRAS, 450, 575

Amorisco N. C., Evans N. W., 2011, MNRAS, 411, 2118

Anderhalden D., Diemand J., 2013, J. Cosmology Astropart. Phys., 4, 009

Angulo R. E., Hahn O., Ludlow A. D., Bonoli S., 2017, MNRAS, 471, 4687

Antonov V. A., 1961, Soviet Ast., 4, 859

Bailin J., Steinmetz M., 2005, ApJ, 627, 647

Bartels R., Ando S., 2015, Phys. Rev. D, 92, 123508

Battaglia G., Helmi A., Breddels M., 2013, New Astron. Rev., 57, 52

Battye R. A., Charnock T., Moss A., 2015, Phys. Rev. D, 91, 103508

Behroozi P., et al., 2015, MNRAS, 454, 3020

Benson A. J., 2005, MNRAS, 358, 551

Benson A. J., Lacey C. G., Baugh C. M., Cole S., Frenk C. S., 2002, MNRAS, 333, 156

Beraldo e Silva L., Lima M., Sodré L., Perez J., 2014, Phys. Rev. D, 90, 123004

Bertone G., Hooper D., Silk J., 2005, Phys. Rep., 405, 279

Bett P., Eke V., Frenk C. S., Jenkins A., Okamoto T., 2010, MNRAS, 404, 1137

Binney J., Tremaine S., 1987, Galactic Dynamics

Blumenthal G. R., Faber S. M., Primack J. R., Rees M. J., 1984, Nature, 311, 517

Bonamigo M., Despali G., Limousin M., Angulo R., Giocoli C., Soucail G., 2015, MNRAS, 449, 3171

Bond J. R., Cole S., Efstathiou G., Kaiser N., 1991, ApJ, 379, 440

Boylan-Kolchin M., Ma C.-P., 2004, MNRAS, 349, 1117

Boylan-Kolchin M., Ma C.-P., 2007, MNRAS, 374, 1227

Boylan-Kolchin M., Bullock J. S., Kaplinghat M., 2011, MNRAS, 415, L40

Buchmueller O., Doglioni C., Wang L.-T., 2017, Nature Physics, 13, 217

Bullock J. S., Boylan-Kolchin M., 2017, ARA&A, 55, 343

Bullock J. S., Kolatt T. S., Sigad Y., Somerville R. S., Kravtsov A. V., Klypin A. A., Primack J. R., Dekel A., 2001a, MNRAS, 321, 559

Bullock J. S., Dekel A., Kolatt T. S., Kravtsov A. V., Klypin A. A., Porciani C., Primack J. R., 2001b, ApJ, 555, 240

Burkert A., 2000, ApJ, 534, L143

Butsky I., et al., 2016, MNRAS, 462, 663

Carucci I. P., Sparre M., Hansen S. H., Joyce M., 2014, J. Cosmology Astropart. Phys., 6, 057

Choi J.-H., Weinberg M. D., Katz N., 2007, MNRAS, 381, 987

Choi J.-H., Weinberg M. D., Katz N., 2009, MNRAS, 400, 1247

Clowe D., Gonzalez A., Markevitch M., 2004, ApJ, 604, 596

Colpi M., Mayer L., Governato F., 1999, ApJ, 525, 720

Cyburt R. H., Fields B. D., Olive K. A., Yeh T.-H., 2016, Reviews of Modern Physics, 88, 015004

Despali G., Giocoli C., Tormen G., 2014, MNRAS, 443, 3208

Despali G., Giocoli C., Bonamigo M., Limousin M., Tormen G., 2017, MNRAS, 466, 181

Di Mauro M., Hou X., Eckner C., Zaharijas G., Charles E., 2019, arXiv e-prints,

Diemand J., Kuhlen M., Madau P., 2007, ApJ, 657, 262

Diemand J., Kuhlen M., Madau P., Zemp M., Moore B., Potter D., Stadel J., 2008, Nature, 454, 735

Diemer B., More S., Kravtsov A. V., 2013, ApJ, 766, 25

Doré O., et al., 2019, arXiv e-prints, p. arXiv:1904.01174

Drakos N. E., Taylor J. E., Benson A. J., 2017, MNRAS, 468, 2345

Drakos N. E., Taylor J. E., Berrouet A., Robotham A. S. G., Power C., 2019, MNRAS, p. 1252

Dubinski J., Carlberg R. G., 1991, ApJ, 378, 496

Duffy A. R., Schaye J., Kay S. T., Dalla Vecchia C., 2008, MNRAS, 390, L64

Dutton A. A., Macciò A. V., 2014, MNRAS, 441, 3359

Eddington A. S., 1916, MNRAS, 76, 572

Einasto J., 1965, Trudy Inst. Astrofiz. Alma-Ata, 5, 87

Fakhouri O., Ma C.-P., Boylan-Kolchin M., 2010, MNRAS, 406, 2267

Farouki R. T., Shapiro S. L., Duncan M. J., 1983, ApJ, 265, 597

Flores R. A., Primack J. R., 1994, ApJ, 427, L1

Frenk C. S., White S. D., 2012, Annalen der Physik, 524, 507

Fulton E., Barnes J. E., 2001, Ap&SS, 276, 851

Gao L., Navarro J. F., Cole S., Frenk C. S., White S. D. M., Springel V., Jenkins A., Neto A. F., 2008, MNRAS, 387, 536

Gao L., Navarro J. F., Frenk C. S., Jenkins A., Springel V., White S. D. M., 2012, MNRAS, 425, 2169

Ghigna S., Moore B., Governato F., Lake G., Quinn T., Stadel J., 1998, MNRAS, 300, 146

Gill S. P. D., Knebe A., Gibson B. K., 2004, MNRAS, 351, 399

Grillo C., et al., 2015, ApJ, 800, 38

Guo Y., Li Z., 2008, Communications in Mathematical Physics, 279, 789

Guo Q., Cole S., Eke V., Frenk C., 2012, MNRAS, 427, 428

Halle A., Colombi S., Peirani S., 2019, A&A, 621, A8

Han J., Cole S., Frenk C. S., Jing Y., 2016, MNRAS, 457, 1208

Hayashi E., Navarro J. F., Taylor J. E., Stadel J., Quinn T., 2003, ApJ, 584, 541

Hernquist L., 1990, ApJ, 356, 359

Hernquist L., 1993, ApJS, 86, 389

Hjorth J., Williams L. L. R., 2010, ApJ, 722, 851

Hunter C., 1977, AJ, 82, 271

Hütten M., Stref M., Combet C., Lavalle J., Maurin D., 2019, preprint, (arXiv:1904.10935)

Ishiyama T., 2014, ApJ, 788, 27

Jauzac M., et al., 2016, MNRAS,

Jiang L., Cole S., Sawala T., Frenk C. S., 2015, MNRAS, 448, 1674

Jing Y. P., 2000, ApJ, 535, 30

Jing Y. P., Suto Y., 2002, ApJ, 574, 538

Just A., Peñarrubia J., 2005, A&A, 431, 861

Kahn F. D., Woltjer L., 1959, ApJ, 130, 705

Kampakoglou M., Benson A. J., 2007, MNRAS, 374, 775

Kazantzidis S., Magorrian J., Moore B., 2004, ApJ, 601, 37

Kazantzidis S., Zentner A. R., Kravtsov A. V., 2006, ApJ, 641, 647

Kazantzidis S., Łokas E. L., Callegari S., Mayer L., Moustakas L. A., 2011, ApJ, 726, 98

Khochfar S., Burkert A., 2006, A&A, 445, 403

King I. R., 1966, AJ, 71, 64

Kitching T. D., et al., 2014, MNRAS, 442, 1326

Klypin A., Kravtsov A. V., Valenzuela O., Prada F., 1999, ApJ, 522, 82

Klypin A., Yepes G., Gottlöber S., Prada F., Heß S., 2016, MNRAS, 457, 4340

Knebe A., Arnold B., Power C., Gibson B. K., 2008, MNRAS, 386, 1029

Knebe A., et al., 2013, MNRAS, 435, 1618

Knollmann S. R., Knebe A., 2009, ApJS, 182, 608

Lacey C., Cole S., 1993, MNRAS, 262, 627

Lee C. T., Primack J. R., Behroozi P., Rodríguez-Puebla A., Hellinger D., Dekel A., 2017, MNRAS, 466, 3834

Macciò A. V., Dutton A. A., van den Bosch F. C., Moore B., Potter D., Stadel J., 2007, MNRAS, 378, 55

Markevitch M., Gonzalez A. H., Clowe D., Vikhlinin A., Forman W., Jones C., Murray S., Tucker W., 2004, ApJ, 606, 819

Mashchenko S., Sills A., 2004, ApJ, 605, L121

Mashchenko S., Sills A., 2005a, ApJ, 619, 243

Mashchenko S., Sills A., 2005b, ApJ, 619, 258

Maulbetsch C., Avila-Reese V., Colín P., Gottlöber S., Khalatyan A., Steinmetz M., 2007, ApJ, 654, 53

McConnachie A. W., 2012, AJ, 144, 4

McMillan P. J., Athanassoula E., Dehnen W., 2007, MNRAS, 376, 1261

Meneghetti M., et al., 2014, ApJ, 797, 34

Merritt D., Graham A. W., Moore B., Diemand J., Terzić B., 2006, AJ, 132, 2685

Michie R. W., Bodenheimer P. H., 1963, MNRAS, 126, 269

Moetazedian R., Just A., 2016, MNRAS, 459, 2905

Moore B., 1994, Nature, 370, 629

Moore B., Ghigna S., Governato F., Lake G., Quinn T., Stadel J., Tozzi P., 1999, ApJ, 524, L19

Moore B., Kazantzidis S., Diemand J., Stadel J., 2004, MNRAS, 354, 522

Motl P. M., Hallman E. J., Burns J. O., Norman M. L., 2005, ApJ, 623, L63

Mróz P., et al., 2019, ApJ, 870, L10

Muldrew S. I., Pearce F. R., Power C., 2011, MNRAS, 410, 2617

Nagai D., 2006, ApJ, 650, 538

Navarro J. F., 1989, MNRAS, 239, 257

Navarro J. F., Frenk C. S., White S. D. M., 1996, ApJ, 462, 563

Navarro J. F., Frenk C. S., White S. D. M., 1997, ApJ, 490, 493

Navarro J. F., et al., 2004, MNRAS, 349, 1039

Navarro J. F., et al., 2010, MNRAS, 402, 21

Neto A. F., et al., 2007, MNRAS, 381, 1450

Nusser A., Sheth R. K., 1999, MNRAS, 303, 685

Ogiya G., Hahn O., 2018, MNRAS, 473, 4339

Ogiya G., Nagai D., Ishiyama T., 2016, MNRAS, 461, 3385

Oguri M., Lee J., 2004, MNRAS, 355, 120

Oguri M., Takada M., Okabe N., Smith G. P., 2010, MNRAS, 405, 2215

Okabe N., Smith G. P., Umetsu K., Takada M., Futamase T., 2013, ApJ, 769, L35

Okoli C., Taylor J. E., Afshordi N., 2018, J. Cosmology Astropart. Phys., 8, 019

Onions J., et al., 2012, MNRAS, 423, 1200

Ostriker J. P., Peebles P. J. E., 1973, ApJ, 186, 467

Ostriker J. P., Peebles P. J. E., Yahil A., 1974, ApJ, 193, L1

Ouellette N. N.-Q., et al., 2017, ApJ, 843, 74

Peñarrubia J., Just A., Kroupa P., 2004, MNRAS, 349, 747

Peñarrubia J., McConnachie A. W., Navarro J. F., 2008a, ApJ, 672, 904

Peñarrubia J., Navarro J. F., McConnachie A. W., 2008b, ApJ, 673, 226

Peñarrubia J., Navarro J. F., McConnachie A. W., Martin N. F., 2009, ApJ, 698, 222

Peñarrubia J., Benson A. J., Walker M. G., Gilmore G., McConnachie A. W., Mayer L., 2010, MNRAS, 406, 1290

Peebles P. J. E., 1969, ApJ, 155, 393

Peebles P. J. E., 1971, Physical cosmology

Pilipenko S. V., Sánchez-Conde M. A., Prada F., Yepes G., 2017, MNRAS, 472, 4918

Planck Collaboration et al., 2016, A&A, 594, A13

Planck Collaboration et al., 2018, arXiv e-prints, p. arXiv:1807.06209

Pontzen A., Governato F., 2013, MNRAS, 430, 121

Poole G. B., Babul A., McCarthy I. G., Fardal M. A., Bildfell C. J., Quinn T., Mahdavi A., 2007, MNRAS, 380, 437

Prada F., et al., 2003, ApJ, 598, 260

Prada F., Klypin A. A., Cuesta A. J., Betancort-Rijo J. E., Primack J., 2012, MNRAS, 423, 3018

Press W. H., Schechter P., 1974, ApJ, 187, 425

Rhodes J., et al., 2017, ApJS, 233, 21

Roberts M. S., Whitehurst R. N., 1975, ApJ, 201, 327

Rubin V. C., Ford W. Kent J., 1970, ApJ, 159, 379

Sales L. V., Helmi A., Battaglia G., 2010, Advances in Astronomy, 2010, 194345

Sánchez-Conde M. A., Prada F., 2014, MNRAS, 442, 2271

Sartoris B., et al., 2016, MNRAS, 459, 1764

Sehgal N., Bode P., Das S., Hernandez-Monteagudo C., Huffenberger K., Lin Y.-T., Ostriker J. P., Trac H., 2010, ApJ, 709, 920

Sereno M., Umetsu K., Ettori S., Sayers J., Chiu I.-N., Meneghetti M., Vega-Ferrero J., Zitrin A., 2018, ApJ, 860, L4

Shaw L. D., Holder G. P., Bode P., 2008, ApJ, 686, 206

Sheth R. K., Mo H. J., Tormen G., 2001, MNRAS, 323, 1

Springel V., 2005, MNRAS, 364, 1105

Springel V., White S. D. M., 1999, MNRAS, 307, 162

Springel V., Yoshida N., White S. D. M., 2001, New Astron., 6, 79

Springel V., et al., 2005, Nature, 435, 629

Springel V., et al., 2008, MNRAS, 391, 1685

Stadel J., Potter D., Moore B., Diemand J., Madau P., Zemp M., Kuhlen M., Quilis V., 2009, MNRAS, 398, L21

Sten Delos M., Bruff M., Erickcek A. L., 2019, arXiv e-prints, p. arXiv:1905.05766

Sunyaev R. A., Zeldovich Y. B., 1970, Ap&SS, 7, 3

Taylor J. E., 2011, Advances in Astronomy, 2011, 604898

Taylor J. E., Babul A., 2001, ApJ, 559, 716

Taylor J. E., Babul A., 2005, MNRAS, 364, 515

Taylor J. E., Navarro J. F., 2001, ApJ, 563, 483

Taylor J. E., Silk J., 2003, MNRAS, 339, 505

Tinker J., Kravtsov A. V., Klypin A., Abazajian K., Warren M., Yepes G., Gottlöber S., Holz D. E., 2008, ApJ, 688, 709

Tomozeiu M., Mayer L., Quinn T., 2016, ApJ, 818, 193

Tormen G., 1997, MNRAS, 290, 411

Tormen G., Bouchet F. R., White S. D. M., 1997, MNRAS, 286, 865

Tormen G., Diaferio A., Syer D., 1998, MNRAS, 299, 728

Tulin S., Yu H.-B., Zurek K. M., 2013, Phys. Rev. D, 87, 115007

Umetsu K., Zitrin A., Gruen D., Merten J., Donahue M., Postman M., 2016, ApJ, 821, 116

Valluri M., Vass I. M., Kazantzidis S., Kravtsov A. V., Bohn C. L., 2007, ApJ, 658, 731

Van Albada T., Bahcall J. N., Begeman K., Sancisi R., 1985, The Astrophysical Journal, 295, 305

Vass I. M., Kazantzidis S., Valluri M., Kravtsov A. V., 2009, ApJ, 698, 1813

Vega-Ferrero J., Yepes G., Gottlöber S., 2017, MNRAS, 467, 3226

Vera-Ciro C. A., Sales L. V., Helmi A., Frenk C. S., Navarro J. F., Springel V., Vogelsberger M., White S. D. M., 2011, MNRAS, 416, 1377

Vera-Ciro C. A., Helmi A., Starkenburg E., Breddels M. A., 2013, MNRAS, 428, 1696

Vera-Ciro C. A., Sales L. V., Helmi A., Navarro J. F., 2014, MNRAS, 439, 2863

Vitvitska M., Klypin A. A., Kravtsov A. V., Wechsler R. H., Primack J. R., Bullock J. S., 2002, ApJ, 581, 799

Wang H. Y., Jing Y. P., Mao S., Kang X., 2005, MNRAS, 364, 424

Watson W. A., Iliev I. T., D'Aloisio A., Knebe A., Shapiro P. R., Yepes G., 2013, MNRAS, 433, 1230

Wechsler R. H., Bullock J. S., Primack J. R., Kravtsov A. V., Dekel A., 2002, ApJ, 568, 52

Wetzel A. R., 2011, MNRAS, 412, 49

Widrow L. M., 2000, ApJS, 131, 39

Widrow L. M., Dubinski J., 2005, ApJ, 631, 838

Wojtak R., Gottlöber S., Klypin A., 2013, MNRAS, 434, 1576

Wong A. W. C., Taylor J. E., 2012, ApJ, 757, 102

Woolley R. V. D. R., 1954, MNRAS, 114, 191

Zemp M., Moore B., Stadel J., Carollo C. M., Madau P., 2008, MNRAS, 386, 1543

Zemp M., Gnedin O. Y., Gnedin N. Y., Kravtsov A. V., 2011, ApJS, 197, 30

Zentner A. R., Bullock J. S., 2003, ApJ, 598, 49

Zentner A. R., Berlind A. A., Bullock J. S., Kravtsov A. V., Wechsler R. H., 2005, ApJ, 624, 505

Zhao D. H., Mo H. J., Jing Y. P., Börner G., 2003, MNRAS, 339, 12

Zhao D. H., Jing Y. P., Mo H. J., Börner G., 2009, ApJ, 707, 354

Zwicky F., 1933, Helvetica Physica Acta, 6, 110

van Kampen E., 2000, preprint, (arXiv:astro-ph/0002027)

van den Bosch F. C., 2002, MNRAS, 331, 98

van den Bosch F. C., Ogiya G., 2018, MNRAS, 475, 4066

van den Bosch F. C., Tormen G., Giocoli C., 2005, MNRAS, 359, 1029

van den Bosch F. C., Ogiya G., Hahn O., Burkert A., 2018, MNRAS, 474, 3043

Appendix A

ICICLE – A Code for Generating Isolated Initial Conditions

The authors have created a publicly available Python package, ICICLE (Initial Conditions for Isolated CoLlisionless systEms), which can create stable initial conditions for spherical, isotropic, collisionless systems with various density profiles. The code currently supports NFW (either exponentially truncated, abruptly truncated, or truncated using the iterative method described in Section 2.2), King, Hernquist and Einasto profiles.

A.1 Files

The main part of the program is in the code "ICICLE.py". The content of this code is described thoroughly in Section A.3; briefly, given a model it returns positions and velocities of n particles within that distribution.

For each model there is an additional file named "ICs_*model*.py". These files contain information about the specific model (the density profile, cumulative mass distribution, gravitational potential and distribution function). The user can specify parameters by use of a parameter file.

A.2 Output

The output is written to the filename specified. The first line of the text file has the following information: the number of particles, the mass of each particle and the value of the gravitational constant. Subsequent lines display the particle number (indexed from 0), the x, y and z positions, and the x, y, and z velocity components.

A.3 Positions and Velocities

In this section we outline the steps needed to select positions and velocities given an isotropic density profile, in a manner similar to Kazantzidis et al. (2004). First, the radial distance for each particle is selected using the cumulative mass distribution, and then a direction for the position vector is selected assuming spherical symmetry. Next, an energy is selected from the energy distribution. Once the position and energy of the particle have been determined, it is straightforward to calculate the velocity of the particle. Finally, the velocity direction is chosen isotropically.

A.3.1 Positions

The radius for each particle is chosen in such a way as to reproduce the mass distribution. Consider a density profile where the mass within a given radius r is $M(< r)$, and the largest radius is $r_{\rm max}$. The mass fraction interior to r is then:

$$F_M(< r) = \frac{M(< r)}{M(r_{\rm max})} \quad . \tag{A.1}$$

If we choose a random variate x uniformly on the interval $[0, 1]$, we can then set $F_M(< r) = x$ and solve for r to find a corresponding radius. In the limit of a large number of particles, the resulting set of radii will reproduce the desired density profile. Given a radius, we can then choose a direction isotropically, by choosing a random point on the surface of a unit sphere.

A.3.2 Calculating The Distribution Function

The distribution function, $f(\mathcal{E})$, is given by Eddington's formula:

$$f(\mathcal{E}) = \frac{1}{\sqrt{8}\pi^2}\left[\int_0^{\mathcal{E}} \frac{1}{\sqrt{\mathcal{E}-\Psi}}\frac{{\rm d}^2\rho}{{\rm d}\Psi^2}d\Psi + \frac{1}{\sqrt{\mathcal{E}}}\left(\frac{{\rm d}\rho}{{\rm d}\Psi}\right)_{\Psi=0}\right] \quad . \tag{A.2}$$

Here $\mathcal{E}$, Ψ and ρ are the relative energy, the relative potential and the density, respectively. black The second, boundary term is equal to $f(0)$ in general (since the first term evaluates to zero when $\mathcal{E} = 0$), so it vanishes for any system with $f(0) = 0$.

Consider the term $\mathrm{d}^2\rho/\mathrm{d}\Psi^2$. This can be expressed as:

$$\begin{aligned} \frac{\mathrm{d}^2\rho}{\mathrm{d}\Psi^2} &= \left(\frac{\mathrm{d}\Psi}{\mathrm{d}r}\right)^{-2}\left[\frac{\mathrm{d}^2\rho}{\mathrm{d}r^2} - \left(\frac{\mathrm{d}\Psi}{\mathrm{d}r}\right)^{-1}\frac{\mathrm{d}^2\Psi}{\mathrm{d}r^2}\frac{\mathrm{d}\rho}{\mathrm{d}r}\right] \\ &\text{or, since} \qquad \frac{\mathrm{d}\Psi}{\mathrm{d}r} = -\frac{GM}{r^2} \\ &\text{and} \qquad \frac{\mathrm{d}^2\Psi}{\mathrm{d}r^2} = \frac{2GM}{r^3} - 4\pi G\rho \\ \frac{\mathrm{d}^2\rho}{\mathrm{d}\Psi^2} &= \left(\frac{r^4}{G^2M^2}\right)\left[\frac{\mathrm{d}^2\rho}{\mathrm{d}r^2} + \left(\frac{r^2}{GM}\right)\left[\frac{2GM}{r^3} - 4\pi G\rho\right]\frac{\mathrm{d}\rho}{\mathrm{d}r}\right] \quad . \end{aligned} \tag{A.3}$$

This form is more convenient in cases where ρ is an analytic function of radius, as it avoids having to take potentially noisy numerical derivatives.

A.3.3 Choosing From the Distribution Function

The probability that a particle located at radius r has a relative energy $\mathcal{E}$ is proportional to $f(\mathcal{E})\sqrt{\Psi - \mathcal{E}}$, with a maximum energy of $\mathcal{E}_{\max} = \Psi(r)$.

Thus, the cumulative distribution function (CDF) $F(< \mathcal{E})$, for a particle at position r with relative potential energy $\Psi(r)$, is:

$$F(< \mathcal{E}) = \frac{\int_0^{\mathcal{E}} f(\mathcal{E})\sqrt{\Psi - \mathcal{E}}\,\mathrm{d}\mathcal{E}}{\int_0^{\Psi} f(\mathcal{E})\sqrt{\Psi - \mathcal{E}}\,\mathrm{d}\mathcal{E}} \quad . \tag{A.4}$$

Choosing a random variate y uniformly on the interval $[0, 1]$, we can set $F(< \mathcal{E}) = y$ and solve for $\mathcal{E}$ to find the corresponding relative energy. In practice, we do this by linear interpolation of a numerically determined CDF.

A.3.4 Velocities

Once a position and a relative energy have been chosen for the particle, the velocity magnitude can be calculated from:

$$\mathcal{E} = \Psi - \frac{1}{2}v^2 \quad . \tag{A.5}$$

Finally, a direction for the velocity vector can be chosen isotropically in the same way as described for the positions.

A.4 Profile options and documentation

The code, a list of supported profile types, and full documentation are available as a package, ICICLE, at the URL: https://github.com/ndrakos/ICICLE.

Appendix B

Alternative Models

B.1 Hayashi et al. 2003

Hayashi et al. (2003) proposed that tidally stripped NFW haloes have the form:

$$\rho(r) = \frac{f_t}{1 + (r/r_{\rm te})^3} \rho_{NFW}(r) \ . \tag{B.1}$$

The parameters f_t and $r_{\rm te}$ give a measure of the reduction in central density, and an effective tidal radius. Both of these parameters can be estimated using a single parameter—the bound mass fraction, $m_{\rm bnd}$, of the satellite (Equations 9 and 10 in the paper):

$$\begin{aligned} \log(r_{\rm te}/r_s) &= 1.02 + 1.38 \log m_{\rm bnd} + 0.37 (\log m_{\rm bnd})^2 \\ \log f_t &= -0.007 + 0.35 \log m_{\rm bnd} \\ &\quad + 0.39 (\log m_{\rm bnd})^2 + 0.23 (\log m_{\rm bnd})^3 \ . \end{aligned} \tag{B.2}$$

Since $m_{\rm bnd}$ is dependent on the method used to truncate the initial NFW profile, we defined $m_{\rm bnd}$ to be the mass of the bound satellite compared to the mass of an untruncated NFW profile within radius $r_{\rm cut}$.

B.2 Peñarrubia et al. 2010

The Peñarrubia et al. (2010) model considers density profiles of the form:

$$\rho(r) = \frac{\rho_0}{(r/r_s)^\gamma [1 + (r/r_s)^\alpha]^{(\beta-\gamma)/\alpha}} \ . \tag{B.3}$$

For this chapter, we only consider NFW profiles, which have $(\alpha, \beta, \gamma) = (1, 3, 1)$. The procedure for determining the evolution of the profile is outlined in the following steps.

Step 1

First, the bound mass fraction of the satellite as calculated. As before, we calculated $m_{\rm bnd}$ as the mass of the bound satellite compared to the mass of an untruncated NFW profile within radius $r_{\rm cut}$. If $m_s/m_s(0) \leq 0.9$, then $(\alpha, \beta, \gamma) \rightarrow (\alpha, 5, \gamma)$.

Step 2

Secondly, $v_{\rm max}$ and $r_{\rm max}$ (the peak of the circular velocity curve and corresponding radius) can be calculated empirically. As originally described in Peñarrubia et al. (2008b), the evolution of various subhalo structural parameters can be described by

$$g(x) = \frac{2^{\mu} x^{\eta}}{(1+x)^{\mu}} \ , \tag{B.4}$$

where $x \equiv m_s/m_s(0)$ is the mass fraction. In Peñarrubia et al. (2010) they showed that for an NFW profile, the best fit parameters are $(\mu, \eta) = (0.4, 0.3)$ for $g(x) = v_{\rm max}/v_{\rm max}(0)$, and $(\mu, \eta) = (-0.3, 0.4)$ for $g(x) = r_{\rm max}/r_{\rm max}(0)$.

Step 3

The scale radius, r_s can be calculated from the circular velocity profile, $V_c = \sqrt{GM(r)/r}$, by noting that $\mathrm{d}V_c/\mathrm{d}r(r_{\rm max}) = 0$. Then,

$$\left.\frac{\mathrm{d}M}{\mathrm{d}r}\right|_{r=r_{\rm max}} = \frac{M(r_{\rm max})}{r_{\rm max}} \tag{B.5}$$

For an NFW ($(\alpha, \beta, \gamma) = (1, 3, 1)$) profile:

$$\begin{aligned} M(r) &= 4\pi\rho_0 r_s^3 \left[\ln\left(\frac{r_s + r}{r_s}\right) - \frac{r}{r_s + r}\right] \\ \frac{\mathrm{d}M(r)}{\mathrm{d}r} &= 4\pi\rho_0 r_s^3 \frac{r}{(r + r_s)^2} \end{aligned} \tag{B.6}$$

while, for a $(\alpha, \beta, \gamma) = (1, 5, 1)$ profile:

$$\begin{aligned} M(r) &= \frac{2}{3}\pi\rho_0 r_s^3 \frac{(r+3r_s)r^2}{(r+r_s)^3} \\ \frac{\mathrm{d}M(r)}{\mathrm{d}r} &= 4\pi\rho_0 r_s^5 \frac{r}{(r+r_s)^4} \end{aligned} \tag{B.7}$$

Overall, the scale radius of a stripped NFW profile is given by:

$$\begin{aligned} \ln\left(\frac{r_s + r_{\max}}{r_s}\right) &= \frac{r_{\max}^2}{(r_{\max}+r_s)^2} + \frac{r_{\max}}{r_s + r_{\max}} \\ &\qquad \text{for } \; m_s/m_s(0) > 0.9 \\ r_s &= \left(\frac{2}{3} + \frac{\sqrt{7}}{3}\right) r_{\max} \;\; \text{for } \; m_s/m_s(0) \leq 0.9 \end{aligned} \tag{B.8}$$

Step 4

Finally, ρ_0 can be calculated by using $v_{\max} = v_{\mathrm{circ}}(r_{\max})$:

$$\begin{aligned} \rho_0 &= \frac{v_{\max}^2 r_{\max}}{G}\left(4\pi r_s^3\left[\ln\left(\frac{r_s + r_{\max}}{r_s}\right) - \frac{r_{\max}}{r_s + r_{\max}}\right]\right)^{-1} \;\; , \\ &\qquad \text{for } \; m_s/m_s(0) > 0.9 \\ \rho_0 &= \frac{v_{\max}^2 r_{\max}}{G}\left(\frac{2}{3}\pi r_s^3 \frac{(r_{\max}+3r_s)r_{\max}^2}{(r_{\max}+r_s)^3}\right)^{-1} \;\; , \\ &\qquad \text{for } \; m_s/m_s(0) \leq 0.9 \;\; . \end{aligned} \tag{B.9}$$

Appendix C

Inner Slope

Fig. C.1 shows changes in the inner slope, γ'/γ, calculated between $r = 0.1\,r_{\rm peak}$ and $r = 0.4\,r_{\rm peak}$. This quantity does not seem to scale in a predictable way with either the orbital parameters or the change in internal energy. There is potentially a trend with the initial separation of the haloes, $r_{\rm sep}$ (represented by the size of the symbols). This is consistent with the findings from Ogiya et al. (2016), who found that the change in inner slope depends on $r_{\rm sep}$.

The relation between γ'/γ and κ is somewhat similar to that between $r'_{\rm peak}/r_{\rm peak}$ and κ. Therefore, we also show the relation between γ'/γ and $r'_{\rm peak}/r_{\rm peak}$ in Fig. C.2. This demonstrates a correlation between these two parameters, suggesting that the complicated changes in $r_{\rm peak}$ may be due to a combination of mass rearrangement and evolution of the inner slope of the remnant.

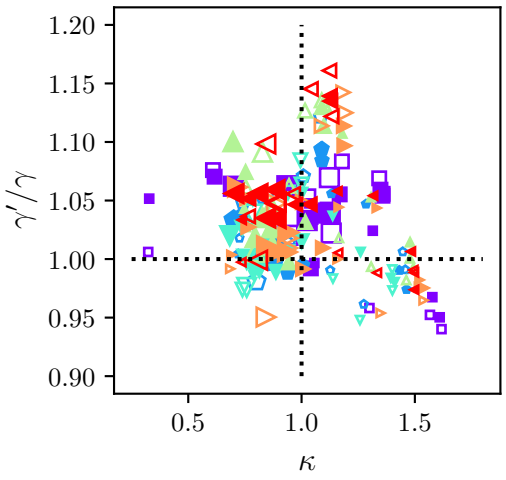

Figure C.1: The change in the inner slope, γ'/γ, calculated between $r = 0.1\,r_{\rm peak}$ and $r = 0.4\,r_{\rm peak}$ as a function of the relative energy change κ. The dotted lines are the expectations for self-similar evolution of the density profile. Colours and symbols are as in Fig. 5.1.

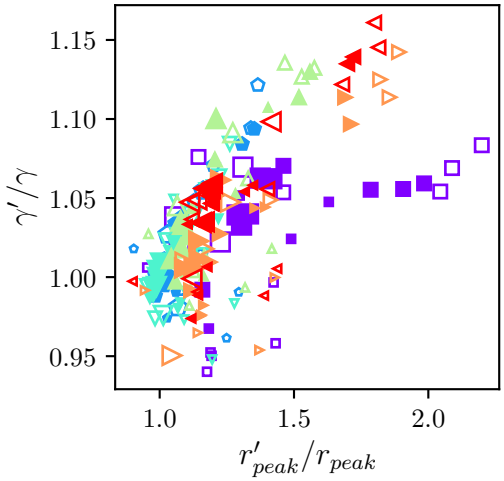

Figure C.2: The change in the inner slope, γ'/γ, calculated between $r = 0.1\,r_{\rm peak}$ and $r = 0.4\,r_{\rm peak}$ compared to the change in the radius corresponding to the peak in the circular velocity curve $r'_{\rm peak}/r_{\rm peak}$. Colours and symbols are as in Fig. 5.1.

Appendix D

Comparison of Different Concentration Measurements

As the traditional definition of the concentration parameter depends on the scale radius r_{-2}, in Fig. D.1 we compare the values measured directly from the density profile, as explained in Section 5.3.2, to the values derived from the NFW and Einasto fits. The Einasto fit predicts larger scale radii than the direct measurement, except in some of the simulations with low initial radial separations, and in general there is considerable scatter between the two sets of measurements. The values of r_{-2} from Einasto and NFW profile fits are in much better agreement, except for the case of the EinLow simulations, where the Einasto fit predicts systematically larger scale radii.

Additionally, we compare concentration measured through either NFW or Einasto fits in Fig. D.2. The two methods roughly agree, though there is some scatter. Some of this scatter may be from systematic errors in NFW fits; it has been shown that NFW fits over-predict the halo concentration by 10–20 per cent for high-ν haloes (Klypin et al., 2016). We find a similar result; although changes in concentration measured from NFW fits are slightly lower than from Einasto fits, the actual concentration values are higher for the NFW fits, particularly for the EinLow simulations.

Since the halo remnants presented in this study are not, in general, self-similar to the ICs, we do not expect the relative change in concentration calculated using the method of Moore et al. (2004), c'_M/c_M, to match the actual value found by profile fitting. To demonstrate this, we compare c'_M/c_M to the change in concentration measured through $c_{\rm Ein} = r_{\rm vir}/r_{-2}$ (calculated from the best Einasto fit) in Fig. D.3. As expected, there is a large discrepancy between these two measurements, further emphasizing that the profile

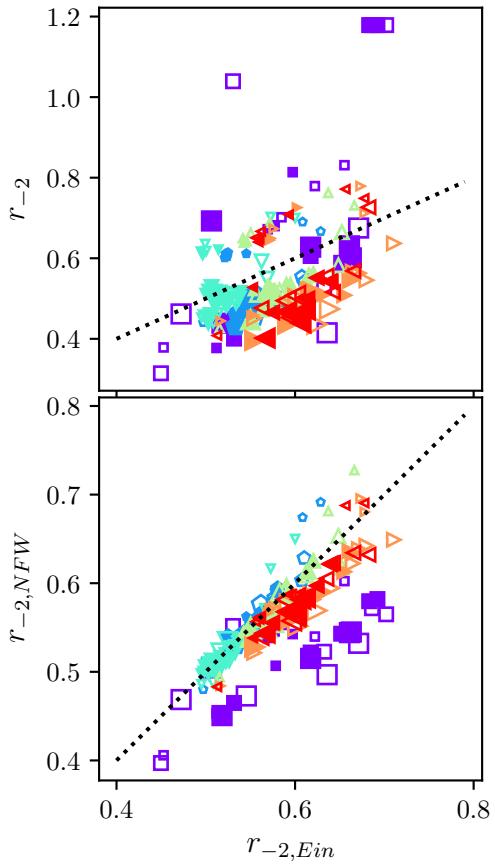

Figure D.1: Comparison of the scale radius measured directly from the slope of the density profile (top), and determined from the NFW fit (bottom), to the value determined from the Einasto fit. Dotted lines indicate a 1–1 relation. Colours and symbols are as in Fig. 5.1.

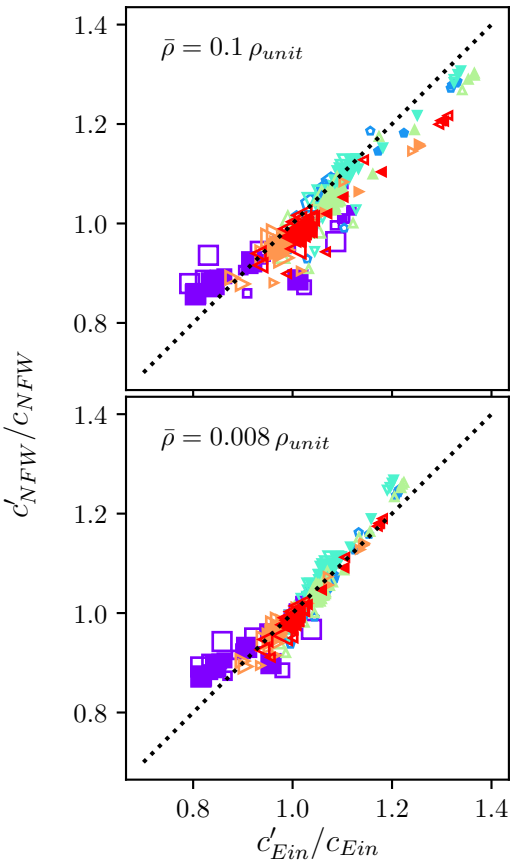

Figure D.2: A comparison of the concentration change calculated from the NFW fit, $c = r_{\rm vir}/r_s$ versus the concentrations calculated from the Einasto fit, $c = r_{\rm vir}/r_{-2}$. The virial radii were calculated using overdensities $\bar{\rho} = 0.1\,\rho_{\rm unit}$ (top) and $0.008\,\rho_{\rm unit}$ (bottom). The dotted line shows where the two definitions are equal. Colours and symbols are as in Fig. 5.1.

remnants do not evolve in a self-similar manner. In Fig. D.4, we also show c'_M/c_M as a function of κ.

Finally, in Fig. D.5 we show the concentration, c, as a function of R for NFW and various Einasto profiles. To calculate $f(x_{\rm peak})$, for Einasto profiles, we used the approximation $x_{\rm peak} \approx 3.15 \exp\left(-0.64\alpha_E^{1/3}\right)$ (Klypin et al., 2016).

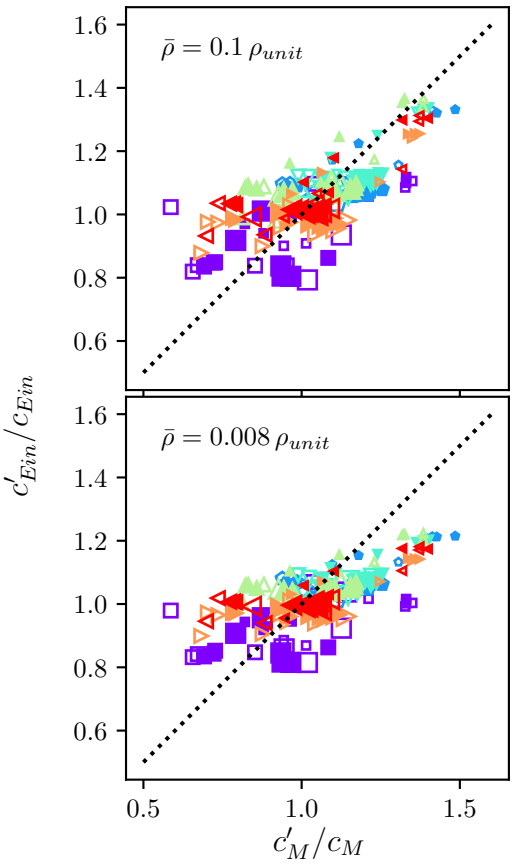

Figure D.3: A comparison of the concentration change calculated from the Einasto fit, $c_{\rm Ein} = r_{\rm vir}/r_{-2}$ versus the concentration calculated as c_M (see Equation (5.12)). The dotted line shows where the two definitions are equal. Top and bottom panels use the overdensity of an NFW profile of concentration 3 ($\bar{\rho} = 0.1\,\rho_{\rm unit}$) and 10 ($\bar{\rho} = 0.008\,\rho_{\rm unit}$) to calculate the virial radii, respectively. Colours and symbols are as in Fig. 5.1.

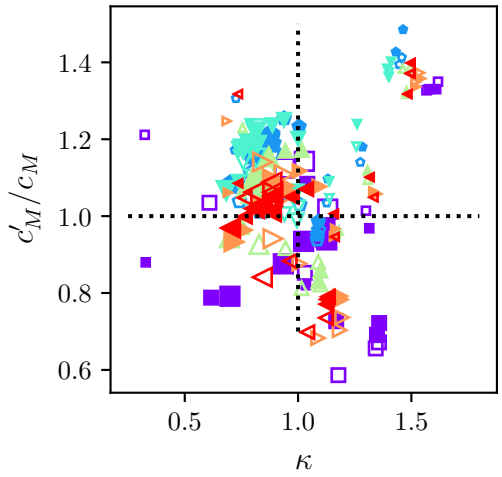

Figure D.4: Concentration change c'_M/c_M as a function of the relative energy change, κ. Colours and symbols are as in Fig. 5.1.

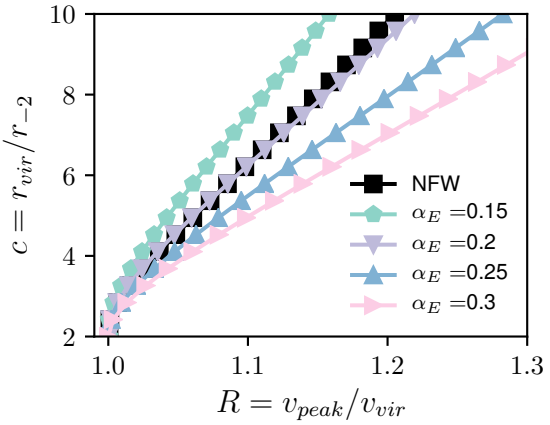

Figure D.5: Relationship between $R = v_{\rm peak}/v_{\rm vir}$ and the concentration, $c = r_{\rm vir}/r_{-2}$ for an NFW profile and Einasto profiles with varying α_E parameters.